SIMULATING RADIATIVE FEEDBACK AND THE FORMATION OF MASSIVE STARS

SIMULATING RADIATIVE FEEDBACK AND THE FORMATION OF MASSIVE STARS

By
MIKHAIL KLASSEN, B.Sc., M.Sc.

A Thesis
Submitted to the School of Graduate Studies
in Partial Fulfillment of the Requirements
for the Degree of

Doctor of Philosophy

McMaster University

DOCTOR OF PHILOSOPHY (2016)
(Physics and Astronomy)

McMaster University
Hamilton, Ontario

TITLE: Simulating Radiative Feedback and the Formation of Massive Stars

AUTHOR: Mikhail Klassen, B.Sc. (Columbia University), M.Sc. (McMaster University)

SUPERVISOR: Professor Ralph E. Pudritz

NUMBER OF PAGES: xxv, 281

Abstract

This thesis is a study of massive star formation: the environments in which they form and the effect that their radiation feedback has on their environments. We present high-performance supercomputer simulations of massive star formation inside molecular cloud clumps and cores. First, we present a novel radiative transfer code that hybridizes two previous approaches to radiative transfer (raytracing and flux-limited diffusion) and implements it in a Cartesian grid-based code with adaptive mesh refinement, representing the first of such implementations. This hybrid radiative transfer code allows for more accurate calculations of the radiation pressure and irradiated gas temperature that are the hallmark of massive star formation and which threaten to limit the mass which stars can ultimately obtain. Next, we apply this hybrid radiative transfer code in simulations of massive protostellar cores. We simulate their gravitational collapse and the formation of a massive protostar surrounded by a Keplerian accretion disk. These disks become gravitationally unstable, increasing the accretion rate onto the star, but do not fragment to form additional stars. We demonstrate that massive stars accrete material predominantly through their circumstellar disks, and via radiation pressure drive large outflow bubbles that appear stable to classic fluid instabilities. Finally, we present simulations of the larger context of star formation: turbulent, magnetised, filamentary cloud clumps. We study the magnetic field geometry and accretion flows. We find that in clouds where the turbulent and magnetic energies are approximately equal, the gravitational energy must dominate the kinetic energy for there to be a coherent magnetic field structure. Star cluster formation takes place inside the primary filament and the photoionisation feedback from a single massive star drives the creation of a bubble of hot, ionised gas that ultimately engulfs the star cluster and destroys the filament.

To Sheila.

Acknowledgments

Stars may form in the vacuum of space, but the same cannot be said of a dissertation. Many people were involved in this enterprise and it could not have come together but for a combination of circumstances and the help of some special individuals.

I would first of all like to thank my supervisor, Ralph Pudritz, for guiding this project, for trusting in my abilities, for connecting me with the right individuals who would be very influential in my research, and for his keen eye towards the big picture. The results of this thesis had a long gestation period. A new radiative transfer code needed to be developed and thoroughly tested. This took much longer than planned, following the old programming maxim that however much time one thinks one needs to debug a code, it will probably take at least twice that long. Ralph Pudritz was patient with me during the *years* it took to develop and debug the radiative transfer code we put into FLASH.

I would also like to express my gratitude for the rest of my supervisory committee, which included Christine Wilson and James Wadsley. They've been supportive of my work and have always given good recommendations and guidance.

In the development of this code, Rolf Kuiper was instrumental. The code we implemented in FLASH is based on a similar code that Rolf wrote for PLUTO. It was not a matter of copying and pasting, however. The method needed to be re-implemented using the code architecture of FLASH, its inherent diffusion solver, various modules that I needed to port from version 2 to version 4 of FLASH, including the raytracer and protostellar evolution module from my M.Sc. thesis. And then nothing worked for the longest time. Patiently, Rolf and my collaborators helped me through each impasse until a working code had come together.

To these collaborators I owe much thanks: Thomas Peters, for his knowledge of and assistance with the hybrid-characteristics raytracer; Robi

Banerjee, for insightful comments on the project at many stages; Lars Buntemeyer, for his suggestions and comments on the manuscript of Chapter 2; and Helen Kirk, for her diligent help collaborating on the filaments project.

The research for this thesis involved a fair amount of travel, and in the places I stayed, many have made me feel welcome, volunteering their time to help me with my research. In Hamburg, this was Robi Banerjee. In Heidelberg, I had help at various times from Ralf Klessen and Rolf Kuiper, as well as Sarah Ragan and Paul Clark. Among my German friends, thanks also to Daniel Seifried, Philipp Girichidis, and Christian Baczynski. In Chicago, during my visits to the FLASH Center, I was helped a great deal by Klaus Weide, with additional help from Anshu Dubey, Dongwook Lee, and Petros Tzeferacos. I also benefited from my interactions with Donald Lamb, Carlo Graziani, and Milad Fatenejad. And though we never met in person, Manos Chatzopoulos helped me with a modified version of an unsplit hydro solver.

In May of 2014, I was accepted to participate as an affiliate the workshop and program "Gravity's Loyal Opposition: The Physics of Star Formation Feedback" at the Kavli Institute for Theoretical Physics (KITP) at the University of Santa Barbara. My participation in the program allowed for many useful conversations that furthered my code development process and research. I am grateful for input from Romain Teyssier, Christoph Federrath, Benoît Commerçon, and Norm Murray.

Some interractions can't take place in person, but must happen over e-mail. I'm grateful to Stella Offner and Mark Krumholz, who answered my research questions over e-mail even before they knew me. It was nice to later share a beer with Mark at *Protostars & Planets VI* in Heidelberg, and a glass of viognier in Santa Barbara with Stella during the KITP program. I'm also grateful to Thierry Sousbie, who agreed to share with me a pre-release version of the DisPerSE code so that Helen Kirk, Samantha Pillsworth, and I could use to launch our study of filaments in molecular cloud simulations.

Closer to home, my colleagues at McMaster University have been tremendous to work with and alongside. I am grateful to them for our many converations, for their help, and for their friendship. These are, especially, Rory Woods, Rachel Ward-Maxwell, Alyssa Cobb, Alex Cridland, Jeremy Webb, Rob Cockcroft, Tara Parkin, Max Schirm, Kaz Sliwa, Samantha Benincasa, Matthew Alessi, Aaron Maxwell, Ben Keller, Kevin Sooley, Matthew McCreadie, Nick Miladinovic, Leo van Nierop, Ben Jackel, Gabriel Devenyi, Elizabeth Tasker, Helen Kirk, René Heller, and Samantha Pillsworth. I am also grateful to the department secretaries, for their tireless work in helping things run smoothly: Tina Stewart, Rosemary McNeice, Mara Esposto, and Cheryl Johnston; and to Hua Wu, the department systems administrator, who can magically discern hard disk failures before they actually happen and stage the appropriate intervention.

Outside of the department, a group of friends in Hamilton kept me sane when I needed to speak to someone who wasn't a scientist: to Tessa Klettl and Nicole Ní Ríordáin, thank you for your friendship; also to my close circle of Seth Enriquez, Owen Pikkert, and Danielle Wong, I owe a great debt of friendship.

After moving to Calgary during the last year of my Ph.D. I was often in need of a place to stay during my regular visits back to Hamilton. Several wonderful people stepped forward and offered me a place to stay during those times and they need to be thanked here. Firstly, thank you to Mandy Tam and Brian Chan, who opened their home in Burlington to me on many occassions. I also stayed with Joel and Sara Klinck, Rory Woods, Gwendolyn and Aaron Springford, Josh Chu, and Preston Steinke. You all opened your home to me at one time or another, and I am hugely grateful.

I am thankful to my longsuffering parents, Adolfo and Elly Klassen, who encouraged me to persist in this Ph.D. and have supported my education from the beginning. Much of this work I owe to their love. An to my mother- and father-in-law, Rosa Lai and Peter Liu: thank you for your encouragement, your faith in me, and the ways in which you have always been willing to help.

Finally, I would be adrift without my wife, Sheila, to whom I have dedicated this thesis. You are my keel and compass. Thank you for sharing in this journey.

"The worthwhile problems are the ones you can really solve or help solve, the ones you can really contribute something to. A problem is grand in science if it lies before us unsolved and we see some way for us to make some headway into it."

Richard Feynman (1918–1988)

Table of Contents

List of Figures

List of Tables

Chapter 1

Introduction

As far as the physical universe is concerned, stars are engines of creation. The process of their formation takes cold molecular gas—mostly hydrogen—and through the action of gravity confines it to a core. The collapse of this core down to extreme conditions of density and temperature occurs when gravity finally overcomes all other forms of pressure support (turbulence, thermal, magnetic, and radiative). This allows for the onset of nuclear fusion reactions that herald stellar birth. The fusion of light elements into heavier ones releases the energy that heats the gas to provide the pressure to hold it up against its own weight and causes it to radiate. Successive cycles of stellar birth and death, some in the form of supernovae, enriched the universe with heavy elements and provided all the raw materials for planets, asteroids, and ultimately life. It is not an exaggeration to say, then, that stars and understanding how they form are extremely important.

In the catalogue of stars existing in our present universe, massive stars are a rare and special breed, yet they exert an influence on their environments that is greatly disproportionate to their number. They supply most of the heavy elements and ultraviolet radiation found in galaxies. They typically end their short lives as supernova explosions, and during their existence exert powerful forces on the interstellar medium (ISM)—consisting of gas (ionized, atomic, and molecular) and dust—in which they are embedded. Their prodigious luminosities drive stellar winds, outflows, and bubbles of ionized gas called HII regions. Finally, by their supernovae, they might also be important sources of mixing and turbulent energy within galaxies.

Massive stars are generally defined as having masses $M_* > 8\,\mathrm{M}_\odot$, and luminosities above $L_* > 10^3\,L_\odot$ [Cesaroni, 2008]. After their main sequence evolution, massive stars end their lives as supernovae. They are born from extremely dense cores and effectively begin their lives as hydrogen-burning stars on the main sequence [Palla and Stahler, 1993] without any pre-main-sequence evolution. This is in contrast to lower-mass stars, that are born on a well-defined “birthline” on the Hertzsprung-Russell (H-R) diagram [Stahler, 1983], which is defined by the onset of deuterium fusion—the first possible nuclear fuel. They then undergo gravitational contraction until their stellar interiors become hot and dense enough for the fusion of hydrogen. The timescale for this collapse is known as the Kelvin-Helmholz time. Protostars may still be accreting new material at rates of about 10^{-5}–10^{-4} $\mathrm{M}_\odot$/yr and undergoing changes in stellar structure. By contrast, massive stars are accreting at rates in excess of 10^{-3} $\mathrm{M}_\odot$/yr and begin fusing hydrogen almost immediately, even while in the mass accretion phase.

For stars this luminous, the formation scenario becomes problematic. Massive stars drive radiative feedback mechanisms that are not available to low-mass stars—radiation pressure and photoionization [Larson and Starrfield, 1971a]. Wolfire and Cassinelli [1987] predicted accretion rates of $\dot{M} \sim 10^{-3}$

$M_\odot$/yr in order to overcome radiation pressure. Some early spherical collapse (i.e. 1D) calculations sought to determine an upper mass limit for stars, given that there ought to be a critical luminosity capable of halting the accretion flow. The Eddington Luminosity, given by

$$L_{\rm edd} = \frac{4\pi G M_* c}{\kappa}, \tag{1.1}$$

characterizes this limit, where G is Newton's constant, M_* the mass of the star, c the speed of light, and κ the specific opacity of the gas (and its dust content) in units of cm^2/g. Depending on the choice of dust model, this resulted in "upper mass limits" for stars in the range of 20–40 $M_\odot$ [Larson and Starrfield, 1971b, Kahn, 1974, Yorke and Krügel, 1977]. This is, of course, in direct contradiction to observations of stars with masses in excess of 100 $M_\odot$ [Crowther et al., 2010, Doran et al., 2013]. This is another indication that massive star formation must differ from low-mass star formation.

The vast majority of stars are formed in clusters embedded in molecular clouds [Lada and Lada, 2003]. Giant molecular clouds (GMCs) are observed to be inhomogeneous across a wide range of scales [Williams et al., 2000], which is understood to be the result of supersonic turbulence in either magnetized or unmagnetized clouds [Vazquez-Semadeni et al., 2000, Mac Low and Klessen, 2004, Elmegreen and Scalo, 2004, Scalo and Elmegreen, 2004]. Supersonic turbulence also results in the formation of filaments, which both observations and numerical simulations have conclusively shown to be the sites of star formation [André et al., 2014, Mac Low and Klessen, 2004]. If the mass per unit length of a filament exceeds a critical value, it will undergo gravitational fragmentation into bound objects that will collapse to form either a single star or a small multiple system.

Massive stars are rare: they constitute the tail end of the mass spectrum, occurring at a frequency only 10% that of stars in the mass range of 1–2 $M_\odot$. Their environments are more extreme: deeply embedded and highly obscured by dust, it has taken the latest generation of instruments (*Herschel* and ALMA) to properly image these environments and study their properties. The observations now tend to favour monolithic collapse model with disk accretion. Models of coalescence, proposed to circumvent the problem of radiation pressure barriers, are no longer necessary, although coalescence may still occur in a rarity of exceptional circumstance such as ultradense protoclusters.

Radiative forces on dust grains are not dynamically important when modeling low-mass stars, hence numerical simulations may employ simpler models for radiative transport. These radiative forces were long thought to limit monolithic collapse models to stars of $\lesssim 40\,M_\odot$ until sufficiently advanced three-dimensional simulations demonstrated that higher masses were possible.

Our understanding of massive stars today is being greatly advanced by the advent of next-generation telescopes and observatories, such as ALMA, and as well as state-of-the-art numerical simulations that carefully incorporate radiative feedback effects into the hydro- and magnetohydrodynamics of star formation. The work described in this thesis develops a new radiative transfer technique for numerical simulations (Chapter 2), allowing us to perform highly accurate simulations of massive star formation (Chapter 3). We demonstrate how accretion through a circumstellar disk is sufficient to explain the origins of massive stars, despite their having super-Eddington luminosities. The formation of radiatively-driven polar outflow bubbles acts to relieve the pressure on incoming material so that accretion can continue.

We then connect up to the scales of massive cluster formation by presenting numerical simulations of turbulent, magnetized cloud clumps (Chapter 4). Here we address the full filamentary nature of molecular clouds that results from the presence of supersonic turbulence. We investigate how the coevolution of magnetic fields, turbulence, and radiative feedback (specifically ionization) from a massive star affects the filamentary geometry of molecular clouds. In cluster-forming clumps, magnetohydrodynamic and turbulence processes are often in balance, leaving gravity to play a strong role in establishing filamentary flow and magnetic field orientation in forming clusters. Feedback from massive stars can also disrupt filaments, halting accretion and disordering the magnetic field.

In this introduction, we will review the paradigm of star formation presented by current observational evidence and outline the theory of massive star formation. This thesis is comprised of three related journal articles, making up Chapters 2–4. We include a summary of each and some explanatory notes on their context within the field and within this thesis.

1.1 Observations of massive stars

Most stars form inside GMCs [McKee and Ostriker, 2007b], the largest structures inside of galaxies, which have physical scales of $\sim$ 20–100 pc and masses between 10^4 and $10^6\,M_\odot$. Volume-averaged densities inside GMCs are about 50–100 cm^{-3}, which is very low, but molecular gas within clouds is highly inhomogeneous. The temperatures inside GMCs of the Milky Way typically range from 10–15 K [Sanders et al., 1993], which gives a sound speed of 0.2 km/s. The velocity dispersion, based on molecular line widths, is measured to be about 2–3 km/s, indicating the present of highly supersonic turbulence with turbulent Mach numbers of $\mathcal{M} = u/c_s \lesssim 50$ [Mac Low and Klessen, 2004], where u is the gas velocity and c_s is the sound speed. GMCs sometimes contain substructures ("clumps") with masses between a few 100 $\mathrm{M}_\odot$ and a few 1000 $\mathrm{M}_\odot$, sizes of up to a few pc, and mean densities of between 10^3 and 10^5 cm^{-3}. Within these, peak densities can easily exceed 10^6 cm^{-3}. The dense clumps (0.25–0.5 pc) can be identified in (sub)mm continuum emission and molecular line tracers and it is inside the dense clumps that massive star formation is taking place [Beltrán et al., 2006, Beuther et al., 2007].

Among these, infrared dark clouds (IRDCs) are the likely precursor environments for massive star formation. IRDCs are dense molecular clouds seen in extinction against the bright mid-infrared background of the galaxy. An example is given in Figure 1.1 from Jiménez-Serra et al. [2014], where the filamentary IRDC G035.39-00.33 is pictured. The IR-quiet high-mass cores found using the *Herschel Space Observatory* are indicated with ligh-blue filled diamonds. IRDCs are cold ($T < 20$ K), highly turbulent (1–3 km/s) and exhibit considerable velocity structure, with variations of 1–2 km/s over the cloud [Pillai et al., 2006]. They are large (1–10 pc in diameter) compared to dense molecular cloud clores (~ 0.1 pc), with gas at densities of $\sim 10^6$ cm^{-3} [Carey et al., 2000]. They range in mass from 120 to 16000 $\mathrm{M}_\odot$ and contain at least one compact core of size $D \lesssim 0.5pc$, with most IRDCs showing multiple cores [Rathborne et al., 2006]. Given the spectrum of core masses inside IRDCs and assuming that most cores will form one star, then most of these will be OB stars.

This formation process is divided into four stages by [Beuther et al., 2007]:

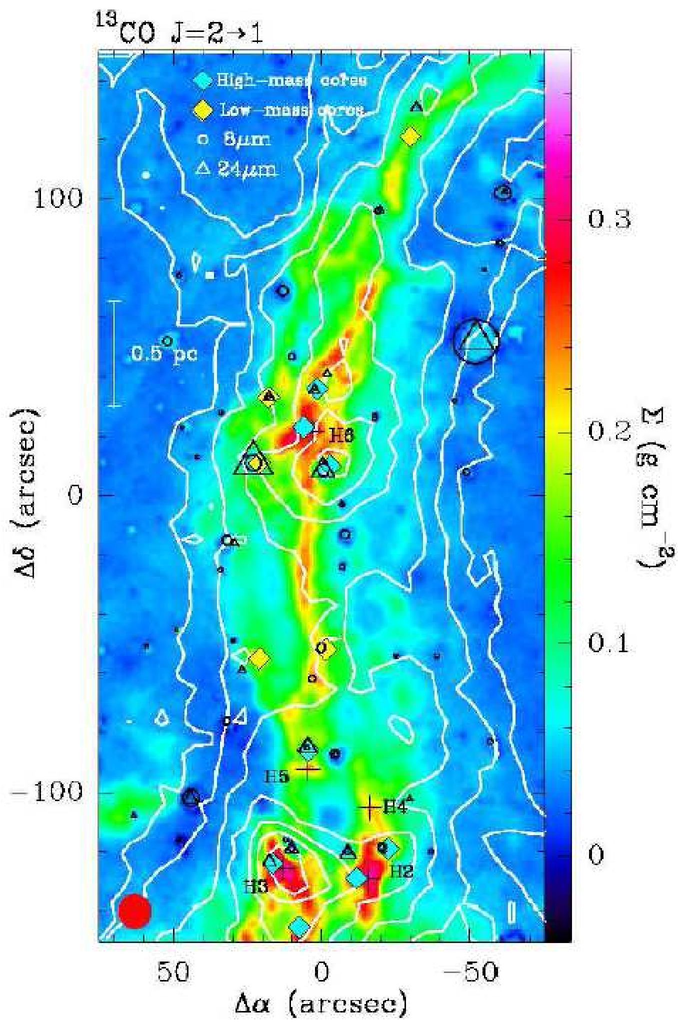

Figure 1.1: Image of the filamentary infrared dark cloud (IRDC) G035.39-00.33. Figure reproduced with permission from Jiménez-Serra, Caselli, Fontani, Tan, Henshaw, Kainulainen, and Hernandez, MNRAS, Volume 439, Issue 2, p.1996–2013, 2014 (Figure 1). White contours show the integrated intensity of the ^{13}CO J=2→1 line emission. These have been superimposed on a mass surface density map from Kainulainen and Tan [2013] (in colour, with an angular resolution of 2"). White contour levels correspond to 33, 40, 50, 60, 70, 80, and 90% of the peak integrated intensity (40 K km s^{-1}). High-mass cores are indicated with crosses and are taken from Butler and Tan [2012]. Black open circles and black open triangles indicate 8 μm and 24 μm sources detected with Spitzer, respectively. Marker sizes are scaled by source flux intensity. Finally, the yellow and light-blue filled diamonds indicate the low-mas cores and IR-quiet high-mass cores, respectively, found by Nguyen Luong et al. [2011] with the *Herschel Space Observatory*.

1. High-mass starless cores (HMSCs)
2. High-mass cores harboring accreting low/intermediate-mass protostar(s) destined to become a high-mass star(s)
3. High-mass protostellar objects (HMPOs)
4. Final stars

HMSCs are difficult to detect, but several candidates have been observed [Sridharan et al., 2005, Olmi et al., 2010]. HMSCs are identified as single-component blackbodies with $T \sim 17$ K. More evolved candidates begin to show a mid-infrared excess [Beuther et al., 2010a], suggestive of the presence of a deeply-embedded protostar. Observations of HMSCs and the transition scenario to HMPOs would support the monolithic collapse hypothesis as the mechanism for forming massive stars. Competing theories such as stellar mergers or the competitive accretion scenario (in which more evolved low- or intermediate-mass stars compete for the gas in a reservoir, accreting via Bondi-Hoyle accretion) predict the absence of HMSCs [McKee and Ostriker, 2007b]. Such observations are extremely rare, but Motte et al. [2007] and Beuther et al. [2015a] identify high-mass starless clumps that will likely collapse to form several massive stars.

Observations by the *Herschel Space Observatory* [Pilbratt et al., 2010] of star-forming regions identify filaments containing high-mass protostellar cores, some of which are associated with HII regions [Hill et al., 2011]. The *Herschel* results favour a star formation scenario in which networks of filaments, followed by the formation of protostellar cores within dense filaments, are the precursors for stars [André et al., 2014].

Filament formation is not completely understood, although turbulence (as well as gravity and magnetic fields) likely play important roles [Hennebelle, 2013]. In particular, the interaction of shocks from supersonic turbulence results in large-scale density enhancements that can take the form of filaments [Ballesteros-Paredes et al., 2007, Pudritz and Kevlahan, 2013].

Prominent filamentary structure is observed in both CO and dust maps for two nearby star-forming clouds: Orion A, with $L \sim 10$ pc, [Bally et al., 1987, Chini et al., 1997, Johnstone and Bally, 1999] and Taurus, with $L \sim 1$ pc, [Abergel et al., 1994, Mizuno et al., 1995, Hartmann, 2002, Nutter et al., 2008, Goldsmith et al., 2008]. As already mentioned, infrared dark clouds also possess filamentary morphology. Myers [2009] noted how filaments would sometimes form hubs in which stellar clusters were observed.

In Figure 1.2 we show a part of the Orion Molecular Cloud complex, in particular the NGC 2024/NGC 2023 field and the Horsehead nebula, reproduced with permission from Megeath et al. [2012]. The image shows the clustered nature of star formation, as captured by the *Spitzer Space Telescope*. Young stars with disks are indicated by the green diamonds, while the red asterisks indicate protostars. The bright central feature is NGC 2024, an HII region. The smaller reflection nebula approximately $20'$ to the south is NGC 2023.

The intersections of some of the densest filaments are associated with massive star formation [Schneider et al., 2012, Peretto et al., 2013]. One of the findings of the *Herschel* mission was the ubiquity of filamentary structure throughout the cold interstellar medium (ISM) [André et al., 2010, Men'shchikov et al., 2010, Molinari et al., 2010, Henning et al., 2010, Motte et al., 2010].

Figure 1.3 shows the Polaris flare imaged using *Herschel*, reproduced

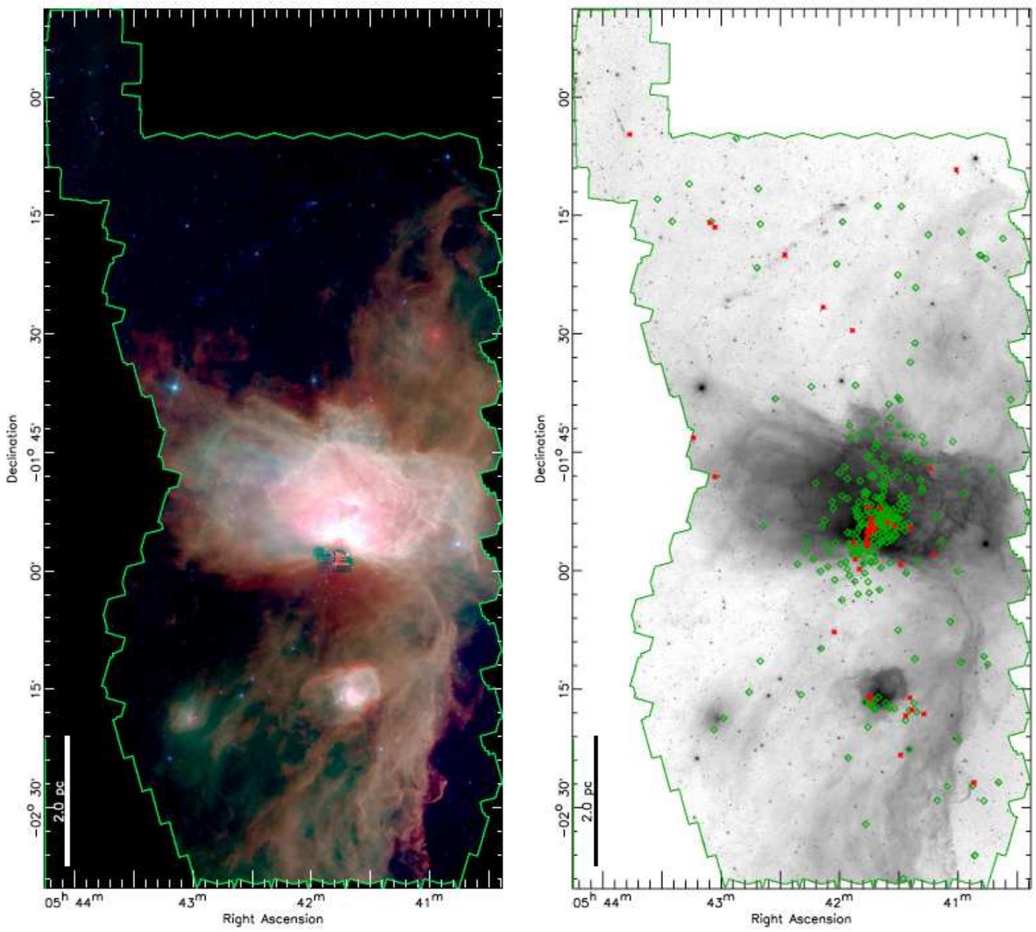

Figure 1.2: Images of a part of the Orion Molecular Cloud, NGC 2024/NGC 2023. Reproduced with permission from Megeath, Gutermuth, Muzerolle, Kryukova, Flaherty, Hora, Allen, Hartmann, Myers, Pipher, Stauffer, Young, and Fazio, AJ, Volume 144, Issue 6, p.192, 2012 (Figure 13). The left image is a mosaic of the NGC 2024/NGC 2023 field with 4.5μm emission coloured in blue, 5.8μm in green, and 24μm in red. The right image shows 4.5μm emission with the positions of dusty YSOs superimposed. Young stars with disks are indicated by green diamonds and protostars with red asterisks. The green outline indicates the surveyed field.

here with permission from André et al. [2014]. The left panel, a 250 μm dust continuum map, exhibits much filamentary structure. Filaments have lengths of ~ 1 pc or more (see scale bar in right panel of Figure 1.3). To extract a map or skeleton of the network of filaments from the image, a curvelet transform [Starck et al., 2003a,b] was first taken, which highlights the filamentary structure. Following this, the DisPerSE algorithm [Sousbie, 2011, Sousbie et al., 2011] is applied. A technical description of the algorithm is included in Chapter 4, but the resulting map is shown in the right panel of Figure 1.3. This has aided observers, such as Arzoumanian et al. [2011], to characterize filament properties.

In their arrangement, filaments are long ($l \sim$ 1–10 pc) and often lie co-linear with their host clouds [André et al., 2014], suggesting a common formation mechanism such as supersonic turbulence or magnetic fields [Li et al., 2013]. Some clouds appear to contain populations of sub-filaments [Arzoumanian et al., 2011, Russeil et al., 2013] and these can sometimes appear as coherent structures in *position-position-velocity* (PPV) maps [Hacar and Tafalla, 2011]. Since astronomers cannot directly measure the line-of-sight spatial dimension, seeing only a 2D projection, PPV maps are a way of gaining information about the third dimension from the line-of-sight velocity. This can be very useful if 3D structures have coherent velocities.

Their radial density profiles are well fit by Plummer-like functions [Arzoumanian et al., 2011]:

$$\rho_p(r) = \frac{\rho_c}{[1 + (r/R_{\rm flat})^2]^{p/2}}, \tag{1.2}$$

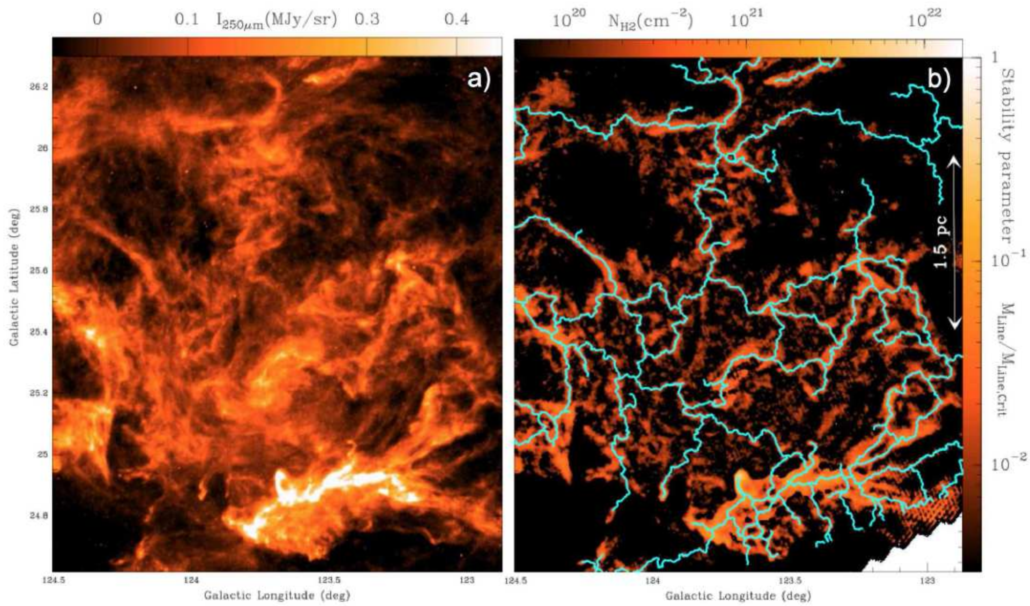

Figure 1.3: An image of the Polaris flare. Reproduced with permission from André, Di Francesco, Ward-Thompson, Inutsuka, Pudritz, and Pineda, Protostars and Planets VI, University of Arizona Press, Tucson, p.27-51, 2014 (Figure 1). The left panel shows a 250 μm dust continuum map taken with *Herschel*/SPIRE. The right panel shows the corresponding column density map, with contrast added by performing a curvelet transform. The DisPerSE filament-finding algorithm [Sousbie, 2011] was then applied, and found filaments traced in light blue. Assuming a typical filament width of 0.1 pc [Arzoumanian et al., 2011], the colour density map indicates the mass per unit length along the filaments (color scale shown on the right edge of the figure).

which is equivalent to column density profile of

$$\Sigma_p(r) = A_p \frac{\rho_c R_{\rm flat}}{\left[1 + (r/R_{\rm flat})^2\right]^{\frac{p-1}{2}}}, \tag{1.3}$$

where ρ_c is the central density of the filament, $R_{\rm flat}$ is the radius of the flat inner region, $p \approx 2$ is the power-law index at radii $r \gg R_{\rm flat}$, and A_p is a constant of order unity that includes the effect of inclination relative to the plane of the sky. The fact that the power-law index p is approximately 2 and not 4, as would be the case for an isothermal cylinder [Ostriker, 1964], suggests that filaments are not isothermal, but rather better fit by polytropic equations of state, $P \propto \rho^{\gamma}$ with $\gamma \lesssim 1$. The temperature profile then goes as $T \propto \rho^{\gamma-1}$. The observed temperature structure in filaments does indeed deviate from isothermal [Palmeirim et al., 2013]. Federrath [2016] claims that the $p = 2$ scaling of the filament density profile results naturally from the collision of two planar shocks that form a filament at their intersection.

In a survey of nearby Gould Belt clouds, the filaments appear to have a characteristic width of $d = 2 \times R_{\rm flat} \sim 0.1$ pc. This filament width appears universal, even being reproduced in numerical simulations, such as the ones we performed in Kirk, Klassen, Pudritz, and Pillsworth [2015]. We analyzed filament properties in column density maps from hydrodynamic and magneto-hydrodynamic simulations. The filaments studied in simulation had physical properties remarkably similar to observations.

Figure 1.4 is reproduced from that paper and shows filament profiles of an equivalent filament taken from a purely hydrodynamic and a mangneto-hydrodynamic simulation. The simulated observations are of a radial column density profile, which is then fit with three different models of idealized cylindrical filaments: the isothermal case presented first in Ostriker [1964], where gravity is balanced by thermal pressure; a modified isothermal case, which is sometimes referred to as a"Plummer-like" profile [Equation 1.3]; and a third model, based on Fischera and Martin [2012], which includes the effects of external confining pressure. These three model profiles are overplotted on our radial column density measurements, and residuals are shown beneath each case (HD or MHD).

We noted that magnetic fields can result in wider, "puffier" filaments, although Seifried and Walch [2015] find that if the magnetic fields are arranged

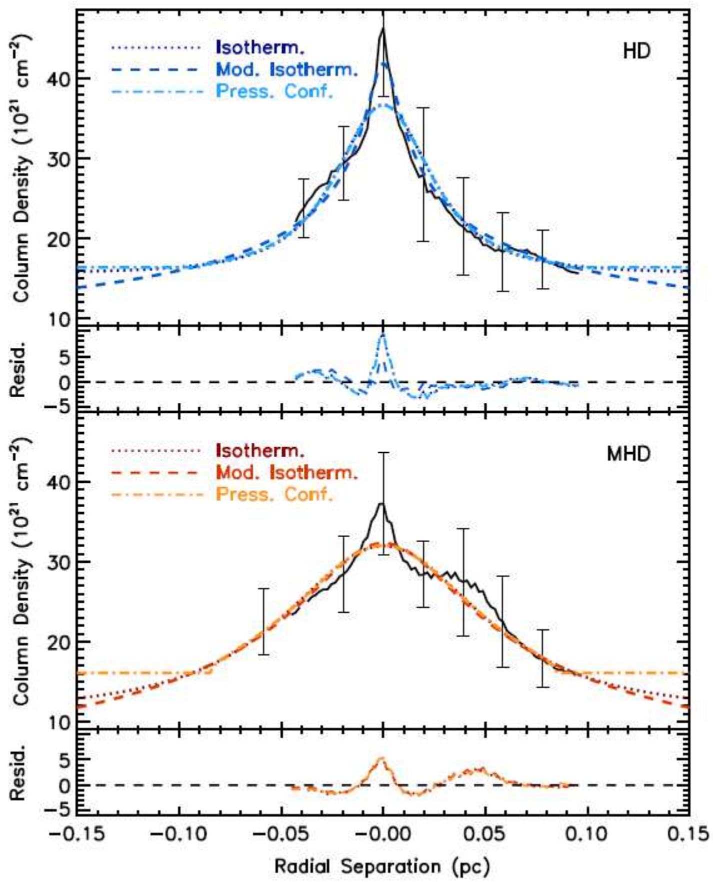

Figure 1.4: Radial column density profiles of simulated filaments. Reproduced with permission from Kirk, Klassen, Pudritz, and Pillsworth, ApJ, Volume 802, 2, p.75, 2015 (Figure 6). The top panel is for a filament taken from a purely hydrodynamic simulation, whereas the lower panel is for the equivalent filament in a magnetohydroynamic simulation. Best-fit models for a purely isothermal cylinder, a modified isothermal model, and a pressure-confined cylinder are indicated. Error bars indicate 1-σ values are variable radial separations.

perpendicular to the filaments, filaments may be slightly narrower than 0.1 pc. The mechanism responsible for the near-universally measured 0.1 pc width is still not understood, although recent theoretical work claims that it is a natural consequence of the physical properties of magnetized, turbulent molecular clouds [Federrath, 2016]. What is significant is that our simulated filaments resemble observed filaments in their characteristics. We study these in Chapter 4, including the interplay of magnetic fields and accretion flows, as well as the destructive effects of photoionization feedback from massive star clusters.

Among the other results of Kirk, Klassen, Pudritz, and Pillsworth [2015], we also found that magnetic fields result in filaments that are less centrally peaked, and less prone to fragmentation. Our simulated filaments exhibited complex structure reminiscent of the filament bundles observed in Hacar et al. [2013]. Complex 3D substructure is also observed in other simulations, such as those by Smith et al. [2014] and Moeckel and Burkert [2015].

The question of magnetic field orientation is of importance to star formation studies because magnetic fields support protostellar cores against gravitational collapse by opposing gravity and have dynamically important effects in molecular clouds. Observations of magnetic field structure on GMC scales shows that molecular clouds are threaded with large-scale magnetic fields [Li et al., 2013] that roughly preserve their overall orientation. Filaments are seen as oriented largely perpendicular or parallel to magnetic fields.

In Figure 1.5, reproduced with permission from Planck Collaboration XXXV [2016], we show the magnetic structure around parts of the Taurus and Ophiucus molecular clouds, as mapped by the *Planck* satellite using 353 GHz dust polarization observations. The resolution is insufficient to map individual cores, but captures the large-scale magnetic field structure of giant molecular clouds. The left panels show the column density and magnetic pseudo-vectors indicating the orientation of the magnetic field are overplotted. A technique called the Histogram of Relative Orientations [Diego Soler et al., 2013] is used to generate the right panels in Figure 1.5. To generate these, the relative angle between the magnetic field pseudo-vector and the gradient in the column density is measured. The gradients in column density serve as a proxy for filamentary structure, and so can be used to generate histograms of the relative orientation of magnetic fields and filaments. We showcase a different technique that we developed in Chapter 4 using the filament spines directly as mapped out using DisPerSE in 3D simulated molecular cloud clumps,

Magnetic field orientation is measured using optical or infrared polarization measurements. Non-spherical dust grains align their long axis perpendicular to the ambient magnetic field [Hoang and Lazarian, 2008]. Light at optical wavelengths from background stars is absorbed by the dust grains, resulting in the starlight being linearly polarized in the direction of the magnetic field. Meanwhile, the dust emits radiation in infrared frequencies, but which appear linearly polarized perpendicular to the magnetic field [Hildebrand et al., 1984, Novak et al., 1997, Vaillancourt, 2007, Davis and Greenstein, 1951, Hildebrand, 1988, Heiles and Haverkorn, 2012].

Polarization measurements, such as in Taurus [see, e.g. Palmeirim et al., 2013, Figure 3] show an alignment perpendicular to the dense filaments. Small filaments, sometimes called "striations" appear to feed into larger filaments and show alignment parallel to these magnetic field orientations. Numerical simulations by Diego Soler et al. [2013] suggest that there exists for molecular clouds a threshold density below which parallel alignment is favoured and above which the relative orientation is more perpendicular.

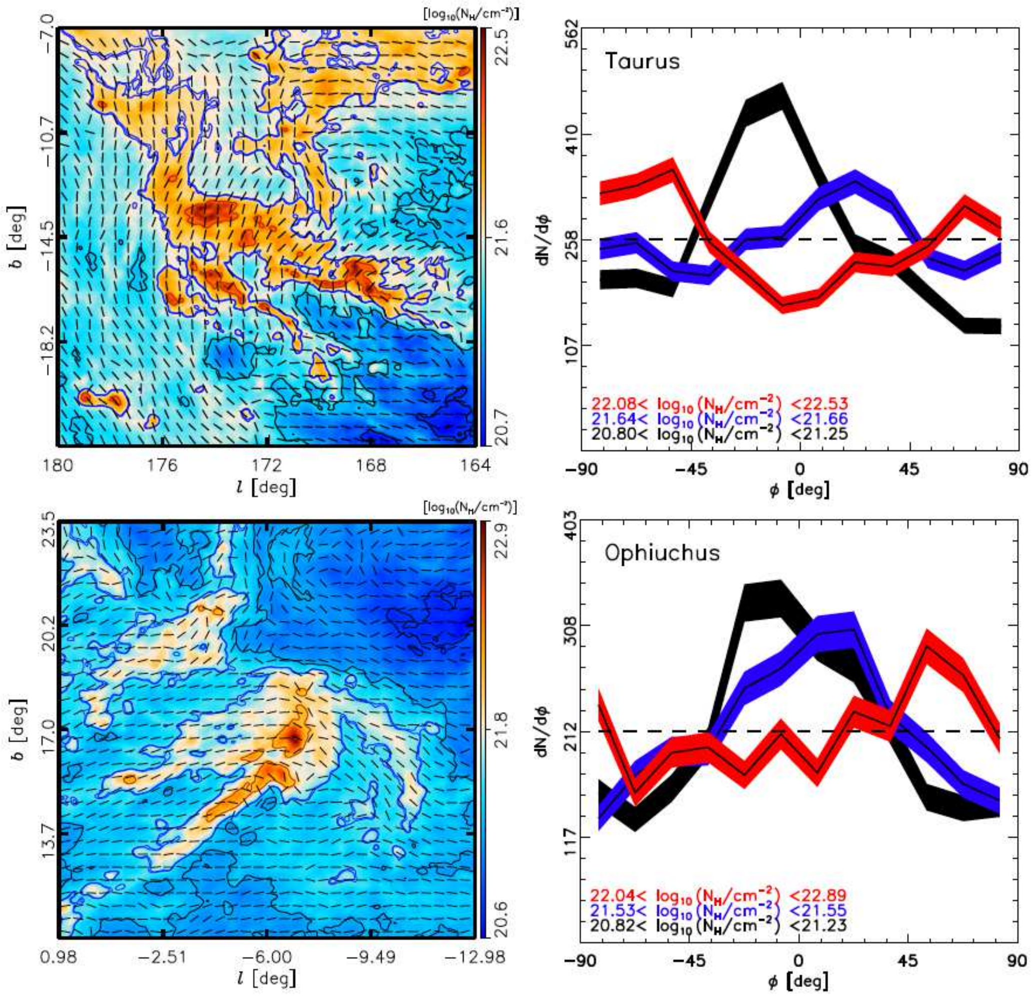

Figure 1.5: Column density maps and histograms of relative orientation (HRO) for parts of the Taurus and Ophiucus molecular clouds. Reproduced with permission from Planck Collaboration XXXV [2016], A&A, 586 (Figure 3). © ESO. Left panels show the column density maps with magnetic pseudo-vectors overlaid. The orientation of these was inferred using the 353 GHz polarization data from the *Planck* satellite. The right panels show the HRO, where the relative orientation is between the magnetic pseudo-vectors and the gradient of the column density in the left panels. The density gradient is a proxy for the filamentary structure in the column density maps. Hence, the HRO gives an indication of the relative orientation of magnetic fields and filaments. Three histograms are produced corresponding to the lowest, an intermediate, and the highest N_{H} density ranges (black, blue, and red, respectively). Where the histograms peak near 0°, it is understood that magnetic fields are aligned with filamentary structure, whereas when the histograms show relatively high counts near ±90°, it is understood that magnetic fields are oriented perpendicular to filamentary structure.

This scenario favours a magnetic origin for dense filaments. The ISM is weakly ionized by cosmic rays and the interstellar radiation field. Dust, which makes up about 1% of the mass of the ISM, also contributes free electrons that have been photoejected. This means that the ISM responds dynamically to the presence of magnetic fields. Motion along parallel field lines is unhindered, but gas moving across field lines or along a gradient in magnetic field strength encounters a magnetic pressure. B-fields can thus channel gas along what appear as striations and onto high-gravity filaments [see Li et al., 2013, Figure 3]. The relative orientation of magnetic fields and filaments is sensitive also the relative energies of magnetic fields and turbulence, characterized by the Alfvén Mach number, given by

$$\mathcal{M}_A = (\beta/2)^{1/2}\,\mathcal{M} = \frac{\sigma}{v_A}, \tag{1.4}$$

where $\beta = 8\pi\rho\sigma^2/\langle B^2\rangle = 2\sigma^2/v_A^2$ is the plasma beta, which describes the ratio of thermal pressure to magnetic pressure. σ and $v_A = B/\sqrt{4\pi\rho}$ are the 1D velocity dispersion and the Alfvén speed, respectively. The latter is the characteristic speed of a magnetohydrodynamic wave. $\mathcal{M}$ is the thermal Mach number.

If sub-Alfvénic ($\mathcal{M}_A < 1$) turbulent pressure is high enough, turbulent pressure extends gas parallel along magnetic fields and filaments appear elongated in the direction of the magnetic field [Li et al., 2013]. If not, gravity contracts material along magnetic field lines to form a filament with a perpendicular orientation.

If the turbulence is super-Alfvénic ($\mathcal{M}_A > 1$), then magnetic fields are not dynamically important, then turbulence can compress gas in any direction to form filaments regardless of the large-scale orientation of intercloud magnetic fields.

In a study of 27 Zeeman measurements towards molecular clouds, Crutcher [1999] was able to characterize their magnetic properties and found them to have Alfvén Mach numbers ranging from $\mathcal{M}_A = 0.3$ to $\mathcal{M}_A = 2.7$, although for some clouds, only a lower bound was obtained. Most had Alfvén Mach numbers close to unity.

Core formation along filaments is also influenced by the magnetic field geometry. Seifried and Walch [2015] performed numerical simulations of a large ($l \sim 1$ pc) filament with magnetic fields oriented parallel or perpendicular. When the field was oriented perpendicular to the filament, stellar cores were formed with an even distribution along the filament. With a parallel orientation, cores were seen first forming at the ends of the filament.

Filaments can be characterized by their line masses, $M_{\rm line}$, also known as the mass per unit length. For an isothermal cylinder (Equation 1.2 with $p = 4$), there exists a critical line mass for which the gravitational force per unit mass is balanced by thermal pressure,

$$M_{\rm line,crit} \equiv \int_0^\infty 2\pi\rho_4(r) r dr = \frac{2c_s^2}{G}, \tag{1.5}$$

where c_s is the isothermal sound speed. Filaments with line masses above this critical value should be unstable to gravitationl collapse unless they are supported by other mechanisms, such as non-thermal gas motions or magnetic fields. Beuther et al. [2015b] present an extreme filament embedded within an IRDC that is supported by turbulent gas motions. If its radial support came only from thermal pressure, it would have a critical line mass of $25\,\mathrm{M}_\odot$/pc.

The measured line mass is closer to 1000 $M_\odot$/pc, but the filament has only fragmented into 12 approximately equally-spaced cores. If turbulent gas motions are included, the critical line mass becomes 525 $M_\odot$/pc, which is more than 20 times higher and much more consistent with the fragmentation pattern observed. The turbulent contribution to the critical line mass was derived in Fiege and Pudritz [2000] and shown to be relevant in Kirk et al. [2015]. We reproduce some radial column density profiles in Figure 1.4. Filaments such as these are prime candidates for massive star formation.

Dense cores embedded within filamentary networks inside molecular clouds have become the new paradigm of star formation [André et al., 2014], reinforced by observational evidence across a wide array of instruments and a wide range of scales. The transition from dense cores to massive stars is characterized by Zinnecker and Yorke [2007] as going from cold dense massive cores (CDMC) to hot dense massive cores (HDMC) to disk-accreting main-sequence star (DAMS), to final main-sequence star (FIMS). The transition from cold (starless) core to hot core results from the formation of an intermediate-mass protostar that can heat up the core. H_2O and later methanol maser emission traces collimated jets and outflows, which appear as soon as protostellar disks begin to form through gravitational collapse of magnetized clouds [Banerjee and Pudritz, 2006, Pudritz et al., 2007b, Seifried et al., 2012b]. The star becomes increasingly luminous (more from hydrogen burning than disk accretion) and begins to photoionize the gas around it and photoevaporate the accretion disk. At this point, gravitationally-confined hypercompact HII regions are observed via hydrogen recombination lines. The disk is dissipated and what remains is a "final" main-sequence star driving an expanding HII region.

There is no agreed-upon upper mass limit for stars. Figer [2005] claims an upper limit of 150 $M_\odot$ from observations of the Arches cluster, and on account of its total absence of stars with initial masses greater that 130 $M_\odot$, despite the fact that for a cluster of its size, typical mass function would predict that Arches should have 18 such stars. Later work, however, showed a strong sensitivity of the derived stellar masses to the choice of extinction law [Habibi et al., 2013]. The relative difference in derived stellar mass for two different extinctions laws could be as great as 30%. Crowther et al. [2010] performed spectroscopic analyses of two stellar clusters, NGC3603 and R136, the latter of which is part of 30 Doradus. Both NGC3603 and R136 are extremely compact stellar clusters and contain some of the most massive stars detected to date. Crowther et al. [2010] estimate that three systems in NGC3063 have initial masses of 105–170 $M_\odot$, while four stars in R136 have masses in the range of 165–320 $M_\odot$. It is important to note that these masses are sensitive to the choice of stellar evolution model, age estimates, and estimates of mass loss due to stellar wind. Nevertheless, it appears that stars with masses above 150 $M_\odot$ are possible and have been observed. How they were able to accrete so much matter despite their extreme luminosities is one of the central questions addressed in this thesis. Its solution motivated the creation of our new hybrid AMR radiative transfer code (described in Chapter 2) and its implementation for massive star formation in Chapter 3.

1.2 Theory of massive star formation

Statements about the gravitational stability of a molecular cloud usually begin with the virial theorem, which, stated one helpful way, is [McKee and Zweibel, 1992, McKee and Ostriker, 2007b]:

$$\frac{1}{2}\ddot{I} = 2\left(\mathcal{T} - \mathcal{T}_S\right) + \mathcal{B} + \mathcal{W} - \frac{1}{2}\int_S \left(\rho \boldsymbol{v} r^2\right) \cdot d\boldsymbol{S}. \tag{1.6}$$

In the first term, $\ddot{I}$, comes from the moment of inertia of the molecular cloud. If the shape of the cloud remains the same, then it tells us whether the cloud is expanding or contracting. $\mathcal{T}$ is the total kinetic plus thermal energy of the cloud and $\mathcal{T}_S$ is the confining surface pressure on the cloud, which includes both thermal and ram pressure. $\mathcal{B}$ is the difference in magnetic pressure between the inside and outside of the molecular cloud. If the magnetic field across the surface takes on a uniform value B_0, then

$$\mathcal{B} = \frac{1}{8\pi}\int_V \left(B^2 - B_0^2\right) dV. \tag{1.7}$$

$\mathcal{W}$ is the gravitational energy of the cloud, usually expressed simply as the binding energy in the case of no external gravitational fields. The final term in Equation 1.6 represents the rate of change of momentum flux across the cloud surface. If $\boldsymbol{v} = 0$ at the surface S, then no gas is crossing the surface of the cloud and this term is zero.

If the magnetic and surface forces are negligible ($\mathcal{B} \approx \mathcal{T}_S \approx 0$), and the cloud is in virial equilibrium ($\ddot{I} = 0$), then we have

$$2\mathcal{T} = -\mathcal{W}. \tag{1.8}$$

This is the simplest possible statement of the virial theorem and the one from which we define the virial parameter, $\alpha_{\rm vir}$,

$$\alpha_{\rm vir} = \frac{2\mathcal{T}}{|\mathcal{W}|}. \tag{1.9}$$

A cloud in virial balance has $\alpha_{\rm vir} \approx 1$. A cloud undergoing gravitational collapse will have $\alpha_{\rm vir} < 1$. In Chapter 4 we simulate two molecular cloud clumps, one with $\alpha_{\rm vir} \approx 1$ and another with $\alpha_{\rm vir} \approx 0.6$, and show that the difference can influence the geometry of the magnetic field as the simulation evolves. The strongly bound cloud drags magnetic fields inwards as it collapses gravitationally. This effect is much less strong in the marginally bound cloud.

Using Equation 1.8, we can define a simple expression of the length and mass scales required for gravitational stability. For a uniform sphere of isothermal gas with radius R and mass M, we have

$$\mathcal{T} = \frac{3}{2} N k_B T, \tag{1.10}$$

where $N = M/(\mu m_H)$ is the number of molecules of mean molecular weight μm_H. k_B is Boltmann's constant and T is the temperature. The gravitational binding energy is $\mathcal{W} = -aGM^2/R$, where a is a constant of order unity that depends on the internal structure of the spherical cloud. For a homogeneous cloud of uniform mass density ρ, $a = 3/5$. This allows us to write the simplified virial thereom as

$$3Mc_s^2 = \frac{3}{5}\frac{GM^2}{R}, \tag{1.11}$$

where we have substitued in the isothermal sound speed $c_s^2 = k_B T/(\mu m_H)$. After a little rearranging, we can write the critical radius for gravitational stability,

$$R_J = \sqrt{\frac{15c_s^2}{4\pi G\rho}}, \tag{1.12}$$

where we have added a subscript J to denote its connection with the Jeans length. A more rigorous stability analysis following Jeans [1902], yields almost exactly the same result. The critical wavenumber at which perturbations grow to non-linear amplitudes and undergo gravitational collapse is:

$$k_J = \sqrt{\frac{4\pi G\rho}{c_s^2}}, \tag{1.13}$$

for which the corresponding wavelength, λ_J, is the Jeans length,

$$\lambda_J = \frac{2\pi}{k_J} = \sqrt{\frac{\pi c_s^2}{G\rho}} = \sqrt{\frac{\pi k_B T}{G\mu m_H \rho}}. \tag{1.14}$$

This naturally defines a mass scale, $M_J = \rho\lambda_J^3$, the Jeans mass, and it is the critical mass above which a sphere of uniform density ρ will undergo gravitational collapse. The corresponding timescale for collapse is called the freefall time and is given by

$$t_{\rm ff} = \sqrt{\frac{3\pi}{32G\rho}}. \tag{1.15}$$

Magnetic fields can provide support against gravitational collapse and are present throughout the ISM. Starting from the simplified statement of the magnetic field energy in Equation 1.7, the magnetic terms can be approximated

$$\frac{1}{8\pi}\int_V \left(B^2 - B_0^2\right) dV \approx \frac{1}{6}\left(B^2R^3 - B_0^2R_0^3\right) \tag{1.16}$$

This assumes the molecular cloud of radius R is inside a much larger virial volume of radius R_0. The flux passing through through the cloud, $\Phi_B = \pi B R^2$, must necessarily pass through the virial surface as well, hence $\Phi_B = \pi B_0 R_0^2$, allowing us to write

$$\frac{1}{6}\left(B^2R^3 - B_0^2R_0^3\right) = \frac{1}{6\pi^2}\left(\frac{\Phi_B^2}{R} - \frac{\Phi_B^2}{R_0}\right) \approx \frac{1}{6\pi}\frac{\Phi_B^2}{R}, \tag{1.17}$$

where, in the last step, we can used $R \ll R_0$ to drop the $1/R_0$ term. Setting $\mathcal{B} = |\mathcal{W}|$ allows us to write a magnetic critical mass,

$$M_\Phi = \sqrt{\frac{5}{2}}\frac{\Phi_B}{3\pi G^{1/2}}. \tag{1.18}$$

Molecular clouds or cores with masses $M < M_\Phi$ remain magnetically supported against collapse, though processes such as ambipolar diffusion can reduce the flux Φ_B threading the cloud or core and allowing it to collapse. Following McKee and Ostriker [2007b], we write the critical mass as

$$M_\Phi \equiv c_\Phi \frac{\Phi_B}{G^{1/2}}, \tag{1.19}$$

where all other factors have been gathered into the coefficient c_Φ. For the idealized case that we followed above, $c_\Phi = \sqrt{5/2}/(3\pi) \approx 0.168$. More exact numerical calculations including the pressure of the intercloud medium by Mouschovias and Spitzer [1976] find $c_\Phi = 0.126$.

For simulations of magnetized molecular cloud cores, it is important to characterize the core's mass-to-flux ratio, usually stated normalized to the critical value,

$$\mu \equiv \frac{M_\mathrm{core}}{\Phi_\mathrm{core}} / \left(\frac{M_\Phi}{\Phi}\right)_\mathrm{crit} = \frac{M_\mathrm{core}}{\int B_z dA} / \frac{c_\Phi}{\sqrt{G}}. \tag{1.20}$$

Observed values for the mass-to-flux ratio in high-mass star-forming cores are typically only slightly supercritical, with $\mu \lesssim 5$ [Falgarone et al., 2008, Girart et al., 2009, Beuther et al., 2010b]. This indicates that magnetic fields are dynamically important in high-mass star formation and may provide a significant amount of support against gravity. This implies that cores will reach much higher masses before they eventually collapse to form stars.

A typical massive core might contain $\sim 100\,\mathrm{M}_\odot$ of molecular gas and have a radius of ~ 0.1 pc [Reid and Wilson, 2005, Sridharan et al., 2005, Beuther et al., 2005]. This gives it a mean density of $\rho \sim 10^{-18}$ g/cm^3, or $n \sim 10^6$ cm^{-3}. The freefall time of such a core is $t_{\rm ff} = 5 \times 10^4$ years. For a core to form within 10^5 years, we require accretion rates of $\dot{M} = M_{\rm core}/t_{\rm ff} \sim 10^{-3}\,\mathrm{M}_\odot/\mathrm{yr}$. Accretion rates this high are never observed or expected in low-mass star formation regions. It is also much higher than the value expected from the thermal sound speed, $c_s^3/G \sim 10^{-6}\,\mathrm{M}_\odot/\mathrm{yr}$ and can only be met in conditions with strong turbulence, since it is the turbulent velocity dispersion, not the sound speed, that is relevant [Myers and Fuller, 1992, McLaughlin and Pudritz, 1997, McKee and Tan, 2003].

Another characteristic feature of high-mass protostars is their short Kelvin-Helmholtz times. This timescale,

$$t_{\rm KH} \sim \frac{GM^2}{RL}, \tag{1.21}$$

where M, R, and L are the mass, radius, and luminosity of the protostar, respectively, describes the conversion of gravitational energy to radiation before the protostar has reached equilibrium. This precedes the onset of nuclear burning. Typical Kelvin-Helmholtz times for high-mass protostars will be a few 10^4 years, which is shorter than the typical formation time of $\sim 10^5$ years.

These short Kelvin-Helmholtz times, relative to freefall times, imply that massive stars effectively begin their lives on the main sequence, burning hydrogen long before they've finished accreting. Their higher effective surface temperatures also mean that they will begin ionizing the surrounding gas even while they are still forming.

Magnetic fields and radiative feedback act together in disks, with magnetic fields serving to extract angular momentum from disks, potentially accelerating the accretion process [Commerçon et al., 2010], resulting in an increased accretion luminosity. Magnetic braking of accretion disks is by itself far too efficient a process, preventing the formation of a Keplerian disk, but this "magnetic breaking catastrophe" is averted by the presence of even small amounts of turbulence [Seifried et al., 2012a].

In summary, massive stars are quite unlike low-mass stars. Their environments are characterized by much higher mean gas densities, they accrete at much higher rates, begin burning hydrogen almost immediately, and influence their surrounds through powerful feedback mechanisms that include photoionization, radiation pressure, and—later, during main sequence evolution—stellar winds. In the next section, we introduce the radiative feedback mechanisms most relevant to this thesis.

1.3 Radiative feedback

Stars influence their environments through their radiation feedback effects. One of the most important feedback mechanisms for the study of stellar populations and the star formation efficiency of molecular clouds is radiative heating. By raising the temperature of the gas, gravitational fragmentation is suppressed by increasing the Jeans mass, which scales as $M_J \sim T^{\frac{3}{2}}$ (see Equation 1.14). This process is relevant even for low-mass stars, which through the heating of their protostellar cores suppress disk fragmentation and the formation of brown dwarfs [Offner et al., 2009].

Stars heat their environments primarily through the interaction of radiation and dust. Dust grains make up about 1% of the ISM by mass and absorb stellar radiation preferentially at UV and optical, heating up in the process. They re-emit this energy at longer, infrared wavelengths. This reprocessing occurs very close to the stars themselves. Collisions between gas and dust ensure that they are in thermal equilibrium. It is usually safe to assume that within molecular clouds, $T_{\rm gas} = T_{\rm dust}$.

In the diffuse ISM the gas can be hotter than the dust, while in the envelopes of protostars, dust temperatures can exceed gas temperatures [Tielens, 2005]. At densities above $n \gtrsim 10^{4.5}$ cm^{-3}, dust-gas coupling is so strong that dust is the dominant coolant and regulates the temperatures. At lower densities, molecular or atomic species are more important coolants [Goldsmith, 2001, Glover and Clark, 2012]. In simulations of star formation involving diffusive schemes of radiative transfer, local thermodynamic equilibrium between dust and gas species is usually assumed [Turner and Stone, 2001, Krumholz et al., 2007b, Commerçon et al., 2011b].

Dense molecular cloud clumps are often sufficiently optically thick that even the radiation field is in thermal equilibrium with the dust, i.e. $T_{\rm rad} \approx T_{\rm dust} = T_{\rm gas}$. Within circumstellar disks, the gas/dust temperature follows the thermal radiation temperature closely, except at the inner boundary nearest the star, where the direct radiation flux is high.

When modeling radiative feedback in molecular clouds using numerical simulations, various simplifications must be made because solving the full set of radiative transfer equations, including scattering, absorption, and emission, along with the full set of (magneto)hydrodynamics equations is computationally infeasible on today's supercomputers. In the optically thick environments in which stars form, radiation diffuses through gas much like heat, and hence it obeys Fick's diffusion law: $\boldsymbol{F} = -c\nabla E/(3\kappa\rho)$, where F is the flux, E is the radiation energy density and κ is the specific opacity of the dust. This can be applied in either the "grey" atmosphere approach, where F, E, and κ are integrated over all frequencies, or via a multi-group approach that splits the radiation field into discrete energy bins and the relevant quantities are integrated over the frequencies within each bin.

A problem arises, however, if the cloud becomes optically thin. In these regions, $\kappa\rho$ becomes sufficiently small that the flux F can exceed cE, violating Special Relativity. To circumvent this problem, a "flux-limiter" was introduced [Alme and Wilson, 1973, Levermore and Pomraning, 1981], so that the diffusion law became

$$\boldsymbol{F} = -\frac{\lambda c}{\kappa\rho}\nabla E, \tag{1.22}$$

where λ is the flux-limiter, a dimensionless function of E and $\kappa\rho$ that in the optically thick limit, $\lambda \to 1/3$, and in the optically thin limit, $\lambda \to \kappa\rho E/|\nabla E|$. Between these two limits, λ is a smoothly-varying function. The result is that in the optically thick limit, Fick's Law is preserved, and in the optically thin limit, the magnitude of the flux does not exceed cE.

Many different functional forms for the flux limiter are possible, and depend on assumptions about the angular distribution of the specific intensity of the radiation [Turner and Stone, 2001]. One of the most popular flux limiters is the one by Levermore and Pomraning [1981],

$$\lambda = \frac{2+R}{6+3R+R^2}, \tag{1.23}$$

where

$$R = \frac{|\nabla E|}{\kappa \rho E}. \tag{1.24}$$

The flux-limited diffusion (FLD) approximation opened a wide frontier of star formation research via numerical simulations of molecular clouds and cores, first in 2D [Yorke and Bodenheimer, 1999, Yorke and Sonnhalter, 2002], and then 3D [Whitehouse and Bate, 2006, Krumholz et al., 2007a]. Modern approaches to flux-limited diffusion use increasing sophistication, such as the hybridization with raytracers that we present in this thesis. Other next generation FLD codes are including multifrequency effects [Kuiper et al., 2010b, Flock et al., 2013] and ionization [Norman et al., 2015]. Other methods for modeling radiative feedback in molecular clouds include characteristics-based raytracing with accelerated Λ-iteration [Buntemeyer et al., 2015], a scheme that passes a collection of parallel rays through the simulation volume across a distribution of angles, determines the flux local to each cell, and then iteratively computes the equilibrium temperature. Another approach is time-dependent Monte Carlo radiative transfer [Harries, 2011, 2015], which follows packets of rays through many scattering, emission, and absorption events—very accurate, but computationally expensive.

FLD, still the most popular approach, can by itself never be a complete solution to the radiative transfer problem. Each parcel of gas will see some energy also from the direct ray from the star. The medium in question is highly anisotropic—filled with filaments, voids, and radiative cavities—so the direct ray will often convey most of the energy. Thus by hybridizing a raytracing approach with a diffusion approach, one achieves the best of both worlds: high accuracy, especially nearest the star, and high efficiency, especially in the optically thick regions.

While the suppression of gas fragmentation through radiative heating is an important feedback effect, it is not unique to massive stars, nor is it one that challenges our understanding of how massive stars form. In fact, radiative heating is partly responsible for massive stars. A dense 100 $M_{\odot}$ core of radius 0.1 pc at a temperature of 20 K contains ~ 80 Jeans masses and yet collapses to form only a single massive star, as we show in Chapter 3 of this thesis. Radiative heating plays an extremely important role in the origin of massive stars.

What *does* challenge the formation of massive stars is radiation pressure, a feedback mechanism that is not dynamically important for low-mass stars. Radiation pressure has been recognized as an important problem in massive star formation since at least the 1970s [Larson and Starrfield, 1971b, Kahn, 1974]. The most massive stars known, with masses of 100–150 $M_{\odot}$, are internally supported against gravity by radiation pressure on electrons. Yet the cross-section for Thompson scattering is an order of magnitude smaller than the cross-section for absorption by dusty gas. How then can a star, which is already near its Eddington limit for stellar structure, accrete dusty gas from its environment, for which it exceeds the Eddington limit by an order of magnitude? Radiation pressure becomes as strong as gravity for stars of roughly 20 $M_{\odot}$.

The resolution to this dilemma lies in the non-sphericity of the accretion process. If accretion proceeds through a disk, the radiation field becomes highly anisotropic, with the short-wavelength radiation, which most contributes to radiative acceleration, being concentrated in the polar direction. The radiative force density is proportional to opacity κ of the gas, which in turn is a function of the frequency of the radiation.

In the plane of the disk, short-wavelength radiation is strongly absorbed within the inner regions of the disk. The long-wavelength radiation, least responsible for radiative acceleration, is more or less isotropic [Yorke and Sonnhalter, 2002]. This is known as the "flashlight effect" [Yorke and Bodenheimer, 1999] and applies even in "grey amospheres". In our simulations, the direct radiation component is assumed to have a spectrum corresponding the effective temperature of the star, and the (grey) opacity is calculated based on this temperature. In pure FLD simulations, the disk has a higher radiation energy density than the polar regions, which results in an anisotropic flux of radiation into the polar regions. Nevertheless, hybrid radiation codes would see an enhancement of the flashlight effect, and the effect is even more pronounced in multifrequency codes [Yorke and Sonnhalter, 2002]. The collimation of the radiation field along the polar axis provides pressure relief on the material in the disk, which may then continue accreting. Two-dimensional (axisymmetric) multifrequency simulations by Yorke and Sonnhalter [2002] of the collapse of a 120 $\mathrm{M}_\odot$ core formed a star with a final mass of $M \approx 43\,\mathrm{M}_\odot$. In three-dimensional simulations, there does not appear to be a fundamental mass limit [Krumholz et al., 2009, Kuiper et al., 2011b].

Is disk accretion sufficient to account for observations of stars with masses greater than $20\,\mathrm{M}_\odot$, or are there other mechanisms by which a star can accrete material? Krumholz et al. [2005a, 2007a, 2009] performed numer-

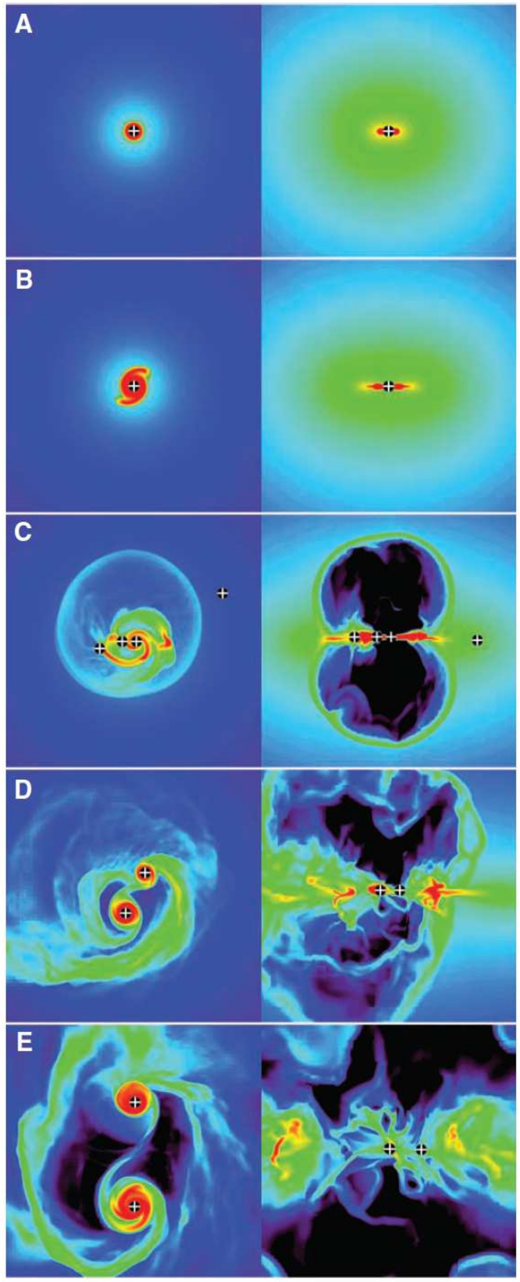

Figure 1.6: Snapshots of a simulation of high-mass star formation. From Krumholz, Klein, McKee, Offner, and Cunningham [2009], Science, Volume 323, 5915, pp.754–757, 2009 (Figure 1). Reprinted with permission from AAAS. State of the simulation is indicated at (A) 17,500 years, (B) 25,000 years, (C) 34,000 years, (D) 41,700 years, and (E) 55,900 years. Left panels show a (3000 AU)^2 face-on view of column density, whereas the right panels show an edge-on volume density slice. Colours are scaled logarithmically from 10^0 to $10^2.5$ g cm^{-2} on the left and 10^{-18} to 10^{-14} g cm^{-3} on the right (black at the minimum and red at the maximum). Stars are indicated with plus signs.

ical simulations of the collapse of a massive protostellar core with radiation feedback, handled via a grey FLD method.

In Figure 1.6, we reproduce with permission a figure from Krumholz et al. [2009] showing the state of a numerical simulation of massive star formation at different times. The left column of panels shows the face-on column density of the simulation, while the right column of panels shows edge-on volume density slices. Each views a 3000×3000 AU area. Stars are indicated using plus signs. In contrast to simulations we performed with our hybrid radiative transfer method (described in Chapter 2), the results of which are detailed in Chapter 3, we only form a single star within the time simulated.

As the simulation evolves, Krumholz et al. [2009] observe the formation radiatively-driven outflow bubbles. Along the edges of the outflow bubble, a fluid instability was observed that resembled the classical Rayleigh-Taylor instability, in which a heavy fluid is supported by a lighter fluid. In this picture, dense fingers of material sunk back down onto the star and circumstellar accretion disk. They argued in analogy to the classical case that radiation was the lighter fluid supporting the dense molecular gas above it, and this resulted in the instability. This “radiative Rayleigh-Taylor” instability has been reproduced in more controlled simulations [Jacquet and Krumholz, 2011], but still only using FLD. As we have pointed out however, FLD is not a complete solution for radiative transfer, and its problems were noted in subsequent work.

Kuiper et al. [2012] performed similar calculations, but involving a “hybrid” radiative transfer method that decomposed the radiation field into a direct, stellar component and a diffuse, thermal component. The stellar radiation field was handled via raytracing method, while the diffuse radiation was handled using an FLD solver. Simulations comparing the FLD-only case to the hybrid case showed Rayleigh-Taylor instabilities were suppressed in the hybrid case. Kuiper et al. [2012] showed that the FLD approximation underestimates the radiative forces acting on the cavity shells because direct irradiation from the star is neglected. In the FLD approach, stellar radiation is assumed to be deposited within a few grid cells around the source. A raytracer can measure the optical depth along different angles and estimate the local absorption and momentum deposition accurately. It also carries the temperature information about the stellar surface, even in the grey case, resulting in a two-temperature approach to radiative transfer. As this energy is absorbed by the dust, it is thermalized and the dust is warmed. Ray tracers also cause optically thick blobs of gas to cast shadows, something that FLD is inherently incapable of (see, e.g. Figure 2.12 in Chapter 2).

The hybrid radiative transfer scheme described in Kuiper et al. [2010b] still suffered from several weaknesses. It was implemented on a spherical grid, which automatically fixes the source immovably at the centre. The "sink" source measured gas passing through an inner grid radius as accretion. The resolution of the grid decreased logarithmically with radius and was non-adaptive. The advantage of this geometry was that the raytrace operation was essentially one-dimensional, making it computationally inexpensive and allowing for efficient multi-frequency radiative transfer.

In order to settle the matter of whether radiative Rayleigh-Taylor instabilities were an accretion mechanism for massive protostars, the hybrid radiative transfer technique needed to be implemented on a general Cartesian grid with adaptive mesh refinement (AMR). Building this code is one of the main technical achievements of the thesis and was published in Klassen et al. [2014], included as Chapter 2 in this thesis. We showed that even in this more general geometry, with moveable sink particles coupled to a protostellar evolution code, the formation of radiative Rayleigh-Taylor instabilities is suppressed (Chapter 3). Disk accretion alone is sufficient for forming massive stars. Another key result that stems from our new methods is that our accretion disks do not fragment into other stars—which contradicts the results of the pure FLD code papers [see, e.g. Krumholz et al., 2009].

Finally, we turn to ionizing radiation as an important feedback mechanism for massive stars. Hydrogen molecules dissociate at photon energies above 11 eV and hydrogen atoms are ionized at photon energies above 13.6 eV. When the rate of photoionization exceeds the recombination rate, gas becomes a hot (10,000 K), ionized plasma known as an HII region. HII regions are associated with OB stars ($M > 8\,\mathrm{M}_\odot$) and begin to form even while the protostar is still embedded within its natal envelope.

HII regions do not become significant feedback mechanisms until fairly late in protostellar evolution [Klessen et al., 2011] because high rates of accretion causes protostellar radii to swell to $\sim 100\,R_\odot$ [Hosokawa and Omukai, 2009], resuling in low surface temperatures. High accretion rates also result in high outflow rates [Tan and McKee, 2003], which confines HII region to the dense collimated outflows and shields much of the accreting material (in the disk) from radiative feedback, preventing early disk evaporation. Once the HII regions become large enough to exceed their protostellar envelopes, they can quickly become a dominant feedback mechanism [Keto, 2007, Klessen et al., 2011] by driving shocks and potentially unbinding the molecular cloud.

Although we did not finish implementing ionization feedback in our hybrid radiative transfer code in time for this thesis, we do include simulations done with solely a characteristics-based raytracer coupled to an equilibrium ionization code for calculating radiative heating, cooling, and photoionization in filamentary, magnetized, and turbulent molecular clouds (see Chapter 4).

1.4 Thesis outline and major contributions

This introduction presents the observational evidence and current paradigm of star formation in order to frame the contributions made by this PhD candidate. The work has focussed around numerical simulations of massive star formation and their environments, both at the clump scale (few pc) where clusters form, and at the core scale (< 1 pc), where individual or low-multiple star systems form. To this end we have taken the FLASH magnetohydrodynamics code and done substantial new development.

My contributions were based on my development of a new hybrid radiative method developed within an adaptive mesh refinement code (FLASH). This required substantial modifications to the FLASH v.4.0 FLD code [Fryxell et al., 2000a, Dubey et al., 2009]. This version had been expanded for the study of high-energy density physics, such as the ignition of laser-confined plasmas for controlled fusion experiments. The code was not designed with cold, dusty molecular gas in mind. I needed to equilibrate the ion and electron species to create a "neutral" medium to serve as my molecular gas, which would have the correct mean molecular weight. This equilibration strategy was originally published in the Appendix to Klassen et al. [2014]. The various shock and energy exchange tests I performed were also detailed in that paper, which is included as Chapter 2 of this thesis. On the development of this hybrid radiation code, we collaborated with Rolf Kuiper, who implemented a similar scheme in the PLUTO astrophysics code and provided technical assistance as we wrote and tested the scheme in FLASH. Additional technical assistance came from the FLASH Center at the University of Chicago, especially from Klaus Weide and Manos Chatzopoulos, who assisted with making some necessary modifications to the equation of state (EOS) unit and hydrodynamics unit to accommodate the new radiative transfer scheme.

Following this, in order to implement the hybrid radiative transfer scheme of Kuiper et al. [2010b], we needed to make use of a raytracer in FLASH . The included laser energy deposition code was too cumbersome and inappropriate for our purposes. We decided instead to port a characteristics-based raytracer that we had used in version 2.5 of FLASH that had originally been implemented by Rijkhorst et al. [2006b], then improved upon by Peters et al. [2010a] and with which I had considerable experience work through my published M.Sc. papers: (1) Klassen, Pudritz, and Peters [2012b] and (2) Klassen, Peters, and Pudritz [2012a]. Porting this code to version 4.0 of FLASH was a process that took months because of the substantial changes in code architecture between versions 2.5 and 3.0 of FLASH .

Next the raytracer needed to be coupled with the FLD code. Taking the discretized, coupled equations of the gas internal energy and radiation diffusion, and with temperature linearization approach borrowed from Commerçon et al. [2011b], I was able to write the new emission and absorption coefficients in the coupling term and modify these in the FLASH radiative transfer routines. I had to replace the explicit temperature update that FLASH was making with an iterative Newton-Raphson temperature update method. This required several additional months of testing to debug and implement an appropriate method for handling the temperature update. In particular, many of the problems did not become apparent until working on the paper for Chapter

3 of this thesis, because we had previously only applied our radiative transfer technique in static test problems or dynamic tests with short timesteps. Simulating protostellar cores with all of the relevant physics (e.g. hydrodynamics) turned on was a much more demanding problem that necessitated more code development and testing. After 2 years of development and the eventual publication of our code paper [Klassen, Kuiper, Pudritz, Peters, Banerjee, and Buntemeyer, 2014, ApJ, 797], we were ready to perform star formation calculations.

I set up a protostellar model based on the initial conditions of both Krumholz et al. [2009] and Kuiper et al. [2010a]. I simulated the collapse of three protostellar cores at masses of 30, 100, and 200 $M_\odot$ and then performed extensive analyses of the resulting data, looking at the mass evolution, disk stability, accretion history, outflow formation, and bubble morphology. The results were published as Klassen, Pudritz, Kuiper, Peters, and Banerjee [2016b, ApJ, 823], and are included in this thesis as Chapter 3. We found that disk accretion is sufficient to explain the formation of massive stars, with the need for other mechanisms, such as radiative Rayleigh-Taylor instabilities of the outflow bubble walls. Our accretion disks become Toomre-unstable, which increases the accretion rate onto the central star, but do not fragment within the time simulated to form companion stars.

All the while I was also engaged in research on the larger context of massive star formation by simulating magnetized, turbulent molecular cloud clumps of around 500, 1000, and 2000 $M_\odot$. These are the environments in which massive stellar clusters are formed and we wanted to take a closer look at the filamentary structure of these environments and their interplay with the larger magnetic field structure. To this end, I set up MHD simulations including supersonic turbulence, with average mass-to-flux ratios akin to what has been observed. We compared the filamentary structure of these to similar simulations I ran without magnetic fields and published the results as part in Kirk, Klassen, Pudritz, and Pillsworth [2015].

To study the relation of magnetic fields to filaments in clouds, I contacted Thierry Sousbie, the author of the DisPerSE code, which has been successfully applied in the analysis of *Herschel* data for the study of filamentary structure. DisPerSE can analyze both 2D images and 3D simulation data and produce a filament skeleton. The technique the DisPerSE uses has been described in Sousbie [2011] and Sousbie et al. [2011]. I included a summary of it in the methods section of Chapter 4. Sousbie supplied me with a pre-release version of DisPerSE and we used it to analyze column density projections of simulation data in Kirk, Klassen, Pudritz, and Pillsworth [2015], a paper to which I contributed the numerical simulations, as well as part of the analysis and writing. We next began developing our 3D analysis capabilities for a study of magnetic field structure in relation to filaments.

A primary goal of Chapter 4 is to trace the role of magnetic fields on star formation within filaments. No study to our knowledge has yet achieved this by following a filament along in a 3D data cube. We believe that this is the first study to achieve this by applying DisPerSE . DisPerSE was incompatible with HDF5 files, which is the default way that FLASH stores its AMR grid data. Helen Kirk initially had done some work remapping this data onto a uniform grid in the FITS file format, but found that DisPerSE frequently ran out of memory when trying to analyze this data. I was able to get this approach to work using tools from the `yt` toolkit to remap FLASH AMR data to a downsampled uniform grid. This was able to fit within memory and DisPerSE produced useable filament skeletons.

The analysis tools I wrote for handling FLASH data and DisPerSE spanned hundreds of lines of code and dozens of subroutines. When I ran out of desktop computing power and memory, I ported DisPerSE to Amazon's cloud computing hardware, where I could leverage scaleable computing hardware on demand with root-level privileges.

The results of our analysis of simulated magnetised turbulent cloud clumps is part of a paper submitted to *Monthly Notices of the Royal Astronomical Society* and revised in response to the referee report [see Klassen, Pudritz, and Kirk, 2016a, arXiv:1605.08835]. We simulated clouds with roughly equal magnetic and turbulent energies ("trans-Alfvénic" clouds) and studied the magnetic field geometry, the filamentary structure, and accretion flows. We found that in such clouds, the virial parameter plays an important role. Highly bound clouds, due to gravitational infall dragging magnetic field lines inward, show more coherent large-scale magnetic field structure. For clouds in virial balance, the magnetic field is chaotic and disorderly, except within the largest, primary filament (the main "trunk"), where the magnetic field lines have been shock-compressed to lie parallel with the long axis of the filament. This paper is reproduced in this thesis as Chapter 4.

One simulation included ionizing feedback from a cluster of stars. Star formation takes place within the main filament. A cluster forms, but is dominated by a single massive star that reaches about 16 $M_\odot$. It drives an HII region that ultimately engulfs the cluster and begins destroying the filament. This makes the connection then, with the work from Chapter 3, where we examined the radiative feedback effects of a massive isolated star in a simplified environment. This star provides sufficient ionizing flux that an HII region forms and begins disrupting the main trunk filament of the cloud clump. Along the edges of the HII region, swept-up material forms a shell and the magnetic fields lines are seen threading parallel to the shell, showing that photoionization feedback modifies the magnetic field geometry.

1.4.1 Chapter descriptions

The chapters of this thesis are presented as electronic copies of journal articles either in print, recently submitted, or in preparation to submit. The case for each one has been indicated in the list below. In lieu of prefacing each chapter with a separate introduction, we include a brief statement on the research's context within the thesis. For each one, I have been the primary contributor (first author), and the author list of each one has been included. Instead of the abstract of each journal article, I have written a short description that better shows the cohesion of the three papers within this thesis.

- **Chapter 2**: *A General Hybrid Radiation Transport Scheme for Star Formation on an Adaptive Grid*
  Authors: **Mikhail Klassen**, Rolf Kuiper, Ralph Pudritz, Thomas Peters, Robi Banerjee, Lars Buntemeyer
  Published: *The Astrophysical Journal*, Volume 797, Issue 1 (December, 2014)

  Description: We present the implementation of a general hybrid radiative transport scheme in FLASH and the general theory. We perform numerical tests of the accuracy of the method. This represents the first time that this type of complete radiative transfer method has been implemented in a general, Cartesian, adaptive mesh refinement (AMR) code

(FLASH in this case). It opens up a wide range of important problems for detailed study, including the evolution of protoplanetary disks, radiative feedback from a cluster a massive stars in turbulent, magnetized environments, and the formation of clusters inside giant molecular clouds.

Contributions: Mikhail Klassen implemented the radiative transfer scheme in FLASH with support from Rolf Kuiper, who had implemented a similar scheme in the PLUTO code. Mikhail the ran the tests described in the paper and analysed the results. Rolf supplied benchmark data. Ralph Pudritz, Thomas Peters, Robi Banerjee, and Lars Buntemeyer assisted in debugging, advised on test selection, and supplied comments to the paper. The main text of the paper was written by Mikhail Klassen.

- **Chapter 3**: *Simulating the Formation of Massive Protostars: I. Radiative Feedback and Accretion Disks*

  Authors: **Mikhail Klassen**, Ralph Pudritz, Rolf Pudritz, Thomas Peters, Robi Banerjee

  Published: *The Astrophysical Journal*, Volume 823, Issue 1 (May, 2016)

  Description: We describe a series of improvements to the hybrid radiative transfer scheme and simulate the collapse of massive protostellar cores. We show each core collapses gravitationally to form a single massive star with all further fragmentation suppressed. We study the formation and evolution of a circumstellar accretion disk. We analyze the disk stability and conclude that while gravitationally unstable, which resulted in the formation of large spiral waves, these spiral waves are still stable against fragmentation. Radiatively-driven bubbles form, but show no signs of radiative Rayleigh-Taylor instabilities. This is the first time that a general 3D framework with a complete treatment of radiation has been applied to this critical problem. The lack of disk fragmentation has major implications for trying to understand how O stars manage to typically reside in binary systems.

Contributions: Mikhail Klassen implemented the necessary code changes and improvements in FLASH needed to run dynamic star formation simulations with hybrid radiation feedback. Members of the FLASH Center at the University of Chicago supplied a new hydro solver and various other modification that helped stabilize the code. Mikhail then ran the simulations and performed the data analysis, as well as wrote the main text of the paper. Comments, suggestions, and theoretical insights on disk stability were supplied by the co-authors.

- **Chapter 4**: *Filamentary Flow and Magnetic Geometry in Evolving Cluster-Forming Molecular Cloud Clumps*

  Authors: **Mikhail Klassen**, Ralph Pudritz, Helen Kirk

  Submitted: Revised in response to referee comments and resubmitted to *Monthly Notices of the Royal Astronomical Society* (May 2016)

  Description: We perform one of the first-ever applications of 3D filament extraction using the DisPerSE algorithm on numerical simulations of massive star-forming molecular cloud clumps—the environments in which protostellar cores are formed. Supersonic turbulence gives rise to a network of filaments, as observed in molecular clouds. We initialize our simulations with realistic magnetic fields and then follow the evolution of the magnetic field geometry. We measure the relative orientation of filaments and magnetic fields. Our cloud clumps are trans-Alfvénic, meaning that the ratio of magnetic energy to turbulent energy is approximately unity. In these clouds, we found that the magnetic geometry is sensitive to the virial parameter. Highly bound clouds show a more coherent magnetic field geometry, with fields tending to align more parallel to filaments and accretion flows tending to drag magnetic field lines inward. This gave the appearance of field lines oriented perpendicular to the main "trunk" filament of our molecular cloud clump. In our marginally bound cloud, the magnetic fields tended to be oriented more perpendicular to filaments in 3D. Photoionisation feedback from massive stars disrupts the filamentary birth environment and modifies the magnetic field geometry in the vicinity of the star cluster. It also cuts off accretion flows and sets the mass of the stars within the cluster.

Contributions: Mikhail Klassen ran the simulations for this paper with input on setup design and parameter selection from Ralph Pudritz and Helen Kirk. Various analysis routines were supplied by Helen Kirk. Mikhail wrote many additional analysis scripts and performed the data analysis of the simulation results. The main text of the paper was written by Mikhail with improvements, recommendations, and corrections supplied by Ralph Pudritz and Helen Kirk.

Due to the nature of "sandwich" theses, there is necessarily some overlap between the chapters written as scientific journal articles. There may be some moderate overlap in the content of the introductions of Chapters 2 and

3, as well as in the numerical methods sections. With Chapter 4, sections describing the FLASH astrophysics code may overlap with similar sections in Chapters 2 and 3, but these are minimal. I note that the work of Chapter 4 is built upon another publication during my Ph.D. work—Kirk, Klassen, Pudritz & Pillsworth (2015, The Astrophysics Journal, **802**) for which I performed the numerical simulations and contributed to the analysis of the data.

Finally, in Chapter 5 we summarize our conclusions and how they fit within the current state of star formation research. We present an outlook to the future of the research field and the simulations that naturally follow from the advances presented within this thesis.

Chapter 2

A General Hybrid Radiation Transport Scheme for Star Formation on an Adaptive Grid

2.1 Introduction

The last several years have seen increasingly sophisticated radiation feedback models implemented in a wide variety of codes to simulate an ever wider array of physical problems. The importance of radiation feedback in the problem of star formation cannot be overstated. It is an essential process in the regulation of star formation rates and efficiencies on galactic scales, the resulting effects on the structure and evolution of galaxies [Agertz et al., 2013], the formation of star clusters and possible regulation of the IMF [Mac Low and Klessen, 2004, McKee and Ostriker, 2007b], the formation of massive stars [Beuther et al., 2007, Krumholz et al., 2007a, Kuiper et al., 2010b, 2011a, Kuiper and Yorke, 2013a,b], and the heating and chemistry of protoplanetary disks and implications for planet formation [Aikawa and Herbst, 1999, Fogel et al., 2011].

Radiation feedback's relevance for star formation has long been understood. The depletion time for a molecular cloud $t_{\rm dep} = M_{\rm gas}/\dot{M}$ is 1–3 orders of magnitude longer than the cloud's freefall time $t_{\rm ff} \sim 1/\sqrt{G\rho}$ [Krumholz and Tan, 2007, Evans et al., 2009], yet simulations that do not include any feedback mechanisms routinely see unrealistically high star formation efficiencies, with $t_{\rm dep} \sim t_{\rm ff}$.

We focus here on radiation feedback, which has been repeatedly demonstrated in simulations as an effective means of suppressing star formation, even radiation from low-mass stars [Offner et al., 2009]. While magnetic fields have been suggested as a mechanism for slowing gravitational collapse, Crutcher [2012] shows that many molecular clouds are 2–3 times supercritical to gravitational collapse. Magnetic fields have the effect of suppressing star formation [Tilley and Pudritz, 2007, Price and Bate, 2009], and a careful treatment of them must be done in any accurate star formation simulation, but it is one of several critical processes in play. Other stellar feedback mechanisms have also been studied, including winds, outflows [Kuiper et al., 2014, Peters et al., 2014], ionization [Peters et al., 2010a], radiation pressure, and supernovae, but many of these are at least in part tied to the stellar radiation [Murray et al., 2010].

We focus on the problem of thermal and momentum radiation feedback and the challenge of implementing highly accurate radiation hydrodynamics into a grid code for general simulations of star formation, leaving ionization effects to future work. Radiation hydrodynamics (RHD) methods have been implemented into several grid codes, e.g. ZEUS [Turner and Stone, 2001], ATHENA [Skinner and Ostriker, 2013], ORION [Krumholz et al., 2007b], RAMSES [Commerçon et al., 2011b, Rosdahl et al., 2013], and PLUTO [Mignone et al., 2007b] by Kuiper et al. [2010a], Flock et al. [2013], Kolb et al. [2013].

Most implementations of radiation hydrodynamics have been limited to the gray flux-limited diffusion (FLD) approximation, in which the radiation flux is proportional to the gradient of the radiation energy, ∇E_r. In this limit, it is usually assumed that the radiation and matter internal energies are tightly coupled, with the radiation and gas temperatures being equal. Further, the energy from stellar sources is deposited within some kernel centred on the radiation sources.

The problem with this approach is that the geometry of the environment surrounding stellar sources of radiation is rarely spherically symmetrical. Stars create outflow cavities and HII regions that are optically thin to radiation. Meanwhile, protostars accrete material through a rotating disk structure that is usually highly optically thick. Outflow cavities provide an outlet for the radiation flux—the so-called "flashlight effect" described in Yorke and Sonnhalter [2002], Krumholz et al. [2005b], and Kuiper et al. [2014, submitted]. Protostellar jets are on the scale of 100–1000 AU or even parsec scales for massive protostars, and HII regions can easily approach the parsec scale as well.

Above all, the birth environments of stars contain supersonic turbulence, which gives rise to filaments that allow stellar radiation a path of easy egress into the optically thin cavities between filaments while remaining optically thick along the direction of the filament. Typical implementations of FLD schemes will fail to take into account this high degree of asymmetry when depositing stellar radiation energy. This may miss important effects.

A particularly important problem in this regard is the formation of a massive star and its associated accretion disk. The intense radiation field from the forming star heats and ionizes the infalling envelope but does far less damage to the highly optically thick accretion disk through which most of gas, destined for the star, flows. Disk accretion therefore becomes the chief mechanism by which massive stars continue to accrete material despite their high luminosity [Kuiper et al., 2010b]. The accretion disk creates an environment with sharp transition regions between optically thick and optically thin, where traditional FLD codes are most inaccurate [Kuiper and Klessen, 2013]. To address this high degree of asymmetry, Kuiper et al. [2010a] implemented a radiation transfer scheme in PLUTO that combined a 1D multifrequency raytrace with a gray FLD code. The method was implemented for spherical polar grids, which meant that the raytrace needed only be carried out in the radial direction.

As an example application of this, Kuiper et al. [2012] studied the stability of radiation-pressure-dominated cavities around massive protostars. Radiatively-driven outflows have the potential to remove a significant amount of mass from the stellar environment that would otherwise be accreted by the protostar. Several mechanisms have been proposed for how a massive protostar could accrete material beyond its Eddington limit. Krumholz et al. [2009] proposed a "radiative Rayleigh-Taylor instability" in which the radiatively-driven shell becomes unstable and material is able resume gravitational infall. But Kuiper et al. [2012] argued that a gray FLD-only radiative transfer scheme underestimates the radiative forces acting on the shell.

We now generalize the method to 3D Cartesian grids with adaptive mesh refinement (AMR) and implement a hybrid raytrace/FLD method in the FLASH astrophysics code. This method extends to multiple sources and does not rely on any special geometry, allowing for the treatment of more general problems such as star cluster formation. Moreover, for the FLD solver step, we implement a two-temperature (2T) radiation transport scheme; that is, we do not force the radiation temperature and matter temperature to be equal everywhere. We discuss the general theory of this approach in section 2.2; the equations to be solved and the numerical methods for FLASH in section 2.3; the tests of our radiation transport scheme in sections 2.4, 2.5, and 2.6; and our final thoughts and discussion in section 2.7.

2.2 Theory

The general idea to split the radiation field into a direct component and a diffuse or scattered component is an old one [see, e.g., Wolfire and Cassinelli, 1986, Murray et al., 1994, Edgar and Clarke, 2003]. The direct component dominates in the optically thin regions, such as in the outflow cavities created by massive stars, or in HII regions, where the temperature of the radiation field is that of the stellar photosphere. Within a few optical depths, inside the optically thick regions, the radiation field becomes dominated by the diffuse, thermal component of the radiation field. The main advantage of splitting the radiation field in this way is accuracy [Murray et al., 1994]. Raytracing is a solution to the radiative transfer problem, whereas FLD is a convenient approximation for the sake of computation. In the optically thin regions such as those noted above, a direct raytrace ignoring scattering is an excellent way of accurately calculating the radiation field, whereas the gray FLD is accurate inside optically thick regions where the temperature of the radiation is equilibrated to the matter temperature. In complex morphologies, with interspersed regions of varying optical depth, FLD is not at all accurate.

This general splitting approach is equivalent to extracting the first absorption event from the FLD solver and allowing the radiation flux to be calculated by a raytracing scheme instead, with all re-emission and secondary absorption handled by the FLD solver. This improves the accuracy in precisely the region where the FLD approximation is worst, namely in regions directly irradiated by discrete radiation sources such as stars.

A hybrid radiation transport scheme splits the flux term,

$$\boldsymbol{F} = \boldsymbol{F}_* + \boldsymbol{F}_{\mathrm{th}}, \tag{2.1}$$

into a direct (stellar) component $\boldsymbol{F}_*$ and a thermal radiation component $\boldsymbol{F}_{\mathrm{th}}$. FLD implementations treat only the transport of a single radiation flux proportional to the gradient in the radiation energy E_r,

$$\boldsymbol{F}_{\mathrm{th}} \propto -\nabla E_r. \tag{2.2}$$

Hybrid schemes decompose the radiation field, transporting the direct component via a raytracer (see 2.3.4) and the indirect component via a diffusion equation. The radiation transport equation, integrated over all solid angle, with the operator-split hydrodynamic terms removed, is

$$\partial_t E_r + \nabla \cdot \boldsymbol{F}_r = \kappa_P \rho \left(4\pi B - cE_r\right), \tag{2.3}$$

with E_r is the radiation energy density, $\boldsymbol{F}_r$ the flux of the radiation energy, σ_P the Planck opacity, $B = B(T)$ the Planck function, and c the speed of light.

In a split scheme the direct component $\nabla \cdot \boldsymbol{F}_*$ is calculated everywhere for all sources. We describe how this is done in section 2.3.4. How the thermal component is handled is the subject of section 2.3.3.

In order to address problems of multiple star formation, as well as the formation of star clusters, a more general approach is needed. Specifically, we generalize the hybrid radiation transfer approach to Cartesian grids with AMR. These kinds of codes already have the ability to follow the gravitational collapse of multiple regions within a simulation, and have excellent implementations of turbulent and MHD processes. They also enable further study of radiatively-driven shells and outflows with adaptive resolution.

The scope of the current paper is the implementation of the general hybrid radiation transfer scheme in an AMR grid code, and tests of its accuracy. As noted in the introduction, there are many important applications of our code which we will take up in subsequent papers, including the formation of a massive star in a turbulent, magnetized, collapsing medium, ionization feedback, and the formation of star clusters.

2.3 Numerical methodology

2.3.1 FLASH

We use the publicly available FLASH high-performance general application physics code, currently in its 4th major version [Fryxell et al., 2000a, Dubey et al., 2009]. The code is modular, and has physics capabilities that now include 2T radiation hydrodynamics (our contribution), magnetohydrodynamics, multi-group flux-limited diffusion, self-gravity, and a variety of options for the equation of state.

The code has been expanded to include sink particles, originally implemented in version 2.5 [Federrath et al., 2010a], and then later ported to version 4.0 [Safranek-Shrader et al., 2012]. Multigroup flux-limited diffusion for radiation hydrodynamics was added in version 4.0 for the study of high-energy density physics (HEDP), such as radiative shocks and laser energy deposition experiments. Despite these original motivations, the code is general and can be applied to astrophysical scenarios.

A time-independent raytracer with hybrid characteristics was added in version 2.5 by Rijkhorst et al. [2006a] and then modified for the study of collapse calculations by Peters et al. [2010a]. The raytracer was used to calculate photoelectric heating and photoionization rates, as well as heating by optically thin non-ionizing radiation, to study HII regions and ionization feedback in molecular clouds [Peters et al., 2010a,d,c, 2011, 2012, Klassen et al., 2012b]. However, this approach is not suitable to propagate non-ionizing radiation in optically thick clouds.

We ported this raytracer into the present version of the FLASH code in order to calculate the irradiation of gas and dust by point sources within the domain and solve the radiation hydrodynamic equations.

FLASH solves the fluid equations on an Eulerian mesh with adaptive mesh refinement (AMR) using the piecewise parabolic method [Colella and Woodward, 1984]. The method is well-suited for dealing with shocks. The diffusion equation is solved implicitly via the generalized minimal residual (GMRES) method. The refinement criterion used by FLASH is an error estimator based on Löhner [1987], which is a modified second derivative normalized by the average of the gradient over one computational cell. It has the advantage of being dimensionless and local, so one has the flexibility to choose the grid variable upon which to refine.

In this paper we describe the implementation of a hybrid radiation transfer scheme, involving raytracing coupled to a flux-limited diffusion (FLD) solver. The raytracer finds the flux each cell receives from all point sources (e.g. stars) in the simulation while the FLD solver evolves the diffuse radiation field. The combined radiation field is used to update the matter temperature.

In the sections below we recapitulate the basic theory and how these equations are implemented in FLASH .

2.3.2 Radiation hydrodynamics

If the radiation fields are assumed to have a blackbody spectrum, then in the absence of magnetic and gravitational fields, and assuming local thermodynamic equilibrium (LTE), the frequency- and angle-integrated radiation hydrodynamic equations in the comoving frame are [Turner and Stone, 2001, Mihalas and Mihalas, 1984]

$$\tfrac{D\rho}{Dt} + \rho\nabla\cdot\boldsymbol{v} = 0 \tag{2.4}$$

$$\rho\tfrac{D\boldsymbol{v}}{Dt} = -\nabla p + \tfrac{1}{c}\kappa_P\rho\boldsymbol{F}_r \tag{2.5}$$

$$\rho\tfrac{D}{Dt}\left(\tfrac{e}{\rho}\right) + p\nabla\cdot\boldsymbol{v} = -\kappa_P\rho(4\pi B - cE_r) \tag{2.6}$$

$$\rho\tfrac{D}{Dt}\left(\tfrac{E_r}{\rho}\right) + \nabla\cdot\boldsymbol{F}_r + \nabla\boldsymbol{v}:\boldsymbol{P} = \kappa_P\rho(4\pi B - cE_r) \tag{2.7}$$

where $D/Dt \equiv \partial/\partial t + \boldsymbol{v}\cdot\boldsymbol{\nabla}$ is the convective derivative. The fluid variables $\rho, e, \boldsymbol{v}$, and p are the matter density, internal energy density, fluid velocity, and scalar pressure, respectively, while $E_r, \boldsymbol{F}_r$, and $\boldsymbol{P}$ are the total frequency-integrated radiation energy, flux, and pressure, respectively. Equations 2.4

and 2.5 express the conservation of mass and momentum, respectively, where the radiation applies a force proportional to $\kappa_P \rho \boldsymbol{F}_r / c$, where κ_P is the Planck mean opacitiy defined in equation 2.9 below.

The hydrodynamic equations must also be closed via an equation of state. We use a gamma-law equation of state for simple ideal gases. The gas pressure P, density ρ, internal energy ϵ, and gas temperature T are related by the equations,

$$P = (\gamma - 1)\rho\epsilon = \frac{N_a k_B}{\mu} \rho T, \tag{2.8}$$

with adiabatic index $\gamma = 5/3$. N_a is Avogadro's number, k_B is the Boltzmann constant, and μ is the mean molecular weight.

The coupling between internal and radiation energy is expressed by equations 2.6 and 2.7. Coupling comes through the emission and absorption of radiation energy. The assumption of LTE lets us write the source function as the Planck function, B, so that matter emits thermal radiation proportional to the rate,

$$4\pi\kappa_P \rho B(T) \equiv \kappa_P \rho c a T^4,$$

where κ_P is the Planck mean opacity,

$$\kappa_P = \frac{\int_0^\infty d\nu \kappa_\nu B_\nu(T)}{B(T)}, \tag{2.9}$$

with

$$B_\nu(T) = \frac{2h\nu^3/c^2}{e^{h\nu/k_B T} - 1}. \tag{2.10}$$

Meanwhile, matter is absorbing radiation out of the thermal field at a rate $\kappa_P \rho c E_r$. Energy lost by the radiation field is gained by the matter and vice versa. We will use the flux-limited diffusion approximation to relate the radiation flux $\boldsymbol{F}_r$ to the radiation energy E_r.

In practice, many grid codes implement the flux-limited diffusion approximation [Turner and Stone, 2001, Krumholz et al., 2007b, Commerçon et al., 2011b], which relates the radiation flux $\boldsymbol{F}_r$ to the radiation energy E_r. In the FLD approximation, the radiation and matter components may be thought of as two fluids, each with their own equation of state, internal energy, temperature, and pressure. The matter component may be further split into ion and electron components, which exchange energy via collisions. This is three-temperature, or "3T" approach is used in the modeling of laboratory plasmas. The FLASH code was extended in version 4 to include 3T radiation hydrodynamics [Lamb et al., 2010, Fatenejad et al., 2012, Kumar et al., 2011]. Energy exchange under the 3T model is included for reference in Section 2.8. In astrophysics, we are more concerned with modeling the gas/dust mixture of the ISM, with the gas sometimes ionized. By setting a unified matter temperature in FLASH , with $T_{\rm ion} = T_{\rm ele} \equiv T_{\rm gas/dust}$, we return to a 2T model, with only matter and radiation temperatures varying and exchanging energy.

Radiation only behaves like a fluid when it is tightly coupled to matter, which occurs only in very optically thick regions. Hybrid radiation schemes more accurately transport the radiation energy through the computational domain.

2.3.3 Flux-limited diffusion

Under the flux-limited diffusion approximation [Levermore and Pomraning, 1981, Bodenheimer et al., 1990], the flux of radiation is proportional to the gradient in the radiation energy density,

$$\boldsymbol{F}_r = -D\nabla E_r, \tag{2.11}$$

where

$$D = \frac{\lambda c}{\kappa_R \rho} \tag{2.12}$$

is the diffusion coefficient. κ_R is the Rosseland mean opacity and λ is the flux limiter that bridges the radiation diffusion rate between the optically thin and optically thick regimes. In the extreme optically thick limit, $\lambda \to 1/3$, which is the diffusion limit. In the extreme optically thin limit, the flux of radiation becomes $F_r = cE_r$, the free-streaming limit.

We use the Levermore and Pomraning [1981] flux limiter, one of the most commonly used,

$$\lambda = \frac{2 + R}{6 + 3R + R^2}, \tag{2.13}$$

with

$$R = \frac{|\nabla E_r|}{\kappa_R \rho E_r}. \tag{2.14}$$

Other flux limiter are possible, such as Minerbo [1978], another popular choice. Different flux limiters result from different assumptions about the angular distribution of the specific intensity [Turner and Stone, 2001].

FLASH solves the radiation diffusion equation 2.7 using a general implicit diffusion solver. Using the method of operator splitting, terms such as advection and hydrodynamic work are handled by the code's hydro solver. The radiation diffusion solver then updates the radiation energy equation by solving

$$\frac{\partial E_r}{\partial t} + \nabla \cdot \left(\frac{\lambda c}{\kappa_R \rho} \nabla E_r \right) = \kappa_P \rho c \left(a T^4 - E_r \right) \tag{2.15}$$

where T is the gas temperature.

To solve this equation, we use the method of the generalized minimum residual (GMRES) by Saad and Schultz [1986]. It is included in FLASH via the HYPRE library [Falgout and Yang, 2002]. The GMRES method is the same one employed by Kuiper et al. [2010a] in their hybrid radiation-transport scheme. It belongs to the class of Krylov subspace methods for iteratively solving systems of linear equations of the form $A\boldsymbol{x} = \boldsymbol{b}$, where the matrix A is large and must be inverted. Matrix inversion is, in general, a very computationally expensive operation, but because A is also a sparse matrix, methods exist for rapidly computing an approximate inverse with relatively high accuracy, outperforming methods such as conjugate gradient (CG) and successive over-relaxation (SOR). The HYPRE library that FLASH uses is a collection of sparse matrix solvers for massively parallel computers.

A difference in matter and radiation temperatures in equation 2.15 results in an energy "excess" on the right-hand side. We must update the matter temperature due to the action of the combined radiation fields. Restating equations 2.6 and 2.7, with operator-split hydrodynamic terms removed, and a stellar radiation source term added, we have

$$\partial_t \rho \epsilon = -\kappa_P \rho c \left(a_R T^4 - E_r \right) - \nabla \cdot \boldsymbol{F}_* \tag{2.16}$$

$$\partial_t E_r + \nabla \cdot \boldsymbol{F}_r = +\kappa_P \rho c \left(a_R T^4 - E_r \right) \tag{2.17}$$

Discretizing equation 2.16 and 2.17, we have

$$\frac{\rho c_V T^{n+1} - \rho c_V T^n}{\Delta t} = -\kappa_P^n \rho c \left(a_R \left(T^{n+1}\right)^4 - E_r^{n+1} \right) - \nabla \cdot \boldsymbol{F}_*, \tag{2.18}$$

and

$$\frac{E_r^{n+1} - E_r^n}{\Delta t} - \nabla \cdot \left(D^n \nabla E_r^{n+1} \right) = +\kappa \rho c \left(a_R \left(T^{n+1}\right)^4 - E_r^{n+1} \right) \tag{2.19}$$

recalling that the specific internal energy $\epsilon = c_V T$, with c_V being the specific heat capacity of the matter. Variables with superscript indices n and $n+1$ take their values from before and after the implicit update, respectively. It is important to remember that the opacity κ_P is temperature-dependent. The source term for stellar radiation takes the form $\nabla \cdot \boldsymbol{F}_*$ and represents the amount of stellar radiation energy absorbed at a given location in the grid from all sources.

The presence of the nonlinear term $(T^{n+1})^4$ makes it difficult to solve for the temperature in 2.18. Assuming that the change in temperature is small, Commerçon et al. [2011b] linearizes this term,

$$\begin{aligned} \left(T^{n+1}\right)^4 &= (T^n)^4 \left(1 + \frac{T^{n+1} - T^n}{T^n} \right)^4 \\ &\approx 4 \left(T^n\right)^3 T^{n+1} - 3 \left(T^n\right)^4 . \end{aligned} \tag{2.20}$$

This allows for equation 2.20 to be substituted into equation 2.18 and for us to write an expression for the updated temperature,

$$T^{n+1} = \frac{3 a_R \alpha \left(T^n\right)^4 + \rho c_V T^n + \alpha E_r^{n+1} - \Delta t \nabla \cdot \boldsymbol{F}_*}{\rho c_V + 4 a_R \alpha \left(T^n\right)^3}, \tag{2.21}$$

where we have used $\alpha \equiv \kappa_P^n \rho c \Delta t$.

The irradiation term, $\nabla \cdot \boldsymbol{F}_*$, is supplied by the raytracer. Its calculation is the subject of section 2.3.4.

The raytrace is performed first in order to calculate $\nabla \cdot \boldsymbol{F}_*$. By substituting equation 2.21 into 2.19 via the approximation of equation 2.20, and making appropriate simplifications, the FLD equation becomes

$$\frac{E_r^{n+1} - E_r^n}{\Delta t} - \nabla \cdot \left(D^n \nabla E_r^{n+1} \right) + \kappa \rho c \left[\frac{\rho c_V T^n}{\rho c_V T^n + 4\alpha a_R \left(T^n\right)^4} \right] E_r^{n+1} = \kappa \rho c a_R \left(T^n\right)^4 \left[\frac{\rho c_V T^n - 4\Delta t \nabla \cdot F_*}{\rho c_V T^n + 4\alpha a_R \left(T^n\right)^4} \right], \quad (2.22)$$

where we have gathered implicit terms on the left-hand side and explicit terms on the right-hand side.

We solve equation 2.22 via the diffusion solver to calculate the updated radiation energy density and temperature, then update the gas/dust temperature via 2.21. This completes the radiation transfer update for the current timestep.

2.3.4 Stellar irradiation

When the effects of scattering and emission are ignored, the equation for the specific intensity of radiation from a point source along a ray assumes a very simple form,

$$I(r) = I_0 e^{-\tau(r)}, \quad (2.23)$$

where I_0 is the specific intensity of the source and $\tau(r)$ is the optical depth from the source up to r:

$$\tau(r) = \int_{R_*}^{r} \kappa_P(T_*)\rho(r')\,\mathrm{d}r' \tag{2.24}$$

The opacity κ_P is a function of temperature and the optical depth is calculated using the temperature of the radiation source, e.g. the effective temperature of a star. ρ is the usual gas density. Rays are traced from individual cells in the computational grid back to the point sources (usually stars) via a characteristics-based method described in Rijkhorst et al. [2006a].

In characteristics-based raytracing, there are two approaches to computing the column density toward sources, each with its own advantages and disadvantages. *Long characteristics* involves tracing rays from the source to each cell in the computational domain. This method is very accurate, but involves many redundant calculations of the column density through cells intersected by similar rays near the source. *Short characteristics* tries to mitigate the redundant calculations by tracing rays only across the length of each grid cell in the direction of the source, then interpolating upwind toward the source to calculate the total column density. The disadvantage of this approach is that the upwind values need to be known ahead of time, which imposes an order on the calculations and makes scaling the code to many processors very problematic. Some amount of numerical diffusivity is also introduced in this approach on account of interpolating column densities at each cell.

As a compromise between these two methods, Rijkhorst et al. [2006a] developed a method they called *hybrid characteristics* that minimizes the number of redundant calculations and can be parallelized. The local contributions to the column density are computed for each block of $n \times n \times n$ cells. Then the values on the block faces are computed and communicated to all processors. Finally, the total column density at each cell is computed by adding the local and interpolated face values.

Peters et al. [2010a] have improved the method to allow collapse simulations with arbitrary many refinement levels and sources of radiation. They added the propagation of (optically thin) non-ionizing radiation and coupled the respective heating terms to a prescription of molecular and dust cooling [Banerjee et al., 2006]. Furthermore, they have linked the radiation module to sink particles [Federrath et al., 2010a] as sources of radiation and implemented a simple prestellar model to determine the value of the stellar and accretion luminosities. In our current implementation, we no longer use a separate cooling function because the thermal evolution is already implicit in the coupled equations of internal and radiation energy, as described in section 2.3.3.

The stellar flux a distance r is given by

$$F_*(r) = F_*(R_*) \left(\frac{R_*}{r}\right)^2 \exp\left(-\tau(r)\right), \tag{2.25}$$

where R_* is the stellar radius, and $F_*(R_*)$ is the flux at the stellar surface, given by

$$F_*(R_*) = \sigma T_*^4. \tag{2.26}$$

T_* is the effective temperature of the stellar surface and σ is the Stefan-Boltzmann constant.

At this time, our raytracing is purely gray; we use the Draine and Lee [1984] dust model and compute the temperature-dependent frequency-averaged opacities, assuming a 1% dust-to-gas ratio. Multifrequency raytracing is relatively straightforward to implement, but the computational costs increase linearly with the number of frequency bins. We leave the implementation of multifrequency effects to a future paper.

Using the stellar flux computed at each cell, we estimate an "irradiation" term, i.e. the amount of stellar flux absorbed by a given cell,

$$\nabla \cdot F_*(r) \approx -\frac{(1 - e^{\tau_{\rm local}})}{\Delta r} F_*(r), \tag{2.27}$$

where $\tau_{\rm local}$ is the "local" contribution to the optical depth through the cell, i.e.

$$\tau_{\rm local} \approx \kappa_P(T_*)\rho\,\Delta r, \tag{2.28}$$

and Δr is the distance traced by the ray through a grid cell. For numerical stability, when $\tau_{\rm local}$ is very small, e.g. 10^{-5}, we estimate the irradiation by Taylor-expanding the exponential,

$$\nabla \cdot F_*(r) \approx -\kappa_P \rho F_*(r), \tag{2.29}$$

which is the optically thin limit.

2.3.5 Opacities

The primary source of opacity in the interstellar medium is dust grains. We use the tabulated optical properties of graphite and silicate dust grains from Draine and Lee [1984]. They evaluate absorption cross-sections for particles with sizes between 0.003 and 1.0 microns at wavelengths between 300 Å and 1000 microns. These tabulated dust properties are widely used both in simu-

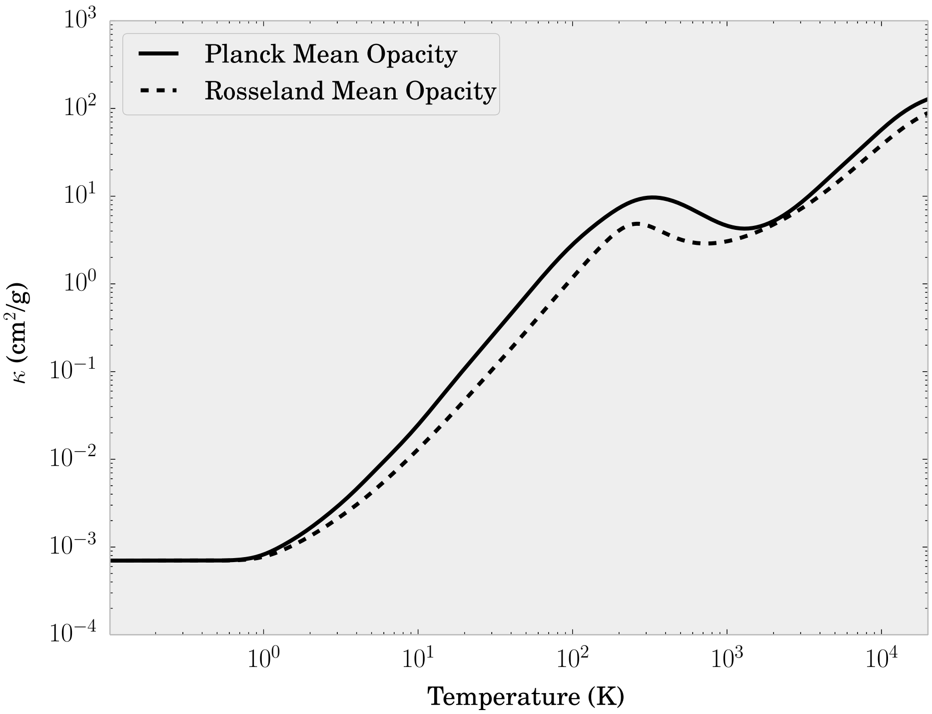

Figure 2.1: Frequency-averaged opacity (in units of cm^2 per gram gas) as a function of temperature for a 1% mixture of interstellar dust grains with gas, based on the model by Draine and Lee [1984].

lations [e.g. Pascucci et al., 2004, Offner et al., 2009, Flock et al., 2013] and in observational work [e.g. Nielbock et al., 2012].

We assume a dust to gas ratio of 1% and integrate the dust opacity over a wavelength range of 1 Å–1000 microns. This is done as a function of temperature, resulting in "gray" (frequency-averaged) temperature-dependent Planck and Rosseland mean opacity tables. Figure 2.1 shows, e.g., the opacity κ over a range of temperatures from 0.1 K to 2000 K. We see that these opacities cover many orders of magnitude.

2.3.6 Radiation pressure

Both the direct radiation field and the diffuse radiation field contribute to the radiation pressure. In the case of the diffuse (thermal) radiation field, FLASH makes the Eddington approximation,

$$P_{\rm rad} = \frac{1}{3}E_r = \frac{aT_{\rm rad}^4}{3}, \tag{2.30}$$

where E_r is the radiation energy density and $T_{\rm rad}$ is the corresponding temperature. Additional momentum is added to the gas from the direct component of the radiation field. We take the stellar fluxes computed by the raytracer (Equation 2.25). These exert a body force

$$f_{\rm rad} = \rho\kappa_P(T_*)\frac{F_*}{c} = -\frac{\nabla \cdot \boldsymbol{F}_*}{c}, \tag{2.31}$$

where $f_{\rm rad}$ is the force density and F_* is the direct stellar radiation flux. The temperature of the direct radiation field is that of the source, $T_* = T_{\rm eff}$, the effective stellar surface temperature.

From equation 2.31 we see that the radiation force density is proportional to the absorbed radiation energy computed by the raytracer, i.e. the force felt by the gas and dust in a local region is proportional to its absorbed stellar radiation energy.

We do not expect our radiation force to change much if it were to be computed with a multifrequency raytracer. The radiation force is proportional to the absorbed flux. In the multifrequency case, infrared radiation can penetrate further into the gas, but also carries less energy. Most of the higher frequencies are all absorbed in the same (few) grid cells. Tests by Kuiper et al.

[2010a] also showed very little deviation between the gray and multifrequency cases.

2.3.7 Summary of the hybrid radiation hydrodynamics method

In summary, we treat radiation hydrodynamics by complementing the fluid dynamics equations to include the effects of radiation (equations 2.4 through 2.7. We have decomposed the radiation field into a direct stellar component and an indirect diffuse component. The method of raytracing is used to calculate the direct stellar radiation field. The method of flux-limited diffusion is used to transport radiation in the diffuse radiation field.

Matter and radiation are coupled by emission and absorption processes, while stars represent sources of radiation energy. This relationship is given in equations 2.16 and 2.17.

We have discretized and linearized equation 2.16 and 2.17 to derive an expression for evolving the matter temperature, given absorption and emission of radiation, the presence of a thermal radiation field, and the flux from discrete stellar sources. This is expressed in equations 2.21 and 2.22.

The next sections describe tests of the radiation transport routines and the reliability of our method.

2.4 Tests of thermal radiation diffusion

2.4.1 Thermal radiative equilibration

To test the accuracy of the matter/radiation coupling, we set up a unit simulation volume with a uniform gas density of $\rho = 10^{-7}$ g/cm^3 initially out of equilibrium with the radiation field [Turner and Stone, 2001]. If the radiation energy dominates the total energy, then any radiation energy absorbed or emitted is relatively small and the radiation field can be said to be unchanging. The matter energy evolves according to equation 2.16, but without the source term, i.e.

$$\frac{\partial e}{\partial t} = \chi c \left(E_r - a_R T^4 \right), \tag{2.32}$$

where $e = \rho\epsilon$ is the volumetric matter energy density, and $\chi = \kappa_P \rho = 4 \times 10^{-8}$ cm^{-1} is the absorption coefficient.

We set the radiation energy density $E_r = 10^{12}$ ergs/cm^3, as in Turner and Stone [2001]. We solve equation 2.32 assuming a constant E_r and plot the results in Figure 2.2 as the solid black lines. The initial matter energy density is $e = 10^{10}$ ergs/cm^3 in the case where the gas cools to equilibrium. In the gas warming case, the initial matter energy density is $e = 10^2$ ergs/cm^3.

The gas is assumed to be an ideal gas with $\gamma = 5/3$ and a mean mass per particle of $\mu = 0.6$.

Figure 2.2 shows the results of numerical simulations with FLASH. The simulation has an adaptive timestep initially set to $\Delta t = 10^{-14}$ s. The maximum timestep size for this simulation was set to $\Delta t = 10^{-8}$ s. The total energy in the simulation volume is conserved to better than 1% over the

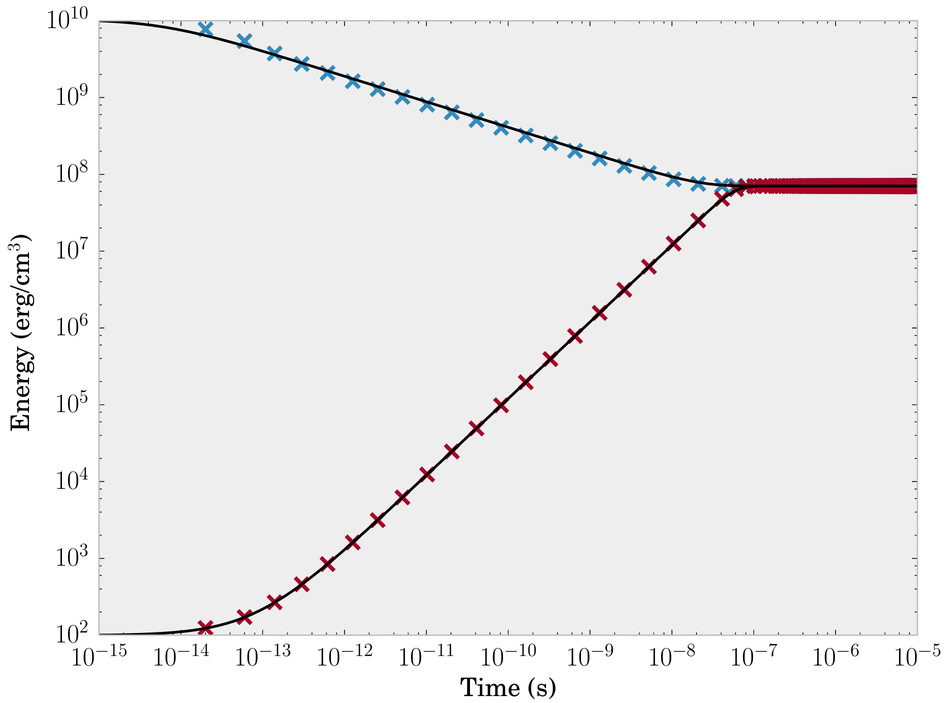

Figure 2.2: Results from matter-radiation coupling tests. The initial radiation energy density is $E_r = 10^{12}$ ergs/cm^3. The matter internal energy density is initially out of thermal equilibrium with the radiation field. Crosses indicate simulation values at every time step, while the solid line is the analytical solution, assuming a constant E_r. Initial matter energy densities are $e = 10^{10}$ ergs/cm^3 (upper set) and $e = 10^2$ ergs/cm^3 (lower set).

duration of the simulation.

2.4.2 1D radiative shock tests

The treatment of radiative shocks is an important benchmark in many radiative transfer codes [Hayes and Norman, 2003, Whitehouse and Bate, 2006, González et al., 2007, Kuiper et al., 2010a, Commerçon et al., 2011b]. We follow the setup described in Ensman [1994] of a streaming fluid impinging on a wall, represented by a reflective boundary condition. The fluid is compressed and a shock wave travels in the upstream direction. The hot fluid radiates thermally, and the radiation field preheats the incoming fluid. By varying the speed of the incoming fluid, sub- or supercritical shocks can be formed. Criticality occurs when there is sufficient upstream radiation flux that the preshock temperature is equal to the postshock temperature. The fluid velocity at which this occurs is called the critical velocity. Numerical simulations can be compared to analytic arguments by Mihalas and Mihalas [1984] for the gas temperature in various parts of the shock to check how well these shock features are being reproduced by the code.

The initial conditions are as follows: an ideal fluid ($\gamma = 5/3$) has a uniform mass density of $\rho_0 = 7.78 \times 10^{-10}$ g/cm^3, a mean molecular weight $\mu = 1$, and is at a uniform temperature of $T_0 = 10$ K. The domain size is $L = 7 \times 10^{10}$ cm.

For the subcritical shock, the fluid moves to the left with a speed $v = 6$ km/s. For the supercritical shock, $v = 20$ km/s. The fluid is given a uniform absorption coefficient of $\sigma = 3.1 \times 10^{-10}$ cm^{-1}.

Upon compression of the gas at the leftmost boundary, the postshock temperature T_2 increases and a radiative flux of order $\sigma_B T_2^4$ is produced, where σ_B is the Stefan-Boltzmann constant. This radiation penetrates upstream to preheat the gas ahead of the shock front to a temperature T_-. This preheating can be clearly seen in Figure 2.3. The shock is considered subcritical so long as $T_- < T_2$.

If the speed of the incoming gas v is increased, there is greater preheating and the preshock temperature approaches the postshock temperature, $T_- \sim T_2$. These temperatures are equal for a critical shock. If the incoming gas speed is increased still further, the temperature of the preshock gas re-

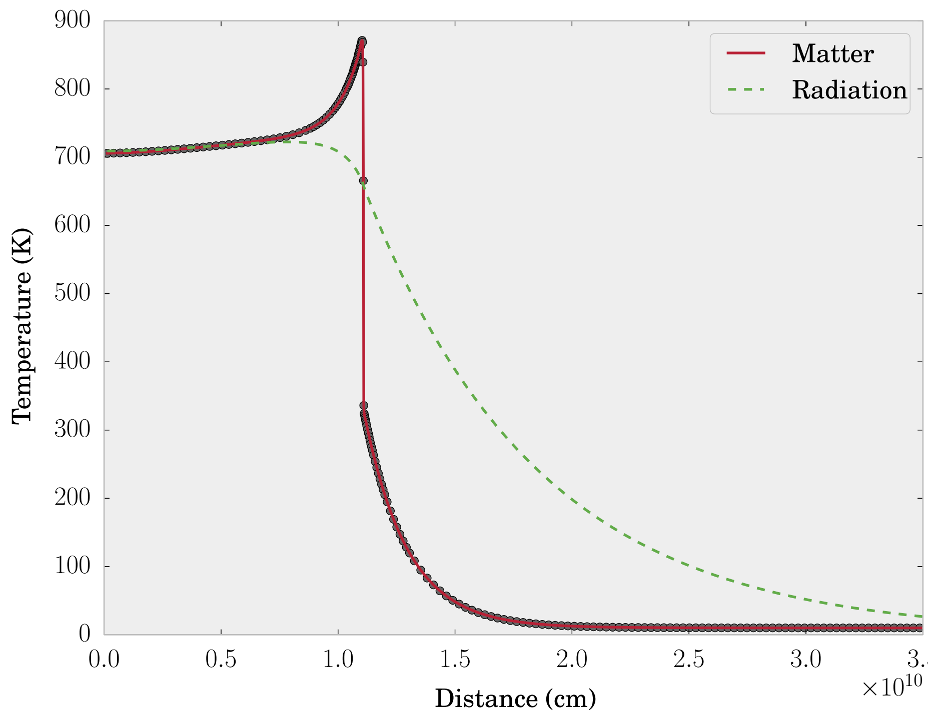

Figure 2.3: Temperature profile for a subcritical radiative shock with a gas velocity of $v = 6$ km/s at time $t = 5.80 \times 10^4$ s. Red and green lines indicates matter and radiation temperatures, respectively. Circles along matter temperature indicate the grid resolution.

mains steady, while the radiative precursor is extended. This is a supercritical shock, as seen in Figure 2.4.

For the subcritical case, if $T_{-} \ll T_2$, an approximate solution is given in Mihalas and Mihalas [1984] for the postshock temperature,

$$T_2 \approx \frac{2\,(\gamma - 1)\,v^2}{R\,(\gamma + 1)^2}, \tag{2.33}$$

where $R = k_B/\mu m_H$ is the ideal gas constant.

For our subcritical case, with an incoming gas velocity of $v = 6$ km/s, this gives $T_2 \approx 812$ K. In our test case, the postshock temperature at the

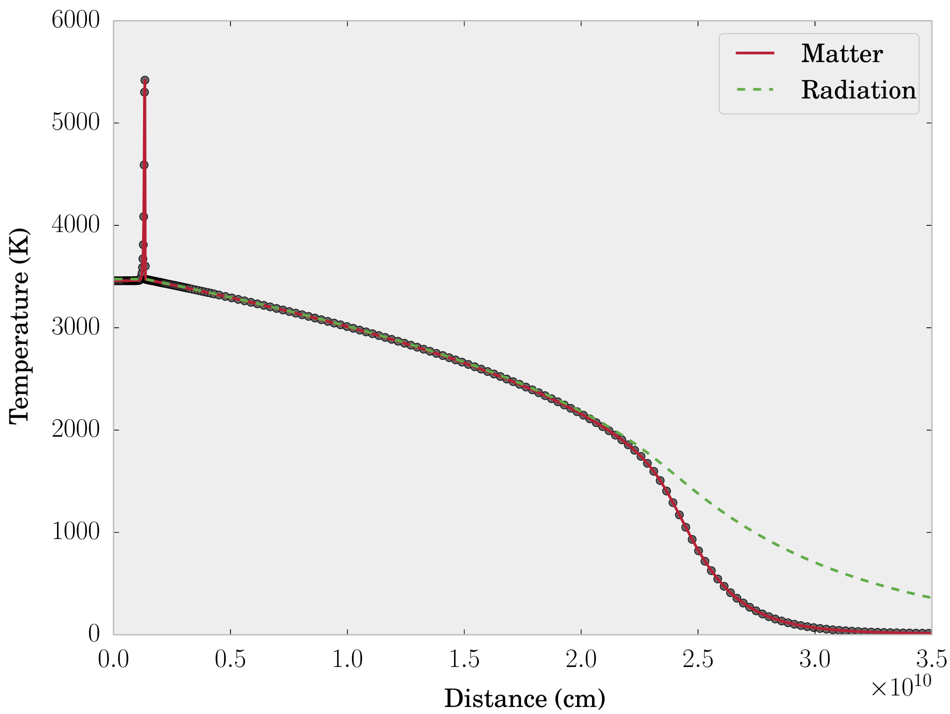

Figure 2.4: Temperature profile for a supercritical radiative shock with a gas velocity of $v = 20$ km/s at time $t = 5.08 \times 10^3$ s. Lines and circles represent the same as in previous figure.

far-left of the domain is 706 K, or about 13% less than the approximate value.

The preshock temperature can be approximated [Mihalas and Mihalas, 1984] by

$$T_- \approx \frac{\gamma - 1}{\rho v R} \frac{2\sigma_B T_2^4}{\sqrt{3}} \sim 279\mathrm{K}. \tag{2.34}$$

The temperature spike at the subcritical shock front is approximated by

$$T_+ \approx T_2 + \frac{3-\gamma}{\gamma+1} T_- \sim 874\mathrm{K}. \tag{2.35}$$

Our preshock temperature reaches 336 K, which is about 20% warmer than the analytic approximation. Similar calculations in Kuiper et al. [2010a]

did not reproduce any preheating due to the 1-T approach in FLD. Our numerical shock temperature $T_+ \approx 871$ K agrees to within better than 1%.

In the supercritical case, the radiation spike has collapsed to a thickness of less than about a photon mean free path. The temperature of the spike is $T_+ \approx 5420$ K, whereas the analytic approximation [Mihalas and Mihalas, 1984] gives

$$T_+ \approx (3 - \gamma)T_2 \sim 4612\mathrm{K}, \tag{2.36}$$

with which our numerical calculations agree to within 18%. Comparing to other FLD implementations on AMR grids, Commerçon et al. [2011b] matches the analytic estimates of the subcritical postshock temperature a little closer (to within 2%). Our scheme captures the preshock heating that the 1-T scheme described in Kuiper et al. [2010a] could not (MAKEMAKE has since been made into a 2-T scheme), but not as closely as Commerçon et al. [2011b], which captures it to within 1%. The subcritical shock temperature we capture comparably well to Commerçon et al. [2011b]. While FLASH has a different refinement criterion from the one used in Commerçon et al. [2011b], this is not likely the cause of the differences. More likely is the different choice of flux limiter (Levermore and Pomraning [1981] vs Minerbo [1978]), which, because of different assumptions about the angular dependence of the radiation field in a particular problem, can yield slightly different solutions, with the greatest differences seen in regions of intermediate to low optical depth [Turner and Stone, 2001]. It is not obvious which flux limiter is best for a given problem, but we have opted for one shared by Kuiper et al. [2010a].

2.5 Irradiation of a static disk

A radiation test of general astrophysical interest is that of a star embedded in a circumstellar disk. The disk itself is optically thick and is surrounded by an optically thin envelope. The setup we use follows Pascucci et al. [2004] and includes a sun-like star surrounded by a flared circumstellar disk similar to those considered by Chiang and Goldreich [1997, 1999] for T Tauri stars. The density structure features steep gradients in the inner disk, which can be challenging for radiative transfer codes, making this an excellent test.

We compare the temperature profile of the disk midplane in our simulation with one calculated using the radiative transfer module called MAKEMAKE implemented in PLUTO [Mignone et al., 2007a] by Kuiper et al. [2010a]. In the comparable setup ($\tau_{550\mathrm{nm}} \sim 100$), the difference between the simulated temperatures and Monte Carlo calculation was $\lesssim 16\%$. However, in the Pascucci et al. [2004] benchmark paper, the temperature variation between different Monte Carlo codes including isotropic scattering is of the same order ($\lesssim 15\%$).

The setup of the flared disk is as follows:

$$\rho(r,z) = \rho_0 \frac{r_d}{r} \exp\left(-\frac{\pi}{4}\left(\frac{z}{h(r)}\right)^2\right), \tag{2.37}$$

where

$$h(r) = z_d \left(\frac{r}{r_d}\right)^{1.125}, \tag{2.38}$$

and

$$r_d = \frac{r_{\max}}{2} = 500 \text{ AU} \tag{2.39}$$

Table 2.1: Simulations of the irradiated disk setup.

$\tau_{\rm gray,abs}$	ρ_0 [g cm^{-3}]	$M_{\rm tot}$ [M$_\odot$]
0.01	8.321×10^{-21}	1.56×10^{-5}
10.1	8.321×10^{-18}	1.56×10^{-2}

$$z_d = \frac{r_{\rm max}}{8} = 125 \text{ AU} \tag{2.40}$$

We set up our computational domain to be a cube of side length 1000 AU, with the radiation source located at one corner. The source has radius $r = R_\odot$ and $T_{\rm eff} = 5800$ K. The domain represents one octant of a disk around a sunlike star. The minimum density is set to $\rho_{\rm small} = 10^{-23}$ g/cm^3 to avoid division-by-zero errors. We run simulations at two different fiducial densities ρ_0, representing the optically thin and optically thick cases. These runs are tabulated in Table 2.1. We use the same fiducial densities as in Kuiper et al. [2010a], but our optical depths are computed for frequency-averaged ("gray") radiation, considering only absorption and neglecting scattering, that is, $\tau = \tau_{\rm abs}$. In Kuiper et al. [2010a] and Pascucci et al. [2004], $\tau = \tau_{\rm abs} + \tau_{\rm sc}$. When only absorption is considered, the optical depths in MAKEMAKE align with our calculation [priv. comm.].

Our simulation volume represents only one octant of the total protostellar disk, with the stellar source placed at one corner of the simulation volume. The masses tabulated in Table 2.1 are the total simulation masses multiplied by 8 so as to represent the total disk mass.

In the optically thin case, the temperature profile of the midplane can be compared to analytic estimates by Spitzer [1978]. The gas/dust tempera-

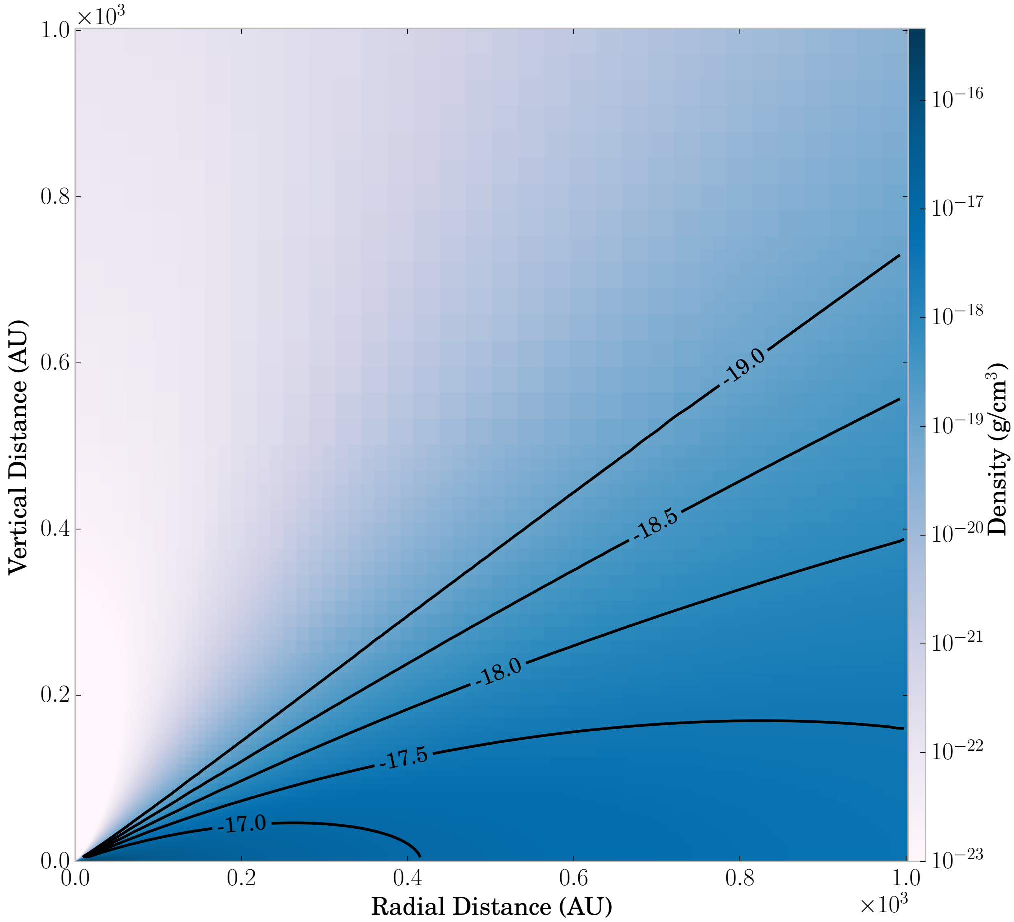

Figure 2.5: Density profile of the Pascucci et al. [2004] irradiated disk setup. Contours show lines of constant density. The radiation source is located at the bottom-left corner of the computational domain.

ture far from the central star ($r \gg R_*$) is given by

$$T(r) = \left(\frac{R_{\rm min}}{2r}\right)^{\frac{2}{4+\beta}} T_{\rm min}, \tag{2.41}$$

where β is the index of the dust absorption coefficient. For Draine and Lee [1984] silicates, $\beta = 2.0508$ in the long wavelength regime [Kuiper and Klessen, 2013]. $T_{\rm min}$ is the temperature at the inner edge of the disk $R_{\rm min} = 1$ AU.

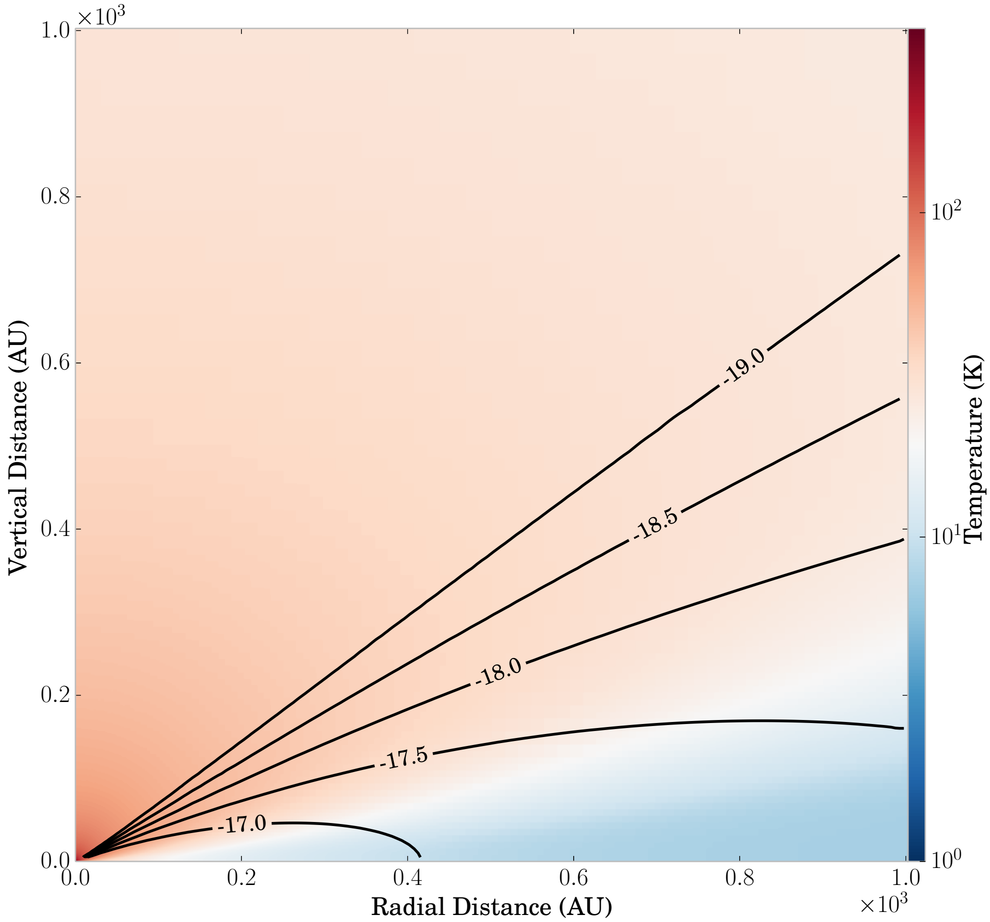

Figure 2.6: Temperature profile of the Pascucci et al. [2004] irradiated disk setup. Contours show lines of constant density. The gas is heated by a radiation source in the bottom-left corner of the computational domain. Note that the temperature has been scaled logarithmically.

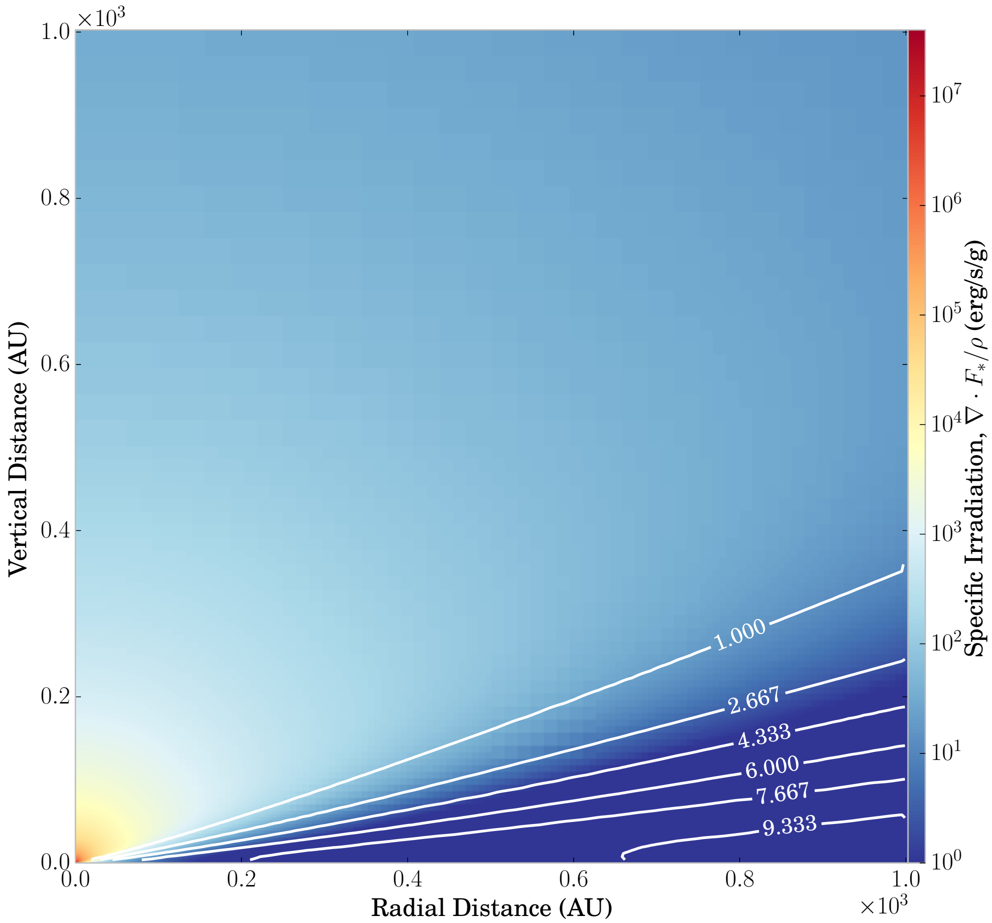

Figure 2.7: Specific irradiation profile of the Pascucci et al. [2004] irradiated disk setup, which shows the stellar radiation energy absorbed per gram of material. Contours show lines of constant optical depth, as computed by a raytrace through the material with frequency-averaged opacities.

In the optically thin regime, diffusion effects are negligible and the radiation field is dominated by the direct component. At radii greater than about 4 AU, our scheme reproduces the Spitzer [1978] estimate to within 10%, and for radii greater than 10 AU, better than 5%.

Figure 2.5 shows the density structure of the protostellar disk in a vertical slice in the optically thick case, with the radiation source positioned at the origin in the bottom-left corner. Contours mark lines of equal density and are labeled by the powers of ten of density.

The flared disk shields some of the stellar radiation. We run the simulation until the temperature of gas reaches an equilibrium state. Without hydrodynamics enabled, the gas can only absorb or radiate energy. We run the simulation for 10^{12} seconds and show the equilibrium temperature in Figure 2.6.

To show the shielding properties of the disk and the energy being absorbed by the gaseous medium surrounding the star, we show the specific irradiation in Figure 2.7, that is, the stellar (direct) radiation energy being absorbed per gram of material. We therefore show lines of equal optical depth τ, as calculated during the raytrace.

We compare the temperatures through the midplane of the disk against the same calculation completed with the MAKEMAKE code by Kuiper et al. [2010a]. Their simulation was done in a spherical polar geometry, which, although not adaptively refined, naturally has more resolution in the polar angular component at small radii, and therefore the scale height of the disk is extremely well resolved.

Figure 2.8 shows the radial temperature profile through the midplane of the disk for the case with fiducial density $\rho_0 = 8.321 \times 10^{18}$ g/cm^3. Three FLASH

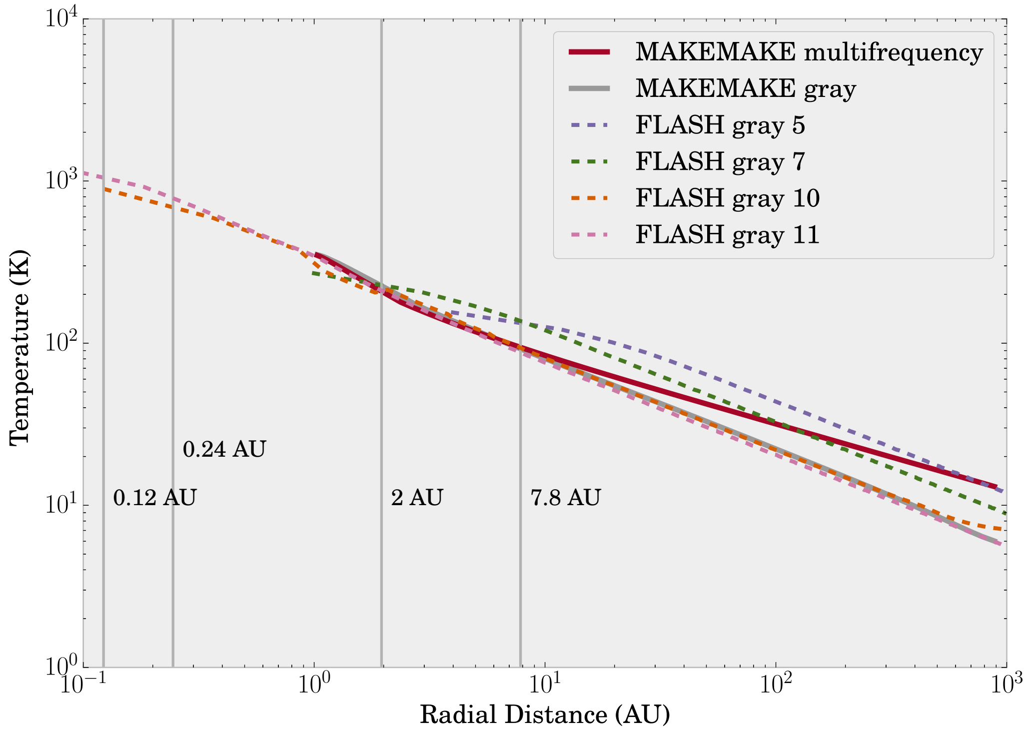

Figure 2.8: Comparison of the midplane temperature profiles in simulations of the hybrid radiation feedback scheme in the Pascucci et al. [2004] benchmark test in the high-density simulation ($\rho_0 = 8.321 \times 10^{-18}$): The implementation in FLASH vs. MAKEMAKE by Kuiper et al. [2010a]. Solid lines belong to simulations using the MAKEMAKE code, completed using a spherical polar geometry, while dashed lines indicate simulations done using the scheme described in this paper using the FLASH code. The number associated with each FLASH run indicates the maximum refinement level. Vertical gray lines in the figure indicate the grid resolution (in AU) for each of the FLASH runs.

runs are compared to two MAKEMAKE simulations. The FLASH simulations use the hybrid scheme as described in this paper, with both gray raytracer and gray FLD solver. These we compare against gray and multifrequency simulations by Kuiper et al. [2010a].

Because the FLASH simulations were completed in a Cartesian AMR geometry, we indicate the maximum refinement level in the figure legend. We compare maximum levels 5, 7, 10, and 11. At 10 levels of refinment, the smallest grid size is 0.24 AU; at 11 levels, it is 0.12 AU. For this simulation to match the results obtained using MAKEMAKE, it is necessary to resolve the scale height (Eq. 2.38) of the disk at its inner edge (≈ 0.1 AU), which we effectively do with 11 levels of refinement, although convergence is already seen with 10 levels of refinment. When the scale height is resolved, the midplane temperature profile converges to the gray radiation result of Kuiper et al. [2010a]. Lower resolution runs show a temperature excess.

2.5.1 Radiation pressure on a static, flared disk

We compute the radiation force density for the stellar radiation component through the midplane of our disk as in Equation 2.31. A similar test was done by Kuiper et al. [2010a], although their cut was not done through the midplane but along a polar angle of $\theta \approx 27°$. FLASH computes an isotropic radiation pressure via the Eddington approximation (Equation 2.30), so we estimate the thermal radiation force density via

$$f_{\mathrm{rad,thermal}} = -\frac{dp_{\mathrm{rad}}}{dx}. \tag{2.42}$$

We use the MAKEMAKE code (revised to be a 2-T solver) to perform the same calculation through the midplane ($\theta \approx 0°$) and compare to FLASH. The results are shown in Figure 2.9. Most of the radiation pressure is due to the direct, stellar component, with the diffuse, reprocessed field adding only a tiny contribution that is more apparent far from the source. The outer boundary is treated as optically thin outflow in MAKEMAKE. In FLASH, we set the "vacuum" outer boundary condition, $dF/dx = -2F$.

In the inner 40 AU, the two codes match to within about 20%, despite

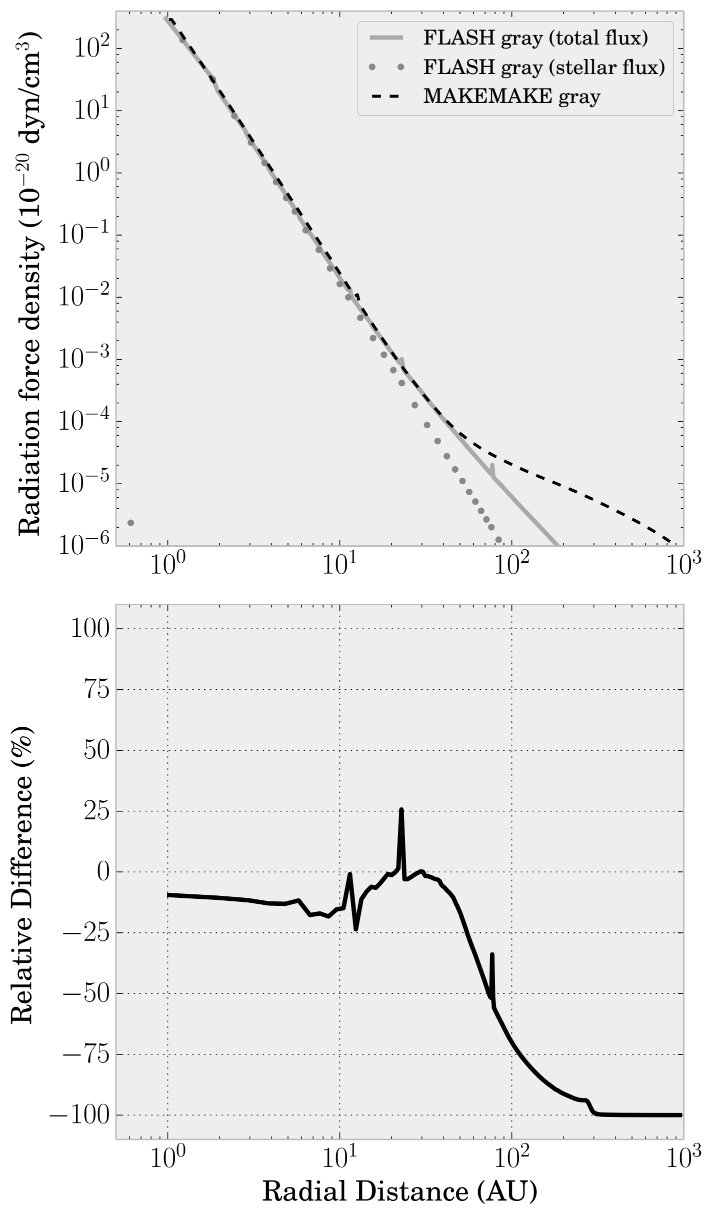

Figure 2.9: Radiation force density through the midplane of the disk. The solid line indicates the radiation force density for the FLASH calculation, resulting from the total flux (direct stellar and thermal). The dotted line indicates the radiation force density due only to the stellar component of the radiation field. We compare the FLASH results to a 2T gray calculation in MAKEMAKE (dashed line). The lower panel indicates the relative difference between the total flux radiation force density in FLASH versus MAKEMAKE.

the radiation force density varying over 6 orders of magnitude. Because the radiation force is proportional to the absorbed radiation flux, the peak in the force density lies at the inner edge of the disk around 1 AU. Beyond 40 AU, the relative difference between the two calculations grows on account of boundary conditions, but the radiation force density is negligible beyond this point (6 orders of magnitude below the peak value).

The FLASH code and updated MAKEMAKE code produce comparable measurements of the radiation pressure. The advantage and key innovation with FLASH, however, is its AMR-capability that allows it to solve more general problems with high accuracy.

2.6 Tests involving multiple sources

Our radiative transfer scheme can accommodate multiple sources in a relatively straightforward way. We must calculate the direct radiation flux from stellar sources in order to compute the irradiation source term, $\nabla \cdot \boldsymbol{F}_*$, at every cell in the computational domain. Therefore, we perform a loop over all sources and sum their flux contributions at each cell.

2.6.1 Two proximal sources in a homogeneous medium

The first multi-source test involves two sources separated by about 658 AU. Each source has a stellar radiation field with $T_{\rm eff} = 5800$K. The medium is uniform and homogeneous, with a density of $\rho = 8.321 \times 10^{-18}$ g/cm^3. We perform this test to contrast our hybrid radiation transfer method with M1 moment methods [Levermore, 1984, González et al., 2007, Vaytet et al., 2010]. M1 moment methods are similar to FLD methods in that they are

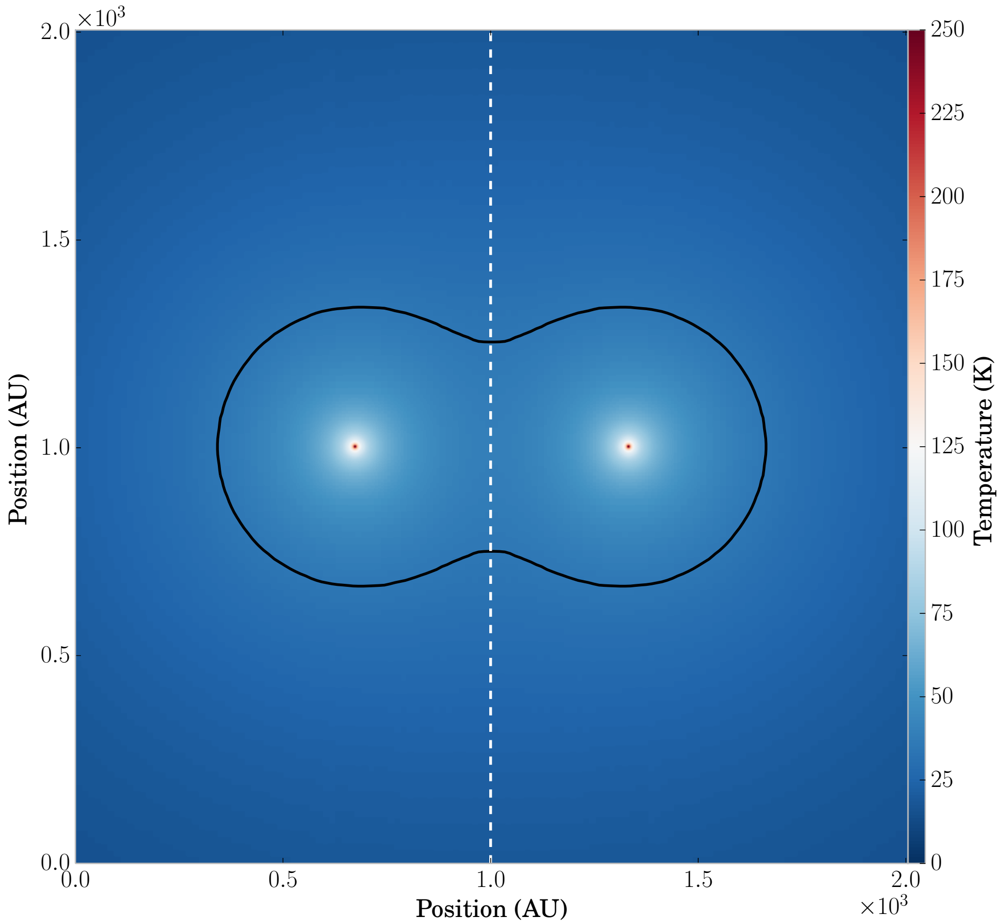

Figure 2.10: Gas temperature after equilibrating with the radiation field driven by two stellar sources ($T = 5800$ K). Vertical dashed line indicates the symmetry axis along which the temperature in figure 2.11 is measured. The black contour marks a gas temperature of $T = 35$K.

both based on taking angular moments of the radiative transfer equation. FLD takes only the zeroth-order moment, and the conservation equations are closed using a diffusion relation based on the gradient of the radiation energy. M1 methods take the first moment of the radiative transfer equation, and the closure of the conservation equations takes a form that preserves the bulk directionality of photon flows. Problems arise, however, when multiple sources are present. With two sources, photons flow in opposing directions, canceling the opposing components of their flow and introducing spurious flows in the direction perpendicular to the line between the two sources [Rosdahl et al., 2013]. Raytracers do not suffer from this artifact because the irradiation at each grid location is calculated along sightlines to each of the sources present in the simulation.

Figure 2.10 shows the simulation setup as well as the temperature of the gas after it has been allowed to equilibrate with the radiation field. We measure the temperature of the gas along the vertical dashed line and plot the result in Figure 2.11.

Figure 2.11 shows the temperature along the dashed line from Figure 2.10, the locus of points equidistant from both radiation sources. Here we compare the simulated temperatures of our hybrid scheme in FLASH against a Monte Carlo calculation performed with RADMC-3D[1] [Dullemond, 2012]. The Monte Carlo calculation was done with 10^9 photons using the "modified random walk" method with scattering neglected, on an uneven grid (101x1x101 cells for the $x \times y \times z$ dimensions) using the same Draine and Lee [1984] dust model as in the rest of this paper.

The FLASH temperatures differ from the Monte Carlo results by less

[1]http://www.ita.uni-heidelberg.de/ dullemond/software/radmc-3d/

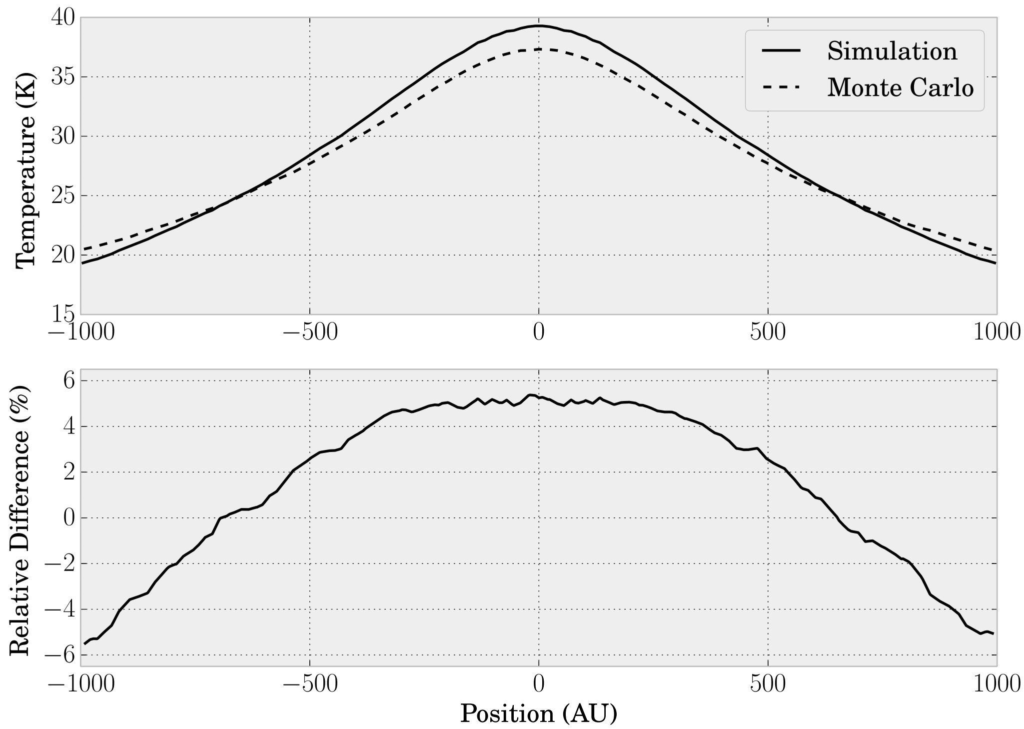

Figure 2.11: Gas temperature along dashed line from Figure 2.10, the locus of points equidistant from both radiation sources. The upper panel shows the gas temperature from our simulation (solid) compared to the Monte Carlo result (dashed). The lower panel shows the relative difference in temperature as a percentage.

than 5%, with FLASH calculating slightly warmer temperatures directly between the sources and slightly cooler temperatures at the edges of the simulation volume. These small differences are most likely due to multifrequency effects.

Monte Carlo calculations are considered the benchmark for accuracy, but are extremely computationally intensive and cannot, in general, be used in dynamic calculations. Simulations of star formation cannot be addressed with full Monte Carlo methods using present-day machines and reasonable time constraints. Moreover, they are highly nontrivial to parallelize. In these cases, approximate schemes such as flux-limited diffusion must be used.

2.6.2 Two sources irradiating a dense core of material

We next create a test setup inspired by Rijkhorst et al. [2006a], where a central concentration was irradiated by two sources. Since FLD methods are based on local gradients in the radiation energy, they cannot properly treat shadowing. In this test we place a dense clump of material at the center of our simulation volume and irradiate it from two angles, creating a shadowed region. We compute the irradiation and equilibrium temperatures.

Our setup contains a mix of optically thin and optically thick regions, creating strong gradients in the radiation energy density. We compare the equilibrium temperatures computed by the hybrid scheme to the temperature computed without diffusion.

The two radiation sources have a temperature $T_{\rm eff} = 8000$ K and are situated in a low-density ($\rho = 10^{-20}$ g/cm^{-3}) medium to the side and below a central density concentration ($\rho = 10^{-17}$ g/cm^{-3}) with radius $R_c = 4 \times 10^{15}$ cm ≈ 267 AU. The side length of the simulation box is about 2000 AU. Hydrodynamics are disabled.

Figure 2.12 shows the simulation setup and the specific irradiation of the gas in a slice through the midplane of the simulation volume. The overlaid grid shows the FLASH AMR block structure, with each block containing 8^3 cells and refining on gradients in density, radiation energy, and matter temperature using the FLASH error estimator described in Section 2.3.1. The simulation was run with a maximum 8 levels of refinement, achieving a maximum resolution of 1.96 AU. The black circle in the centre marks the central density concentration.

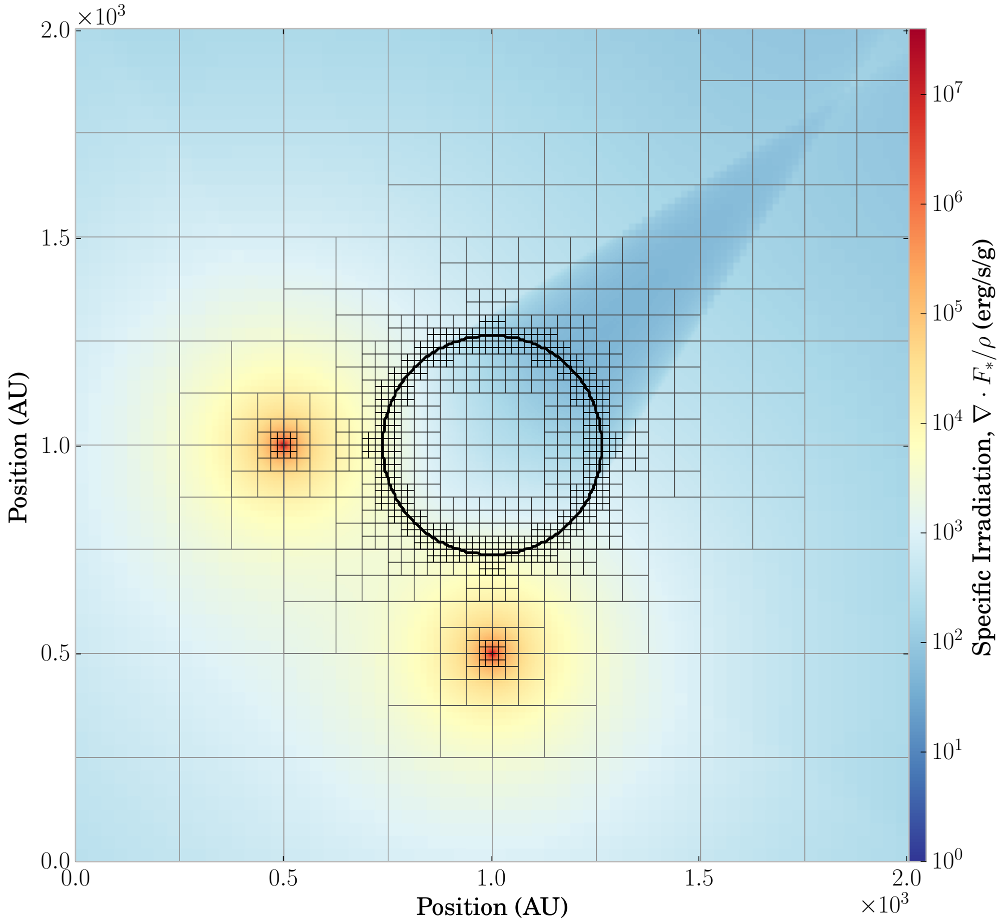

Figure 2.12: Specific irradiation by two sources in an otherwise homogeneous medium at $\rho = 10^{-20}$ g/cm^3, but for a central density concentration indicated by the black circle, where the density is $\rho = 10^{-17}$ g/cm^3. The two sources are stellar sources with effective temperatures of 8000K. The FLASH block AMR structure is also shown, with each block containing 8^3 cells.

The central density concentration casts a shadow on the side opposite of the central concentration.

Figure 2.13 shows the gas temperature after the simulation has been given time to reach equilibrium. Here we see warming of a region just interior to the central overdensity where strong density gradients exist.

To visualize the radiation flux, we plot a vector field of the radiation

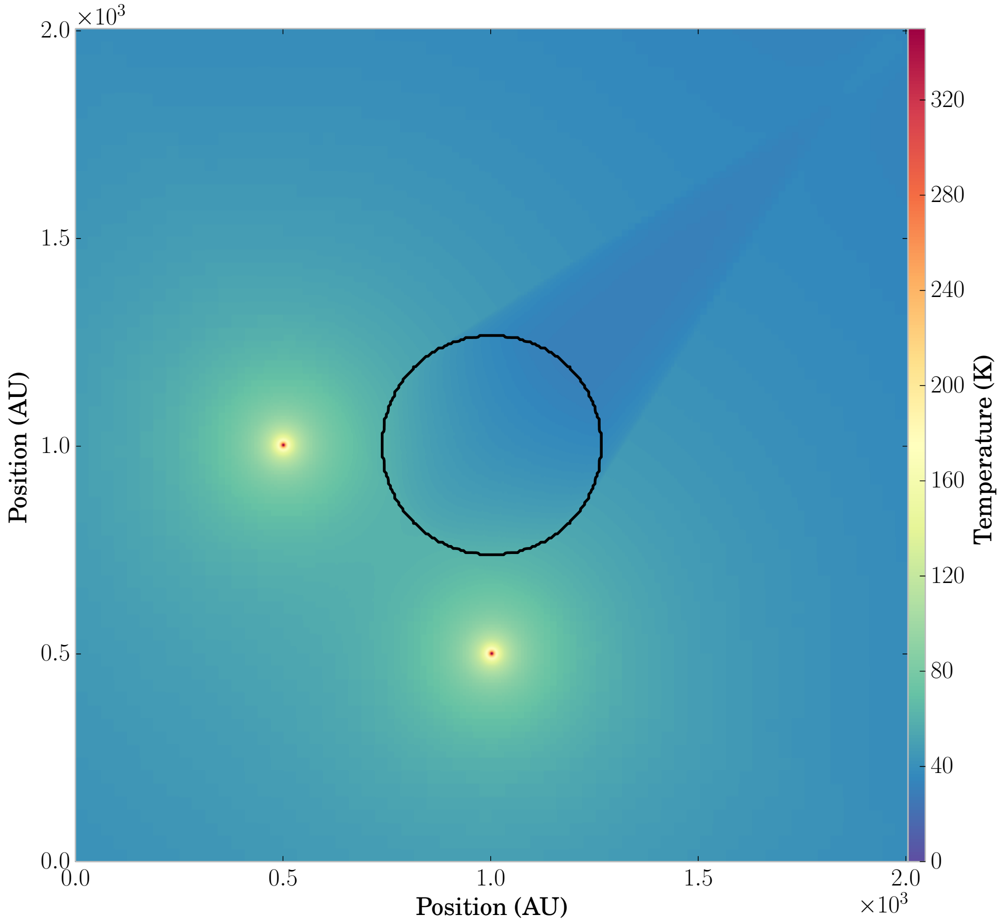

Figure 2.13: Same as in figure 2.12, but instead showing the gas temperature.

flux, given by Equation 2.11. This is shown in Figure 2.14 overplotted on the total radiation energy density. The vector field represents how the radiation energy is being diffused by the FLD solver. The two radiation sources irradiate the central overdensity, heating it. It then drives radiation back into the surrounding medium via diffusion. There is also a radiation energy gradient across the central overdensity. The black circle marks the central overdensity, as in the previous two figures. In Figure 2.14 we see a halo of radiation energy just outside the circle on the side nearest to the two radiation sources also

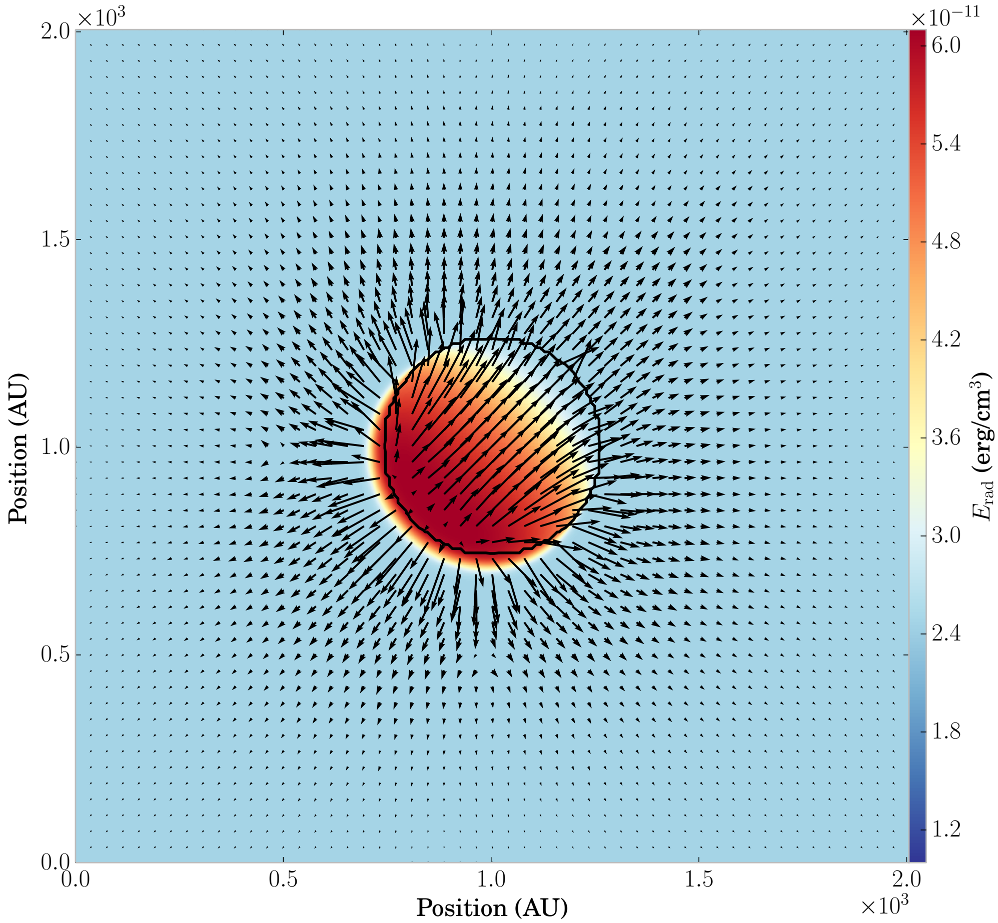

Figure 2.14: Radiation energy density with the thermal radiation flux $\boldsymbol{F}_r = -D\nabla E_r$ overplotted as a vector field. The gradients in the radiation energy density are steepest near the spherical overdensity in the centre, on the side facing the two sources.

resulting from the diffusion of radiation.

We now compare this to the zero-diffusion case by performing the same calculation with the diffusion term set to zero. The gas equilibrates with the radiation field imposed by the sources, but this energy is not allowed to diffuse. Figure 2.15 shows the difference in the resultant equilibrium temperature as a percentage of the relative difference. The result is that the central overdensity

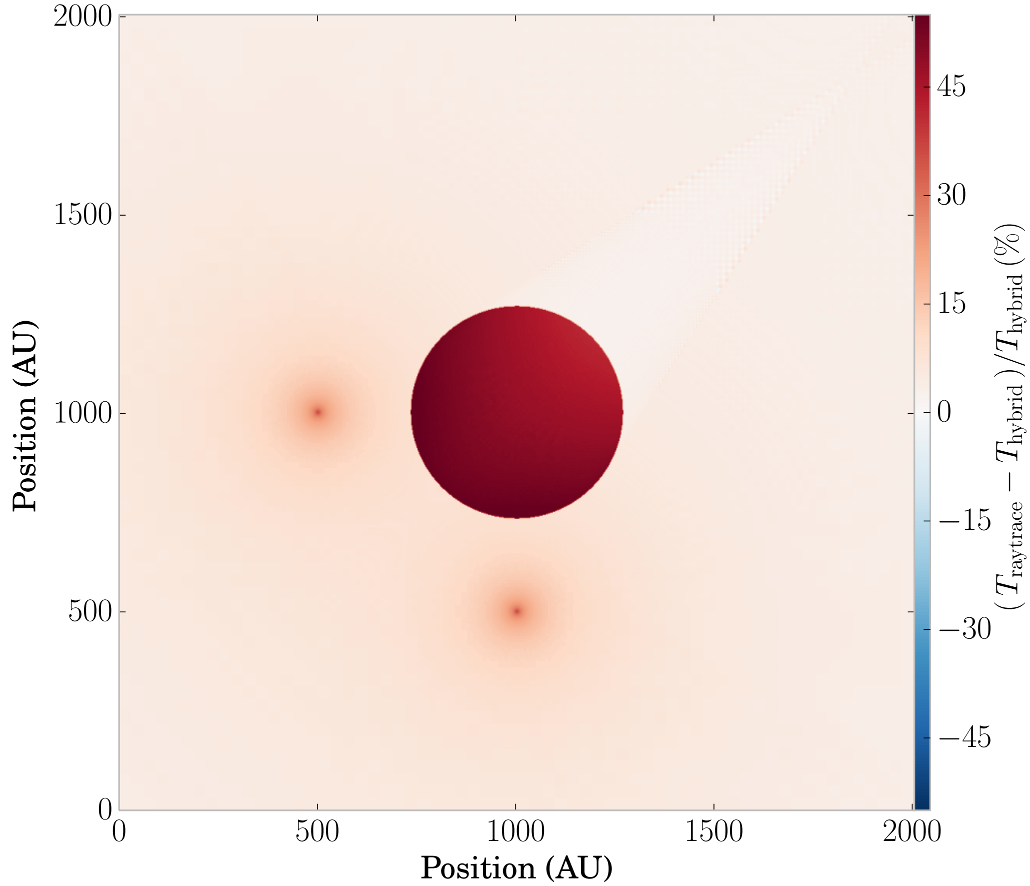

Figure 2.15: The temperature difference (in percent) in the raytrace case compared to the hybrid radiation transfer case.

is approximately 50% hotter. It cannot cool by diffusing its radiation energy into the surrounding medium.

Because the re-emission terms are often left out of raytracing-methods for the sake of simplicity and computational cost, they are unsuitable and inaccurate in simulations containing optically thick material, although re-emission is often treated using a cooling function to extract the energy. In optically thick envelopes surrounding young stellar objects, radiation is reprocessed as the envelope of gas absorbs and re-emits the radiation in the infrared.

2.7 Discussion and Summary

We have described the implementation of a hybrid radiation transfer scheme in a 3D Cartesian AMR framework. To the best of our knowledge, this is the first such implementation. Our hybrid scheme splits the radiation field into a direct (stellar) component and a diffuse (thermal) component. A specialized raytracer is used to solve for the direct flux, the absorption of which by dusty, molecular gas constitutes an energy source term that heats the dust. The dust emits radiation thermally, and the thermal radiation field is evolved via flux-limited diffusion. The gas is assumed in thermal equilibrium with the dust, whose temperature is evolved according to both direct and indirect radiation fields.

Radiation feedback from massive stars takes manifold forms: heating of dust grains, which are coupled to the gas; radiation pressure; ionizing radiation, leading to the formation of HII regions; jets and stellar winds; and finally supernovae. We have implemented the first two, with future work intent on implementing ionizing radiation. Various authors have drawn attention to the potential for ionizing radiation to disrupt molecular clouds [Matzner, 2002, Krumholz et al., 2006, Walch et al., 2012], at least in low-mass clouds, while in larger clouds, star formation may be fed through accretion along filaments, with ionizing radiation feeding into the low-density voids between filaments Dale et al. [2012]. The effect of ionizing radiation, through heating of the gas and suppression of fragmentation, also leads to higher Jeans masses and more massive stars [Peters et al., 2010c].

As a mechanism for disrupting giant molecular clouds, Murray et al. [2010] argue that radiation pressure from starlight interacting with dust grains plays a dominant role, at least in the case of the most massive clusters inside GMCs.

In implementing our radiative transfer scheme, the addition of the ray-tracer helps overcome some of the main limitation of a purely FLD approach. The primary limitation of the FLD approach is the assumption that the flux always travels in the direction down the radiation energy gradient. This assumption is reasonable in purely optically thick regions, but breaks down in regions where radiation sources ought to be casting shadows.

Furthermore, some FLD implementations assume that the radiation field is everywhere in thermal equilibrium with the gas. This is not always true, especially radiatively critical shocks. We have relaxed this assumption and allowed the radiation temperature and the gas temperature to differ from each other.

The primary advance over the hybrid implementation of Kuiper et al. [2010a] is the generalization to 3D Cartesian AMR from the specialized geometry of a spherical polar grid. Spherical coordinates are ideal for studying the radiation field from a single, central source. By their nature, spherical grids have higher effective resolution closer to the center, precisely where it is most needed simulations of accretion disks around massive stars. In our test problem of a static, irradiated disk [Pascucci et al., 2004], we required 11 levels of refinement before we could resolve the scale height of the disk near the inner boundary.

However, when generalizing to multiple point sources of radiation, Cartesian geometry becomes a natural choice. This enables us to approach a much larger array of problems. FLASH is a highly scalable MHD code with driven turbulence, sink particles and protostellar evolution. The addition of our hybrid radiation transfer unit greatly complements FLASH 's abilities.

One of the most general problems this enables us to study is the effect of radiative heating and momentum feedback around massive, accreting protostars. These objects reside deep within dense envelopes and accrete material through a disk. Whether disk accretion is the only mechanism, or whether raditiave Rayleigh-Taylor instabilities are another viable mechanism has not yet been fully settled. High resolution simulations, resolving in particular the regions of intermediate optical depth using adaptive mesh refinment, and including the effects of turbulence and MHD ought to be able to resolve the remaining controversies.

We have also connected the hybrid radiation scheme to sink particles, which we will use to model the formation of protostars in larger-scale simulations of molecular cloud clumps. The protostellar properties such as stellar radius and luminosity are evolved using a subgrid model [Klassen et al., 2012b] that directly feeds into the radiation transfer subroutines. The sum of FLASH's capabilities now enable the study of clustered star formation in turbulent, filamentary, and magnetized environments.

The code also presents opportunities for further development. The raytracer, as implemented by Rijkhorst et al. [2006a] and Peters et al. [2010a], contained ionization feedback, which we will soon implement in our hybrid radiation framework. Multifrequency effects will also be included in future versions of the code.

2.8 Appendix to Chapter 2: 3T radiation hydrodynamics

FLASH is a code that is supported by a team of developers at the DOE-supported Alliances Center for Astrophysical Thermonuclear Flashes (ASCI) at the University of Chicago[2]. Recent development has added significant capabilities for plasma and high-energy-density physics. These included a "3T" radiation hydrodynamics solver [Lamb et al., 2010, Fatenejad et al., 2012, Kumar et al., 2011] that evolves an ion fluid, and electron fluid, and a radiation "fluid". 3T implies that each fluid has its own temperature, with $T_{\rm ele} \neq T_{\rm ion} \neq T_{\rm rad}$.

These three fluids are coupled in the following way:

$$\partial_t(\rho e_{\rm ion}) + \nabla \cdot (\rho e_{\rm ion}\boldsymbol{v}) + P_{\rm ion}\nabla \cdot \boldsymbol{v} = \rho\frac{c_{v,\rm ion}}{\tau_{ei}}\left(T_{\rm ele} - T_{\rm ion}\right) \tag{2.43}$$

$$\partial_t(\rho e_{\rm ele}) + \nabla \cdot (\rho e_{\rm ele}\boldsymbol{v}) + P_{\rm ele}\nabla \cdot \boldsymbol{v} = \rho\frac{c_{v,\rm ele}}{\tau_{ei}}\left(T_{\rm ion} - T_{\rm ele}\right) - \nabla \cdot \boldsymbol{q}_{\rm ele} + Q_{\rm abs} - Q_{\rm emis} \tag{2.44}$$

$$\partial_t(\rho e_{\rm rad}) + \nabla \cdot (\rho e_{\rm rad}\boldsymbol{v}) + P_{\rm rad}\nabla \cdot \boldsymbol{v} = \nabla \cdot \boldsymbol{q}_{\rm rad} - Q_{\rm abs} + Q_{\rm emis} \tag{2.45}$$

The ion and electron components exchange energy via Coulomb collisions. The electron and radiation components exchange energy through absorption and emission processes. In our case, $Q_{\rm abs} = \kappa_P \rho c E_r$ and $Q_{\rm emis} = \kappa_P \rho c a T^4$, where a is the radiation constant. The $\nabla \cdot \boldsymbol{q}_{\rm ele}$ and $\nabla \cdot \boldsymbol{q}_{\rm rad}$ terms

[2]http://flash.uchicago.edu/

represent the sources or sinks of energy flux for the electron or radiation components.

It has already been shown how the radiation energy sources (stars) couple to the matter fluid. It remains to be shown how the two components of the matter fluid exchange energy in the FLASH code framework.

The equations to be solved are the specific internal energy updates.

$$\frac{de_{\rm ion}}{dt} = \frac{c_{v,\rm ion}}{\tau_{ei}}(T_{\rm ele} - T_{\rm ion}) \tag{2.46}$$

$$\frac{de_{\rm ele}}{dt} = \frac{c_{v,\rm ele}}{\tau_{ei}}(T_{\rm ion} - T_{\rm ele}) \tag{2.47}$$

The hydrodynamic terms from equations 2.43 and 2.44 are handled separately by the hydro solver (operator splitting). Replacing $de = c_v dT$, we can write the coupled differential equations in terms of temperature:

$$\frac{dT_{\rm ion}}{dt} = \frac{m}{\tau_{ei}}(T_{\rm ele} - T_{\rm ion}) \tag{2.48}$$

$$\frac{dT_{\rm ele}}{dt} = \frac{1}{\tau_{ei}}(T_{\rm ion} - T_{\rm ele}) \tag{2.49}$$

where $m = c_{v,\rm ele}/c_{v,\rm ion}$ is the ratio of the electron and ion specific heats.

This is implemented via a relaxation law, with the temperature ($T = e/c_v$) update

$$T_{\rm ion}^{n+1} = \left(\frac{T_{\rm ion}^n + mT_{\rm ele}^n}{1+m}\right) - m\left(\frac{T_{\rm ele}^n + T_{\rm ion}^n}{1+m}\right)\exp\left[-(1+m)\frac{\Delta t}{\tau_{ei}}\right] \tag{2.50}$$

$$T_{\rm ele}^{n+1} = \left(\frac{T_{\rm ion}^n + mT_{\rm ele}^n}{1+m}\right) + \left(\frac{T_{\rm ele}^n + T_{\rm ion}^n}{1+m}\right)\exp\left[-(1+m)\frac{\Delta t}{\tau_{ei}}\right] \tag{2.51}$$

The equilibration time, τ_{ei}, is given by,

$$\tau_{ei} = \frac{3k_B^{3/2}}{8\sqrt{2\pi}e^4} \frac{(m_{\text{ion}}T_{\text{ele}} + m_{\text{ele}}T_{\text{ion}})^{3/2}}{(m_{\text{ele}}m_{\text{ion}})^{1/2}\bar{z}^2 n_{\text{ion}} \ln \Lambda_{ei}}, \tag{2.52}$$

where e is the electron charge, m_{ion} and m_{ele} are the ion and electron masses, respectively, $\bar{z}$ is the mean ionization level, n_{ion} is the ion number density, and $\ln \Lambda_{ei}$ is the Coulomb logarithm.

With these updated temperatures, the internal energies are updated:

$$e_{\text{ele}}^{n+1} = e_{\text{ele}}^{n} + c_{v,\text{ele}}^{n}(T_{\text{ele}}^{n+1} - T_{\text{ele}}^{n}) \tag{2.53}$$

$$e_{\text{ion}}^{n+1} = e_{\text{ion}}^{n} + c_{v,\text{ion}}^{n}(T_{\text{ion}}^{n+1} - T_{\text{ion}}^{n}) \tag{2.54}$$

Chapter 3

Simulating the Formation of Massive Protostars: I. Radiative Feedback and Accretion Disks

3.1 Introduction

The formation of high-mass stars ($M \gtrsim 8$ M$_\odot$) has been a subject of intense study and considerable controversy for several decades. Despite being slight in abundance, with only 2 or 3 high-mass stars for every 100, they exert enormous influence on the galaxies and host clusters in which they reside [Zinnecker and Yorke, 2007]. Their extreme nature demands attention because the mechanisms of their formation are not immediately obvious. A defining feature of massive stars is that the timescale for their gravitational contraction, the Kelvin-Helmholtz time, is shorter than the timescale for accretion. This implies that the star begins nuclear burning before it has finished accreting to its final mass. During this phase, powerful feedback mechanisms due to radiation pressure and photoionization [Larson and Starrfield, 1971b] become important—mechanisms that are either absent or insignificant for low-mass star formation.

Observations exist for stars in excess of $150\,\mathrm{M}_\odot$ [Crowther et al., 2010]. The 30 Doradus region inside the Large Magellanic Cloud contains at least 10 stars with initial masses in excess of 100 $\mathrm{M}_\odot$ [Doran et al., 2013]. There is no consensus on the precise upper mass limit for stars, although it may lie somewhere within 150–300 $\mathrm{M}_\odot$ [Figer, 2005, Crowther et al., 2010]. Assuming that such masses can be reached by accretion, then we must ask whether the accretion proceeds through a circumstellar disk alone, or additionally through other mechanisms. In addition, a large body of theoretical and numerical work shows that it is essential to adopt a three-dimensional treatment that includes a careful implementation of the radiation field. Many different theoretical and observational approaches have been undertaken to address this.

Massive stars are expected to reach the main sequence while still deeply embedded in molecular envelopes [Stahler et al., 2000]. This makes observing high-mass protostars and their circumstellar disks challenging, although a growing number of candidates have been detected in recent years. Beltran and de Wit [2015] summarize the observations of accretion disks around luminous young stellar objects (YSOs). Where observations of circumstellar disks are available, their rotation rates appear consistent with Keplerian velocities. For massive protostars ($M_* = 8$–30 $\mathrm{M}_\odot$), accretion disks generally range in size from a few hundred AU to a few thousand AU. These sizes are consistent with the disks formed in simulations presented in this paper.

Observations with the Atacama Large Millimeter/submillimeter Array (ALMA) are also revealing the properties of disks around massive protostars.

Very recent observations highlighted the discovery of a Keplerian-like disk around a forming O-type star, AFGL 4176 [Johnston et al., 2015]. Model fits to line and continuum emission are consistent with a 25 $M_\odot$ star surrounded by 12 $M_\odot$ disk with a radius of 2000 AU. The velocity structure, as traced by CH_3CN, is consistent with Keplerian rotation. These observations are in excellent agreement with the results of our simulations of a 100 $M_\odot$ protostellar core.

Early 1D calculations sought to estimate the upper mass limit for stars, given that the accretion flow onto a star should be halted at some critical luminosity. The Eddington Limit describes this maximal luminosity and depends on the ratio of radiative to gravitational forces, including the specific opacity of the gas and dust. Since the luminosity scales with the mass of the star more strongly than gravity, there should exist a natural upper mass limit for stars in the spherically-averaged case. Studies such as Larson and Starrfield [1971b], Kahn [1974], Yorke and Krügel [1977] found upper mass limits around 20–40 $M_\odot$, although such calculations are always sensitive to the choice of dust model. The interstellar medium is about 1% dust by mass. Stellar radiation impinges on dust particles, imparting momentum. This momentum is transferred to the gas via drag forces. In 1D, a sufficiently luminous star (roughly 20 $M_\odot$ or more) should be able to arrest and even reverse the accretion flow via radiation pressure alone, thus setting an upper mass limit for the star. How one chooses to model the dust opacity will affect the upper mass limit that results from these kinds of 1D calculations.

These theoretical 1D mass limits have been confirmed by simulations [Yorke and Krügel, 1977, Kuiper et al., 2010a]. Kahn [1974] suggested that the envelope of material around the protostar would likely fragment, leading to anisotropic accretion. The importance of geometry was later shown [Nakano, 1989] and circumstellar disks highlighted as an accretion channel. These disks form easily in the presence of rotation. Yorke and Sonnhalter [2002] studied slowly-rotating nonmagnetic cores in 2D simulations that assumed axial symmetry. Their simulations modeled the collapse of high-mass cores and included frequency-dependent radiation feedback handled via flux-limited diffusion (FLD). The effect of the disk is to channel radiation into the polar directions, a phenomenon known as the "flashlight effect" [Yorke and Bodenheimer, 1999]. This radiation is also most responsible for radiative accelerations. Even so, Yorke and Sonnhalter [2002] still only formed stars with masses $\lesssim 43\,\mathrm{M}_{\odot}$.

Radiatively-driven outflows are expected to form in the vicinity of massive stars. Krumholz et al. [2009], using a frequency-averaged flux-limited diffusion approach to radiative transfer, proposed that as the stars become more luminous, rather than blowing away all the gas enveloping the cavity, radiation would pierce through the cavity wall. Meanwhile, dense fingers of material would rain back down onto the massive protostar. This "radiative Rayleigh-Taylor" instability is analogous to the classical Rayleigh-Taylor instability, but with radiation taking the place of the lighter fluid. These instabilities may allow the star to continue accreting material. Jacquet and Krumholz [2011] showed that these instabilities can arise under the right circumstances even around HII regions.

This mechanism, however, may not be necessary to explain how massive stars achieve their prodigious masses. Kuiper et al. [2010a] demonstrated that with a much more accurate treatment of the radiation field, including both FLD as well as ray-tracing of energy directly from the star, disk accretion alone was sufficient to achieve stellar masses larger than any previously achieved in a simulation.

The question becomes whether a classically two-dimensional fluid instability holds in a 3D environment, and whether it is appropriate to model the stellar radiation field as a fluid. Kuiper et al. [2010b] decomposed the radiation field into a direct component and a diffuse component. The diffuse component, which consisted entirely of thermal radiation re-emitted by dust, was handled by an FLD solver. Meanwhile, the direct component consisted of the stellar radiation and was treated by a multifrequency raytracer. In simulations using this "hybrid" technique for radiation transfer, the radiative Rayleigh-Taylor instability was absent [Kuiper et al., 2012]. Kuiper et al. [2010a] found that it was necessary to model and to resolve the dust sublimation front around the accreting protostar. With dust sublimation, matter becomes transparent to radiation in the extreme vicinity of the protostar. Rather than being blown away, it can now be accreted by the protostar.

These and subsequent simulations have shown that stars in excess of $100\,\mathrm{M}_{\odot}$ may form by disk accretion without the need for new fluid instabilities [Kuiper et al., 2010a, 2011a, 2012]. However, these simulation also have their limitations. They were performed on grids with a spherical geometry and a sink cell fixed at the center. The advantage of this geometry is that it allowed for extremely high resolution near to the source. The radial grid resolution increases logarithmically towards the center. Kuiper et al. [2010a] was able to resolve down to 1 AU in the vicinity of the star. Raytracing is also easy to implement in this geometry as rays travel only along the radial dimension. The disadvantage of this setup is that it only handles a single immovable source, fixed at the center. Fragmentation of the pre-stellar core was neglected, and the source cannot drift even as the disk becomes gravitationally unstable. While the resolution at small radii is very good, large-scale structure (particularly at large radii) are poorly resolved. These would be better handled in an adaptive mesh framework.

The combined limitations of this body of work motivated our implementation of hybrid radiation transport on an adaptive, 3D Cartesian grid in FLASH [Chapter 2], first for the study of massive stars and their outflow cavities, then more general problems of star formation in clusters. In Klassen et al. [2014] we demonstrated the accuracy of our method in solving the radiative transfer problem with a battery of benchmark tests, most of which were static. In this paper, we apply our method to the dynamical problem of following the gravitational collapse of a molecular cloud core to form a massive protostar. We also describe improvements and some necessary modifications that were made to the code in order for us to simulate massive star formation.

We performed three different computationally-intense simulations of protostellar cores collapsing gravitationally. These cores were of three different initial masses, 30 $M_\odot$, 100 $M_\odot$, and 200 $M_\odot$, respectively. Their initial conditions emulated earlier studies of massive star formation, but that had different radiatively feedback techniques or different grid geometries. In our case, we formed only a single massive star in each simulation, with final masses of 5.48 $M_\odot$, 28.8 $M_\odot$, and 43.7 $M_\odot$. The simulations were run for 81.4 kyr (0.85 $t_{\rm ff}$), 41.6 kyr (0.79 $t_{\rm ff}$), and 21.9 kyr (0.59 $t_{\rm ff}$), respectively. The formation of a massive protostar was accompanied by the formation of an accretion disk that grew in mass until becoming unstable, triggering a factor of 2–10 increase in the accretion rate, but which did not undergo further fragmentation into mutlpile stars. The strong radiative feedback from the massive protostars did not halt accretion, which continued through the disk, but launched radiatively-driven bubbles in the $100\,\mathrm{M}_\odot$ and $200\,\mathrm{M}_\odot$ simulations, in which the stars had super-Eddington luminosities.

Below we describe the setup of these simulations and their results in detail. Section 3.2 provides the background to the physical and numerical models we employ. Section 3.3 details the simulation setup. The results of these simulations are discussed in Section 3.4, while some nuances, caveats, as well as the direction of future simulations are discussed in Section 3.5. We summarize our results in Section 3.6.

3.2 Physical and numerical model

3.2.1 Radiation transfer

The details of our radiative transfer method are covered in Klassen et al. [2014], but we summarize the basics of the method here. The code was further developed to handle dynamical star formation calculations. These improvements are described in sections 3.2.2 and 3.2.3. The radiation field is decomposed into a direct, stellar component and a diffuse, thermal component [Wolfire and Cassinelli, 1986, Murray et al., 1994, Edgar and Clarke, 2003, Kuiper et al., 2010b], for which we can apply different methods that are better suited to each type of radiation:

$$\boldsymbol{F} = \boldsymbol{F}_* + \boldsymbol{F}_r \tag{3.1}$$

The direct radiation flux from a protostar $F_*(r)$ measured a distance r

from the star is given by

$$F_*(r) = F_*(R_*) \left(\frac{R_*}{r}\right)^2 \exp\left(-\tau(r)\right), \tag{3.2}$$

where $F_*(R_*) = \sigma T_{\rm eff}^4$ is the flux at the stellar surface R_*, where σ is the Stefan-Boltzmann constant and $T_{\rm eff}$ the effective surface temperature of the protostar. The stellar flux is attenuated both geometrically with distance from the source, and by intervening material that is scattering or absorbing starlight. The latter effect is captured by the exponential term in Eq. 3.2, where

$$\tau(r) = \int_{R_*}^{r} \kappa(T_*, r')\rho(r')dr' \tag{3.3}$$

is the optical depth.

Raytracing is a method that is well-suited for treating the direct radiation field, determining for each grid cell the flux of photons arriving directly from the photosphere of any stars within the simulation. A raytracer making use of the fast voxel traversal algorithm [Amanatides et al., 1987] is used to calculate optical depths to every cell in the computational domain, from which we calculate the local stellar flux. This flux depends on the integrated optical depth along the ray. The amount of stellar radiation absorbed by a grid cell depends on the local opacity,

$$\nabla \cdot F_*(r) \approx -\frac{1 - e^{-\kappa_P(T_*)\rho\Delta r}}{\Delta r} F_*(r) \tag{3.4}$$

where κ is the specific opacity and ρ is the matter density.

This absorbed energy enters the coupled energy equations as a source term:

$$\frac{\partial(\rho\epsilon)}{\partial t} = -\kappa_P \rho c \left(a_R T^4 - E_r\right) - \nabla \cdot \boldsymbol{F}_* \tag{3.5}$$

$$\frac{\partial E_r}{\partial t} + \nabla \cdot \boldsymbol{F}_r = +\kappa_P \rho c \left(a_R T^4 - E_r\right) \tag{3.6}$$

Here E_r is the radiation energy, κ_P is the Planck opacity, and a_R is the radiation constant. The temperature in Equation 3.5 is solved for implicitly (see Section 3.2.3), which is used in equation 3.6. Equation 3.6, in turn, is solved implicitly using the flux-limited diffusion approximation [Levermore and Pomraning, 1981],

$$\boldsymbol{F}_r = -\left(\frac{\lambda c}{\kappa_R \rho}\right) \nabla E_r, \tag{3.7}$$

where κ_R is the Rosseland mean opacity, c is the speed of light, and λ is the flux-limiter. Different choices for the flux limiter have been made in the literature, and are based on slightly different assumptions about the angular distribution of the specific intensity of the radiation field. The flux limiter always takes on values between 0 and $\frac{1}{3}$ [Levermore and Pomraning, 1981, Turner and Stone, 2001].

We use the Levermore and Pomraning [1981] flux limiter, one of the most commonly used,

$$\lambda = \frac{2+R}{6+3R+R^2}, \tag{3.8}$$

with

$$R = \frac{|\nabla E_r|}{\kappa_R \rho E_r}. \tag{3.9}$$

Another popular choice of flux limiter is the one by Minerbo [1978].

The advantage of FLD methods is their speed and relative accuracy in regions of high optical depth. And while massive stars form in very dense envelopes of molecular gas [Sridharan et al., 2002, Hill et al., 2005, Klein et al., 2005, Beltrán et al., 2006], within the dust sublimation front, or inside the radiatively-driven outflow cavities that form around massive stars, the radiation field is highly anisotropic. The FLD approximation, however, assumes that flux is in the direction antiparallel to the gradient of the radiation energy E_r. FLD methods can become less accurate in regions transitioning from optically thin to optically thick, or in regions with highly anisotropic radiation fields.

The addition of stellar sources of radiation in FLD-only radiation transfer codes is often handled via an isotropic source term that considers the luminosity of the star:

$$\frac{\partial E_r}{\partial t} + \nabla \cdot \left(\frac{\lambda c}{\kappa_R \rho} \nabla E_r \right) = \kappa_P \rho c \left(a T^4 - E_r \right) + \sum_n L_n W(\mathbf{x} - \mathbf{x}_n) \tag{3.10}$$

The coupling of radiation energy from the stars to the gas is mediated by a weighting function centered on the stellar locations and appears as a source term in the radiation energy diffusion equation. The weighting function W, which might be a spherical Gaussian function, mediates the radiation energy contributed by a sink particle n, located at $\mathbf{x}_n$, which has a luminosity L_n. The luminosity may be computed via a model for protostellar evolution or an estimate based on a zero-age main sequence (ZAMS) star, but if the weighting function is symmetric, then the radiation is still administered isotropically. Unfortunately, these regions, if circumstellar disks are present or assumed, are often the grid cells where the radiation field can be very anisotropic.

Using solely a raytracer has major disadvantages as well. For computational efficiency, scattering and non-stellar source terms are often neglected, which implies that this method is accurate only in optically thin regions where the radiation field is dominated by stellar sources. In reality, the presence of optically thick regions means radiation is absorbed, re-emitted at lower energy, or scattered by particles. This occurs especially in the envelopes around massive protostars, where the gas and radiation become tightly coupled. For reasons of technical complexity or computational cost, raytracers have typically been avoided for dynamical star formation calculations, though Monte Carlo raytracers are sometimes used in post-hoc analysis of data. In numerical simulations, diffusion codes are popular, which perform well under conditions of tight matter-radiation coupling. That said, Buntemeyer et al. [2015] re-implemented a characteristics-based raytracer in FLASH to calculate the mean radiation intensity at each cell using the Accelerated Lambda Iteration (ALI) approach [see Trujillo Bueno and Fabiani Bendicho, 1995], allowing for dynamical star formation simulations without a major loss of accuracy.

Monte Carlo raytracers are another species of raytracer worth mentioning because of their popularity and accuracy. These follow the path of many photon packets and solve the full radiative transfer problem including many generations of photon absorption, re-emission, and scattering. With enough simulated photons, highly accurate estimations of temperature may be made. However, these methods are so computationally expensive that they are not typically implemented in dynamical calculations. There are exceptions, however. Dynamical simulations with Monte Carlo radiative transfer were performed by Harries et al. [2014], Harries [2015].

By decomposing the radiation field into a direct component and a diffuse component, and computing the first via a raytracer and the second via the diffusion approximation, the worst flaws of each method are minimized. It is not that different radiative transfer methods are active in different parts of the grid. Rather, at each location in the grid, the raytracer is computing the incident stellar flux, though it may be extremely attenuated far from any sources. Meanwhile, the FLD solver is also operating on the entire grid to diffuse the thermal radiation, with the incident stellar flux appearing as a source term. This is how the two methods are linked. As a result, we compute a more accurate equilibrium gas temperature and radiative force. The flashlight effect is enhanced and circumstellar disks more effectively shield incoming material from stellar radiation.

The validity of this hybrid radiative transfer approach and its application to various problems of star formation has been demonstrated by Kuiper et al. [2010b, 2012], Kuiper and Klessen [2013], Klassen et al. [2014] and the method has been implemented in other adaptive mesh codes [Ramsey and Dullemond, 2015].

3.2.2 Further developments of the hybrid radiation transfer code

Since the publication of Klassen et al. [2014], we have been applying our code to gravitational collapse calculations. One drawback of the previous implementation was that our hydrodynamics solver was not taking into account any dynamical effects resulting from gradients in the radiation field. The only direct consequence of the diffuse thermal radiation field was the addition of an isotropic radiation pressure, $P_{\mathrm{rad}} = E_r/3$, to the total pressure.

We have now switched our hydro solver from a split method to the unsplit hydro solver included in FLASH, with modifications for handling radiation in the flux-limited diffusion approximation that follow the equations of Krumholz et al. [2007b], which are similar to the implementation described in Zhang et al. [2011]. Our simulations were done with a pre-release version of this modified unsplit hydro solver. It has since been released as part of FLASH version 4.3. Diffuse thermal radiation no longer contributes an isotropic radiation pressure to the total pressure. Instead, the gradient of the radiation energy density and the flux limiter are considered in the momentum equation (see Equation 3.12 below).

Directionally split solvers sequentially consider rows of cells in 1D and solve the Riemann problem at cell boundaries. The x, y, and z dimensions are solved in turn. Unsplit solvers consider a larger kernel of cells and can include more cross-terms in the solving of the hydrodynamic equations. Unsplit solvers are better at minimizing grid artifacts and preserving flow symmetries.

The relevant set of radiation hydrodynamic equations follows the mixed-frame formulation of Krumholz et al. [2007b], keeping terms up to $O(v/c)$ and dropping terms insignificant in the streaming, static diffusion, and dynamic diffusion limits. Mixed-frame implies that the radiation quantities are written in the lab frame, but fluid quantities, in particular the fluid opacities, are written in the comoving frame. The approach begins with writing the radiation hydrodynamics equations in the lab frame, applying the flux-limited diffusion approximation in the comoving frame, and then transforming back into the lab frame and retaining terms to order v/c. The mixed-frame approach is advantageous because it conserves total energy and is well-suited for AMR codes. For a detailed derivation, see Krumholz et al. [2007b].

In practice, it is not exclusively the domain of the hydro solver to operate on the set of equations below. Rather, like most similar astrophysics codes, FLASH employs operator-splitting for handling diffusion and source terms. The most important feature of the solver modifications mentioned above consists in making the hydro solver "flux-limiter aware", rather than restricting the effect of flux limiting to the diffusion solver.

FLASH solves the following equations for the mass, momentum, internal energy of the gas and radiation field energy density:

$$\frac{\partial \rho}{\partial t} + \nabla \cdot (\rho \boldsymbol{v}) = 0 \tag{3.11}$$

$$\frac{\partial (\rho \boldsymbol{v})}{\partial t} + \nabla \cdot (\rho \boldsymbol{v}\boldsymbol{v}) + \nabla p + \lambda \nabla E_r = \frac{\kappa_P}{c}\boldsymbol{F}_* - \rho \nabla \Phi \tag{3.12}$$

$$\begin{aligned} \frac{\partial (\rho e)}{\partial t} + \nabla \cdot (\rho e \boldsymbol{v} + P\boldsymbol{v}) &= -\kappa_P \rho c \left(a_R T^4 - E_r\right) \\ &+ \lambda \left(2\frac{\kappa_P}{\kappa_R} - 1\right) \boldsymbol{v} \cdot \nabla E_r - \nabla \cdot \boldsymbol{F}_* \end{aligned} \tag{3.13}$$

$$\begin{aligned} \frac{\partial E_r}{\partial t} - \nabla \cdot \left(\frac{c\lambda}{\kappa_R \rho} \nabla E_r\right) &= -\nabla \cdot \left(\frac{3-f}{2} E_r \boldsymbol{v}\right) \\ &+ \kappa_P \rho c \left(a_R T^4 - E_r\right) - \lambda \left(2\frac{\kappa_P}{\kappa_R} - 1\right) \boldsymbol{v} \cdot \nabla E_r \end{aligned} \tag{3.14}$$

In the above equations, ρ, v, p, e, and T are the gas density, velocity, pressure, specific internal energy, and temperature, while E_r, λ, c, and a_R are the radiation energy density, the flux limiter, the speed of light, and the radiation constant. Φ is the gravitational potential. κ_P and κ_R are the Planck and Rosseland mean opacities. f denotes the Eddington factor,

$$f = \lambda + \lambda^2 R^2. \tag{3.15}$$

In the optically-thick limit, the flux limiter λ and the Eddington factor f both approach 1/3, whereas in the optically-thin limit these approach 0 and 1, respectively.

This set of equations becomes equivalent to the one solved in Klassen et al. [2014] under the following simplifications: first, replace all ocurrences of λ and f, except in the diffusive term of (3.14), by the value appropriate for the diffusion limit, 1/3; second, omit the Lorentz transformation terms.

The Appendix of Klassen et al. [2014] also no longer applies, since we have since switched to a two-temperature model. FLASH 's original flux-limited diffusion solver was designed to handle separate electron and ion matter species, and the Appendix to Klassen et al. [2014] described how equilibrate their temperatures. We have done away with this distinction and deal only with a single matter species (molecular gas).

We tested the flux-limiter-aware hydro solver on a classic benchmark for the combined effects of radiation and fluid motion, the 1-D critical radiation shock test. In this setup, gas flows at a given speed to the left and strikes a wall, which we implement as a reflecting boundary condition. This creates a shock that travels upstream. The compressed gas is heated and radiates energy upstream. The radiation field is coupled to the gas, and so the incoming material is preheated before encountering the shock. Semi-analytic estimates by Mihalas and Mihalas [1984] allow for the comparison of measured temperatures.

The test is described in greater detail in Klassen et al. [2014]. We use a ratio of specific heats $\gamma = 5/3$ and a mean molecular weight $\mu = 0.5$. In Klassen et al. [2014], we obtained adequate results with our radiation code on this benchmark, but our preshock temperature for the subcritical case were overshooting the semi-analytic value considerably (by $\sim 20\%$).

Figure 3.1 gives the revised calculation using the current version of hydrodynamics and radiation modules. The postshock temperature of $T_2 =$

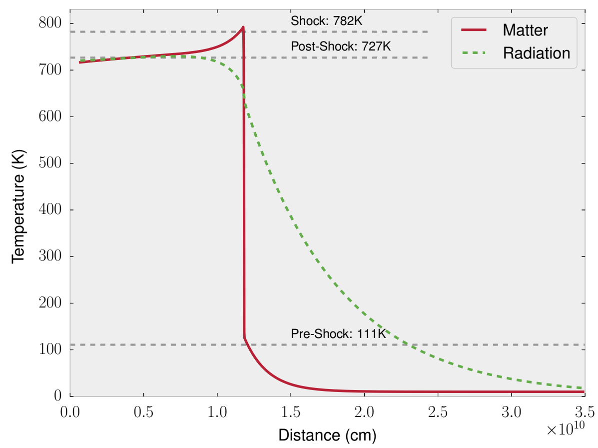

Figure 3.1: Temperature profile of a 1D subcritical radiating shock with a gas velocity of $v = 6$ km/s at a time $t = 5.8 \times 10^4$ s. The red solid line and green dashed line indicate the matter and radiation temperatures, respectively. Gray horizontal dashed lines were added to indicate the semi-analytic estimates for the temperature in the preshock, shock, and postshock regions. Stated temperatures are the semi-analytic estimates for the various regions surrounding a subcritical shock.

717 K agrees to within 2% of the semi-analytic estimate. The temperature ($T_+ = 792$ K) inside the shock agrees with the analytic value of 782 K to within 2%. Finally, the preshock temperature, where our code previously had the most difficulty matching semi-analytic estimates, is $T_- = 125$ K, compared to an expected value of 111 K—a difference of 13%.

In simulations of supercritical shocks, the revised code showed no major improvements over the results of Klassen et al. [2014].

3.2.3 Temperature iteration

In Klassen et al. [2014], equation 21, we expressed the implicit temperature update as

$$T^{n+1} = \frac{3a_R\alpha\left(T^n\right)^4 + \rho c_V T^n + \alpha E_r^{n+1} - \Delta t \nabla \cdot \boldsymbol{F}_*}{\rho c_V + 4a_R\alpha\left(T^n\right)^3}, \tag{3.16}$$

where we have used $\alpha \equiv \kappa_P^n \rho c \Delta t$. The approach follows Commerçon et al. [2011b] and involves a discretization of the coupled energy evolution equations, followed by a linearization of the temperature term, $(T^{n+1})^4$. We have now added a Newton-Raphson iteration to the temperature update (Eq. 3.16), which was not previously necessary because all of the benchmark tests in Klassen et al. [2014] involved either very short timesteps or were static irradiation tests. In a star formation simulation, the time steps are much longer, and the temperature in a cell could change by a significant amount (more than 10%) in a single time step. The emission term scales as T^4 and the opacities are also temperature-dependent. When the equations of internal and radiation energy transport were discretized, we retained the opacity κ from the previous time index n because $\kappa = \kappa(T^{(n)})$ is a function of temperature T and the updated temperature $T^{(n+1)}$ had yet to be determined. Provided the temperature does not change dramatically, this approach is acceptable, but in our later dynamical calculations involving star formation, longer timesteps and strong irradiation from the massive protostar meant that Equation (3.16) needed to be applied via a Newton-Raphson iteration. We thus modified the code to cycle the temperature update until the changes fell within safe tolerances: a minimum of 3 iterations, a minimum relative error of 10^{-5}, and a minimum absolute error of 1 K.

3.2.4 FLASH

We have implemented the above radiative transfer method in the publicly available general-purpose magnetohydrodynamics code FLASH [Fryxell et al., 2000a, Dubey et al., 2009], now in its fourth major version. FLASH solves the equations of (magneto)hydrodynamics using the high-order piecewise-parabolic method of Colella and Woodward [1984] on an Eulerian grid with adaptive mesh refinement (AMR) by way of the PARAMESH library [MacNeice et al., 2000]. Flux-limited diffusion is handled via a general implicit diffusion solver using a generalized minimum residual (GMRES) method [Saad and Schultz, 1986] that is part of the HYPRE libraries [Falgout and Yang, 2002] for parallel computation.

3.2.5 Pre-main sequence evolution and sink particles

FLASH has a modular code framework and can thus be easily extended with new solvers and physics units. It has been modified to handle Lagrangian sink particles for representing stars [Federrath et al., 2010a] or star clusters [Howard et al., 2014]. These particles exist within code grid and interact with the gas in the grid via mutual gravitation. A sink particle represents a region in space that is undergoing gravitational collapse. They were first implemented in grid codes because it was computationally infeasible to continue resolving the gravitational collapse of gas down to stellar densities. Instead, regions of runaway collapse are identified and sink particles created in their place. We understand that at the center of a sink particle resides a protostar that accretes from the gas reservoir around it—any gas above a threshold density is added to the mass of the particle (see details in section 3.3.1).

The pre-main sequence evolution of a protostar involves changes in stellar structure that result in changes in radius, effective surface temperature, and luminosity. For massive stars, they continue to grow and accrete material even after they have reached the main sequence. When modeling the radiative feedback of stars, it is important to capture all of these transitions. The amount of radiation injected into the simulation depends heavily on how the stellar properties are modeled.

Klassen et al. [2012b] explored the pre-main-sequence evolution of protostars and a protostellar model was implemented in FLASH based on the one-zone model described in Offner et al. [2009]. The star is modeled as a polytrope, and the stellar properties (mass, radius, luminosity, effective surface temperature) are evolved self-consistently as the star accretes material. The model was designed with high accretion in mind and is robust even when accretion rates are highly variable or episodic. We demonstrated in Klassen et al. [2012b] that one-zone protostellar evolution models can handle high and extremely variable accretion rates. We compared our results to Hosokawa and Omukai [2009], who had a more sophisticated treatment of the stellar structure evolution for massive protostars with high accretion rates and showed acceptable agreement (but see Haemmerlé and Peters, 2016 for a critical assessment of high-mass pre-main-sequence evolution models). Krumholz et al. [2009] also use protostellar evolution model. While not perfect, these models represent a more accurate treatment of the protostellar evolution, especially the stellar radius and surface temperature, than the traditional approach of fitting to a ZAMS model. These stellar properties are of great importance when calculating radiative feedback. The evolution of the sink particles formed in our simulations is described in section 3.4.1.

In each simulation, we witnessed the sink particle form at the center of the simulation volume. Given the comparable disk and stellar masses during the early evolution of the system, when the disk did become gravitationally unstable, the sink particle was perturbed from its location at the center of the simulation volume. The total displacement over the course of the simulation was less than 1000 AU in each simulation, almost all of which was in the plane of the disk. The higher the mass of the initial protostellar core, the less the sink particle moved.

3.2.6 Opacity and dust model

For radiative transfer calculations, we must consider the properties of interstellar dust. In the typical interstellar medium, the dust-to-gas ratio is about 1% by mass. We use the opacity tables of Draine and Lee [1984] that compute the optical properties of interstellar dust composed of graphite and silicates. These opacities we average over frequency to compute temperature-dependent dust opacities. In Figure 2.1 of Chapter 2 we showed the matter temperature-dependent Rosseland and Planck mean dust opacities. The former is appropriate for treating radiation in the diffusion approximation, whereas we use the latter when calculating the absorption or emission of radiation by dust. We use the same opacities in this paper.

We assume $T_{\rm gas} = T_{\rm dust} = T_{\rm matter}$, which is appropriate for most simulations of massive star formation, and which most FLD simulations assume. We distinguish between matter and radiation ($T_r = (E_r/a_R)^{0.25}$) temperatures, which exchange energy via emission and absorption. A third temperature that we calculate is the surface effective temperature of the star, which is used to calculate the direct radiative flux from the star.

The opacities are calculated for temperatures ranging between 0.1 K to 20000 K. However, in regions of hot gas, especially surrounding the protostar, it is necessary to consider dust sublimation, which modifies the opacity. We account for this in the form of a correction factor to the opacity, $\kappa(\boldsymbol{x}) = \epsilon\,(\rho, T_{\rm gas})\,\kappa(T)$. To estimate the temperature at which dust begins sublimating, we use the formula by Isella and Natta [2005],

$$T_{\rm evap} = g\rho^{\beta}, \tag{3.17}$$

where $g = 2000$K, $\beta = 0.0195$, and ρ is the gas density. This formula is based on a power-law approximation to the dust properties as determined by Pollack et al. [1994]. The correction factor we use is a smoothly-varying function of density and gas temperature, as in Kuiper et al. [2010a]:

$$\epsilon(\rho, T) = 0.5 - \frac{1}{\pi}\left(\frac{T(\boldsymbol{x}) - T_{\rm evap}(\boldsymbol{x})}{100}\right) \tag{3.18}$$

Figure 3.2 shows the form of this function for two different gas densities, one high and one low. The vertical lines in the figure show the sublimation temperature $T_{\rm evap}$ for the two different densities, computed via equation 3.17 and used in equation 3.18 to scale the dust opacity. Dust sublimation plays a crucial role in the inner regions of the disk nearest to the star. It both allows material to continue accreting and radiation an escape channel into the lower-density polar regions around the protostar.

One minor artifact of this method is that if gas temperatures drop, dust spontaneously reforms. More sophisticated dust treatments, including dust formation times or gas mixing, are theoretically possible, but would not substantively change the results of our simulation. The only regions affected by dust sublimation are the grid cells immediately surrounding the star, where the gas is sufficiently hot.

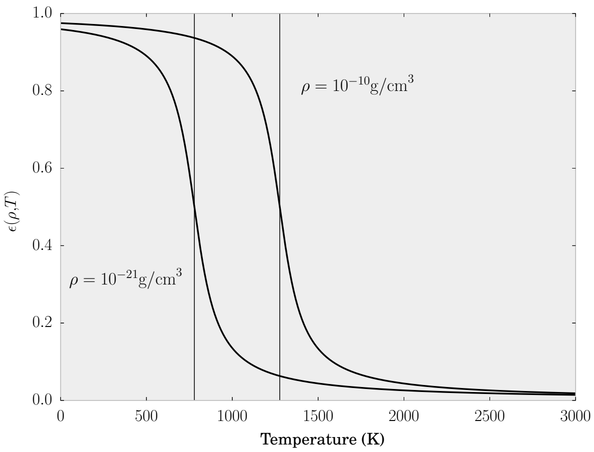

Figure 3.2: Dust opacity correction to account for dust sublimation in regions of high gas temperature. Here we show the correction as a function of gas temperature for two different gas densities, $\rho = 10^{-21}$ and 10^{-10} g/cm^3. The vertical lines indicate the sublimation temperatures $T_{\rm evap}$ for the given gas densities. The approach is identical to Kuiper et al. [2010a].

3.2.7 Radiation pressure

The radiation field imparts momentum on the gas via dust-coupling. Dust grains absorb radiation and receive an impulse. Drag forces then transfer momentum to the gas, and we assume that the coupling is strong enough that we do not need to consider the dust and gas as separate fluids, although there are some circumstances, such as in champagne flows of HII regions [Tenorio-Tagle, 1979], where the dust and gas can begin decoupling [see, e.g., Ochsendorf et al., 2014].

Because our radiation field is decomposed into direct and diffuse components, so also does our radiation pressure have direct and diffuse components. The implementation in FLASH and tests of accuracy are detailed in Chapter 2. To summarize, the body force exerted by the direct radiation field is given by Equation 2.31 from Chapter 2,

$$f_{\mathrm{rad}} = \rho \kappa_P(T_*) \frac{F_*}{c} = -\frac{\nabla \cdot \boldsymbol{F}_*}{c}, \tag{3.19}$$

where T_* is the temperature of the photosphere, which is the characteristic temperature of the direct radiation field. We see that the force is proportional to the absorbed radiation energy in a grid cell. The stellar flux, also, depends on the optical depth (see Equation 3.2). In the gray radiation approximation, the optical depth is integrated using the stellar surface temperature for the opacity calculation (see Equation 3.3). This is because interstellar dust has a strong frequency dependence and most of the energy and momentum is carried by the high-frequency radiation. The result is that most of the energy and momentum from the direct radiation is deposited in an area close to the star. However, as the dust sublimates and an optically thin cavity begins to form, more of the direct radiation is able to escape into the polar direction.

For the diffuse (thermal) radiation field, the updated hydrodynamics solver incorporates the effects of radiation on the momentum of the gas.

While we currently use a frequency-averaged opacity model, we do not expect there to be large deviations in radiation pressure when compared to a multifrequency approach. The reason for this is that while low frequency radiation can penetrate further into the gas, it also carries much less energy compared to the higher-frequency components.

3.3 Numerical simulations

Our goal was to emulate the initial conditions of the simulations of Krumholz et al. [2009] and Kuiper et al. [2010a, 2011a] to determine what effect our improved numerical and physical treatment has on the massive star formation problem. Each paper sought to address the question of how massive stars continued to accrete despite their enormous luminosities. As noted in the introduction, the main difference between their methods was the type of radiative transfer code used, with the former using an FLD-based scheme on a Cartesian AMR grid in ORION and the latter using a hybrid raytrace/FLD scheme implemented in PLUTO on a fixed, spherical grid. Krumholz et al. [2009] showed simulations in which a radiative Rayleigh-Taylor instability fed material back onto the star and disk, whereas Kuiper et al. [2012] argued that dust sublimation and a more accurate treatment of the radiation field in proximity to the star allows for a stable radiatively-driven cavity to form around the star, and for material to continue accreting through the disk. In the latter radiation scheme, since the stellar radiation is first carried by a raytracer, it is the optical depth along each ray that determines the star's impact. Pure FLD schemes use a kernel centered on the star to mediate the radiative energy injection, typically isotropically. In both cases, it was found that radiation pressure did not imply an upper mass limit for star formation.

As in the mentioned papers, the volume we simulate has a side length of 0.4 pc, with an central core of radius 0.1 pc residing inside. The core is initially cold ($T_0 = 20$K) and the molecular gas and dust has a matter density profile that follows a power-law,

$$\rho(r) \propto r^{-p}, \tag{3.20}$$

with $p = 1.5$. The density is scaled by a multiplicative constant to give the desired total core mass (30, 100, or 200 $M_\odot$). To avoid a cusp, a quadratic smoothing function over the central 6 cells smooths out the singularity.

The core is initially in solid-body rotation. We choose an angular rotation rate to match that used in Kuiper et al. [2010a], $\Omega_0 = 5 \times 10^{-13}$ s^{-1}. Krumholz et al. [2009] set their rotation so that the ratio of rotational kinetic energy to gravitational binding energy,

$$\begin{aligned}\beta_{\rm rot} &= \frac{\frac{1}{2}I\Omega^2}{U_{\rm grav}} = \frac{\left(\frac{3-p}{5-p}\right)M_{\rm core}R^2\Omega^2/3}{\left(\frac{3-p}{5-2p}\right)GM_{\rm core}^2/R} \\ &= \left(\frac{5-2p}{5-p}\right)\frac{R^3\Omega^2}{3GM_{\rm core}},\end{aligned} \tag{3.21}$$

is 2% for a core with a power-law profile with index p. Our rotational energy ratios are higher (see Table 3.1). Higher rotation rates result in larger accretion disks, which should be more prone to fragmentation at larger radii. The rotation rates of disks eventually settle into Keplerian motion around the central star.

3.3.1 Sink particles

Our simulations are initialized without any stars present, but sink particles are allowed to form naturally according to their formation criteria [Federrath et al., 2010a] and act as the ray source location in the raytracing code. Sink particles interact with the gas via mutual gravitation and are not held fixed at the center of the simulation volume, a key difference between our simulation and those of Kuiper et al. [2010a], wherein the source was held fixed at the center of the spherical grid and represented by a sink cell. Material crossing the inner grid boundary at $r_{\rm min} = 10$ AU was considered accreted onto the star. In Krumholz et al. [2009] the sink particles were allowed to form in regions that were Jeans-unstable and undergoing gravitational collapse (as in our case), according to the sink particle algorithm in ORION [Krumholz et al., 2004].

In order to form a star, gas must be Jeans unstable. The Truelove et al. [1997] criterion states that the Jeans length must be resolved by at least four grid cells, this imposes a natural density threshold for sink particle formation. If the sink radius, $r_{\rm sink}$, is equal to the Jean's length, $\lambda_J = (\pi c_s^2/(G\rho))^{1/2}$, then the threshold density becomes

$$\rho_{\rm thresh} = \frac{\pi c_s^2}{4 G r_{\rm sink}^2}, \tag{3.22}$$

where the factor of 4 in the denominator comes from the Truelove criterion and the sink radius is defined by the grid scale, $r_{\rm sink} = 2.5\Delta x$. Given our grid resolution of $\Delta x \approx 10$ AU, this results in a threshold density of $\rho \sim 10^{-14}$ g/cm^3 for all of the simulations described in this paper.

The sink particles in Krumholz et al. [2009] followed an implementation described in Krumholz et al. [2004], with the threshold density and Jeans criterion determining sink particle creation. The sink particle algorithm of Federrath et al. [2010a] that we use is stricter, checking also for convergent flow, a gravitational potential minimum, and a negative total energy ($E_{\rm grav} + E_{\rm th} + E_{\rm kin} < 0$) within a control volume.

3.3.2 Resolution

In order to resolve the dust sublimation region around the accreting star, we operate with 11 levels of refinement on our Cartesian grid, resulting in a grid resolution of $\Delta x_{\rm cell} = L/2^{l_{\max}+2} = 10.07$ AU. Krumholz et al. [2009] used a similar resolution in their simulations.

For our refinement criterion we choose to resolve the Jeans length with 8 grid cells, that is

$$\lambda_J = \sqrt{\frac{15 k_B T}{4\pi G \mu \rho}} \geq 8 \Delta x_{\rm cell}, \tag{3.23}$$

where k_B is Boltzmann's constant, T is temperature, G is Newton's constant, $\mu = 2.33$ is the mean molecular weight in our simulation, and ρ is the gas density.

Additionally, any block containing the sink particle is refined to the highest level.

3.3.3 Turbulence

Star-forming environments inside molecular clouds are turbulent [Larson, 1981, Evans, 1999], and turbulence plays a crucial role in regulating star formation [Mac Low and Klessen, 2004, McKee and Ostriker, 2007b, Federrath and Klessen, 2012]. However, in this paper we are studying the role of radiation feedback in massive star formation, revisiting important simulations in the scientific literature, but without some of the previous limitations. It is essential, then, that other complexities, such as the inclusion of initial turbulence and magnetic fields, be left out until the 'basic case' has been treated and fully studied. In forthcoming papers, we aim to study star formation in more realistic environments featuring turbulence and magnetic fields.

Table 3.1: Protostellar core collapse simulation parameters

Physical simulation parameters					
Parameter			M30	M100	M200
Cloud radius	[pc]	R_0	0.1	0.1	0.1
Power law index		p	1.5	1.5	1.5
Total cloud mass	[$\mathrm{M}_\odot$]	M_{tot}	30	100	200
Number of Jeans masses		N_{J}	13.03	79.33	224.37
Peak (initial) mass density	[g/cm^3]	ρ_c	2.58×10^{-15}	8.84×10^{-15}	1.77×10^{-14}
Peak (initial) number density	[cm^{-3}]	n_c	6.62×10^8	2.27×10^9	4.54×10^9
Initial temperature	[K]	T	20	20	20
Mean freefall time	[kyr]	t_{ff}	95.8	52.4	37.0
Sound crossing time (core)	[Myr]	t_{sc}	0.569	0.569	0.569
Rigid rotation angular frequency	[s^{-1}]	Ω_{rot}	5.0×10^{-13}	5.0×10^{-13}	5.0×10^{-13}
Rotational energy ratio		β_{rot}	35.1 %	10.5 %	5.3 %
Numerical simulation parameters					
Simulation box size	[pc]	L_{box}	0.40	0.40	0.40
Smallest cell size	[AU]	Δx	10.071	10.071	10.071
Simulation outcomes					
Final simulation time	[kyr]	t_{final}	81.4	41.6	21.9
Number of sink particles formed		n_{sinks}	1	1	1
Final sink mass	[$\mathrm{M}_\odot$]		5.48	28.84	43.65

3.3.4 Summary

We performed a total of three supercomputer simulations, varying the initial core mass across these. We selected initial cores with masses of $30\,\mathrm{M}_\odot$, $100\,\mathrm{M}_\odot$, and $200\,\mathrm{M}_\odot$. We kept all other parameters consistent between these simulations, including initial temperature, rotation rate, resolution, etc.

The initial conditions and final sink particle properties are summarized in Table 3.1. In addition to the simulations listed, we performed supplementary simulations of the 30 $\mathrm{M}_\odot$ and 100 $\mathrm{M}_\odot$ protostellar core setups at lower rotation rates so that $\beta_{\mathrm{rot}} = 2\%$ (see Equation 3.21). These lower rotation results did not change our conclusions.

3.4 Results

In this section we discuss the results from the three simulations described in the section above and summarized in Table 3.1.

3.4.1 General description: different phases of massive star formation

The evolution of the protostellar core proceeds through approximately four stages: (1) collapse, (2) disk formation, (3) disk instability, and (4) radiation feedback. The gas is initially spherically symmetric in all our simulations and begins to contract gravitationally. Before long, a Jeans instability at the center of the volume results in the creation of a sink particle representing the gravitational collapse to stellar densities. The sink particle begins accreting material from the surrounding gas.

Figure 3.3 shows snapshots taken from our 100 $M_{\odot}$ simulation at approximately 15, 25, 35, and 40 kyr of evolution, as indicated. The left column shows the density projected along the z-axis, giving a face-on view of the protostellar disk. Each frame is centered on the location of the sink particle. The column densities in the first column are scaled from $\Sigma = 10^{0}$ g/cm^2 to $10^{2.5}$ g/cm^2. The column on the right shows the edge-on view, also centered on the sink particle, where a slice has been taken and volume densities within the slice plotted. The color of the indicated volume densities are scaled from $\rho = 10^{-18}$ g/cm^3 to 10^{-14} g/cm^2.

In this figure, each row shows the state of the simulation at the indicated time, zoomed in to a (3000 AU)^2 region around the sink particle. At 15 kyr (first row), the core has undergone gravitational collapse and a small

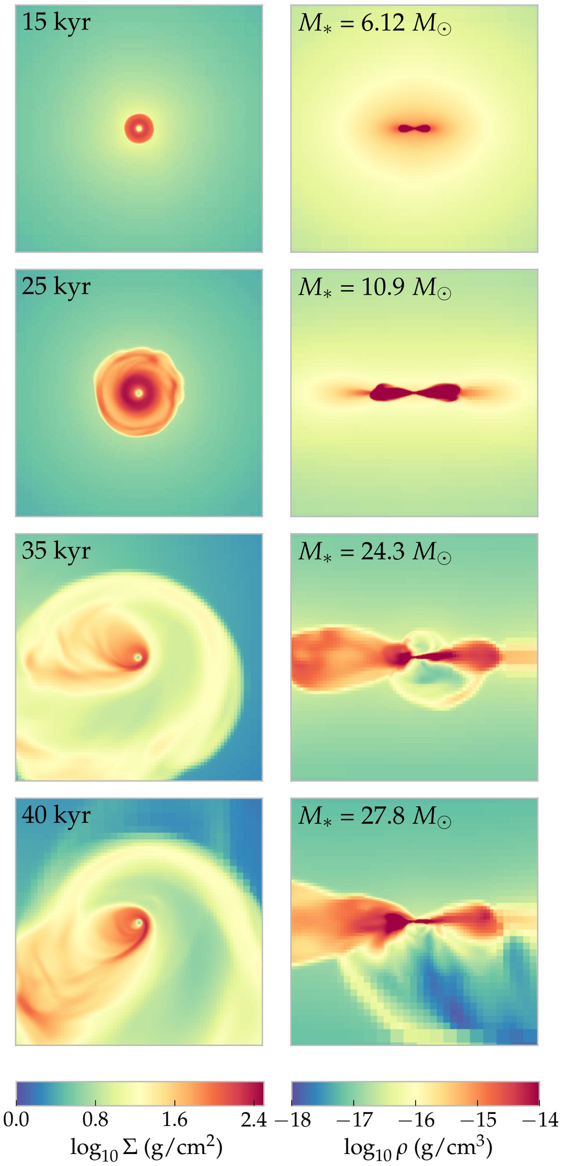

Figure 3.3: A series of panels from our $100\,\mathrm{M}_\odot$ simulation showing the time evolution of the disk in face-on and edge-on views. The times are indicated in the upper left corner of each row. The left column shows the projected gas density of the disk within a (3000 AU)^2 region. The colors indicating column densities are scaled from $\Sigma = 1$ g/cm^2 to $10^{2.5}$ g/cm^2. The right column is a slice of the volume density taken to show the edge-on view of the protostellar disk. The window is (3000 AU)^2 and the colors are scaled from $\rho = 10^{-18}$ g/cm^3 to 10^{-14} g/cm^3. The mass of the star in each pair of panels is indicated in the top-left of the second panel of each row.

protostellar disk has formed around the sink particle. In the second row, at 25 kyr, the disk is just beginning to undergo a gravitational instability. We see the formation of ripples at the edges of the disk, as well as a ring of dense material in the outer region of the disk. After a further 10 kyr of evolution, this disk shows clear spiral density waves (third row, Figure 3.3) and two radiatively-driven bubbles, one on either side of the accretion disk. The final row of Figure 3.3 shows the end state of the simulation. The radiatively-driven bubble below the disk has continued to expand and is now more than 2000 AU across, while dense material flowing above the ray origin has momentarily quenched the direct radiation field above the disk and caused the bubble to disappear. In the face-on view, dramatic spiral density waves still swirl around the protostar, which continues to accrete material at a high rate ($\dot{M} \sim 10^{-3}\,\mathrm{M}_{\odot}/\mathrm{yr}$).

When we compare this sequence of stages in each simulation, they all tell a similar story. In the 30 $\mathrm{M}_{\odot}$ core simulation, the star does not become quite luminous enough to drive bubble formation, but we still witness disk instability and the formation spiral waves. In the 200 $\mathrm{M}_{\odot}$ core simulation, the formation of star and disk proceed through the same stages, except the star is even more massive (reaching almost 44 $\mathrm{M}_{\odot}$) and so luminous that large outflow bubbles are formed on both sides of the disk and continue to grow until the end of the simulation.

We run each simulation until the timestep becomes too short to be practical. A strict upper limit on the simulation timestep is set by the gas velocities and the resolution. A highly luminous star will launch powerful outflows. These gas motions must be resolved. We observe velocities exceeding 10^7 cm/s. With a grid resolution of $\sim 10^{14}$ cm, this gives an upper limit to the timestep of $\Delta t_{\mathrm{sim}} \leq 10^7$ seconds, which is shorter than a year.

At the time when we halted our simulations, each simulation had produced only a single sink particle. For an initial core mass of $30\,\mathrm{M}_\odot$, the resulting sink attained a final mass of $5.48\,\mathrm{M}_\odot$ after 81.4 kyr of evolution. The simulation that began with a core mass of $100\,\mathrm{M}_\odot$ produced a star of $28.84\,\mathrm{M}_\odot$, whereas our $200\,\mathrm{M}_\odot$ simulation produced a star of $43.65\,\mathrm{M}_\odot$.

The freefall time for a sphere of uniform density ρ is given by

$$t_{\mathrm{ff}} = \sqrt{\frac{3\pi}{32G\rho}}, \tag{3.24}$$

where G is Newton's constant. It represents the characteristic timescale for gravitational collapse. We estimate the freefall for our protostellar cores using the mean density. More massive cores have shorter freefall times, resulting in higher accretion rates onto the protostar. The simulations ran for 0.85, 0.79, and 0.59 freefall times for each of the initial 30 $\mathrm{M}_\odot$, 100 $\mathrm{M}_\odot$, and 200 $\mathrm{M}_\odot$ core simulations, respectively.

We show the sink particle evolution in Figure 3.4 as a function of time. In the upper left panel we show the mass histories of the star formed in each simulation. One interesting feature of these is that each possesses a 'knee', where the rate of accretion shifts from one steady value to another relatively steady value. The knee appears to occur simultaneously with the disk instability, and we explore this below.

The accretion rate is shown in the upper right panel for Figure 3.4 and shows the same transition to higher accretion rates. This occurs between 0.35 and 0.55 freefall times. The accretion rate increases by a factor of about 2–10, while also become more variable. We attribute both the increase in accretion rate and its increased variability to a transition in the accretion disk, which

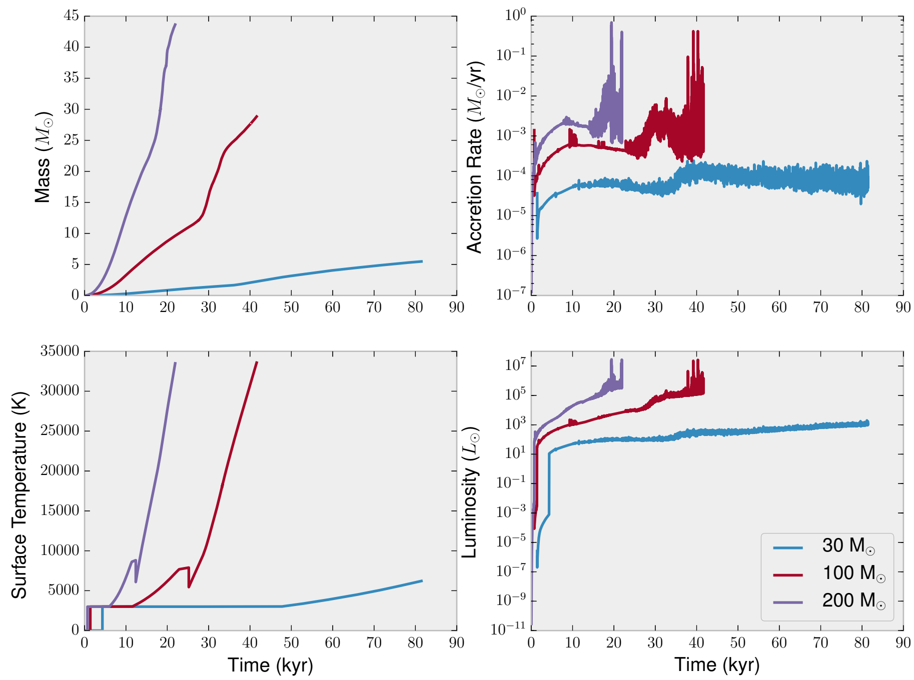

Figure 3.4: The time-evolution of the sink particle formed in each of the three simulations (30, 100, and 200 $M_\odot$ initial core mass). The sink particle represents the accreting protostar and its internal evolution is governed by a protostellar model. The top-left panel shows its mass. The top-right panel indicates the accretion rates onto the sink particles. The effective surfance temperature of the protostar is estimated by a protostellar model and is indicated in the bottom-left panel. The star radiates both due to the high accretion rate and its own intrinsic luminosity due to nuclear burning. The total luminosity of the sink is the sum of these two, and each sink particle's total luminosity is shown in the bottom-right panel.

we discuss in detail below in section 3.4.2.

The bottom two panels of Figure 3.4 show the effective surface temperature (left) and luminosity (right) of the star, respectively. The temperature is given by a protostellar model that we introduced into the FLASH code in Klassen et al. [2012b] and is based on a one-zone model described in Offner et al. [2009]. The drop in temperature observed in the 100 $M_\odot$ and 200 $M_\odot$ runs is on account of a swelling of the stellar radius at a time when the accreting protostar undergoes a change in its internal structure, switching from a convective to a radiative structure. The much larger stellar radius is initally cooler. The luminosity shown in the bottom right panel of Figure 3.4 shows the combined stellar luminosity and accretion luminosity, $L_{\rm acc} \propto GM_* \dot{M}_*/R_*$. This impact of protostellar evolution on the radiative feedback is in general agreement with earlier models of high-mass core collapse using 1D stellar evolution modeling (Kuiper and Yorke, 2013b, but compare Haemmerlé and Peters, 2016).

We note that in each of our three main simulations, only a single sink particle is formed. This is in contrast to the similar calculation by Krumholz et al. [2009], which formed a binary companion with an orbital semi-major axis of 1280 AU. The secondary was about 1000 AU away from the central star, which is similar to the radius of the circumstellar accretion disks we form.

In Figure 3.5 we plot the evolution of the mass accretion rate as a function of the stellar mass for the sink particle in each of our three simulations. We apply a moving average filter of 1000 datapoints to smooth out the accretion rate, which is highly variable, especially at late times. We were unable to evolve the simulation to the point were accretion shuts down onto the sink particle. The figure is similar to Figure 11 in Kuiper et al. [2010a], but which featured simulation with axial and midplane symmetries. The 2D axisymmetric geometry of those simulations allowed for much longer runtimes. At late times accretion is seen to shut down, on account of both gas reservoir depletion and radiative feedback. We were unable to run our 3D non-axisymmetric simulations for the same duration, and so in Figure 3.5 we do not yet see strong evidence of a shutdown in accretion and the gas reservoir is still far from fully depleted.

In the corresponding 3D simulation of Kuiper et al. [2011a], the accretion disk also shows the formation of spiral arms and highly variable accretion rates, but no disk fragmentation. But the simulation could only be performed up to 12 kyr of evolution, hence, further evolution of the circumstellar disk, including binary formation, remains uncovered.

Before disk instability sets in, the accretion rate onto the star is governed more by spherically symmetric collapse of the initial core. Girichidis et al. [2011a] examined the collapse of a singular isothermal sphere [Shu, 1977] and the scaling of accretion rate with the number of Jeans masses N_J present in initial the protostellar core. We therefore compare the maximal accretion rate before disk instability sets in to the number of Jeans masses, and find that there is a linear relationship between accretion and N_J. The Jeans mass is given by

$$M_J = \frac{\pi^{5/2}}{6} \frac{c_s^3}{G^{3/2} \rho^{1/2}}, \tag{3.25}$$

where c_s is the isothermal sound speed and ρ is the mean density of the spherical protostellar core. Thus, the number of Jeans masses present is

$$N_J = \frac{M_{\rm core}}{M_J} \tag{3.26}$$

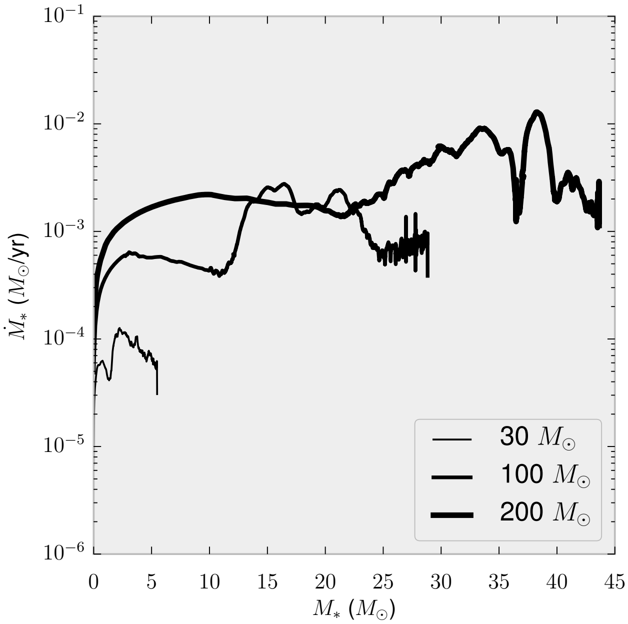

Figure 3.5: The accretion rate plotted as a function of stellar mass for each of our three main simulations. The line thickness scales in order of ascending initial mass for the protostellar core.

The linear scaling in accretion rate followed

$$\dot{M}_* = 9.638 \times 10^{-6} N_J \ \ \mathrm{M}_\odot \, \mathrm{yr}^{-1}. \tag{3.27}$$

The 30, 100, 200 $\mathrm{M}_\odot$ simulations contained 13.0, 79.3, and 224.4 Jeans masses, respectively, assuming isothermal 20 K gas. An approximately linear scaling is consistent with the theoretical results of Girichidis et al. [2011a], although they were following the self-similar collapse of a singular isothermal sphere [Shu, 1977] with power-law profiles $\rho \propto r^{-2}$.

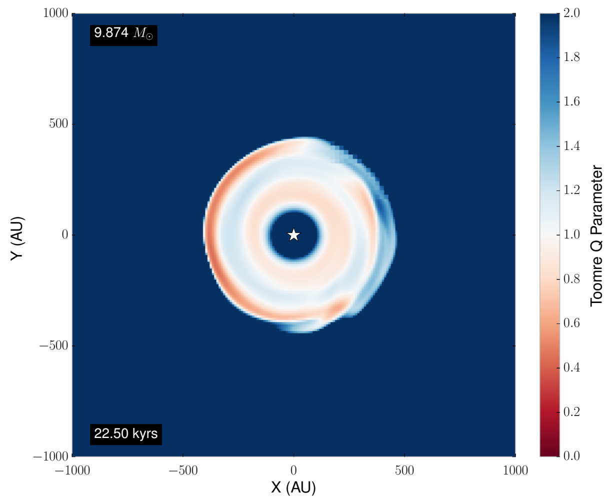

Figure 3.6: The Toomre Q parameter, which quantifies the gravitational stability of disks. Values of $Q < 1$ are unstable to gravitational fragmentation and are colored in red. Stable regions are colored blue. Here we see the disk in our 100 $M_\odot$ simulation becoming marginally unstable. The period of time immediately after this marks a strong increase in the accretion rate of material onto the star. The mass of the star is indicated in the top-left.

3.4.2 Disk formation and evolution

The initial rotation results in the gradual formation of a disk around the sink particle. The disk assumes a flared profile and material continues to accrete onto both the sink particle and the disk. In Figure 3.4, the slower, steady accretion at the beginning of each simulation coincides with the growth phase of the disk around the sink particle.

To measure the disk stability, we consider the Toomre Q parameter,

$$Q = \frac{c_s \kappa}{\pi G \Sigma}, \tag{3.28}$$

where c_s is the sound speed, κ is the epicyclic frequency, G is Newton's constant and Σ is the column density. The Toomre stability criterion [Toomre, 1964]

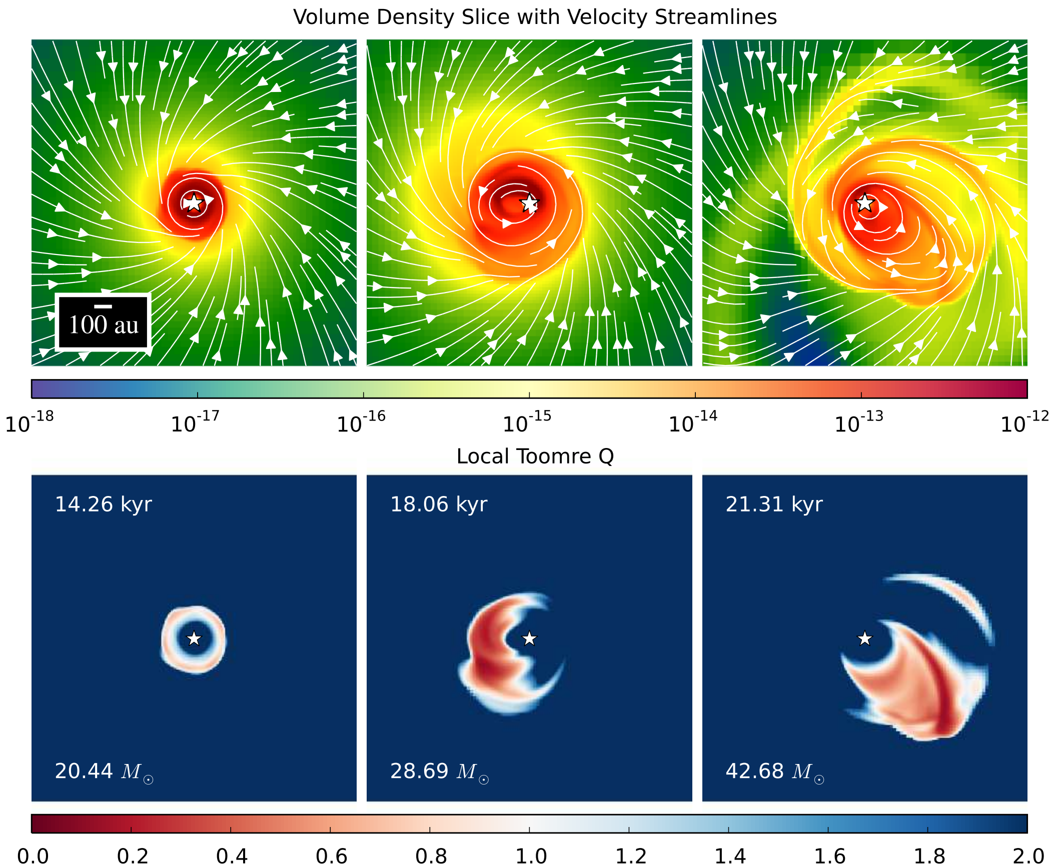

Figure 3.7: Sequence of snapshots from the 200 $M_\odot$ simulation showing face-on volume density slices (top row) and the local Toomre Q parameter (bottom row) in a $(3000\ \mathrm{AU})^2$ region centered on the location of the sink particle. Scale bars have been added to show the volume density (in g/cm^2) and the value of the Q parameter (see Equation 3.28). Values of $Q < 1$ indicate disk instability. Velocity streamlines have been added to the volume density slice. The mass of the star is indicated in the bottom-left of each panel in the bottom row.

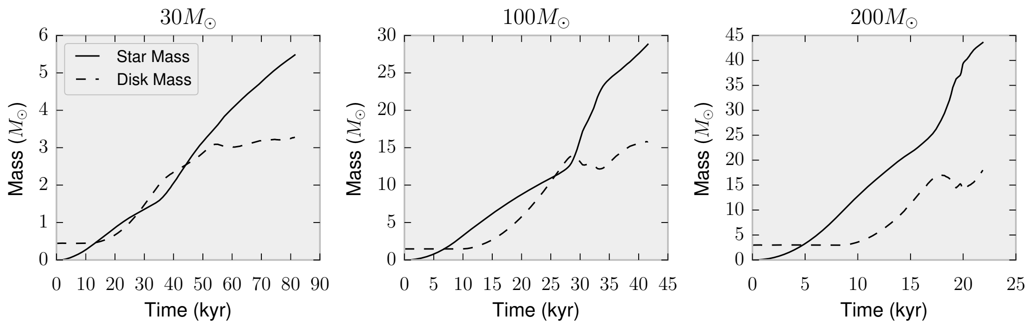

Figure 3.8: The evolution of our three simulations, with initial core masses indicated above each frame. These show the simultaneous growth of the star and disk masses in each simulation.

predicts a disk instability for values of $Q < 1$. The epicyclic frequency κ is equal to the angular velocity Ω for Keplerian disks. In the case of rigid rotation, $\kappa = 2\Omega$. The gas in our simulation starts out in rigid body rotation, but the disk then becomes Keplerian.

In Figure 3.6 we show the local Toomre Q value in our 100 $M_\odot$ simulation at 22.5 kyr, the point in time just as the circumstellar accretion disk is becoming marginally unstable. Regions colored in blue show stable regions, while regions colored are unstable. White regions have a value for $Q \approx 1$, and are marginally stable. Within 5 kyr, the disk becomes highly asymmetric and the sink particle is perturbed from the center of the simulation volume. This event is accompanied by a marked increase in the accretion rate onto the sink particle, reaching values above $10^{-3}\,M_\odot/\mathrm{yr}$. The accretion rate is also far more variable during this phase of evolution, as is clearly visible in Figure 3.4. Analysis of the Toomre Q parameter in the other simulations tells the same story: material accretes onto the disk, trigging an eventual disk instability, resulting in increased accretion onto the star.

We show a sequence of snapshots from the 200 $M_\odot$ simulaion in Figure

3.7. This time, we have paired a measurement of the local Toomre Q parameter (bottom row) with a volume density slice through the midplane of the disk (top row). The snapshots were taken at the same times, with the times indicated. The panels have been centered on the sink particle at show a (3000 AU)^2 region. In the volume density slices we have overplotted velocity streamlines that indicate the flow of material onto and through the circumstellar disk. We see that the flow merges with the spiral arms and that the spiral arms appear to act as accretion channels for material.

In Figure 3.8, we show the simultaneous growth of the star and disk masses in each of our three simulations. The disk mass is measured by considering a cylindrical volume, centered on the sink particle, and measuring the total gas mass contained within this cylinder. We choose a radius of 1000 AU, and a total height of 1000 AU. The resulting volume is large enough to capture the main extent of the disk, including approximately 2 pressure scale heights. The final disk masses of our three simulations were 3.3, 15.8, and 18.0 $\mathrm{M}_\odot$ for our 30, 100, and 200 $\mathrm{M}_\odot$ simulations, respectively.

In the 100 $\mathrm{M}_\odot$ and 200 $\mathrm{M}_\odot$ simulations, the 'knee' in the stellar mass evolution, corresponds to an instability of the disk. It loses its axisymmetry and forms large spiral arms. At this time, Figure 3.8 shows that the disk mass ceases to grow monotonically and we measure a temporary decrease in the overall disk mass. This may, however, be due to spiral arms flinging material outside the 1000 AU radius of the cylinder we are using to measure the disk mass.

The final disk masses were measured at 3.3 $\mathrm{M}_\odot$, 15.8 $\mathrm{M}_\odot$, and 18.0 $\mathrm{M}_\odot$ for our 30 $\mathrm{M}_\odot$, 100 $\mathrm{M}_\odot$, and 200 $\mathrm{M}_\odot$ simulations, respectively. The latter two are relatively close in mass, but the disk accretes faster in the 200 $\mathrm{M}_\odot$

case. It also has the highest time-averaged star mass to disk mass ratio (1.96). The 30 $M_\odot$ simulation had the lowest time-averaged star-to-disk mass ratio (1.07), with the 100 $M_\odot$ falling in between with 1.45.

3.4.3 Disk fragmentation

Contrary to a very similar calculation performed by Krumholz et al. [2009], we do not form a binary star as the disk goes unstable, or any additional sink particles. Despite the instability of the disk, fragmentation is not seen. This is a significant result given that spectroscopic surveys show a high binary fraction among massive stars. Chini et al. [2012] performed a high-resolution radial velocity spectroscopic survey of massive stars within the Milky Way galaxies that included about 250 O-type stars and 540 B-type stars. Their results indicated that over 82% of stars with masses above 16 $M_\odot$ form close binaries. This fraction drops precipitously for lower-mass stars.

How many stars are expected to form per protostellar core? Goodwin and Kroupa [2005] argue from dynamical constraints and observations that protostellar cores should produce only 2 or 3 stars. This contrasts with some numerical simulations, in which the protostellar core fragments into a greater number of stars, as in Goodwin et al. [2004] or the simulations of Krumholz et al. [2009]. It also contrasts with our simulations, which show a massive disk that does not fragment into more stars.

We examine several approaches to the question of fragmentation. First, we follow the analysis of Rogers and Wadsley [2012], who studied the fragmentation of protostellar disks and derived a Hill criterion for the spiral arms [although, see Takahashi et al., 2016]. These are the sites most likely to begin

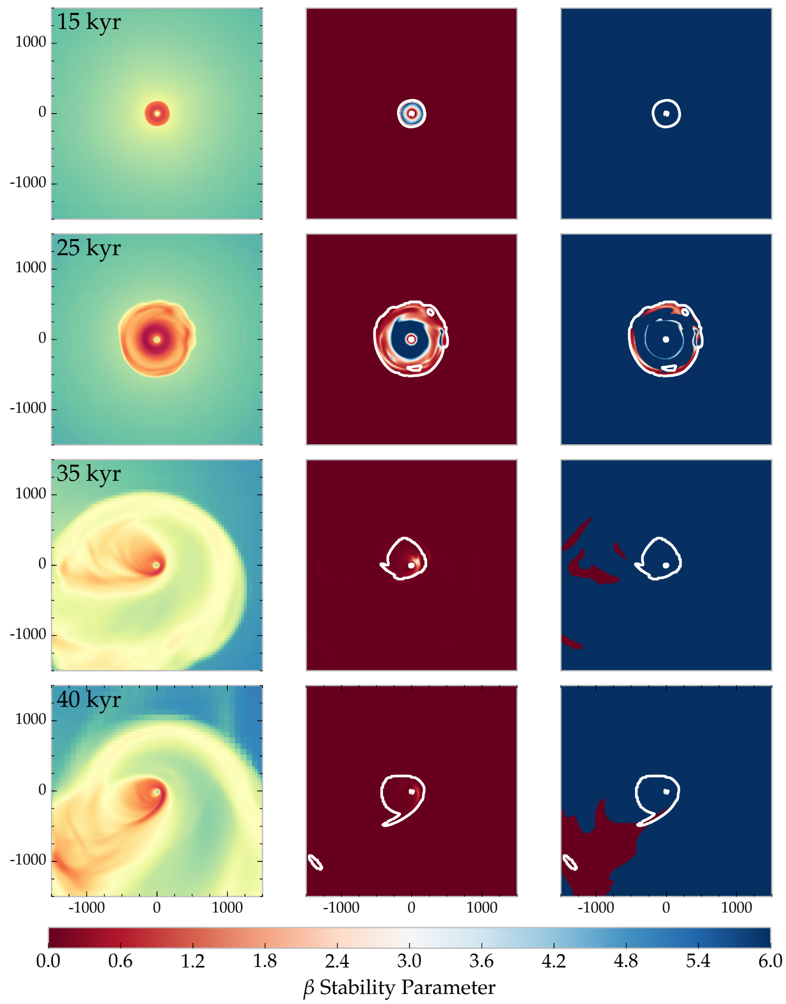

Figure 3.9: An analysis of the local stability of the entire protostellar disk from the 100 $M_{\odot}$ simulation. The rows show the state of the simulation at the stated times, which are identical to the ones shown in Figure 3.3. The left column shows the column density of the disk. The center column shows the β stability parameter for the entire disk. The right column shows the β stability parameter again, but with Toomre-stable regions ($Q > 1$) masked out. Colored in red, therefore, are only those regions that are both Toomre-unstable and β-unstable. These are expected to be gravitationally unstable. The white contour in the panels of the middle and right columns indicate those regions where the density exceeds the threshold for sink particle formation, $\rho_{\rm thresh} = 1.4 \times 10^{-14}$ g/cm^3.

fragmenting. They discovered that if the width of these spiral arms is less than twice the Hill radius, then fragmentation of the spiral arms is expected because the self-gravity of that spiral arm segment dominates the tidal forces from the star (manifested as rotational shear).

To quantify this, we look at the Hill radius, as defined in Rogers and Wadsley [2012],

$$H_{\rm Hill} = \left[\frac{G\Sigma l^2}{3\Omega^2}\right]^{1/3}, \tag{3.29}$$

where G is Newton's constant, Σ is the column density of the spiral arms segment, l is the width (thickness) of the spiral arm, Ω is the angular velocity, assuming a Keplerian disk. Here Σl^2 is a measure of the mass contained within the Hill sphere.

The Hill criterion for stability against fragmentation is

$$\frac{l}{2H_{\rm Hill}} > 1. \tag{3.30}$$

Rogers and Wadsley [2012] demonstrate the validity of this criterion through hydrodynamic simulations of protostellar disks, finding gravitational fragmentation occurring when $l/(2H_{\rm Hill}) < 1$. We test whether the spiral arms present in our own calculation are indeed stable by looking at snapshots from our simulations at an evolved state. We then took a cross-section of the spiral arm where column densities were greatest and measured the mass along the cross section and the angular rotation rate. In each case the spiral arms were 100 AU wide, and the masses through a section of the spiral arms at the cross section were 0.033 $\mathrm{M}_\odot$, 0.15 $\mathrm{M}_\odot$, and 0.29 $\mathrm{M}_\odot$ for the 30, 100, and 200 $\mathrm{M}_\odot$ simulations, respectively. Meanwhile, the rotation rates at these locations were

$\Omega = 3 \times 10^{-10}$, 6×10^{-10}, and 6×10^{-10}, respectively. Finally, this resulted in Hill criterion values of $l/(2H_{\text{Hill}}) = 2.95$, 2.82, 2.26, respectively, consistent with the lack of fragmentation observed in our simulations.

This analysis nevertheless focuses on the role of shear stabilization in spiral arms. We now turn to the role of cooling and disk fragmentation across the entire disk. Gammie [2001] and Johnson and Gammie [2003] investigated nonlinear gravitational instability in numerical models of thin, Keplerian disks. By considering the cooling time τ_c and the angular rotation rate Ω, a stability parameter can be defined,

$$\beta = \tau_c \Omega, \tag{3.31}$$

which must be greater than some critical value in order for the disk to remain gravitationally stable. Gas with short cooling times relative to the orbital period is expected to cool rapidly—opening the way to fragmentation if the gas is also sufficiently self-gravitating. The critical value for β is established via numerical simulations, but depends critically on which heating and cooling mechanisms are present in the simulation. The cooling time can be defined as the internal energy of the gas, divided by its cooling rate. For optically thick disks, Johnson and Gammie [2003] found fragmentation occurs for values of $\beta = \langle \tau_c \rangle \Omega \sim 1$, where $\langle \tau_c \rangle$ is the disk-averaged cooling time. It is important to note that the β-criterion for stability does not replace the Toomre Q stability criterion, but rather complements it. That is, a disk must be both Toomre-unstable and have a Gammie β less than some critical value for fragmentation to occur.

We choose to look at the local cooling rate. Since we possess information about the rate of radiative flux loss from the disk, we define the cooling time as

$$\tau_c = \frac{E}{\langle |\boldsymbol{F}_{\rm rad,z}| \rangle}, \tag{3.32}$$

where E is the column internal energy integrated through the disk. Meanwhile, $\langle |\boldsymbol{F}_{\rm rad,z}| \rangle$ is the mean radiative flux in the vertical direction (away from the disk). Our cooling time, therefore, is a direct function of the mean density, temperature, and opacity of a vertical column through the circumstellar disk. Since we know the rotation rate at each point, we then calculate a local $\beta = \tau_c \Omega$.

In Figure 3.9 we compare side-by-side the column density and disk stability for the circumstellar disk in our 100 $\mathrm{M}_\odot$ simulation, taking snapshots from the simulation at the same times as in Figure 3.3. As in that earlier figure, we show the column density in the left column. The middle column shows the value for β throughout the disk. We see that the cooling time is short relative to the orbital period and the disk should be prone to rapid cooling. Recall that Johnson and Gammie [2003] found that fragmentation occurs for values of $\beta \sim 1$.

However, if we consider only those regions which are *also* Toomre-unstable, as we do in the right column of Figure 3.9, we see that most parts of the disk remain stable. In generating the panels for this column, we created an image mask, i.e. we filter the pixels based on value of the Toomre Q parameter at that location and then draw the β parameter. Regions where $Q > 1$ are colored uniformly in blue; these regions are stable regardless of the value of β. Additionally, we draw a white contour in the panels of the middle and right columns to indicate those regions where the density exceeds the threshold for sink particle formation, $\rho_{\rm thresh} = 1.4 \times 10^{-14}$ g/cm^3.

For our $100\,\mathrm{M}_\odot$ simulation, the threshold density for sink particles is $\rho_{\mathrm{thresh}} = 1.4 \times 10^{-14}$ g/cm^3. We draw a white contour in Figure 3.9 to indicate those regions within a disk slice possessing densities greather than this threshold value.

Taken together, the disk is largely stable across much of its extent. Nevertheless, Figure 3.9 shows the disk is not completely stable everywhere, at least predicted by linear stability analysis. This can be seen especially in the final set of panels at 40 kyr. There appears an island of high density gas that is both Toomre-unstable and β-unstable at about 1200 AU separation from the central star. This is a candidate region for collapse. Given more time it could indeed collapse to form a single wide binary companion to the central star. As pointed out in Takahashi et al. [2016], fragmentation is a nonlinear outcome of gravitational instability and highly dependent on initial conditions. They demonstrate that the only necesssary condition for the formation of spiral arms is that $Q < 1$, and the only necessary condition for the fragmentation of these arms is $Q < 0.6$. Taken together with our stricter sink particle criteria, as described in Section 3.3.1, this accounts for the lack of secondary fragmentation over the timescales simulated.

The gravitational collapse that formed the first star in our simulation, and the strong radiative accelerations produced by the intense luminosity of that massive star, conspire with the Courant condition to strongly limit the timestep size of our simulation. The timestep is now so small that the simulation has now effectively stalled.

3.4.4 Radiatively-driven bubbles

In the vicinity of a massive star, the radiative force can exceed the force of its gravitational attraction, resulting in radiatively-driven winds or bubbles, and possibly halting any further accretion. Radiation pressure is also one of the main mechansism for the disruption of giant molecular clouds (GMCs) and the cumulative radiation pressure from star clusters may drive large-scale galactic outflows [Murray et al., 2010, 2011].

The Eddington luminosity describes the force balance between radiation and gravity:

$$L_{\rm edd} = \frac{4\pi G M_* c}{\kappa}, \tag{3.33}$$

where κ denotes the opacity of the absorbing medium. We estimate the direct radiation pressure using temperature-dependent gray opacity [see Figure 2.1 in Chapter 2] for the dust. The body force on the dust grains is given by

$$f_{\rm rad} = \rho \kappa_P \left(T_{\rm eff}\right) \frac{F_*}{c}, \tag{3.34}$$

where $\kappa_P = \kappa_P(T_{\rm eff})$ is the Planck mean opacity, $T_{\rm eff}$ is the effective temperature of the star, estimated by protostellar model, and F_* is the stellar flux.

In Figure 3.10, we show the evolution of the stellar radiative flux in each of our three simulations. It is plotted here as a function time and compared, in each case, to the star's Eddington luminosity. We see that only in the $100\,\mathrm{M}_\odot$ and $200\,\mathrm{M}_\odot$ simulations does the star become bright enough to exceed the Eddington limit. The excess radiation pressure in these two more massive simulations results in the formation of radiatively-driven outflow bubbles that expand away from the star above and below the accretion disk, sweeping up a

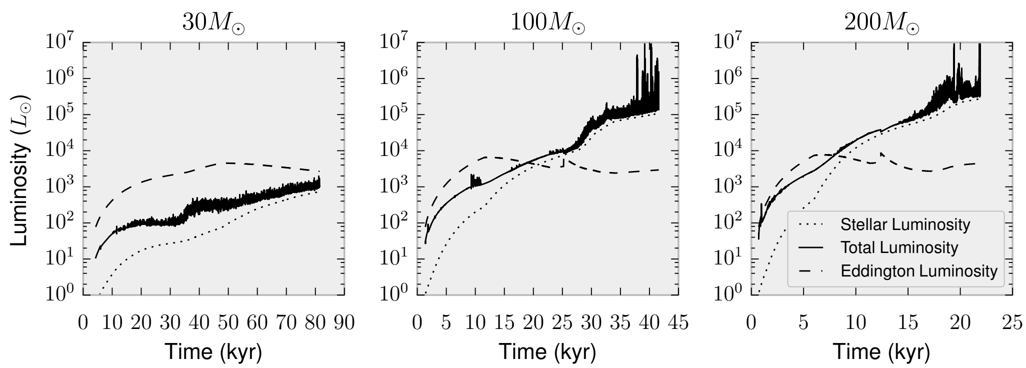

Figure 3.10: The evolution as a function of time of the total luminosity (solid line) of the star formed in each of our three main simulations. In each case it is compared to the star's Eddington luminosity (dashed line), the threshold where radiation forces exceed gravitational forces. In the $100\,\mathrm{M}_\odot$ and $200\,\mathrm{M}_\odot$ simulations, the star's luminosity becomes super-Eddington. It is in these simulations that radiatively-driven bubbles are observed.

shell of material and leaving a low-density gas in their wake. Radiation spills into these more optically thin regions via a kind of 'flashlight effect' [Nakano, 1989, Yorke and Bodenheimer, 1999, Yorke and Sonnhalter, 2002], helping to drive the outward expansion of the bubble. The flashlight effect as described in Yorke and Bodenheimer [1999] is the anisotropic distribution of radiative flux around a star after the formation of a circumstellar disk. The disk in effect channels the radiation along the polar axis, creating a 'flashlight'.

We note also that in the low-mass $30\,\mathrm{M}_\odot$ simulation, the star's luminosity remains sub-Eddington, but continues to creep steadily upward. At the time that we halted the simulation, the star's accretion rate, though not exceptionally high ($10^{-4}\,\mathrm{M}_\odot/\mathrm{yr}$), was showing no signs of slowing down (see Figure 3.4). At this rate, the star might yet have become radiant enough to drive an outflow bubble.

Based purely on the above considerations, it might be surprising that accretion continues unabated even after the star goes super-Eddington. How-

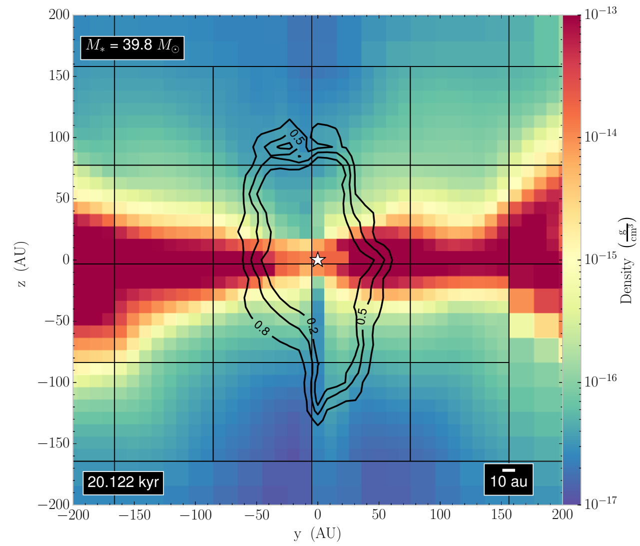

Figure 3.11: Volume density slice of a (400 AU)^2 region through our 200 $M_\odot$ simulation, showing an edge-on view of the circumstellar disk. The slice is centered on the sink particle, representing a 39.8 $M_\odot$ star. FLASH's block structure is shown in the grid, with each block containing 8^3 cells. Overplotted are contours showing dust fraction. Nearest the star, the dust is completely sublimated. Contours show dust sublimation correction factors of 0.2, 0.5, and 0.8.

ever, the above estimation of the Eddington luminosity did not account for dust sublimation, which occurs at the inner edge of the disk. In our simulations, the dust sublimation was approximated by Eqs. (3.17) and (3.18), and this results in a low opacity in regions where the gas has been heated to high temperature. Radiative forces can no longer couple to the gas via the dust, and the gas continues to move inward and accrete onto the star. In Kuiper et al. [2010a], Kuiper and Yorke [2013a] it was shown that the inclusion of the dust sublimation front was a requirement for continued accretion via the protostellar disk and enhanced the anisotropy of the radiation field, contributing to the flashlight effect. Our resolution (10 AU) is not quite as high as those (1.27 AU radially at the inner edge of the disk) in Kuiper et al. [2010a], but we also show continued disk accretion and a strong flashlight effect.

Figure 3.11 shows the dust sublimation front at a snapshot in time from our most massive (200 $M_\odot$) core simulation, after about 20 kyr of evolution. We plot an edge-on volume density slice intersecting the sink particle and circumstellar disk and showing a region 400 AU wide on a side. The FLASH block-grid structure is overplotted for reference. Each block contains 8^3 cells. The sink particle, representing a $39.8\,M_\odot$ star, is located at the center of the frame and is in the process of driving a radiative bubble. The star has grown to almost 20% of the initial mass of the protostellar core. Figure 3.11 shows contours of dust fraction overplotted. A value of 0.0 implies total dust destruction and a value of 1.0 implies no sublimation. We show contours at values of 0.2, 0.5, and 0.8. Dust sublimation regions are also optically thin, and Figure 3.11 shows clearly how radiation is channeled in the polar direction.

In the classical Rayleigh-Taylor instability, a heavy fluid cannot be stably supported by a light fluid. In Figure 3.12, we plot the net acceleration based on the radiative and gravitational forces present. The data is taken from our 200 $M_\odot$ simulation, after 21.8 kyr of evolution. The radiative acceleration includes both the direct and the diffuse radiation field, while the gravitational acceleration include the attractions of both the star and the self-gravity of the gas. The figure shows the volume density of the gas in a slice centered on the sink particle so that an edge-on view of the disk is shown. Overplotted are the acceleration vectors with magnitude coded in the color. The direct radiation field exerts very powerful accelerations immediately surrounding the star. This energy is absorbed and reprocessed so that the diffuse radiation field dominates the radiative accelerations in shadowed regions, the disk, and far away from the star.

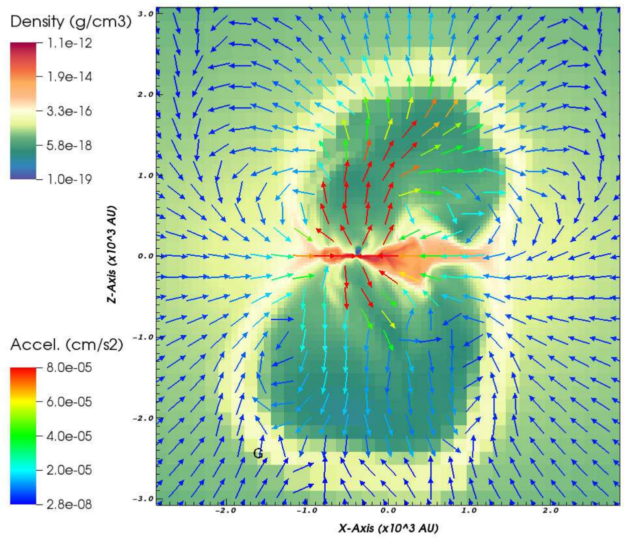

Figure 3.12: Acceleration vectors showing the net acceleration (in units of cm/s^{-2}) of the gas due to radiative forces and gravity (both the gravity of the star and the gas). Vectors are overplotted on a background indicating volume density slice of an approximately (6000 AU)^2 region through our 200 $M_\odot$ simulation after about 21.8 kyr of evolution, showing an edge-on view of the circumstellar disk and radiatively-driven bubble. The slice is centered on the sink particle, representing a 43.5 $M_\odot$ star.

The star has reached a mass of 43.5 $M_\odot$ and has driven a radiative bubble above and below the disk. While along the edge of the lower bubble wall, there is a null surface in the acceleration—the radiative and gravitational forces roughly cancel, though momentum is likely still causing the bubble to expand. On the upper edge, however, we see that a net outward acceleration extends well beyond the bubble wall, ensuring that the bubble will continue to expand outward. It also means that the classic condition for the Rayleigh-Taylor instability (that of a heavy fluid supported by a light fluid) is not met. The acceleration vector is outwards, so that the “lighter” fluid (FLD approximates the radiation field as a fluid) sits atop the heaver fluid of the bubble wall. This is another reason why our bubbles appear roughly uniform

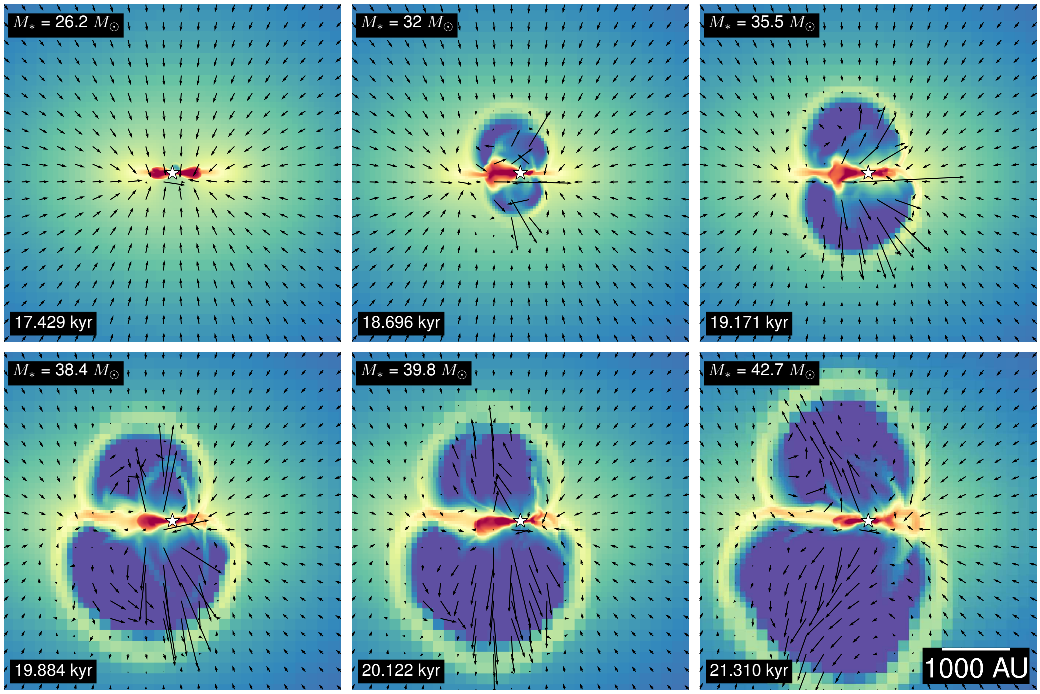

Figure 3.13: Edge-on volume density slices, centered on the sink particle, showing in a (5000 AU)^2 region the evolution of a radiatively-driven bubble in our 200 $M_\odot$ simulation. Shown are six snapshots at different points in the simulation with the times indicated. Velocity vectors have been overplotted. Volume densities have been scaled from $\rho = 10^{-17}$ g/cm^3 to 10^{-13} g/cm^3. The mass of the star is indicated in the top-left of each panel.

and show no signs of the Rayleigh-Taylor instability. We checked the bubble in the 100 $M_\odot$ simulation and there, too, there was net outward acceleration. We therefore conclude that Rayleigh-Taylor instabilities are absent in these early phases, which are instead dominated by net outward acceleration driven by the radiation field.

In Krumholz et al. [2009], the Rayleigh-Taylor instability that was observed in their simulations served to feed material back onto the disk and the star. If the disk can be fed continually, either from the outer regions of the simulation, or from material escaping the polar outflow, then the star should be able to continue accreting, provided the thermal radiation pressure within the disk itself is not so strong as to reverse the accretion flow. In contrast, Kuiper et al. [2012] modeled the high-mass pre-stellar core collapse comparing two different schemes for radiative feedback, namely the hybrid scheme used also in this investigation and the FLD-only scheme used in Krumholz et al. [2009]; as a result, only simulations using the FLD approximation yield a radiative Rayleigh-Taylor instability, simulations with the hybrid scheme show stable outflows for stars in the super-Eddington regime. Kuiper et al. [2010a] showed that the anisotropy of the radiation field prevents the thermal radiation from ever becoming strong enough to halt disk accretion. It then becomes a question as to whether the disk can be continually fed.

Figure 3.13 clearly shows that collapsing gas is deflected along the walls of the bubble, and flows onto the disk. Here we look at the gas density and velocities in a series of slices from our $200\,\mathrm{M}_\odot$ simulation. We centered individual slices on the position of the sink particle and took an edge-on view of a $(5000\ \mathrm{AU})^2$ region. The slice intersects the circumstellar accretion disk and shows a radiatively-driven bubble forming. The second-to-last panel was taken at the same time as Figure 3.11, which is also near the end of our simulation. The star's luminosity is super-Eddington in each of the panels shown (compare Figure 3.10) and the outflow bubbles develop uniformly, both above and below the disk, and grow to be over 2000 AU in diameter. Interior to these bubbles is evidence of smaller bubbles, expanding in successive waves and finally bursting their walls.

We overplot velocity vectors to show the gas motion. Interior to the radiatively-driven bubbles, the gas is being driven away from the star asymmetrically. The direct radiation field from the star is highly sensitive to the gas distribution: it is strongly attenuated in the disk plane, whereas the polar direction is more optically thin. The result is rarified gas being accelerated to high velocity along the polar axis. The highest measured velocity can be over 60 km/s. There is no evidence of Rayleigh-Taylor instability.

Outside of the radiatively-driven bubble, we see gas continuing to fall gravitationally towards the star. This motion is deflected at the bubble wall and we observe gas moving along the bubble walls and onto the accretion disk. Material simply flows along the bubble wall and in this way continues to supply the protostellar disk with matter. We note that the details may depend on opacity effects: while our work uses gray atmospheres, long-wavelength radiation was seen to accelerate matter outside the cavity walls in multifrequency simulations by Kuiper et al. [2010a, 2011a, 2012].

The motion of the star relative to its massive, asymmetric disk results in the star becoming periodically buried in disk material. This has the result of temporarily reducing the direct irradiation of the polar cavities. It is also the likely reason for the formation of successive shells of outward-moving material visible in Figure 3.13. It also contributes to the sometimes asymmetric appearance of the radiatively-driven bubbles, as seen in Figure 3.3 for the 100 $M_\odot$ simulation.

Given the symmetric nature of the initial conditions of the simulation, one might expect the formation of radiatively-driven bubbles with North-South symmetry. The Cartesian grid structure easily introduces small numerical perturbations that break axial symmetry and trigger gravitational instability and spiral wave formation, but these do not explain the breaking of plane symmetry. Pringle [1996] showed analytically that even initially flat disks with a central radiation source are subject to a warping instability caused by radiative torques. Also, small numerical perturbations can also be introduced by the diffusion solver that iterates over grid cells until specific global convergence criteria are met. If the solution is converged, then the current iteration ceases without needing to visit the remaining grid cells. This then breaks North-South symmetry. Eventually, differential shadowing in each hemisphere by material spilling onto the star then results in the asymmetric bubbles as seen in our simulation.

3.4.5 Accretion flows and outflows

Finally, we analyzed the accretion flows in our simulation at various times. To do this, we found it very helpful to create a type of graph profiling the material moving towards or away from our sink particle as a function of the polar angle as measured from the 'north' vector at the location of the star.

We used `yt`'s profiling tools to examine the radial velocity at the location of the sink particle, being careful to subtract the sink particle's own motion from the gas velocity. We then produced an azimuthally-averaged gas velocity profile as a function of polar angle.

We show two examples of this in Figure 3.14, where we look at gas motions around the star formed in our $100\,\mathrm{M}_\odot$ simulation. The first panel shows the state of the simulation after 20.28 kyr. The star's mass is about $8.9\,\mathrm{M}_\odot$. The panel has two inset frames, one showing a representation of gas density, the other the magnitude of the gas velocity, both within an edge-on slice centered on the star. Colorbars have been omitted for the inset frames so as not to overly complicate the figure. We profile the gas motions within a spherical volume, centered on the sink particle, with a radius of 1000 AU. The inset frames show a slice through this volume, i.e. their width of 2000 AU

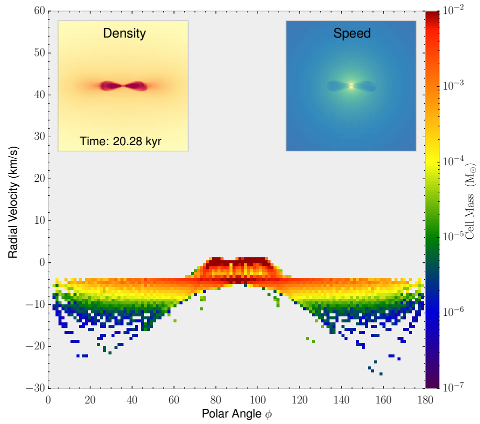

(a) t = 20.28 kyr, $M_* = 8.88\,\mathrm{M}_\odot$

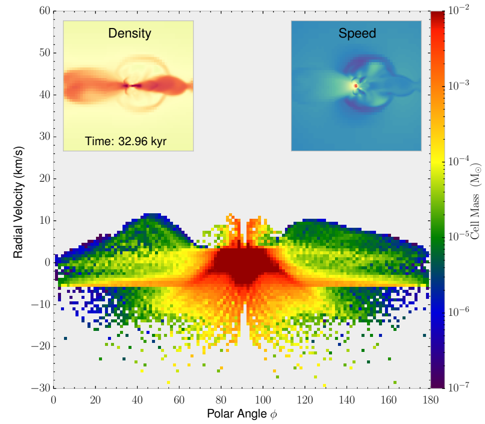

(b) t = 32.96 kyr, $M_* = 21.73\,\mathrm{M}_\odot$

Figure 3.14: Azimuthal accretion and outflow profile at two different times during the $100\,\mathrm{M}_\odot$ simulation within a 1000 AU radius centered on the sink particle. In each of these we measure the azimuthally-averaged radial velocity of the gas relative to the star. This gives a picture of how much gas is moving towards or away from the star as a function of the polar angle. The first panel shows the simulation after the formation of a flared protostellar disk. The disk is even and hasn't yet gone unstable. The second frame shows the state of the simulation after the star has gone super-Eddington and a radiatively-driven bubble has formed. Gas is accelerated to around 10 km/s away from the star in the regions above (20°–70°) and below (110°–160°) the disk.

matches the diameter of the profiling volume.

The main panel has been colored like a two-dimensional histograph, where the color indicates the amount of gas (in units of solar masses) measured at a particular radial velocity and along a particular polar angle, while averaging along the azimuthal angle. In the left panel of Figure 3.14, we see steady inward gas motion across virtually all angles. This can be seen in the horizontal line at $v_r = -4$ km/s. Some of the fastest inward gas motion happens along angles ±30° from the rotation axis. This is seen in the gas components with radial velocities from $v_r = -10$ to -20 km/s.

At a polar angle of $\sim 90°$ (the plane of the protostellar disk) we see a dense gas component with a radial velocity of $v_r \sim 0$ km/s. This is the gas that is within the accretion disk and is orbiting the star in the plane of the disk. We observe that this radially stationary component is spread over a range of angles, from about 75° to about 105°.

Within the disk plane is another velocity component that indicates gas moving inward. At $\phi = 90° \pm 5°$ is some of the highest density gas, moving with a velocity of about $v_r = -4$ km/s. This we understand to be disk accretion. At this time in our $100\,\mathrm{M}_\odot$ simulation, the star's accretion rate is $\dot{M} \approx 3 \times 10^{-4}\,\mathrm{M}_\odot/\mathrm{yr}$.

In the second panel of Figure 3.14, the $100\,\mathrm{M}_\odot$ simulation is shown at a later time, at almost 33 kyr of evolution. The star has grown to about $21.7\,\mathrm{M}_\odot$. The disk has already gone Toomre-unstable and is no longer axisymmetric. Gas orbiting the star inside the accretion disk moves in elliptical orbits and the measured accretion rates onto the particle are much higher ($\dot{M} \approx 1$–$2 \times 10^{-3}\,\mathrm{M}_\odot/\mathrm{yr}$).

The inset frames show the density and gas velocity magnitude in a slice as before. The density slice shows a swept-up shell of material that is being radially driven by the star. It also shows the highly asymmetric accretion disk. The radiatively-driven wind shows up in the angles of 20°–70°, which is the region above the protostellar disk, and 110°–160°, the region below the disk. Some of these outflows reach 12 km/s.

What is also interesting about this panel is that the inward gas motion at all polar angles has accelerated. This is evidenced by the horizontal line at $v_r = -6$ km/s. This is gas outside the radiatively-driven bubble undergoing gravitational infall. Within the plane of the disk, $\phi = 90° \pm 10°$, an enormous amount of gas is seen moving radially inward, mostly with relatively low velocities between 0 km/s and −6 km/s, but some with radial velocities approaching −20 km/s. This is accretion flow in the disk. There is also a gas component that has a positive radial velocity within this spread of polar angles with some gas even reaching 8–10 km/s. We expect that the star's own motion relative to some component of the gas would produce a positive radial velocity. As the fairly massive disk becomes gravitationally unstable, it also becomes asymmetric. Given that at this stage the disk and stellar masses are still comparable (see Figure 3.8), gravitational interactions between star and disk will displace the star from the center. However, we measure the sink particle speed as only about 1 km/s in the frame of the simulation volume. More likely, some gas orbiting the star in an eccentric elliptical orbit reaches a high radial velocity.

Seifried et al. [2015] ran simulations of comparable mass (100 $M_\odot$) protostellar cores without radiation feedback and found that in both cases, provided that there at least some initial turbulence present, accretion onto the star proceeded along a relatively small number of filamentary channels. Figure 3.7 suggests that spiral arms arising from disk instability may aid in focusing accretion along them. This occurs despite not having any initial turbulence in our simulation. Figure 3.14 also suggests that most accretion happens in the plane of the disk.

3.5 Discussion

The purpose of this paper is to use our powerful new hybrid radiative feedback technique introduced in Klassen et al. [2014] to understand massive star formation: (1) how do they accrete so much material, (2) what is the role of the disk, (3) does their radiation feedback shut down accretion, and (4) what is the nature of the radiatively-driven bubbles formed by massive stars once they become super-Eddington. All of these questions depend on having a highly accurate radiative feedback method.

Our hybrid radiative transfer scheme is based on a similar one that Kuiper et al. [2010b] implemented in spherical geometry, also for the study of accretion onto massive stars and their radiative feedback. Our main advance over this scheme is its implementation in a Cartesian geometry with adaptive mesh refinement and its generalization to multiple source terms (stars). We believe that the adoption of hybrid radiative transfer schemes will become more common and it has already been implemented in at least one other AMR code [Ramsey and Dullemond, 2015].

After implementing this method in FLASH , we revisited a problem central to the study of massive stars, but where previous treatments had either left out a treatment of the direct radiation field or were performed in a constrained geometry. The problem focussed on a scaled-up protostellar core with a power-law density profile in slow rigid body rotation. While idealized, it has all the necessary parts to show the role that radiation plays and the relative importance of the disk.

Despite the absence of any initial turbulence, gravitational instabilities within the protostellar accretion disk eventually destroy the symmetry of the gas distribution. Our analysis of the local Toomre Q parameter for the disk shows how gravitational instability is inevitable as the disk becomes more massive. In each of our three main simulations, the disk went gravitationally unstable in the same way, leading to the formation of spiral arms and an increase in the accretion rate by a factor of 2–10.

Had the simulations included initial turbulence, fragmentation might have presented. Observations of giant molecular clouds show supersonic turbulence down to length scales $l > \lambda_s = 0.05$ pc [Ballesteros-Paredes et al., 2007], where λ_s is the sonic scale below which gas motions are subsonic. While supersonic turbulence is essential for providing the density enhancements that result in clumps and cores within GMCs, below the sonic scale subsonic turbulence is less important than thermal pressure in resisting self-gravity and does not contribute to further fragmentation [Padoan, 1995, Vázquez-Semadeni et al., 2003]. High-mass protostellar objects show line widths in NH_3 of about 2.0 km/s [Sridharan et al., 2002], and molecular cores associated with ultracompact HII regions show linewidths of 3.1 km/s [Churchwell et al., 1990]. Turbulence is thus associated with high-mass protostellar cores.

Turbulence will likely have an effect on the morphology of radiatively-driven outflow bubble. In our simulations, these bubbles showed a smooth, round morphology, likely because they were expanding into a medium without any local density enhancements. Had the medium been turbulent, the expanding bubble would have engulfed the filaments. Future simulations will explore the relationship to turbulence and radiatively-driven bubbles.

The formation of massive stars is an interplay between gravity and radiation, though with MHD and turbulence playing comparably important roles. For practical reasons, the gray atmosphere (frequency-averaged) approximation is still often used in numerical simulations of radiative feedback, although this is slowly changing as codes become more sophisticated and supercomputers faster. Presently our code uses the gray approximation for both the direct radiation transfer (ray-tracer) and diffusion (FLD). Compared to frequency-dependent approaches, gray radiative transfer will underestimate the optical depth of UV radiation and overestimate the optical depth of infrared radiation. UV radiation will be absorbed closer to the star and infrared radiation will penetrate deeper into the disk, resulting in warmer midplane temperatures [Kuiper and Klessen, 2013].

With magnetic fields, hydromagnetic outflows occur very early [see Banerjee and Pudritz, 2007, simulations of a hydromagnetic disk wind]. This occurs long before a massive protostellar core even appears. Thus, in the MHD case, the first outflow channel is not created by a radiatively-driven bubble, but by the MHD outflow. This significantly affects bubble evolution in the early phases, and providing an even lower impediment to outflow as studied in Kuiper et al. [2015] using a sub-grid module for early protostellar outflows. At the same time, magnetic fields are known to suppress disk formation and keep them sub-Keplerian [Seifried et al., 2011a, 2012b].

Our simulations do not show the formation of any Rayleigh-Taylor type instabilities in the wall of the radiatively-driven bubble. The bubble continues expanding with the shell sweeping up material and deflecting the gravitational infall of new material. Figure 3.13 shows that material flows along the bubble walls and thus find its way into the accretion disk. Simulations of massive star formation including frequency-dependent irradiation feedback [Kuiper et al., 2010a, 2011a, 2012] show that the mass on top of the cavity wall can already be accelerated into an outflow by the long-wavelength radiation of the stellar spectrum. As the bubble expands, its shell is pushed into regions of lower resolution. We therefore rule out radiative Rayleigh-Taylor instability contributing to disk accretion or direct accretion onto the star.

As a caveat on our simulation, our grid refinement was set using a Jeans length criterion, which resulted in high-density regions being highly refined, and saving the computational cost elsewhere. This, however, meant that as radiatively-driven bubbles expanded, they were not always resolved at the highest level. It is conceivable that the lower resolution suppressed the formation of Rayleigh-Taylor instabilities in the bubble wall. Krumholz et al. [2009] also had no refinement criteria that focussed explicitly on bubble walls, although they do refine any grid cell where the gradient in the radiation energy density exceeds a 15% relative value. We are investigating approaches to selectively enhancing the resolution of the bubble wall. Nevertheless, given the fact that the net gas acceleration at the bubble wall is often outward or null, and that momentum appears to be carrying on the expansion even when acceleration is null, we conclude that radiative Rayleigh-Taylor instabilities do not form in the types of environments simulated in this paper.

While radiation pressure may play the dominant role in regulating star formation by disrupting GMCs [Murray et al., 2010], other important feedback mechanisms are also present and have been left out of the simulations presented in this paper. The other main ways that massive stars disrupt their environments is through the formation of HII regions and jets.

HII regions are formed around protostars when the flux of UV photons from the star becomes great enough that a bubble of ionized hydrogen forms. These expanding regions of hot (10^4 K), ionized gas are formed around massive stars. Their impact has been studied in various numerical simulations [Peters et al., 2010a, Dale et al., 2014, Walch et al., 2015], which show that they do not halt accretion onto massive stars, but may act together with stellar winds to reduce the final star formation efficiency. We chose to study radiatively-driven outflows in isolation, but have simulated ionizing feedback in the past [Klassen et al., 2012b,a]. Ionizing radiation has not yet been fully tested in the most recent version of the FLASH code, but forthcoming simulations will include ionization feedback and we anticipate that the added thermal pressure would accelerate bubble expansion, though leakage would occur in turbulent environments. The extremely high accretion rates would initially confine any HII region to the star's immediate vicinity. As optically thin voids form inside the radiatively-driven bubbles, the extreme UV radiation from the massive star would ionize this gas. In our simulations, the sloshing of the high mass disk around the star, as well as the high accretion rates mean that the ionizing radiation is still relatively trapped and the circumstellar disk is not at risk of being photoevaporated (and thus limiting the final mass of the star).

Newly formed protostars and their protostellar disks launch powerful jets and outflows that can carry a significant amount of mass and momentum. Observations show that even low-mass stars launch jets [Dunham et al., 2014]. The launching mechanism for these jets is magnetic in nature [Blandford and Payne, 1982, Pudritz and Norman, 1983, Lynden-Bell, 2003, Banerjee and Pudritz, 2006, Pudritz et al., 2007a], but can be difficult to resolve in simulations of GMC evolution. Subgrid feedback models have been developed that show that jets can reduce the average star mass by a factor of ~ 3 [Federrath et al., 2014]. The removal of stellar material limits the efficiency of star formation and influences the initial mass function, with HII regions inflated by radiation pressure predominating in clusters of massive protostars [Fall et al., 2010].

The launching of jets is fundamentally a magnetic phenomenon and magnetic fields alter the star formation process in important ways that we have not captured in this paper. Magnetic fields suppress star formation through added magnetic pressure support and radiation-magnetohydrodynamic simulations show that magnetic braking of protostellar disks increases radial infall and the accretion luminosity [Commerçon et al., 2011a]. The addition of even subsonic turbulence, however, greatly reduces the magnetic braking efficiency [Seifried et al., 2015].

Our results give an interesting twist to the idea that the accretion of massive stars may be limited by the formation of secondary stars in their gravitationally unstable accretion flows, the so-called fragmentation-induced starvation scenario [Peters et al., 2010a,d,c, 2011]. These models naturally explain that massive stars tend to form in clusters [Peters et al., 2010a], the observed clustering and number statistics of ultracompact H II regions [Peters et al., 2010d] as well as characteristic properties of poorly collimated high-mass outflows [Peters et al., 2014]. This work is based on larger-scale models compared to our present simulations, with a simulation box of several pc size, a 1000 $M_\odot$ initial core, and 98 AU grid resolution. Most importantly, the assumed initial condition is optically thin in the infrared, and the highly optically thick accretion flow around high-mass stars is beyond their resolution limit. Therefore, the radiative heating in these simulations could be treated using raytracing, which gave comparable results to a more accurate Monte Carlo computation [Peters et al., 2010c]. Peters et al. [2011] speculated that the gravitational fragmentation seen in their radiation-magnetohydrodynamical simulations might continue down to smaller scales, based on the observation that massive stars form with accretion rates of the order $10^{-3}\,M_\odot/\mathrm{yr}$, which requires non-Keplerian disks. Our present simulations show that this is indeed the case. However, this gravitational instability does apparently not lead to the formation of companion stars on the smallest scales, so that fragmentation-induced starvation only occurs on scales larger than the disk scale. Future simulations run from different initial conditions will shed further light on this issue.

3.6 Conclusion

Numerical simulations of star formation is a truly rich field with many outstanding challenges. Attempting to capture all of the relevant physical processes and assess their relative importance is an ongoing process, and here we simulate some of the most important physical mechanisms that come into play to affect massive star formation.

We have made important strides in improving existing radiation feedback codes and implementing them in a magnetohydrodynamics code with adaptive mesh refinement, building on the work done by many other authors and collaborators. Klassen et al. [2014] introduced our hybrid radiative feedback method, blending together the accuracy of a raytracer with the efficiency of a flux-limited diffusion method, as in Kuiper et al. [2010b] but in a more general 3D Cartesian geometry.

In this paper we have made a major new advance in the study of massive star formation by using this new tool. By simulating protostellar cores of different masses ($30\,\mathrm{M}_\odot$, $100\,\mathrm{M}_\odot$, $200\,\mathrm{M}_\odot$), we showed that even stars with masses over $40\,\mathrm{M}_\odot$ may continue to accrete despite their high luminosity. Through radiation pressure they succeed in driving expanding bubbles that sweep up material and possibly channel gas over their shells back onto the disk. Over the time periods and at the resolution limits we tested, these shells do not show any signs of breaking apart or becoming unstable, but this may still change with the introduction of turbulence and greater resolution in future simulations.

The results presented in this paper are in excellent agreement with recent observations of massive, embedded protostars [Beltran and de Wit, 2015, Johnston et al., 2015], which show the presence of Keplerian accretion disks of similar radius and mass to what we measure in our simulations. In particular, ALMA observations of AFGL 4176 by Johnston et al. [2015], which show a 25 $M_\odot$ forming O7-type star surrounded by a 12 $M_\odot$ Keplerian-like disk, strongly resemble the results of our 100 $M_\odot$ simulation.

Protostellar disks grow rapidly and become Toomre unstable. These instabilities do not result in further star formation, but instead form spiral arms and an assymetric disk that channels material onto the star at rates 2–10 times faster than before. The disk mass begins to level out at around this same time while the stellar mass continues to grow.

We now summarize the results of our investigation as follows:

- Each of our three simulated massive protostellar cores produced only a single star, despite a Toomre analysis showing their circumstellar disks to be unstable.

- After 81.4 kyr of evolution, our 30 $M_\odot$ simulation showed a star with a mass of 5.48 $M_\odot$, while our 100 $M_\odot$ simulation formed a 28.84 $M_\odot$ mass star and our 200 $M_\odot$ simulation formed a 43.65 $M_\odot$ star. The latter two were about 30 and 100 times super-Eddington in their luminosity, respectively, and drove powerful winds occassionally achieving speeds of greater than 50 km/s.

- Despite becoming locally Toomre Q unstable and forming spiral arms, the accretion disks do not fragment gravitationally to form more stars, at least for the duration of our simulations. We use the Hill criterion analysis of Rogers and Wadsley [2012] to show that these spiral arms are still stable against fragmentation. We also find that the combined

Gammie [2001] and Toomre conditions for fragmentation predict fragmentation of the disk to potentially form a binary companion at ~ 1200 AU radius, but this has not (at least, yet) occurred.

- Accretion onto massive protostars occurs very efficiently through a protostellar disk, despite an extremely high flux of photons. Towards the ends of our simulations, accretion rates were about $5 \times 10^{-5}\,\mathrm{M}_{\odot}/\mathrm{yr}$, $6 \times 10^{-4}\,\mathrm{M}_{\odot}/\mathrm{yr}$, and $1.5 \times 10^{-3}\,\mathrm{M}_{\odot}/\mathrm{yr}$ for the 30, 100, and 200 $\mathrm{M}_{\odot}$ simulations, respectively. These showed no signs of slowing down significantly and we speculate that our stars could have gone on to accrete a significant fraction of the total core mass.

- Optically-thick circumstellar disks are responsible for the flashlight effect, i.e. the channeling of flux along the polar axis and into the polar cavities. Dust sublimation reduces the optical depth, but also allows radiation to more easily escape into the polar cavities.

- After the stars luminosities exceeded the Eddington limit, they drove radiative bubbles, sometimes in successive shells that could appear pierced by stellar winds.

- Material was observed flowing along the outer shell of these bubbles back onto the circumstellar disk, but the outer shell itself did not show signs of a Rayleigh-Taylor instability. Net gas acceleration at the bubble wall is outward or close to zero. We conclude that radiative Rayleigh-Taylor instabilities do not form in the types of environments simulated in this paper.

Future simulations will explore the effects of turbulence, ionizing feedback, and magnetic fields, each of which contributes to the star formation efficiency and cloud lifetime in important ways. Although our model is idealized, it allows us to investigate several key processes in great detail that would have been difficult to tease apart if more physics had been included in our model. The way forward will be to look at each in turn.

Acknowledgments

We thank the referee for providing a very useful report that helped improve the paper. The development of this hybrid radiation transfer code benefited from helpful discussions with Romain Teyssier, Christoph Federrath, Klaus Weide, and Petros Tzeferacos, and from two visits by M.K. to the FLASH Center at the University of Chicago. We also thank Henrik Beuther, Thomas Henning, and Ralf Klessen for interesting discussions about observations and theory. Manos Chatzopoulos supplied the modified unsplit hydrodynamics solver that improved the accuracy of our simulations. M.K. acknowledges financial support from the National Sciences and Engineering Research Council (NSERC) of Canada through a Postgraduate Scholarship. R.E.P. is supported by an NSERC Discovery Grant. R.K. acknowledges financial support by the Emmy-Noether-Program of the German Research Foundation (DFG) under grant no. KU 2849/3-1. T.P. acknowledges support from the DFG Priority Program 1573 *Physics of the Interstellar Medium*. The FLASH code was in part developed by the DOE-supported Alliances Center for Astrophysical Thermonuclear Flashes (ASCI) at the University of Chicago[1]. This work was made possible by the facilities of the Shared Hierarchical Academic Research

[1]http://flash.uchicago.edu/

Computing Network (SHARCNET: www.sharcnet.ca), SciNet at the University of Toronto, and Compute/Calcul Canada.

We are grateful to KITP, Santa Barbara, for supporting M.K. as an affiliate (for 3 weeks), R.E.P. as an invited participant (for 2.5 months), and R.K. as an invited participant (1 week) in the program "Gravity's Loyal Opposition: The Physics of Star Formation Feedback," where some of this research was supported by the National Science Foundation under Grant No. NSF PHY11-25915. R.E.P. also thanks the MPIA and the Institut für Theoretische Astrophysik (ITA) in the Zentrum für Astronomie Heidelberg for support during his sabbatical leave (2015/16) during the final stages of this project.

Much of the analysis and data visualization was performed using the `yt` toolkit[2] by Turk et al. [2011].

[2] http://yt-project.org

Chapter 4

Filamentary Flow and Magnetic Geometry in Evolving Cluster-Forming Molecular Cloud Clumps

4.1 Introduction

Observations of nearby molecular clouds obtained with the *Herschel Space Observatory* [Pilbratt et al., 2010] have shown them to be highly filamentary, with filaments being the clear sites for star formation [André et al., 2010, Könyves et al., 2010, Henning et al., 2010, Men'shchikov et al., 2010, Hill et al., 2011, Polychroni et al., 2013, André et al., 2014] and the intersections of filaments the sites of clustered and massive star formation [Schneider et al., 2012, Peretto et al., 2013]. Myers [2009] also showed that star clusters form within "hubs", with multiple parsec-length filaments radiating from them like spokes. Star formation on a galactic scale is very inefficient, and so efforts to understand it have focussed on the physics of molecular clouds, which are now being imaged with unprecedented resolution. Older observations see gradients along the long axis of a filament [e.g. Bally et al., 1987, Schneider et al., 2010], while a few new observations, such as from CLASSy [Storm et al., 2014], are high enough resolution to see velocity gradients *across* filaments [Fernández-López et al., 2014].

Beuther et al. [2015b] recently imaged a massive filamentary infrared dark cloud (IRDC 18223), observed in 3.2mm continuum and in molecular line data. This massive filament has a line mass of about 1000 $M_\odot$/pc. Along its length, 12 massive cores have formed with approximately even spacing. This extremely high line mass and fragmentation pattern requires additional support, either in the form of supersonic turbulence or magnetic fields. Line data suggests a kinematic origin of this filament, suggesting that large-scale flows or rotation might have played a role.

The relevance of magnetic fields to the star formation process is already well established [McKee and Ostriker, 2007b, Crutcher, 2012, Li et al., 2014], but direct measurement of magnetic fields remains difficult. One of the best-studied regions of star formation is the Taurus molecular cloud. Molecular line observations of ^{12}CO show striations aligned with the local magnetic field [Heyer et al., 2008] as traced by background starlight polarization. This observation is also confirmed by Palmeirim et al. [2013], who suggest that material may be accretion along these striations and onto the larger B211 filament. Planck Collaboration XXXIII [2016] also confirm that magnetic fields effect filament formation, based on observations of polarized dust emission in the Taurus and Musca clouds.

Optical, infrared, and submillimetre polarisation measurements, depending on the gas density, remain the best way of mapping the plane-of-sky magnetic field orientation. Optical properties are seen in absorption, whereas regions of higher extinction are best probed in the infrared. Non-spherical dust grains to align their long axis perpendicular to the ambient magnetic field [Lazarian, 2007, Hoang and Lazarian, 2008]. Starlight in the optical regime linearly polarized parellel to the long axis of the grains is absorbed, while the grains themselves emit infrared radiation. Thus, infrared light is polarized perpendicular to the magnetic field [Hildebrand et al., 1984, Novak et al., 1997, Vaillancourt, 2007], while optical light is polarized parallel to the magnetic field [Davis and Greenstein, 1951, Hildebrand, 1988, Heiles and Haverkorn, 2012]. Polarization of submillimetre radiation is produced by thermal dust emission by aligned grains and is also oriented perpendicular to the magnetic field [Alves et al., 2014]. This allows for the measurement of magnetic field orientations.

The orientation of magnetic fields relative to the filaments in star-forming regions is of dynamical importance. One of the proposed mechanisms for the interaction between magnetic fields and filaments is that magnetic fields could channel material along the field line orientation, allowing filaments to form by gravitational contraction [Nakamura and Li, 2008]. Low density filaments or striations should be oriented parallel to magnetic fields, channeling material onto the larger filaments [cf. Cho and Vishniac, 2000, Cho and Lazarian, 2002, Vestuto et al., 2003, Li et al., 2008].

On galactic scales, the recent publication of the Planck polarization data [Planck Collaboration XXXV, 2016] shows that galactic magnetic fields have a strong tendency to be parallel to diffuse filamentary clouds with column densities below $N_H \approx 10^{21.7}$ cm^{-2}, and perpendicular to dense filaments of higher column density.

Li et al. [2013] examined the orientation of the filamentary giant molecular clouds of the Gould Belt ($N_H \sim 2 \times 10^{21}$–$2 \times 10^{22}$ cm^{-2}) relative to the magnetic fields of the intercloud medium (ICM) and found a bimodal distribution. Most clouds are oriented either perpendicular or parallel to ICM B-fields, with offsets typically less than 20 degrees. This strongly suggests the dynamical importance of magnetic fields in the formation of filaments. The physical scales observed in Li et al. [2013] were generally a few parsecs to a few tens of parsecs, up to an order of magnitude larger than our clump-scale simulations. The alignment of the large-scale magnetic field with the large-scale structure of the cloud was studied, showing a bimodal distribution with peaks near parallel and perpendicular relative orientation.

Given that the magnetic field energy dominates the gravity and thermal energy in the diffuse ISM, these results clearly point to the fact in diffuse gas, magnetic fields directs infall along them, resulting in the creation of dense, self-gravitating filaments oriented perpendicular to the field on impact. Field aligned flow of the more diffuse ISM arising from galactic scale, Parker instabilities can readily create the dense molecular filaments as it falls back towards the galactic plane [Gomez de Castro and Pudritz, 1992].

Magnetic fields may also play a role in the stability of filaments. Virial analysis by Fiege and Pudritz [2000] showed that, depending on orientation, magnetic fields may work to stabilize filaments against gravitational collapse or have the opposite effect. Toroidal fields assist gravity in squeezing filaments, while the poloidal fields threading filaments offer a magnetic pressure support against gravity.

Our research has focused on comparing numerical simulations of magnetized molecular cloud clumps to observations, with the aim of better understanding the co-evolution of the magnetic fields, filamentary structure, and star formation. We have examined scales on the order of a few parsec, far smaller than the Gould Belt clouds examined in Li et al. [2013], but on the same physical scales as the Serpens South cloud [e.g. Sugitani et al., 2011, Kirk et al., 2013] and the Taurus B211 filament [Palmeirim et al., 2013].

In Kirk, Klassen, Pudritz, and Pillsworth [2015] [henceforth simply Kirk et al., 2015], we examined the structure of magnetized and unmagnetized filaments via numerical simulations, showing that simulated filaments have properties consistent with observed filaments, specifically the radial column density profiles, with similar shapes and extents to those observed. Magnetic fields can offer pressure support to filaments, and were observed to be somewhat "puffier" than their unmagnetized counterparts. Turbulence was also observed to play a critical role in supporting the filament against collapse, consistent with the observations by Beuther et al. [2015b] of the massive, turbulent filament. This paper is the follow-on and extension of the investigations into simulated filaments begun in Kirk et al. [2015].

Magnetohydrodynamic (MHD) simulations provide an experimental laboratory for studying the evolution of the turbulent ISM within a magnetic field. Diego Soler et al. [2013] examined the relative orientations of density gradients and magnetic fields in 3D MHD simulations with decaying turbulence. Isodensity contours serve to trace filaments in this technique. Here too, filaments were seen to lie parallel to magnetic field lines at low densities, but switch to perpendicular in high density regions. This effect was more pronounced in simulations with high magnetisation.

Characterizing the relative energies of turbulence and magnetic fields is the turbulent Alfvén Mach number,

$$\mathcal{M}_A = (\beta/2)^{1/2}\,\mathcal{M} = \frac{\sigma}{v_A}, \tag{4.1}$$

where $\beta = 8\pi\rho\sigma^2/\langle B^2\rangle = 2\sigma^2/v_A^2$ is the plasma beta, which describes the ratio of thermal pressure to magnetic pressure. σ and $v_A = B/\sqrt{4\pi\rho}$ are the 1D velocity dispersion and the Alfvén speed, respectively. The latter is the characteristic speed of a transverse magnetohydrodynamic wave. Because we are dealing with supersonic turbulence, if makes more sense to use the velocity dispersion, rather than the sound speed to characterize the gas motion. $\mathcal{M} = v/c_s$ is the thermal Mach number of the turbulence, where v is the gas speed. If the turbulence is sub-Alfvnic ($\mathcal{M}_A < 1$) and turbulent pressure is high enough, the filament appears elongated in the direction of the magnetic field. If not, gravity draws material along B-fields to form a filament with a perpendicular orientation. If the turbulence is super-Alfvénic ($\mathcal{M}_A > 1$), then magnetic fields are not dynamically important and turbulence can compress gas in any direction to form filaments regardless of the large-scale orientation of intercloud magnetic fields. Molecular clouds are observed to possess Alfvén Mach numbers of order unity [Crutcher, 1999] and this is where we situate our own simulations.

Falceta-Gonçalves et al. [2008] performed MHD simulations with varying degrees of turbulence. They examined sub-Alfvénic ($\mathcal{M}_A = 0.7$) and super-Alfvénic ($\mathcal{M}_A = 2.0$) cases. Field lines were ordered in the sub-Alfvénic case, but observed to be random in the super-Alfvénic case. They did not examine a transitional case near $\mathcal{M}_A \sim 1$. These cases are highly relevant because many molecular clouds are observed to have Alfvén Mach number close to unity [Crutcher, 1999]. In this paper, we investigate these trans-Alfvénic cases.

We perform numerical simulations of rotating, magnetised, turbulent molecular cloud clumps. The large-scale modes of the supersonic turbulence create a primary filamentary structure, which we term the "trunk". The simulations also show many secondary filamentary structures consisting of more diffuse gas, some of these appearing as off-shoots from the main trunk. Our two simulations have similar initial conditions, but differ primarily in two aspects: total mass and virial parameter. The latter of these, the virial parameter, measures the boundedness of the cloud clump and turns out to be crucial in understanding the magnetic field structure. The more massive of the two simulations is highly bound, and gravitational infall of material drags magnetic fields into coherent large-scale patterns. Meanwhile, the cloud in virial balance, i.e. where the kinetic energy balances the gravitational binding energy, shows no such large-scale ordering of the magnetic field. The supersonic and trans-Alfvénic turbulence has enough energy to create disorder in the magnetic field geometry.

On the very largest scales, i.e. the scale of entire simulated volume ($\sim$ 2–4 pc), we find that the molecular cloud clump does show some weak alignment patterns similar to observations on somewhat larger scales in Li et al. [2013], i.e. that gas above a certain density shows a weak bimodal distribution tending towards either parallel or perpendicular alignment with the overall structure of the molecular cloud, although the Gould Belt clouds studied in Li et al. [2013] are physically larger (10s-of-parsecs), but of comparable density ($N_H \sim 5 \times 10^{21}$ cm^{-2}). This effect is most prominent in the more massive and more gravitationally bound simulation.

We then apply a filament-finding algorithm and measure the B-field orientation local to the filaments in 3D, as well as other variables of interest, such as density or velocity. This allows a view of what is happening along the filaments. Supersonic turbulence, as usual, rapidly creates a network of filaments and voids and because of its trans-Alvfénic nature, the ordered initial (vertical) field is gradually disordered with time. In the strongly bound cloud model, we see magnetic fields aligning with the filamentary structure, especially at higher gas densities. Inside the virialized cloud, by contrast, the magnetic field is more randomly aligned relative to the filamentary structure. In the massive, highly bound (subvirial) scenario, the velocity field in the densest gas is both collapsing onto the filament as well as flowing along the main (cluster forming) filament, the latter flow dragging the magnetic field with it into parallel alignment.

Finally, feedback from massive stars resulting in the formation of HII regions creates blisters inside these molecular cloud clumps. In the more massive (subvirial) of our two simulations, we include star formation and the effects of photoionizing radiative feedback. A cluster of 7 stars is formed along the main trunk filament. One star grows to reach $16\,\mathrm{M}_\odot$ and its luminosity comes to dominate all the rest. It forms an HII region that eventually engulfs the entire cluster and begins to eat away at the filament. We observe that the expanding HII region sweep up a shell of gas that appears threaded with magnetic field lines.

In the following sections we first describe our numerical methods (Section 4.2), lay out our results for filamentary and magnetic structure during early cloud evolution (Section 4.3), analyze the effects of radiative feedback

Table 4.1: Simulation parameters

Parameter			MHD500	MHD1200
Physical simulation parameters				
cloud radius	[pc]	R_0	1.00	1.94
total cloud mass	[$M_\odot$]	$M_{\rm tot}$	502.6	1209.2
mean mass density	[g/cm^3]	$\bar{\rho}$	4.26e-21	1.39e-21
mean number density	[cm^{-3}]	$\bar{n}$	1188.98	388.841
mean initial column density	[g/cm^{-2}]	$\bar{\Sigma}$	0.0262	0.0167
mean initial column (number) density	[cm^{-2}]		7.33×10^{21}	4.66×10^{21}
mean molecular weight		μ	2.14	2.14
initial temperature	[K]	T	10.0	10.0
sound speed	[km/s]	$c_{\rm s}$	0.19	0.19
1D velocity dispersion	[km/s]	$\sigma_{\rm 1D}$	0.64	0.55
rms Mach number		$\mathcal{M}_{\rm RMS}$	6.0	6.0
mean Mach number		$\mathcal{M}$	4.36	3.71
mean freefall time	[Myr]	$t_{\rm ff}$	1.02	1.78
sound crossing time	[Myr]	$t_{\rm sc}$	10.4	20.2
turbulent crossing time	[Myr]	$t_{\rm tc}$	1.73	3.36
magnetic field flux density	[μG]	Φ	28.5	15.0
Alfvén speed	[km/s]	v_A	1.23	1.13
Alfvén Mach number		$\mathcal{M}_A$	0.92	0.99
mass-to-flux ratio		λ	2.33	2.82
virial parameter		$\alpha_{\rm vir}$	0.95	0.56
angular rotation frequency	[s^{-1}]	$\Omega_{\rm rot}$	1.114×10^{-14}	1.114×10^{-14}
rotational energy fraction		$\beta_{\rm rot}$	1.0 %	3.2 %
critical thermal line mass	[$M_\odot$/pc]	$M_{\rm line}^{\rm crit}$	30.1	35.4
critical turbulent line mass	[$M_\odot$/pc]	$M_{\rm line}^{\rm crit}$	190.5	138.5
Numerical simulation parameters				
simulation box size	[pc]	$L_{\rm box}$	2.0	3.89
smallest cell size	[AU]	Δx	50.35	391.68
Simulation outcomes				
final simulation time	[kyr]	$t_{\rm final}$	161.3 kyr	326.4

during later cloud evolution (Section 4.4), and then discuss our results (Section 4.5).

4.2 Numerical methods

We explore the relationship between the structure of molecular gas inside cloud clumps and the presence of magnetic fields through numerical simulation. MHD simulations, initialized with a turbulent velocity field, allow us to explore the three-dimensional structure of turbulence and filaments. Projections can then be made of this three-dimensional data to produce column density maps for closer comparison to astronomical observations.

Through the application of structure-mapping algorithms, we can extract the (2D or 3D) filamentary networks evident in the simulation data (from column or volume density). Once the filamentary structure is mapped, we can compare local magnetic field orientation to study how orientation might be related filament characteristics.

The analysis of *Herschel* results has seen the widespread application of image analysis algorithms for filament detection. These include the *getfilaments* algorithm by Men'shchikov [2013] and DisPerSE [1] [Sousbie, 2011, Sousbie et al., 2011].

We opted to use DisPerSE , which maps out the topological features in an image or datacube, such as peaks, voids, or filaments. It has the advantage of being applicable also to 3D data cubes built from our simulation data. Previously, DisPerSE had seen wide use for analysis of *Herschel* observations [e.g. Arzoumanian et al., 2011, Peretto et al., 2012, Hennemann et al., 2012, Schneider et al., 2012], but we used it in a new way—on 3D star formation simulation data for examining the 3D structure of molecular gas filaments. This is in contrast to analyzing filaments solely in projection and is one of the first times this has been done in 3D for studies of filaments inside molecular clouds [see Smith et al., 2014, for another example].

4.2.1 Numerical simulations

We perform numerical magnetohydrodynamic simulations using the FLASH AMR code [Fryxell et al., 2000b] in its version 2.5. It makes use of the PARAMESH library to solve the fluid equations on an adaptive Eulerian grid

[1] http://www2.iap.fr/users/sousbie/

[Olson et al., 1999, MacNeice et al., 2000]. The code has been expanded to include Lagrangian sink particles [Banerjee et al., 2009, Federrath et al., 2010b], radiative heating and ionization feedback [Rijkhorst et al., 2006b, Peters et al., 2010b], and self-consistent protostellar evolution [Klassen et al., 2012b].

4.2.2 Initial conditions

We performed numerical simulations, which we label `MHD500` and `MHD1200`, of two molecular clouds at different scales, one (`MHD500`) more compact and close to virial equilibrium ($\alpha_{\rm vir} = 0.95$), with approximately $500\,\mathrm{M}_\odot$ of material in a volume of side length 2.0 pc, and the second (`MHD1200`) containing about $1200\,\mathrm{M}_\odot$ of material in a volume of side length 3.89 pc and considerably more subvirial ($\alpha_{\rm vir} = 0.56$). These molecular clouds have column densities similar to those observed for Gould Belt clouds. The column density of the `MHD500` cloud has an average value of $N_H = 7.33 \times 10^{21}$ cm^{-2} and a peak value of $N_H = 3.4 \times 10^{23}$ cm^{-2} at the start of the simulation. The `MHD1200` cloud has an average column density of $N_H = 4.66 \times 10^{21}$ cm^{-2} and a peak value of $N_H = 2.13 \times 10^{23}$ cm^{-2} at the start of the simulation. Comparing to Figure 7 from Li et al. [2013], we see that the average value of the column densities and the magnetic fields correspond to Gould Belt clouds, while the peak column densities correspond to cloud cores.

The initial conditions are very similar to those we performed for Kirk et al. [2015] and the `MHD500` simulation is the same in both papers. Previously, we examined filaments properties, comparing purely hydrodynamic simulations with MHD simulations. In this paper, we focus on magnetized molecular cloud clumps, and include a simulation (`MHD1200`) that has star formation and photoionizing feedback in order to study the effect this form of radiative feedback has on filamentary structure and the magnetic field orientation. In Kirk et al. [2015] we did not include radiative feedback as part of our study.

Molecular clouds are observed to have non-thermal linewidths attributed supersonic turbulence [Larson, 1981, 2003]. We initialize our simulations with a turbulent velocity field that is a mixture of compressive and solenoidal modes with a Burgers spectrum, $E_k \propto k^{-2}$ [Federrath et al., 2008, Girichidis et al., 2011b]. Kolmogorov turbulence ($E_k \propto k^{-5/3}$) would be expected for incompressible fluids. The largest modes in our simulations have characteristic size scales on the order of box width (3.89 pc and 2 pc, for our `MHD1200` and `MHD500` simulations, respectively). See also Larson [1981], Boldyrev [2002], Heyer and Brunt [2004]. The turbulent velocities represent only an initial condition, and are allowed to decay. We do not continuously drive turbulence during the simulation, which would be an artificial injection of energy. We use the same turbulent initial velocity field for both simulations so that the structures arising from the turbulence will be similar. The root-mean-square (RMS) velocity and Mach number of each simulation is the same, and we initialized the simulations with root-mean-square velocities equal to 6 times the isothermal sound speed, but the mass-weighted average Mach number between our two simulations differs (see Table 4.1).

Observations of dense molecular cloud cores forming high-mass stars show column density profiles consistent with power laws [Pirogov, 2009]. Hence, we initialize our simulations with density profiles of the form $\rho(r) \propto r^{-3/2}$. We simulated two different initial conditions, looking at a high mass case (1200 $M_\odot$) and a low mass case (500 $M_\odot$). The low-mass simulation was run without any radiative feedback, whereas in our high-mass simulation we allowed stars to influence their environments via ionizing feedback.

Observations of molecular cloud cores with sizes in the range of 0.3–2.1 pc and masses up to several thousand $M_{\odot}$ show velocity gradients consistent with a ratio of rotational to gravitational energy, $\beta_{\mathrm{rot}} \lesssim 7\%$ [Pirogov et al., 2003]. Numerical simulations of molecular clouds are sometimes initialized in rigid body rotation a low β_{rot} [e.g. Peters et al., 2010c].

Our molecular cloud clumps are initialized in slow rigid body rotation about the z-axis. The rotation rate is set to $\Omega = 1.114 \times 10^{-14}\ \mathrm{s}^{-1}$ in both cases, which corresponds to a ratio of rotational kinetic to gravitational binding energy, β_{rot} of 1% in the `MHD500` simulation and 3.2% in the `MHD1200` simulation.

We quantify magnetic field strengths via a mass-to-flux ratio, normalized against a critical mass-to-flux ratio:

$$\lambda = \frac{M/\Phi}{(M/\Phi)_{\mathrm{crit}}} \tag{4.2}$$

Crutcher et al. [2010] finds molecular clouds to typically have magnetic field strengths such that $\lambda \sim 2$–3, so we initialize our simulations with the values in this range. The mass-to-flux ratio quantifies the dynamical importance of the magnetic field relative to gravity. The critical mass-to-flux ratio ($\lambda_{\mathrm{crit}} \sim 0.13/\sqrt{G}$) is the value needed for gravitational energy to be balanced by the magnetic energy [Mouschovias and Spitzer, 1976]. For massive star forming regions, $\lambda \lesssim 5$ [Falgarone et al., 2008, Girart et al., 2009, Beuther et al., 2010b].

The magnetic field is initially uniform at aligned parallel to the z-axis.

Using equation 4.1, we calculate the RMS Alfvén Mach number of each simulation, an important measure into whether the magnetic fields will dominate the turbulence. The `MHD500` cloud has an RMS Alfvén Mach number of 0.92, while the `MHD1200` cloud has an RMS Alfvén Mach number of 0.99, i.e. both clouds have Alfvén Mach number very close to unity and are essentially trans-Alfvénic, meaning they are in the regime where turbulence threatens to destroy any orderly magnetic field structure the cloud may have inherited from the inter-cluster medium (ICM). This regime is of interest because most clouds have Alfvén Mach numbers close to unity Crutcher [1999].

Finally, we compare the kinetic energy to the gravitational energy by calculating the virial parameter [Bertoldi and McKee, 1992] for each of our clouds. The virial parameter,

$$\alpha_{\rm vir} = \frac{2\mathcal{T}}{|\mathcal{W}|} \approx \frac{5\sigma^2 R}{GM}, \tag{4.3}$$

measures the boundedness of the clouds. Most clouds have virial parameters of $\alpha_{\rm vir} = 0.5$–5 [see Figure 6, Rosolowsky, 2007] and a cloud with $\alpha_{\rm vir} < 1$ is expected to collapse gravitationally, while clouds with $\alpha_{\rm vir} \approx 1$ are marginally stable against collapse. In Equation 4.3, R is the radius of the cloud, G is Newton's constant, M is the mass of the cloud, and σ is the velocity dispersion, usually measured from line width observations. We find the one-dimensional velocity dispersion by taking the mass-weighted average velocity in our simulation,

$$\sigma = \left(\frac{\int \rho(\boldsymbol{r}) |\boldsymbol{v}(\boldsymbol{r})|^2 dV}{3 \int \rho(\boldsymbol{r}) dV} \right)^{1/2}, \tag{4.4}$$

where the number 3 in the denominator is the geometrical factor accounting for the number of dimensions. The virial parameter of the `MHD500` simulation is 0.95, i.e. marginally bound, while the `MHD1200` is substantially sub-virial at $\alpha_{\mathrm{vir}} = 0.56$.

We provide a summary of our simulation parameters in Table 4.1.

4.2.3 Filament-finding

Filamentary structure results from collisions between supersonic shocks [review; Mac Low and Klessen, 2004, Schneider et al., 2011, Pudritz and Kevlahan, 2013]. Once the simulations are sufficiently evolved, filamentary structure is well developed. This always preceeds any star formation within the cloud clump. We took the evolved simulation output for our filaments analysis.

Identifying filamentary structure is challenging, and a variety of techniques have been developed for this task. One of the most straightforward approaches is based on structure-characterisation. Hennebelle [2013] set characteristic density thresholds for molecular clumps. Filaments represented elongated clumps. In Planck Collaboration XXXII [2016], a Hessian matrix is defined for every pixel of the dust intensity map. By solving for the eigenvalues of this matrix, the local curvature is defined and filamentary structure can be extracted. The authors then construct a mask based on the intensity contrast relative to the background dust map, curvature, and the signal-to-noise of the polarization fraction. This selects the most significant ridge-like structures in the all-sky *Planck* map.

In Planck Collaboration XXXIII [2016], the Musca, and Taurus B211 and L1506 filaments are analyzed. Their physical scales are 2–10 pc and were resolved with $4.'6$ angular resolution, which corresponds to a scale of 0.3 pc and

0.2 pc and the distances of Musca (200 pc) and Taurus (140 pc) respectively. This is much larger than our simulated grid resolution ($\Delta x \approx 50$ AU and 400 AU, for our `MHD500` and `MHD1200` simulations, respectively). These filaments in Musca and Taurus appear clearly in the dust intensity and polarization maps. DisPerSE is applied to identify the filament ridges. Magnetic fields are seen to be ordered with low dispersion of the polarization angle around filaments, suggesting the dynamical importance of magnetic fields.

Another approach is the "histogram of relative orientations" (HRO) developed by Diego Soler et al. [2013], which is based on a computer vision algorithm called the Histogram of Oriented Gradients. Gradients in either the volume density or column density are used to indicate filaments, as filaments must lie perpendicular to the gradient vector. The relative angle between the gradient and the magnetic field orientation may then be used as a proxy for the relative orientation of magnetic fields and filaments. If the magnetic field is parallel to the density gradient, it thus lies perpendicular to the filament.

Applying this technique to magnetohydrodynamic simulations, they showed how there exists a threshold density above which the relative orientation switches from parallel to perpendicular. This threshold density was dependent on the magnetic field. The technique was also applied by the Planck Collaboration for the analysis of Gould Belt clouds using the polarization of thermal dust emission observed by the *Planck* satellite at 353 GHz [Planck Collaboration XXXV, 2016]. Gradients were measured in the column density maps and compared to the magnetic orientation inferred from polarimetry. They also found that magnetic fields went from having mostly parallel or no alignment at low density, to mostly perpendicular alignment at high density.

The Planck Collaboration is the current state-of-the-art in mapping the relative orientation of galactic magnetic fields around nearby clouds, and has added greatly to the available measurements and statistics of dust polarisation [Planck Collaboration XXXII, 2016, Planck Collaboration XXXIII, 2016, Planck Collaboration XXXV, 2016].

One disadvantage of the HRO method is that density gradients do not, by definition, imply the presence of filaments. Cores, sheets, and bubbles are coherent structures with density gradients that one would want to exclude from a study of filaments. DisPerSE can be sensitive to noise, but will only select filamentary structure. The use of DisPerSE in 3D magnetohydrodynamic calculations is also a valuable complement to extensive observational surveys.

Since this paper analyzes not only filaments, but also radiatively driven bubbles (see Section 4.4), we chose to identify the filamentary structure directly. This also follows up on our successful use of DisPerSE to map structure in filaments in Kirk et al. [2015]. Density gradients would be present even if filamentary structure were not, as in the case of a sheet or a dense cloud core. For this reason, we opted to apply DisPerSE in 3D, but then constructed histograms of relative orientation in a manner similar to Diego Soler et al. [2013].

In this paper we have borrowed from techniques used by Li et al. [2013] for revealing large scale structure, and the DisPerSE algorithm for identifying individual filaments. DisPerSE has seen wide application in the analysis of *Herschel* results [see, e.g. Arzoumanian et al., 2011, Hill et al., 2011, Schneider et al., 2011, Peretto et al., 2012], and applied to 3D hydrodynamic simulations in Smith et al. [2014]. The analysis of 3D data is necessarily more complicated and performing "by-eye" assessments more complicated. There is also currently no way of ensuring that the filament skeletons extracted from the simulation grid at discrete points in the time map to the same structures in 3D. These filaments are constantly moving, shifting, and evolving. They might merge or dissipate or become disrupted by stellar feedback.

While the filament skeletons extracted by DisPerSE are sensitive to the input parameters (lower persistence or noise thresholds tend to identify more striations), these structures are real topoligical features in the volumetric density maps. The properties of simulated filaments were compared to observed filaments in our earlier study [Kirk et al., 2015] and found to be in agreement.

FLASH uses an adaptive mesh composed of blocks containing $8 \times 8 \times 8$ cells. The grid is refined as needed to resolve the gravitational collapse. FLASH writes simulation plot files at specified intervals containing information about the state of the simulation and the values of grid variables. These represent global state of the simulation at a discrete point in time and are the primary output that we analyze. We refer to plot files often throughout this text.

Hierarchical grid structure is preserved in these plot files using the HDF5 file format. We used `yt` [Turk et al., 2011], a general-purpose data analysis tool for computational astrophysics, to load the FLASH output data and resample it to a uniform grid. Memory constraints meant that we mapped the density information to a $256 \times 256 \times 256$ uniform grid and wrote the output to a FITS file, a format compatible with DisPerSE . The remapping to a uniform grid results in the loss of some information at the highest gas densities but preserves the large-scale structure throughout the simulation volume. The remapping is necessary because DisPerSE does not currently support hierarchical grid structures. At a 256^3 sampling, the grid resolution is 1611 AU (0.00781 pc) for our `MHD500` simulation and 3134 AU (0.01519 pc) for our `MHD1200` simulation.

It is on these remapped FITS files that DisPerSE operates, first to generate the Morse-Smale complex, then to extract the filament skeleton. The Morse-Smale complex is computed by finding all the critical points (where $\nabla\rho(x, y, z) = 0$). The maxima define a set of descending manifolds (the regions where all integral lines traveling along the gradients share the same maximum), while the minima define a dual set of ascending manifolds (the integral lines all share the same minimum). The intersection of these two manifolds defines a new set that is called the Morse-Smale complex. The simulation volume is partitioned into a natural tesselation of cells. The line segments connecting maxima and passing through saddle points are a natural way to define filaments. In cosmological studies, connecting dark matter haloes in the way allows for mapping of the cosmic web [Sousbie et al., 2011]. In molecular clouds, we use it to trace filaments. For visualization and analysis, we can use these filament skeletons together with the original un-resampled HDF output files from FLASH to retrieve other variables of interest along their extent (e.g. magnetic field information).

We apply this process to several plot files from each simulation. The calculation of the Morse-Smale complex is particularly computationally intensive. To handle this, we used Amazon's Elastic Compute Cloud (EC2), especially their `c3.8xlarge`-type compute-optimized instances which provide 32 virtual CPUs and 60 GiBs of attached memory on demand. DisPerSE can then be run in parallel across these cores.

In order to avoid tracing filaments in the noise of the data, and in order to select only the most prominent filaments, DisPerSE measures the "persistence" of topological structures. Local maxima and minima form pairs of critical points. The absolute difference in value between these two is the persistence. A persistence cut removes pairs below a given threshold, but the topology of structures consisting of high-persistence points remains. By selecting the appropriate persistence threshold, we can avoid tracing filaments within the noise. “Noise” in our simulations would actually be small-scale density perturbations resulting from the high-wavenumber part of the turbulent power spectrum. These might appear as striations, lumps, or voids.

Another challenge when it comes to visualizing this data in 3D was that filaments span a large dynamic range in density. Because we simulated molecular cloud cores with a power-law density distribution, as are typically observed, and superimposed a supersonic velocity field on top of this, 3D plots of the filamentary structure require the selection of isosurfaces at particular densities. A volume rendering approach using raytracing requires a particular transfer function designed to highlight gas at particular densities. When the filament changes density along its length it can be difficult to plot the morphology using standard techniques.

To give an observer’s picture, we take the output from these evolved simulations and project the density along each of the coordinate axes to produce column density maps from different perspectives. We then project the 3D filamentary skeletons onto these column density maps. Often there is clear alignment between the filament maps and the column density maps. Other times, the filamentary structure found in 3D is not obviously visible in 2D projection.

To produce a plane-of-sky magnetic field map, we perform a density-weighted projection along the same coordinate axes. We project the components of the magnetic field that lie perpendicular to the axis of projection.

This gives us, at every location in our map, the integrated local magnetic field orientation. By weighting the magnetic field projection by density, we favour contributions to the magnetic field orientations local to filaments in the line of sight. Also, any observations of light polarization by dust would be weighted by dust density, which traces the gas density.

To measure the orientation of the magnetic field relative to the filament, we trace the filament skeletons and interpolate B_x, B_y, and B_z to find the local magnetic field orientation at the filament spine. We then measure the angle formed by the unit vectors of filament orientation and magnetic field orientation.

An important measure of the dynamical importance of a filament segment is the mass-per-unit-length, sometimes called the dynamical mass or line mass of a filament. An equilibrium analysis can be used to define a critical value for stability, as was done in Ostriker [1964] who showed that for an isothermal cylinder, the mass per unit length is

$$m_{\rm crit} = \frac{2c_s^2}{G} = \frac{2k_B T}{\mu m_H G}, \tag{4.5}$$

where c_s is the sound speed, G is Newton's constant, k_B is Boltzmann's constant, T is the temperature, μ is the mean molecular weight, and m_H is the mass of the hydrogen atom [see also Inutsuka and Miyama, 1997, Fiege and Pudritz, 2000]. More generally, the total velocity dispersion should be used, since filaments are the products of supersonic motions and therefore may have nonthermal support, i.e. $m_{\rm crit} = 2\sigma^2/G$ [Fiege and Pudritz, 2000].

Line masses in excess of this critical value will undergo gravitational collapse and fragmentation to form protostars, with the most massive stars likely to be formed at the intersection of filaments [Schneider et al., 2012, Peretto et al., 2013]. When using column density maps with traced filaments, one way of estimating the local mass-per-unit-length along filaments is to multiply the column density value by the characteristic filament width. Arzoumanian et al. [2011] characterized the filaments in *Herschel* observations of IC 5146 as having a median width of 0.10 ± 0.03 pc. By estimating filament line masses in the column density projections from our simulation data, and pairing it with filament maps and magnetic field information, we can investigate whether relative orientation might be a function of the underlying line masses.

4.3 Filament and B-field alignments: early cloud evolution

We simulated molecular cloud clumps of various initial masses with an initially spherically symmetric density profile, upon which a supersonic velocity distribution was imposed. Supersonic turbulence gave the gas a filamentary structure across many scales in density. In this section, we examine cloud and magnetic field properties during the first 250 kyr of cloud evolution before radiative feedback becomes important.

In Figure 4.1, we take a representative plotfile from the `MHD1200` simulation, after just over 250 kyr of evolution. We ran DisPerSE with a persistence threshold of 10^{-17} g/cm^3, which selects some of the major-trunk filaments within the volume. Gas below a density of 10^{-22} g/cm^3 is excluded from consideration. The persistence threshold was adjusted manually until only major filaments were being selected. Small-scale turbulence can cause DisPerSE to

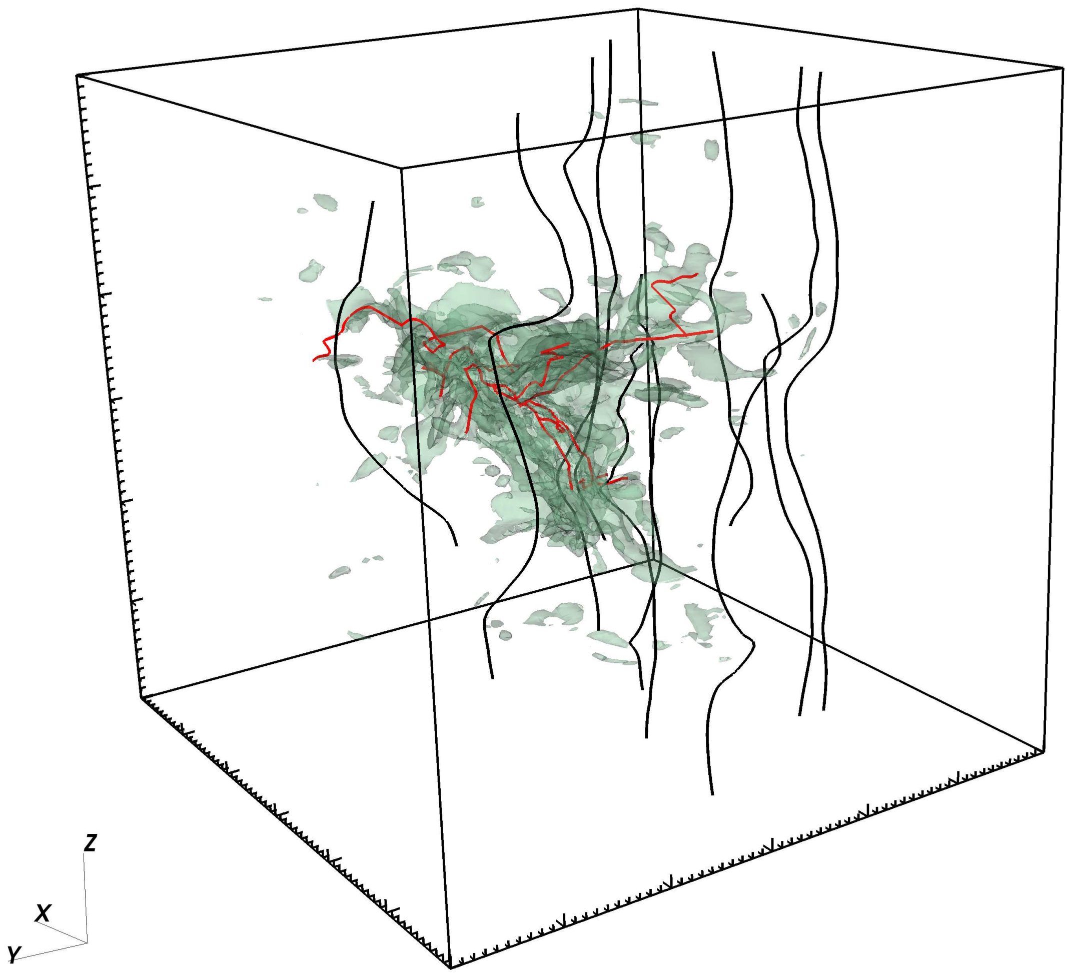

Figure 4.1: 3D plot of gas density from the `MHD1200` simulation at 250,000 years of evolution. Green isosurfaces indicate gas at densities of $n = 3.1 \times 10^3$ cm^{-3} ($\rho = 1.1 \times 10^{-20}$ g/cm^3). Red lines indicate filament skeleton selected by DisPerSE . Black lines are magnetic field lines at 8 randomly selected locations within the volume.

identify many potentially spurious short-length filaments that we did not wish to include in our analysis. A higher persistence threshold removes these from consideration.

Figure 4.1 highlights in green the $n = 3.1 \times 10^3$ cm^{-3} ($\rho = 1.1 \times 10^{-20}$ g/cm^3) isosurface. The box enclosing the rendering depicts the entire simulation volume, with a side length of 3.89 pc.

Traced in red are the main filaments as DisPerSE identifies them, satisfying the selection criteria described above. They align with some of the obvious filamentary structure visible in the rendering.

To visualize what is happening with the magnetic field, we draw magnetic field lines that trace the orientation of the magnetic field from 8 randomly sampled locations. Recall that the magnetic field is initially aligned with the z-axis of the simulation volume. Over 250 kyr, the structure of the magnetic field has evolved in response somewhat to the slow rigid body rotation of the gas about the z-axis, but much more to the turbulent velocity field. The Alfvén Mach number quantifies the relative energies of the turbulence and magnetic fields. Our simulated clouds have Alfvén Mach numbers of approximately unity, indicating an approximate equipartition in energies. By contrast the energy in rotation is only a few percent of the gravitational binding energy, which is greater even than the kinetic energy in the `MHD1200` simulation. Figure 4.1 shows large deflections in the magnetic field from the initial orientation.

While Figure 4.1 illustrates the structure of the magnetic field and filaments, we use projections to confirm whether structures seen in projection align with the filamentary structure that is traced in 3D. Studies of the filamentary nature of molecular clouds rely on some proxy of the column density

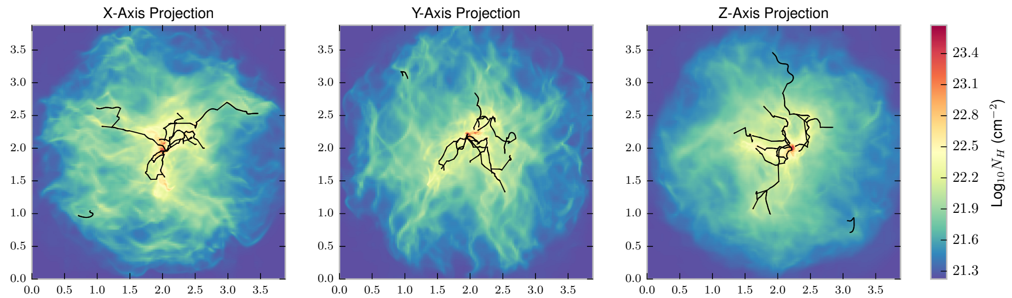

Figure 4.2: 2D column density maps along each of the coordinate axes with projections of the filament skeleton overplotted. Data is same as in Figure 4.1

(dust emission or integrated line intensity over some range of velocities). Density is seen in projection and hence may be hiding important structure inside the third dimension. Efforts to extract information about the 3D structure of molecular gas often make use spectral velocity data, with examples from simulations [e.g. Ward et al., 2012] and observations [Hacar and Tafalla, 2011, Hacar et al., 2013]. In the latter case it was found that filaments often have coherent velocity structures, with subsonic velocity dispersions, and marginal stability. In Kirk et al. [2015] we also noted evidence of this kind of fine structure in numerical simulations.

In Figure 4.2 we take the same data as in Figure 4.1, but in order to verify that apparent structures in projection match the structures found by DisPerSE in 3D we also project the filament skeleton into each of the three coordinate axes and plot them side-by-side. Column densities range from about 0.01 g/cm^2 to about 1.0 g/cm^2, while the mean initial column density of the simulation was 0.02 g/cm^2. The black lines in Figure 4.2 indicate the projected filaments. We see that most of the major structures are captured by this technique. This confirms that at least some of the observed major structures in the column density plots are not just the result of projection ef-

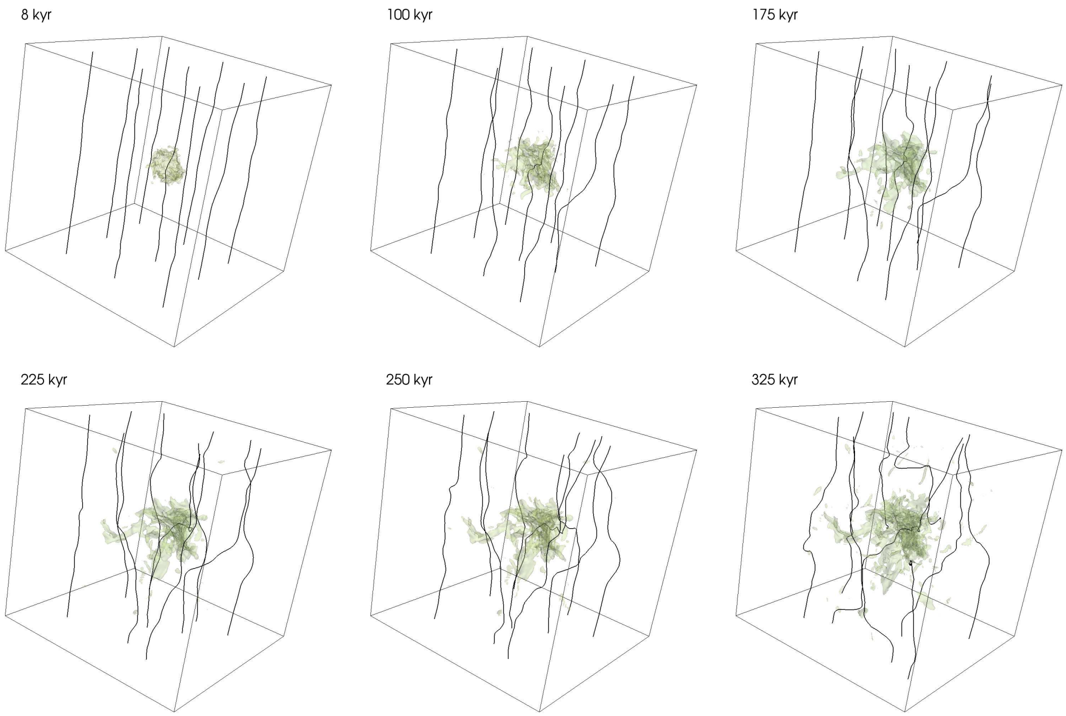

Figure 4.3: B-field streamline evolution over the course of 325 kyr in our `MHD1200` simulation. The green density contour is as in Figure 4.1. Box depicts entire simulation volume with $L = 3.89$ pc on a side. Turbulence and rotation largely account for the changes in local magnetic field orientation.

fects, but correspond to true filamentary structures in 3D. Smith et al. [2014] also found correspondence when comparing 2D and 3D DisPerSE-mapped filaments from simulations, except that filaments seen in column density projection did not belong to a single structure, but were made up of a network of sub-filaments reminiscent of those observed by Hacar et al. [2013].

4.3.1 Large-scale magnetic field orientation

The initial condition for our simulations is a molecular cloud core embedded in a uniform magnetic field. The field lines are initially oriented parallel to the z-axis. In ideal MHD, the fluid is assumed to be perfectly conducting, and so the magnetic field moves with the fluid. The ideal MHD limit is a good approximation for the interstellar medium (ISM), with non-ideal effects such as ambipolar diffusion or Ohmic dissipation only becoming relevant at the scales of protostellar disks, and even in simulations of these they have often been ignored.

Hence, in Figure 4.1, in which the magnetic field lines show significant deformation, the structure of the magnetic field is the result of gas motions: the initial solid body rotation of the molecular cloud clump, the turbulent velocity field, and the slow gravitational collapse. These motions will drag field lines.

We show the evolution of this field line dragging through the series of panels in Figure 4.3 in which we have plotted the magnetic field lines at 6 different snapshots in time, with the density isocontour of $\rho = 1.1 \times 10^{-20}$ g/cm^3 ($n = 3.1 \times 10^3$ cm^{-3}) highlighted, as in Figure 4.1. The first panel shows the state of the simulation at 8 kyr. The magnetic field lines are almost perfectly parallel with the z-axis, which was the initial condition. In the next panel, at 100 kyr, their state reflects some field line dragging due to the turbulent velocity field and solid body rotation. The deformation becomes more and more extreme from one panel to the next, with the last panel at 325 kyr reflecting very little of the original structure of the magnetic field.

Molecular clouds are observed to have large-scale velocity gradients across them, which some have interpreted as rotation, although this is contentious [Phillips, 1999]. We have initialized our simulations with an initial solid body rotation of $\Omega = 1.114 \times 10^{-14}$ s^{-1}, giving them an orbital timescale of $t_{\rm orbit} = 2.8$ Myr, which is longer than the freefall time of each simulation, but on the same order of magnitude. It is also of the same order of magnitude as the turbulent crossing time (see Table 4.1). Nevertheless, the ratio

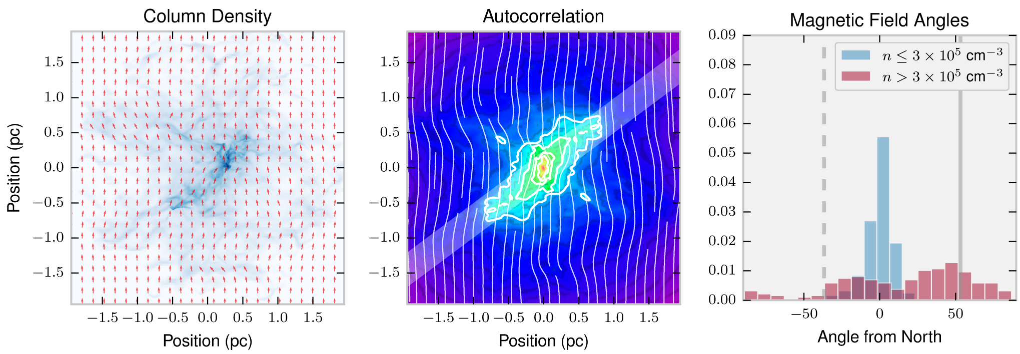

Figure 4.4: *Left:* Column density maps along the y-axis of our `MHD1200` simulation at 250 kyr of evolution with density-weighted projected magnetic field orientation overplotted in red arrows. *Middle:* The autocorrelation of the previous column density map, which highlight self-similar structure. Contours highlight levels from 1% to 10% of peak correlation values. The diagonal bar represents cloud orientation and is the best fit line through the pixels contained within the outermost contour, weighted by the base-10 logarithm of the autocorrelation values. Magnetic field lines based on the values measured for the left panel are overplotted. *Right:* The histogram of magnetic field orientations based on the values measured for the left panel, normalized so that the total area is 1. The orientations are measured relative to "north". The blue histogram shows the low-density gas, while red indicates only the orientations of high-density gas. The vertical grey lines indicate the angle of the best fit line to the large-scale structure (solid right line), and the angle offset by 90° (dashed left line).

of rotational kinetic energy to gravitational energy, parameterized by $\beta_{\rm rot}$, is still only about 1–3%. Turbulence and gravity are expected to have a much greater influence over the dynamics and the geometry of the magnetic field. Over time, strong turbulence will randomize the orientation of an initially coherent magnetic field. In highly super-Alfvénic clouds, turbulence dominates the magnetic energy, the magnetic geometry is random [Falceta-Gonçalves et al., 2008].

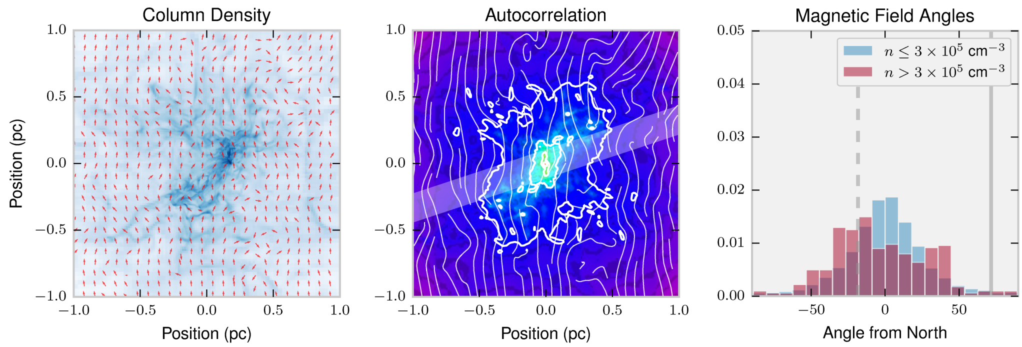

Figure 4.5: The same as in Figure 4.4, except using `MHD500` at 150 kyr of evolution. Because of the higher average gas density, we draw contours in the middle panel from 0.1% to 10% of peak correlation values. The best-fit line is still calculated based on the outermost contour. The data is taken at approximately the same number of freefall times as in the `MHD1200` simulation.

4.3.2 Magnetic fields in 2D

In Li et al. [2013], the authors took observations of molecular clouds in the Gould Belt with physical sizes of a few to a few tens of pc. Many of these clouds have large-scale elongated structure. The authors were interested in the magnetic field orientation relative to orientation of the large-scale structure of the cloud. Plotting these clouds in galactic coordinates (see their Figures 1 and 2), they then took the autocorrelation of the extinction maps. The autocorrelation map is produced by taking a copy of the image and displacing it in x and y coordinates, and at each such displacement calculating the sum of the product of the overlapping pixels. The map of this highlights any self-similar structure. Any elongated structures feature prominently in the autocorrelation maps. Li et al. [2013] then contoured various levels in the autocorrelation maps and took the best-fit linear regression to the pixel positions in the contours, giving the long-axis orientation of the molecular cloud. The angle of this could then be compared to the angles of magnetic field measurements derived from polarimetry data.

Motivated by the Li et al. [2013] approach, we perform a similar analysis on our simulation data. In Figure 4.4 we show data from our `MHD1200` simulation at 250 kyr of evolution, while in Figure 4.5 we show data from our `MHD500` simulation after 150 kyr of evolution. Although taken at different times, the data are at the same number of freefall times in each simulation ($t_{\rm ff} \approx 0.14$). The freefall time,

$$t_{\rm ff} = \sqrt{\frac{3\pi}{32G\bar{\rho}}}, \tag{4.6}$$

is a natural measure of the gravitational timescale of the simulation. The first panel from the left shows the map of projected mean density. This is very similar to a column density projection, except that each sample in the integral is itself weighted by density. We opted for this approach because it brings dense structures into stronger relief and produces clearer autocorrelation maps. We then overplot the magnetic field vectors in red. The magnetic field values are density-weighted averages computed by integrating through the simulation volume along the same projection axis. Unlike polarimetric observations, we can measure the magnetic field everywhere.

The middle panel of Figure 4.4 shows the autocorrelation of the "column density" plot from the left panel after downsampling to a 200x200 pixel greyscale image. The largest modes in the initial turbulent velocity field create a main filament "trunk" that is home to some of the highest-density gas in the simulation. In performing an autocorrelation of the column density map, the large-scale structure is also the most similar, and features prominently in the autocorrelation map. We contour several levels, from 1% (the outermost

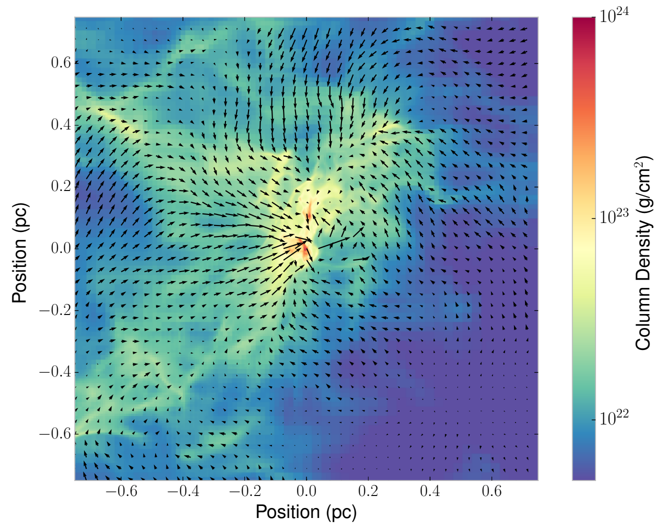

Figure 4.6: A zoom-in of the `MHD1200` cloud, in the same region as that shown in Figure 4.4 (left panel), centred on the highest-density gas and framing a (1.5 pc)^2 region. Column density is shown in colour with density-weighted projected velocity vectors overplotted, which emphasizes the motion of the higher-density gas. The initial Alfvén Mach number is 0.99, and the initial virial parameter is $\alpha_{\rm vir} = 0.56$, i.e. the cloud is highly bound and undergoing gravitational collapse.

contour) to 10% of the peak value. We then fit a linear function to the pixel coordinates inside the 1% contour, weighing each pixel by its base-10 logarithm value. In this way, we select the orientation of the long axis of the main structure in our molecular cloud clump. This approach is similar to that of Li et al. [2013], who used the pixel positions of the contour. We found better results using the pixels interior to a given contour, with a weighting based on their pixel value.

We are interested in measuring the magnetic field orientation and comparing it to the orientation of cloud clump. We overplot in blue the magnetic field lines on the autocorrelation map. The field lines are based on the magnetic field measurements taken from the left panel. We see that they are still largely oriented vertically, especially in the lower-density regions, but appear to align

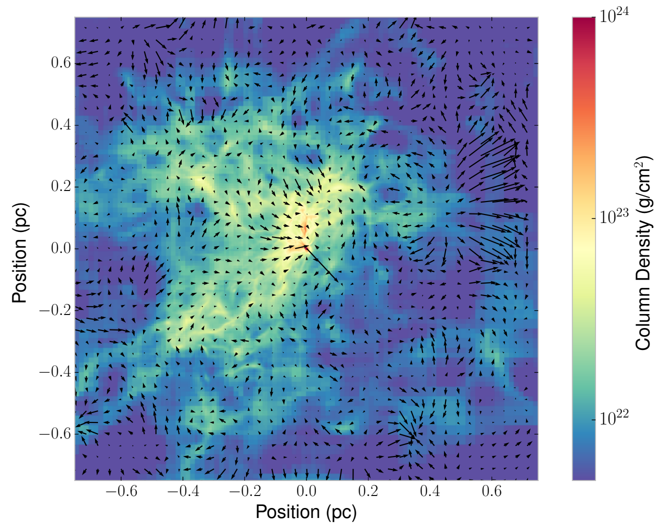

Figure 4.7: A zoom-in of the MHD500 cloud, in the same region as that shown in Figure 4.5 (left panel), centred on the highest-density gas and framing a $(1.5 \text{ pc})^2$ region. Column density is shown in colour with density-weighted projected velocity vectors overplotted, which emphasizes the motion of the higher-density gas. The initial Alfvén Mach number is 0.92, slightly lower than the MHD1200 case in Figure 4.6. However, the initial virial parameter is $\alpha_{\rm vir} = 0.95$, i.e. the turbulent kinetic energy is roughly in equilibrium with the gravitational binding energy.

weakly with main trunk filament and some other high-density branches.

The right panel of Figure 4.4 shows two histograms and two vertical grey lines. The solid right line gives the angle of the "trunk" filament from the middle panel, measured relative to vertical, while the dashed left line is offset by 90°, i.e perpendicular to the trunk. The histogram in blue is based on the density-weighted magnetic field averages measured for the left panel, where the underlying average gas density is below 3×10^5 cm^{-3}. We see that most gas is still aligned vertically, with relatively little deflection (±10°) from its original orientation (vertical). However, shown in red is the distribution of magnetic field orientations for gas with a mean density $n > 3 \times 10^5$ cm^{-3} ($\rho \gtrsim 10^{-18}$ g/cm^3). This relatively high density gas has somewhat a bimodal distribution, showing preferred alignment with the main filament trunk (the right peak in the distribution). The smaller left peak in the distribution is towards a perpendicular alignment with the filament (the left vertical grey line), but not exactly perpendicular. Accretion flow onto the main trunk filament has dragged magnetic field lines along with it such that they are deflected towards the filament. This accretion flow is responsible for this second (left) peak in the bimodal distribution.

We now compare this to Figure 4.5 (the virialized cloud simulation), which applies the same analysis to the `MHD500` simulation. The analysis is done in the same way, except that for the autocorrelation map contours we plot evenly-spaced levels between 0.1% and 10% of the peak value. The `MHD500`, being the tighter, more compact cloud with a higher overal gas density relative to the `MHD1200` simulation, is actually less bound.

The measurements for Figure 4.5 are taken at the same number of freefall times as compared to the `MHD1200` simulation to allow for a fair comparison.

The higher overall gas densities in `MHD500` meant a more strongly peaked central value in the autocorrelation map. For this reason, we contoured down to 0.1% of the peak value in the middle panel of Figure 4.5 to trace more of the overall structure.

The magnetic field orientations appear much more chaotic in Figure 4.5, despite the sound speed and RMS Mach number of the turbulence being the same in both simulations. The initial Alfvén Mach numbers are also virtually identical, suggesting that the magnetic field structure should be similarly ordered or disordered. This is, however, not the case. The difference is entirely on account of the relative boundedness of each cloud.

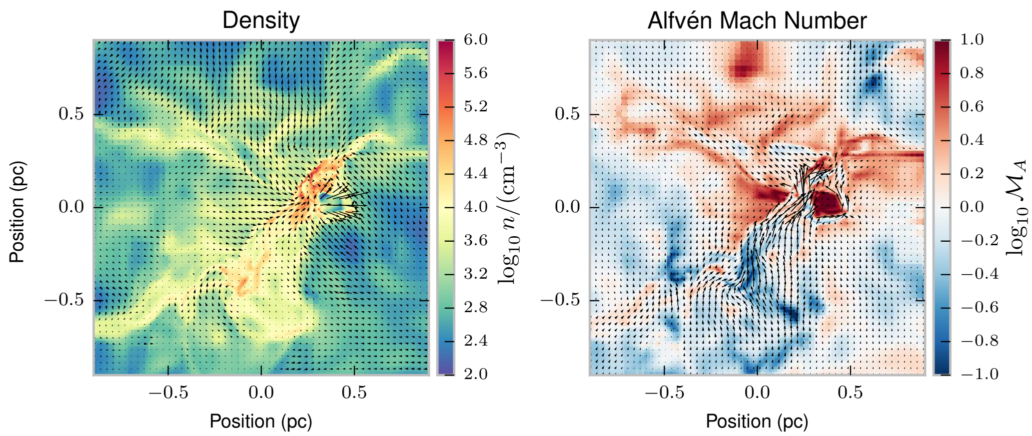

Figure 4.8: *Left:* Volume density slice through the molecular cloud of our `MHD1200` simulation after 250 kyr of evolution with arrows indicating the velocity field. The colours cover a range in volume densities from $n = 100$ cm^{-3} to $n = 10^6$ cm^{-3}. Photoionization feedback from a cluster of stars (not shown) has begun forming an HII region at the side of the main trunk filament. *Right:* Local Alfvén Mach number with arrows indicating the magnetic field. The colours are scaled logarithmically from $\mathcal{M}_A = 10^{-1}$ (blue) to $\mathcal{M}_A = 10^1$ (red). White regions have values for the Alfvén Mach number of $\mathcal{M}_A \approx 1$, indicating that the turbulent energy is balancing the magnetic energy. Sub-Alfvénic regions ($\mathcal{M}_A < 1$) have stronger magnetic fields.

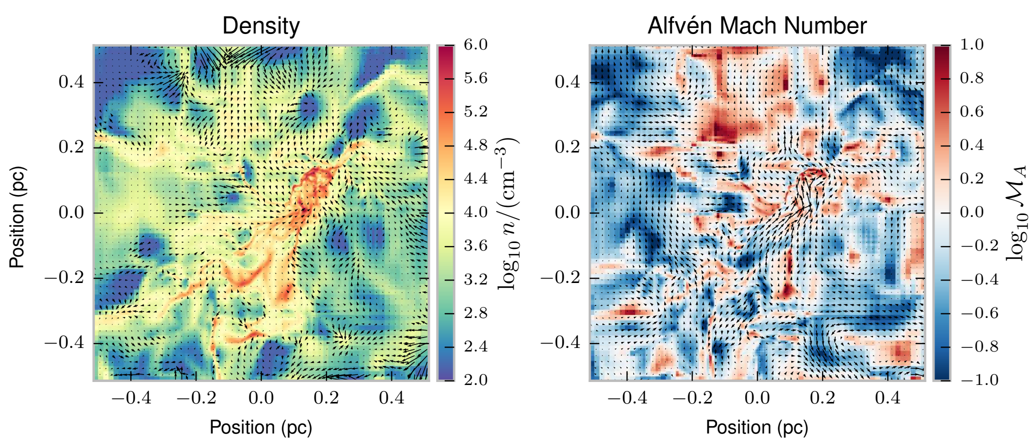

Figure 4.9: The same as in Figure 4.8, except for the `MHD500` simulation. As the simulation volume is smaller, the panels have been made proportionally smaller, while still centering on the densest part of the simulation. The snapshot of the simulation is taken after 150 kyr of evolution, which is earlier than in `MHD1200`, but at the same number of freefall times to permit better comparison.

The virialized cloud in `MHD500` shows no strong preferred ordering of the magnetic field in 2D, as is seen in the right panel of Figure 4.5. Figure 4.5 also shows less obvious large-scale structure, as evinced by the autocorrelation map, which appears much more square when compared to Figure 4.4. This is on account of `MHD500` being in virial equilibrium. `MHD1200`, being the more bound cloud, has undergone strong gravitational collapse onto the central filamentary structure, which appears very prominently in the autocorrelation map. The gravitational collapse has dragged the magnetic field structure with it, which accounts for the more regular structure seen in Figure 4.4 compared to Figure 4.5.

The lower-density gas ($n \leq 3 \times 10^5$ cm^{-3}) forms an approximately Gaussian distribution in angle relative to "North", centered at 0°. This distribution is shown in blue in the right panel of Figure 4.5. The higher-density gas ($n \leq 3 \times 10^5$ cm^{-3}), shown in red, is spread over many angles, but, if anything, tends to be oriented more perpendicular to the main trunk filament, an angle indicated by the left vertical gray line.

Comparing our simulations, we note this pattern: similar to Diego Soler et al. [2013], Planck Collaboration XXXV [2016], the low-density case tends towards parallel orientation and the high-density case towards perpendicular orientation, but in our case we are comparing gas at similar densities from two different simulations with different average densities.

In Figure 4.6 we show the column density projection of the same region as in the left panel of Figure 4.4 of the `MHD1200` simulation. We then overplot the density-weighted average velocity vectors to show the average flows onto the main filament. We see a pattern of flow both along the long axis of the main trunk filament and accretion onto the filament radially. The flow appears to converge onto the central, densest region. Compare this to Figure 4.7, which is the equivalent but for the `MHD500` simulation, displaying the same region as in the left panel of Figure 4.5. The density-weighted average velocity shows a pattern of randomly-oriented flows. The difference, again, can be entirely attributed to the degree of boundedness in each case, with `MHD1200` undergoing strong gravitational collapse and `MHD500` exhibiting a relative balance of kinetic and gravitational energies.

To examine the relationship between magnetic field ordering and the Alfvén Mach number more closely, we plot volume density slices through the center of our simulations showing the gas structure and compare these to slices of the local Alfvén Mach number. We also compare the velocity and magnetic field structure. We show these in Figures 4.8 and 4.9 for the `MHD1200` (strongly bound) and `MHD500` (virialized) models, respectively.

These two figures were taken at the same number of freefall times, $t_{\rm ff} \approx 0.14$, which corresponds to about 250 kyr in the `MHD1200` simulation and 150 kyr in the `MHD500` simulation. In Figure 4.8, we see that the velocity field is channeling mass both onto the main trunk filament and along it. This resembles the mass flows measured for the cluster-forming region in the Serpens South molecular cloud studied in Kirk et al. [2013]. Material appears to be flowing along the long axis of our main trunk filament, feeding a tight cluster of stars that is driving the H II region already visible in the left panel of Figure 4.8. There is also material flowing onto the main filament radially, and this radial accretion appears stronger than the flows along the filament's long axis, as it was in Kirk et al. [2013]. The right panel of Figure 4.8 shows the local Alfvén Mach number. More sub-Alfvénic regions possess stronger magnetic fields and slower accretion flows. The magnetic field is depicted with arrows in the right panel, showing how the magnetic field has been concentrated into the main trunk filament so that it lies parallel with the filament long axis.

In Figure 4.9 we see the result of trans-Alfvénic turbulence in virial balance with the gravitational forces in the `MHD500` simulation. Recall that both simulations were initialized with the same turbulent velocity field, similar mass-to-flux ratios, and the same radial density profile. The `MHD500` simulation is actually at higher average density—a more compact setup. However, after 150 kyr of evolution, the magnetic field has become disordered and the local Alfvén Mach number is a patchwork of ripples, alternating islands of sub- and super-Alfvénic regions, encircled with magnetic fields that do not possess very much coherent large-scale structure. There is some similarity with the `MHD1200` simulation, however: the field is generally aligned within the main filament, lying parallel to the long axis.

The consensus so far is that turbulence plays a major role in trans-Alfvénic molecular clouds. In the trans-Alfvénic regime, neither turbulence nor magnetic fields have the clear upper hand. Unlike the sub-Alfvénic regime, which dominates in the diffuse ISM and where magnetic fields clearly channel flows, filaments are more the result of turbulence and not of slow accretion flow along dominant field lines. The large-scale turbulent modes give rise to the primary filaments—the trunk—via shock compression, and magnetic field lines are dragged along with the gas, pushed together so that they lie together within the main filaments, parallel to their axes. In super-Alfvénic clouds, magnetic fields are not dynamically important. Falceta-Gonçalves et al. [2008] explored cases of numerical simulations with Alfvén Mach numbers of 0.7 and 2.0, but did not explore the space around $\mathcal{M}_A = 1$, a dynamically interesting transition region.

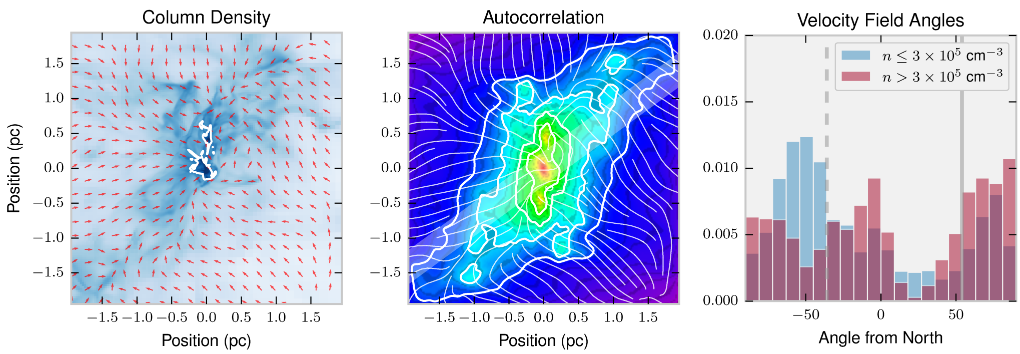

Figure 4.10: *Left:* Density projection along the y-axis of our MHD1200 simulation at 250 kyr of evolution with density-weighted projected velocity field overplotted in red arrows. *Middle:* The autocorrelation of the previous column density project, which highlight self-similar structure. Contours highlight levels from 1% to 10% of peak correlation values. The shaded diagonal bar represents cloud orientation as previously calculated for Figure 4.4. Velocity streamlines based on the values measured for the left panel are overplotted. *Right:* The histogram of the velocity field orientations based on the values measured for the left panel, normalized so that the total area is 1. The orientations are measured relative to "north". The blue histogram shows the low-density gas distribution, while red indicates only the orientations of high-density gas. The vertical grey lines indicate the angle of the best fit line to the large-scale structure (solid right line), and the angle offset by 90° (dashed left line).

In our case, wherein turbulence and magnetic forces are nearly in balance, we show that the discriminating factor is likely whether gravity dominates over the other energies. The MHD1200 simulation was substantially sub-virial ($\alpha_{\rm vir} = 0.56$), whereas magnetic fields were chaotic in the virially-balanced case of MHD500.

4.3.3 Velocity fields in 2D

In Figures 4.10 and 4.11, we show the large-scale velocity patterns in projection for the MHD1200 and MHD500 simulations, respectively. In each of these figures,

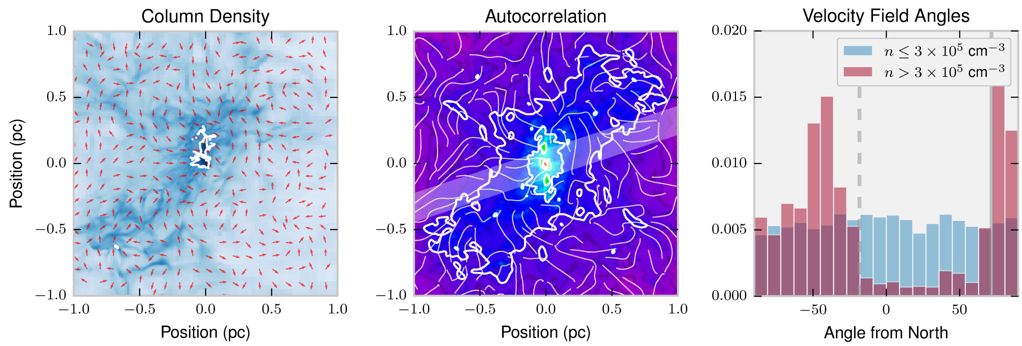

Figure 4.11: The same as in Figure 4.10, except using `MHD500` at 150 kyr of evolution. Because of the higher average gas density, we draw contours in the middle panel from 0.1% to 10% of peak correlation values. The best-fit line is still calculated based on the outermost contour. The data is taken at approximately the same number of freefall times as in the `MHD1200` simulation.

the left panel shows the mean projected gas density in blue. Overplotted are velocity vectors computed by taking the density-averaged mean velocity along the line of sight. The white contour is the threshold density used in the right panel to separate "low" and "high" density gas.

The middle panels compute the autocorrelation of the mean gas density, just as we had done previously for Figures 4.4 and 4.5. The only difference in this case is that the overplotted streamlines reflect the velocity structure instead of the magnetic field structure.

Finally, the right panels in Figures 4.10 and 4.11 show the histograms of the velocity field orientation angles, relative to "north" (the z-axis), based on the angles in every pixel of the left panel. The data is divided into "low-density" and "high-density" pixels, based on the mean gas density along the line of sight, with $\rho = 10^{-18}$ g/cm^3 ($n = 2.8 \times 10^5$ cm^{-3}) as the threshold. The high-density regions are contoured in the left panel of each figure, and show a dense core region in each case.

The velocity angle histogram in Figure 4.10 shows a bimodal distribution for the low-density gas in blue for the `MHD1200` simulation. These do not perfectly align with the parallel and perpendicular main trunk filament angles (the right and left vertical grey lines, respectively), but do follow a general pattern: most of the low-density gas is flowing onto main trunk filament at an angle roughly perpendicular to it, with a smaller fraction of the gas also flowing along the main filament.

The high-density core region shows a high degree of flow along the main filament with another significant portion coming in laterally. This is shown by the red histogram.

In the `MHD500` simulation, the histogram of gas velocities shows a different picture. The low-density gas is randomly oriented. There are no preferred accretion channels and gas appears to flow in all directions. This is in strong contrast to the high-density gas of the inner core region (shown in red), which shows extremely strong flow along the main trunk filament, and roughly perpendicular to it. This region is likely undergoing gravitational collapse and the main filament appears to set up accretion pathways, either along and perpendicular to it, to supply this central region with gas.

4.3.4 Magnetic field orientation relative to filaments in 3D

What is happening to the relative orientation of the filaments and the magnetic field lines at the level local to the filaments? Using the filamentary structure extracted from the 3D data cubes by DisPerSE , we analyze the filament spines by visiting the vertices and locally measuring the tangent vector, the magnetic field vector, and other physical variables such as the mass density. This procedure allows us to construct histograms of the relative orientation of the magnetic field and the filament orientation.

We take the relative angle θ of the filament tangent vector and magnetic field vector. Some authors measure $\cos\theta$ or $\cos(2\theta)$, but trigonometric projection can cause histograms to suggest a strong trend toward $\cos\theta = \pm 1$. (Imagine a unit circle evenly sampled in the angular dimension. A histogram of the cosine of these angles will collect more samples in the bins nearest $\cos\theta = \pm 1$ unless the bin width is carefully modified as a function of θ.) To avoid these problems, we produce histograms in relative angle only.

We are also careful to compare to the case of random orientation. Because of the two angular degrees of freedom in three-dimensional space, a histogram of relative orientation will have a higher proportion of vectors with angles closer to perpendicular than parallel. Any true tendency in nature towards a parallel or perpendicular orientation of filaments relative to magnetic fields should therefore be measured relative to the case of random alignment.

For our `MHD1200` simulation, for the series of time points under consideration, which were selected to be spaced roughly evenly throughout the simulation, we partition the data into three density groups: "low" ($n/\mathrm{cm}^{-3} < 5000$), "medium" ($5000 < n/\mathrm{cm}^{-3} < 50000$), and "high" ($n/\mathrm{cm}^{-3} > 50000$). These are the first three columns shown in Figure 4.12. The final column gives the histogram for all data, making no density cuts. In this figure, the rows represent the time evolution of these histograms of relative 3D orientation. The times at which these histograms were taken are indicated the top-left corner of the first panel in each row.

In each panel, two histograms are shown. In blue is the distribution

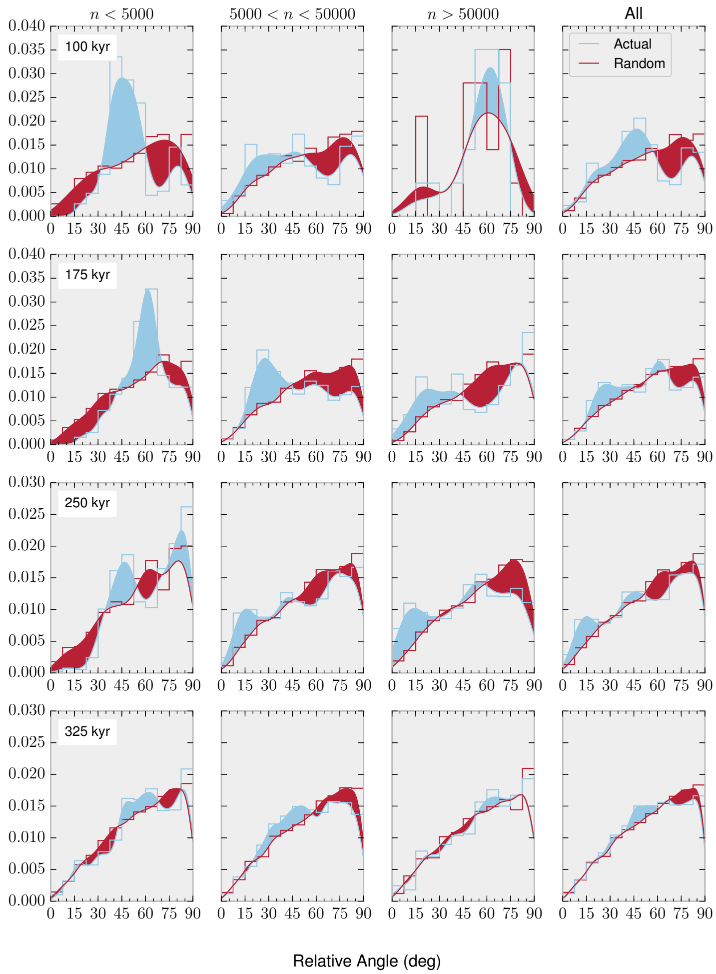

Figure 4.12: Sequence of histograms from the `MHD1200` simulation. The area under each curve has been normalized to 1. By tracing along the filaments in 3D through the simulated volume, we produce histograms of the relative orientation of the magnetic field and the filament. In each panel, we compare the relative orientation measured in the data (blue) with the histogram that would have resulted if the magnetic field had been randomly oriented (red). In addition to a standard step-shaped histogram, a kernel density estimate (KDE), with a Gaussian kernel, has been run over the data and is shown via the smooth curves, providing a continuous analog to the discretely-binned histogram data. Shaded areas indicate either an exceess relative to random (blue) or a deficit (red). Each row of panels gives the state of the simulation at the indicated time. Columns restrict the relative orientation data to the indicated density regims, as measured locally along the filament spine. The last column applies no density selection.

of relative angles presented by our data—the “Actual” case. We compare the measured relative angles to the case of random orientation, shown in red and labeled “Random”. In this case, the local magnetic field is assigned a random orientation in 3D space and the relative orientation to the filament is measured. The sample size for the “Random” case therefore matches the “Actual” case.

In addition to performing the standard step-shaped histogram with 12 bins over 90° of angle, we apply a kernel density estimate (KDE) using Gaussian kernels. KDEs are a continuous analog to the traditional histogram with its discrete number of bins. Figures 4.12 and 4.13 show both representations. Additionally, we shade any “excess” (blue) or “deficit” (red) relative to the “Random”.

In studying Figure 4.12, the `MHD1200` simulation, a few trends appear. Although containing more mass overall, the volume of the `MHD1200` is also much larger, causing the mean gas density in the `MHD1200` simulation to be about one third the value in the `MHD500` simulation. We see that in the “All”-density column there is a deficit in the distribution of relative angles around 90°. This pattern shows up in many of the panels where the data has been further segmented based on underlying mass density.

In the low-density column, where we measure relative angles at filaments segments situated in gas at densities $n < 5000\ \mathrm{cm}^{-3}$, there is neither a trend towards parallel nor perpendicular orientation. Instead, there is an excess relative to random at angles between 30° and 75°. This low-density regime represents the outer regions of our simulation volume. The magnetic fields lines, initially coherent and oriented parallel to the z-axis, have been dragged inward during the molecular cloud clump’s gravitational collapse. In the outer regions of the simulation volume, this inward dragging may account for the observed excess at "middle" angles.

At relatively early times, after 100 kyr of evolution (first row of Figure 4.12), most of the gas is still at low density. It has not had time to collapse to higher density, i.e. into the main trunk filament. In the low-density gas histogram, the peak is measured around 45° relative orientation between filaments and B-field. This may be on account of the main filament trunk having this approximately this orientation, which may just be starting to form as a result of the largest turbulent modes. At this time, there is very little gas with densities above 5000 cm^{-3}.

As the simulation progresses, we observe increased power at near-parallel orientations. See, especially, the "intermediate" and "high"-density panels at 250 kyr of evolution, with corresponding deficits at near-perpendicular orientations. An interesting thing happens between 250 kyr and 325 kyr. Between these times, star formation has occurred in this simulation, and radiative feedback has injected energy into the molecular cloud clump. The measured relative orientations between the magnetic field and the filamentary structure in 3D is much closer to random than in any of the other panels. We attribute this to the energy injected through radiative feedback from high-mass stars, an effect we discuss further in section 4.4. Radiative feedback is already underway by 250 kyr, but by 325 kyr has largely disrupted the main filament trunk. The radiative feedback is in the form of ionizing radiation from a tight cluster of massive stars that lead to the formation of an expanding HII region.

At 175 and 250 kyr, we see a feature indicating alignment of the filamentary structure and the magnetic field. It is seen in the medium and high density panels, and also appears more modestly in the "all data" panel on the right. As the simulation progress, this feature is apparently washed out, because the alignment isn't seen in the last row. Again, this is on account of radiative feedback from star formation.

It is important to note that DisPerSE was run on each simulation plotfile separately, and the filamentary structure extracted from each will be different. The persistence and noise thresholds were held the same for the sake of consistently, but the simulation evolves over time and central regions become denser due to gravitational infall. Therefore the skeletons that DisPerSE extracts from the set of plot files, though they come from the same simulation, may not necessarily strongly resemble each other. This is in contrast to what was done in Kirk et al. [2015], wherein the filament skeletons were found in 2D column density projections and the skeletons kept consistent between time slices using by-hand adjustments as necessary. Owing to the considerably higher complexity of doing this with 3D skeletons and having sparser time sampling, we did not attempt to map out the exact same filaments at each time slice.

Nevertheless, the filament skeletons extracted from one column density projection to the next were largely similar, and Kirk et al. [2015] demonstrated that the properties of our FLASH-simulated filaments matched those of filaments observed in nature.

In Figure 4.13 we show the same analysis performed on our `MHD500` simulation. `MHD1200` and `MHD500` both have the same angular rotation rate, similar ratios of rotational kinetic energy to gravitational energy, the same initial temperature and RMS Mach number turbulence. We initialized both from the same turbulent velocity field, hence they would have developed similar initial structure. The difference is that `MHD500` is tighter and more compact,

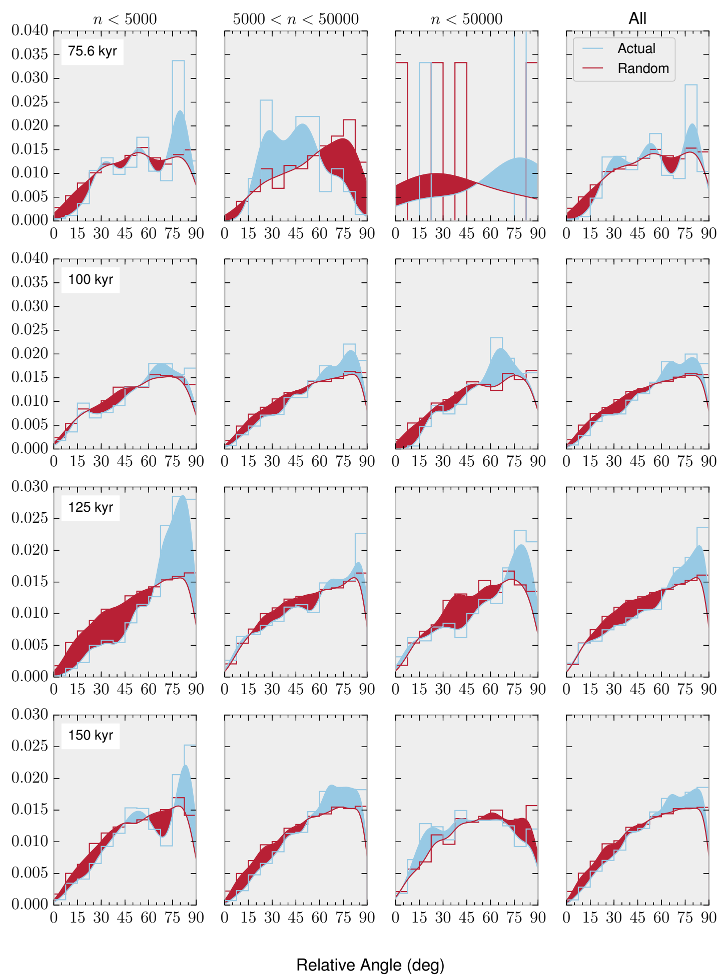

Figure 4.13: The same as in Figure 4.12, except for our `MHD500` simulation.

with a higher average gas density ($\bar{n}_{500} \approx 1200$ vs $\bar{n}_{1200} \approx 390$ cm^{-3}).

At early times it is difficult to discern any pattern in the relative orientations. Most of the gas has not yet collapsed to very high density, and the orientations appear relatively close to random distributed.

This changes as the simulation evolves. In the panels at 100 kyr and 125 kyr, the data shows a tendency towards a perpendicular relative orientation. This is visible even in the low-density panels where $n < 5000$ cm^{-3}. At late times (150 kyr, final row), however, this trend is less clear. The high-density ($n > 50000$ cm^{-3}) at 150 kyr appears either to have reversed the trend, or else the orientations have simply become closer to random. In Figure 4.14, we showed how at 150 kyr the `MHD500` simulation becomes magnetically critical, meaning that the magnetic flux is sufficient to support against further gravitational collapse. We also showed how the virial parameter, which measures the ratio of kinetic to graviational energy increases sharply toward 150 kyr. We interpret this as gravitational energy being converted to kinetic energy during gravitational collapse, in particular as the cloud clump becomes magnetically critical.

Whereas in the `MHD1200` simulation we saw kinetic energy being injected in the form of radiative feedback from massive stars, in the `MHD500` simulation, in which we did not simulate star formation, gravitational energy is converted to kinetic energy, with similar results: the relative orientation of the magnetic field to the filamentary structure becomes closer to random with the injection of kinetic energy.

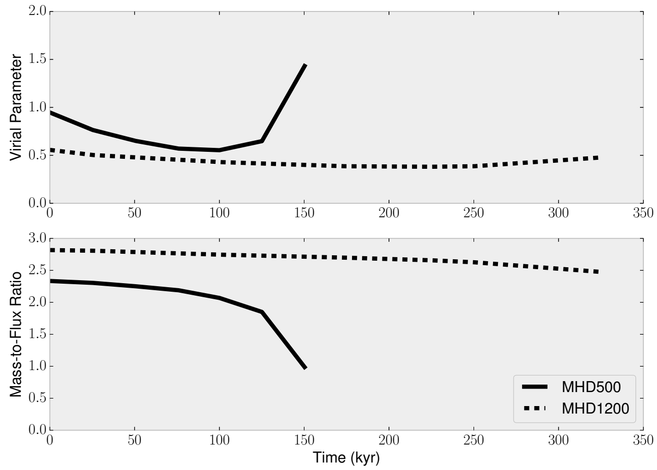

Figure 4.14: The evolution of the virial parameter and the mass-to-flux ratio of our two simulations. These parameters remain fairly steady throughout the MHD1200 simulation, but the MHD500 becomes magnetically critical during gravitational collapse. The added magnetic support causes some of the gas in the outer regions to rebound, adding kinetic energy.

4.3.5 Virial parameter and mass-to-flux ratio

In Table 4.1 we listed the simulation parameters for our two simulations, which we named MHD500 and MHD1200, because they contain about 500 $M_\odot$ and 1200 $M_\odot$, respectively. They have very similar Alfvén Mach numbers, valued at close to unity, meaning that the energy in their magnetic fields roughly balances the turbulent energy.

Another parameterization of the magnetic field strength is the mass-to-flux ratio λ (see Equation 4.2), which compares the gravitational field strength to the magnetic field, which provides support against gravity. If $\lambda < 1$, the magnetic field will prevent gravitational collapse. Both of our simulations are initialized with mass-to-flux ratios around 2–3.

The two simulations differ in only a few ways, but perhaps the most important is the virial parameter. We quoted the initial values at 0.95 and

0.56 for the `MHD500` and `MHD1200`, respectively. The virial parameter gives the ratio of kinetic energy to gravitational energy (see Equation 4.3).

We plot the evolution of both the virial parameter and the mass-to-flux ratio in Figure 4.14. The `MHD1200` simulation begins substantially sub-virial, meaning that as an unmagnetized cloud clump, it would be highly bound and undergo gravitational collapse. Since its mass-to-flux ratio is also supercritical, it does indeed undergo gravitational collapse.

The value of the virial parameter remains relatively level throughout the simulation, decreasing slightly over time as the cloud collapses, but then beginning to increase against around 250 kyr, the time at which massive star formation has resulted in kinetic energy being injected into the simulation via radiative feedback. The mass-to-flux ratio decreases monotonically throughout the simulation as a result of magnetic field lines being dragged slowly inward, following the gravitational collapse.

The `MHD500` simulation behaves rather differently. The simulation evolves quickly, and the virial parameter goes from marginally bound (0.95) to 0.55 after 100 kyr, following which it increases dramatically to 1.43 after 150 kyr. This trend is attributable to what is happening with the mass-to-flux ratio. The simulation begins slightly more magnetized than the `MHD1200` simulation. Magnetic field lines are dragged inward following the gravitational collapse of the gas (which is, on average, 3 times denser than that of the `MHD1200` simulation). The `MHD500` simulation becomes magnetically critical after 150 kyr, meaning that magnetic support is able to prevent further collapse. Gravitational energy gets converted to kinetic energy as the collapse is halted. This increase in kinetic energy is reflected in the virial parameter.

4.4 Star formation and the effect of radiative feedback

How does radiative feedback from a forming massive star (which we find in the `MHD1200` simulation) affect the filamentary structure of the cloud? In particular, can it destroy or alter the filamentary accretion flow so as to shut down accretion onto the massive star?

To answer these questions, we ran our `MHD1200` simulation including radiative feedback from star formation. We use a characteristics-based raytracer coupled to a simplified version of the DORIC radiative cooling, heating, and ionization package [Frank and Mellema, 1994, Mellema and Lundqvist, 2002, Rijkhorst et al., 2006b] implemented in FLASH for the study of star formation and HII regions [Peters et al., 2010b].

The `MHD1200` forms a cluster of massive stars near the center of the simulation volume, directly within the main trunk filament. Schneider et al. [2012], Peretto et al. [2013] observe that the intersections of filaments are the sites of clustered and massive star formation. The main trunk filament in our simulation shows various smaller branches connecting with it. The cluster of massive protostars that forms in our simulation eventually becomes luminous enough to begin ionizing the gas around it and form a HII region with the appearance of a blister on the side of main trunk filament, similar to the Cocoon nebula in IC 5416 [Arzoumanian et al., 2011], although the Cocoon nebula is an HII region powered by only a single B star.

The formation of the HII region ultimately begins to disrupt and destroy the main filament, creating an expanding cavity of hot (10^4 K) gas and injecting a lot of kinetic energy. The HII region, driven mainly by a single

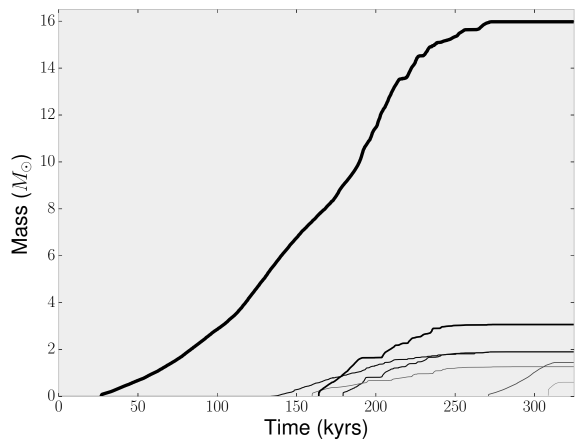

Figure 4.15: The evolution of the sink particles formed in the `MHD1200` simulation. 7 particles are formed near the center of the simulation volume inside the main trunk filament and make up a tight cluster. These accrete mass, the largest of which reaches nearly 16 $\mathrm{M}_\odot$.

massive star that grows to $16\,\mathrm{M}_\odot$, comes to envelope the entire star cluster and shuts off accretion onto every star.

Figure 4.15 shows the mass evolution of the stars formed in the `MHD1200` simulation. A total of 7 stars are formed, although only one of them becomes a massive star, achieving about 16 $\mathrm{M}_\odot$. Of the others, one reaches $3\,\mathrm{M}_\odot$, while the others remain below $2\,\mathrm{M}_\odot$. The luminosity of the massive star dominates all the others, achieving a total luminosity of $L_{\mathrm{tot}} = 22942\,L_\odot$. This star powers the formation of the HII region. The 10,000 K gas within this region supplies the thermal pressure needed to drive the outward expansion of the bubble and form the blister that eventually begins to disrupt the main filament. A star with a mass of 16 $\mathrm{M}_\odot$, in a cluster of 7 stars with a total mass of 26.16 $\mathrm{M}_\odot$ is at the high end—but still observed—range for embedded star clusters [Weidner et al., 2010].

We take a closer look at the evolution of the most massive star in Figure

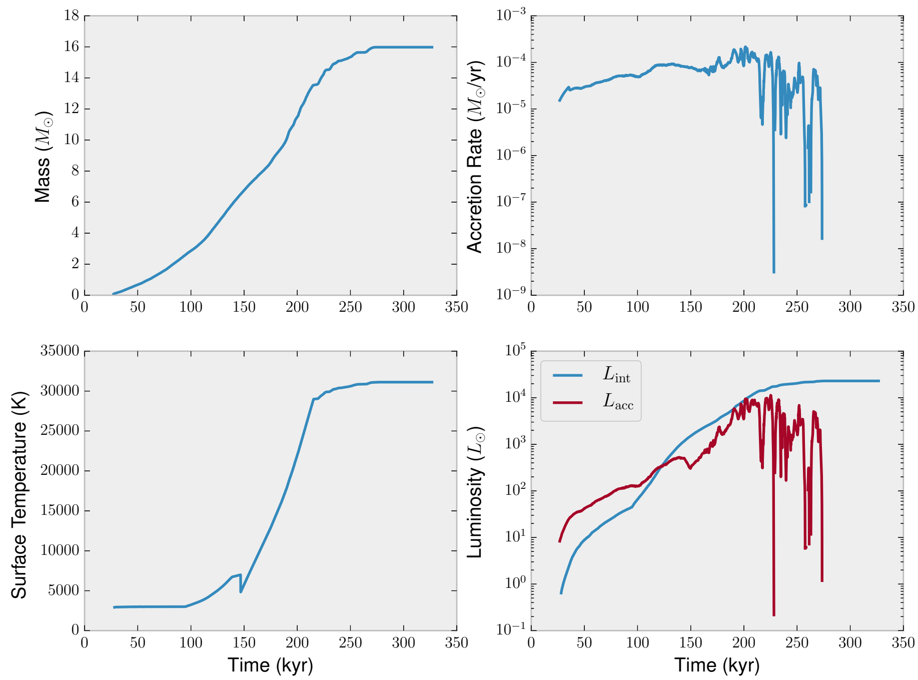

Figure 4.16: Evolution of the most massive star formed as part of the `MHD1200` simulation, which reaches a maximum mass of 16 $M_\odot$. The top-left panel shows the history of the mass of the sink particle representing this star. The top-right panel shows the evolution of the accretion rate in units of $M_\odot$/yr. The bottom-left panel is the history of the effective (surface) temperature, as computed by our protostellar model. The bottom-right panel shows the intrinsic luminosity and the accretion luminosity of the star.

4.16, which plots the evolution of several of its properties. The top-left panel shows the mass evolution as in Figure 4.15, but only for the most massive star. After about 250 kyr of evolution, the mass of the star begins to plateau as it envelopes itself in the HII region of its own making. Less gas reaches the star and its accretion is shut off. We see this play out in the top-right panel of the figure, which shows the accretion rate reaching a maximum of around 1–2 $\times 10^{-4}$ $M_\odot$/yr, but then beginning to drop off. After 275 kyr, the accretion rate has shut off completely and the star ceases to grow. In this panel, we have applied a small amount of smoothing via a moving average filter.

In the bottom-left panel of Figure 4.16 we plot the evolution of the effective (surface) temperature of the star. This is computed via a protostellar evolution model that we first implemented in FLASH in Klassen et al. [2012b] and used in the study of HII region variability in Klassen et al. [2012a]. In particular, the notch seen in the surface temperature near 150 kyr is due to a change in protostellar structure as the star's radius swells and the surface cools temporarily. From 150 to 225 kyr, the surface temperature increases dramatically, which results in a high flux of ionizing photons. The HII region starts to form during this time as the massive star begins to ionize the gas in its vicinity.

The bottom-right panel of Figure 4.16 shows the evolution of star's intrinsic luminosity (from nuclear burning or Kelvin-Helmholtz contraction during the earliest phases) and the accretion luminosity. Initially, accretion is the dominant luminosity, but is overtaken by the star's intrinsic luminosity after about 125 kyr of evolution, when the star is between 4 and 6 $\mathrm{M}_\odot$. We see that the accretion luminosity shuts off completely around 275 kyr.

We repeat the column density autocorrelation analysis in Figure 4.17, this time for the terminal plotfile at 325 kyr of evolution. We zoom in on the inner $(1.2\ \mathrm{pc})^2$ of the simulation. The effects of the forming HII region are seen in the column density plot as a blister on the side of the main filament. Photoionizing feedback injects a large amount of kinetic energy—the gas inside the HII region is 10^4 K. The orientation of the magnetic field vectors for the high-density gas ($n > 2.8 \times 10^5\ \mathrm{cm}^{-3}$) is almost random, being spread out fairly evenly across all angles.

The consequences for the magnetic field in a slice through the centre of

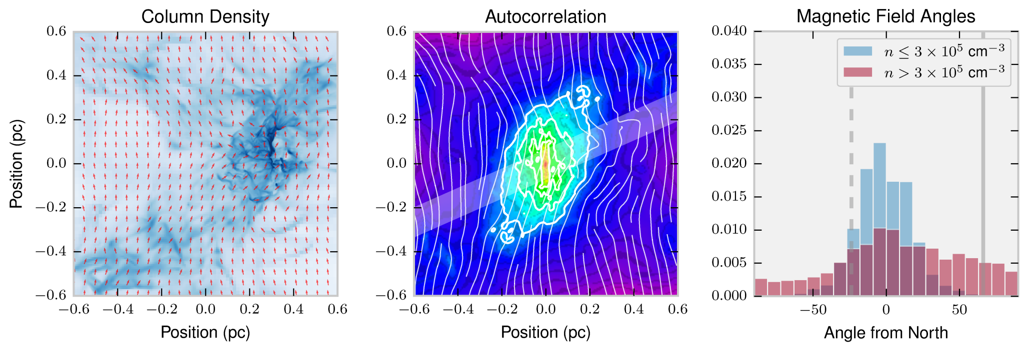

Figure 4.17: The same as in Figure 4.4, except for the final state of the `MHD1200` simulation at 325 kyr of evolution. Photoionization feedback from a massive star of $\sim 16\,M_\odot$ has created an expanding HII region.

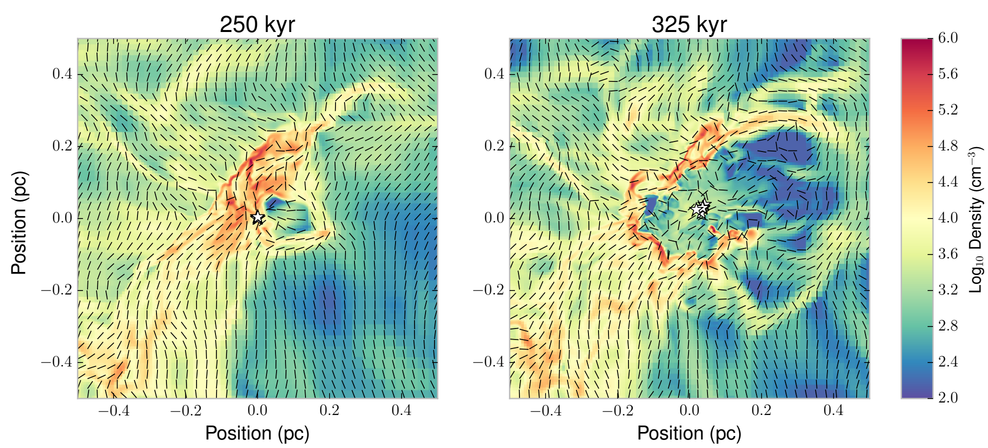

Figure 4.18: Volume density slices through the center of the `MHD1200` simulation volume showing an expanding HII region as a result of ionizing feedback from the cluster of stars. A single massive star of nearly 16 $M_\odot$ dominates all the others and has a luminosity of nearly 23,000 $L_\odot$. This drives a bubble of hot (10,000 K) ionized gas, forming a blister on the side of the main trunk filament. The left panel shows the state of this bubble after 250 kyr of evolution, while the right panel shows the state of the bubble after 325 kyr, near the very end of the simulation. Overplotted on each are magnetic field vectors based on the magnetic field orientation in the plane of the slice.

the simulation volume are shown in the two panels of Figure 4.18. This figure shows a volume density slice through the centre of the simulation volume at 250 kyr and 325 kyr. A $(1\ \mathrm{pc})^2$ window is centered on the star cluster in the left panel, and this window position is kept when plotting the second panel. Volume densities are coloured from a minimum at $n = 100\ \mathrm{cm}^{-3}$ to $n = 10^6\ \mathrm{cm}^{-3}$. We then overplot a magnetic vector map, using the magnetic field orientations in the plane of the slice, rather than performing a density-weighted projection as was done to generate Figures 4.4 and 4.5.

As the HII region grows, the expanding bubble sweeps up a shell of material. The panel on the right of Figure 4.18 shows the magnetic field lines being swept up with this wall of material, consistent with other observations and theoretical work [see, e.g., Lyutikov, 2006, Dursi and Pfrommer, 2008, Arthur et al., 2011, van Marle et al., 2015]. The magnetic field becomes compressed along the bubble wall. Meanwhile, the magnetic field inside the bubbble is chaotic and disordered. We recall that in our 3D filaments analysis, Figure 4.12 showed how any coherent orientation of the magnetic field relative to the filamentary structure is largely erased by the end of the simulation (325 kyr), with the relative orientation approaching the random distribution. This is especially true for the highest-density gas, which is also where the massive stars formed and their radiative feedback injected the most kinetic energy.

Arthur et al. [2011] also found that when an HII region expands into a turbulent medium, the magnetic field tends to become ordered, lying parallel to the ionization front. This is consistent with what we observe in Figure 4.18. They also reported that the magnetic field within the ionized region tended to be oriented perpendicular to the front, whereas in our case the field nearest the star cluster has the appearance of random orientation.

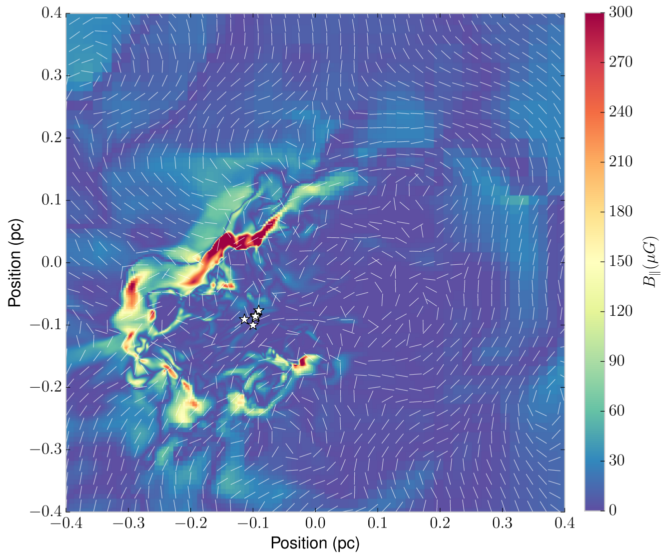

Figure 4.19: A slice through the simulation volume of the `MHD1200` simulation at 325 kyr showing the line-of-sight magnetic field strength around the HII region driven by the cluster of stars in the lower-left corner of the image. Magnetic field vectors are overplotted giving the plane-of-sky magnetic field orientation.

The Rosette Nebula within the Monoceros molecular cloud is an example of an observed region with ongoing massive star formation that provided an opportunity to study the effect of an expanding HII region within a magnetized environment. Planck Collaboration XXXIV [2016] were able to fit an analytical model to this HII region using *Planck* 353 GHz dust polarisation data that was able to reproduce the observed rotation measure data. An enhancement of the line-of-sight magnetic field by about a factor of 4 was seen inside shell swept up by the HII region.

Results from the *Planck* mission offer opportunities to compare numerical simulations and high-resolution observations. We plotted the line-of-sight magnetic field strength from our `MHD1200` simulation at 325 kyr, when the HII region is already evolved. We show this in Figure 4.19. The plot centres on an area similar to that shown in the right panel of Figure 4.18. We again overplot the plane-of-sky magnetic field vectors. The enhancement of the line-of-sight magnetic field strength in the shell of the expanding HII region is roughly a factor of 4–10, depending on which part of the shell is probed. The magnetic field strength inside the HII region varies over 1–20 μG, similar to the ambient field strength in our simulation and in agreement with the ambient field estimates in Planck Collaboration XXXIV [2016], though the studied HII region in Rosette is much larger ($R \sim 20$ pc) than our simulated volume ($L \sim 4$ pc).

Massive stars are a possible mechanism for driving turbulence in molecular clouds. They also complicate the picture of how magnetic fields ought to be orientated around filamentary clouds, randomizing it in some places, while possibly sweeping together field lines within expanding shells of material. We can expect sites of active star formation, especially massive star formation, to disturb the order of the magnetic field inherited from the intercloud medium.

4.5 Discussion

In Kirk et al. [2015], we analyzed the properties of filaments resulting from hydrodynamic and magnetohydrodynamic simulations, finding that magnetic fields resulted in "puffier" filaments that were less prone to gravitational fragmentation. The filamentary structure was extracted from column density projections, but no analysis was done on the relative orientation of the magnetic field and the filament. This was taken up by other authors [Seifried and Walch, 2015], who analyzed linear initial filament configurations and showed that perpendicular magnetic fields can result in filaments thinner than the proposed univeral filament width of 0.1 pc [Arzoumanian et al., 2011]. Different field configurations and turbulence will result in different fragmentation patterns.

One of the key differences between our simulations and those of Seifried and Walch [2015] is the origin of the filaments. Seifried and Walch [2015] start with a single filament as an initial condition, whereas we form a network of filaments in a molecular cloud clump. In our simulations, filaments are the result of supersonic turbulence. In Seifried and Walch [2015], turbulence is present, but affects the fragmentation pattern of the gas; it is not responsible for the filament's structure.

4.5.1 Magnetic fields, filament formation, and dynamics

What is the case in nature? Do flows of gas along the magnetic fields of the intercloud medium result in filament-shaped clouds, or does supersonic turbulence help define both the filamentary structure and the magnetic field structure? Various scenarios for filament formation have been studied. In the supersonic turbulence scenario, colliding shocks create a network of filaments where dense gas can stagnate [e.g. Hartmann et al., 2001, Padoan et al., 2001, Arzoumanian et al., 2011]. These colliding shocks may be driven by stellar feedback, supernovae, or other sources of turbulence. Our own use of a random initial supersonic velocity field with a turbulent power spectrum is motivated by this scenario. The relative orientation of magnetic fields in this scenario will depend on the relative strengths of gravity, turbulence, and the magnetic field, as we have shown in this paper. For trans-Alfvénic turbulence, gas compression can happen both perpendicular or parallel to magnetic fields.

A related scenario is colliding flows or cloud-cloud collisions [see, e.g. Redfield and Linsky, 2008, Banerjee et al., 2009, Inoue and Fukui, 2013]. In the local ISM, cloud-cloud collisions may be responsible for the observed filamentary morphology [Redfield and Linsky, 2008]. In cloud-cloud collisions, the magnetic fields may thread the massive, filamentary cloud cores perpendicular to the filaments [Inoue and Fukui, 2013]. Compression of Warm Neutral Medium (WNM) flows (possibly through turbulence) can trigger the condensation of cold gas structures, even filaments with magnetic field alignment as the shear of the turbulent flow stretches gas condensations into sheets and filaments [Audit and Hennebelle, 2005, Inoue and Inutsuka, 2009, Heitsch et al., 2009, Saury et al., 2014]. The ubiquity of filaments may thus be explained as generic turbulence sheers gas condensations into filaments, and magnetic fields may help keep these as coherent structures [Hennebelle, 2013]. The alignment reported in Planck Collaboration XXXII [2016] between matter structures in the diffuse ISM and magnetic fields could be a signature of the Cold Neutral Medium (CNM) filaments through turbulence.

Another mechanism for forming filamentary molecular clouds is B-field channeled gravitational contraction [e.g. Nakamura and Li, 2008]. Here Lorentz forces imply that gas motion along magnetic fields is unhindered, whereas gas moving perpendicular to field lines encouters a magnetic pressure. This means that gravity can channel gas along field lines, fragmenting the cloud into filaments that perendicular to the B-field, but parallel to each other.

In a related scenario, anisotropic sub-Alfvénic turbulence has the effect of spreading gas preferentially along magnetic fields. In this case, filaments appear parallel to magnetic field lines. These latter two scenarios are considered for Gould Belt clouds by [Li et al., 2013].

Which of these scenarios is true likely depends on the local environment:

the relative strengths of turbulence and magnetic fields, the physical scales under consideration, the enclosed mass and boundedness of the region, the isotropy of the turbulence, and the star formation history of the region.

4.5.2 Effects on massive star formation

In Chapter 3, we simulated the evolution of an isolated, massive protostellar core using a new hybrid radiative transfer code introduced in Chapter 2. In a core with a radius of 0.1 pc and an initial mass of 100 $M_\odot$, we were able to form a star of 16 $M_\odot$ mass in around 30 kyr, which is much faster than what we see in this chapter's simulations. This star then proceeded to grow to almost 30 $M_\odot$ in another 10 kyr. The accretion rates in this chapter are also an order of magnitude lower than in the isolated protostellar core simulation. What limits the accretion onto massive stars in the filamentary molecular cloud clump scenario? For one, turbulence may slow accretion by reconfiguring the gas reservoir into a network of filaments. Stars form along supercritical filaments, and initially have only these from which to draw mass. Accretion flows onto and along these filaments must then supply new material in order for the stars to continue growing. Magnetic fields, depending on their configuration, limit or enable these accretion flows, and provide additional support against gravitational collapse.

We use sink particles to represent stars as a practical necessity [Krumholz et al., 2004]. The size of the sink particle is ultimately set by the grid—it needs to have a radius of at least 2 grid cells in order to resolve the Jeans length with at least 4 cells [the Truelove criterion, Truelove et al., 1997]. The sink particle radius in our `MHD1200` simulation was set to $R_{\rm sink} = 1.758 \times 10^{16}$ cm, which is

1175 AU, or 3 grid cells. At this radius, the sink particle completely encloses the protostellar disk, through which much of the accretion takes place [Kuiper et al., 2011a]. Beuther et al. [2009] concluded from a study of 12 protostellar disk candidates, that the disks were fed from infalling outer envelopes and their radii were less than 1000 AU.

Ultimately, the mechanism that shut off accretion in the `MHD1200` simulation was photoionization feedback. We did not include ionizing radiation in Chapter 3, which studied protostellar core collapse and disk accretion. Here, photoionization is cutting off the gas supplied by filamentary flow, strongly limiting the gas reservoir for the star cluster.

4.6 Conclusions

We performed realistic simulations of the evolution of turbulent, magnetized molecular clouds of various mean densities and Alfvén Mach numbers close to unity. To each we applied the same turbulent velocity field, with an RMS Mach number of 6 in both cases. The mass-to-flux ratio was between 2 and 3, consistent with observations. We measured the virial parameter of each simulated cloud. The `MHD500` simulation was initialized in virial balance, whereas the `MHD1200` simulation had an initial virial parameter of 0.56, meaning that the gravitational binding energy substantially exceeded the kinetic energy.

The largest filaments formed in our simulation were on the order of 1–2 pc in size, i.e. the size of our simulated region, and in each simulation we identified the primary structure, which we refer to as the main "trunk" filament using autocorrelation maps of the column density projection. We then measured the distribution of magnetic field vectors relative to the orientation of this primary filament.

We then applied the DisPerSE algorithm to extract the 3D filamentary structure from these simulations. We trace along the filaments and measure the orientation of the filament and local physical variables, such as density and the magnetic field.

In summary, we make two major conclusions:

1. *The gravitational binding of a cloud has a profound effect on relative orientation of B-fields and dense filaments. For strongly bound clouds, we see the magnetic fields aligned with filaments in accretion flows along filaments.* For trans-Alfvénic molecular clouds, coherent magnetic field structure depends on coherent velocity field structure. *The filaments within them are largely the result of supersonic turbulence, not of slow accretion flows along magnetic field lines.* Most clouds are observed to have Alfvén Mach numbers near unity. Simulations tend to focus on cases where the clouds are clearly sub-Alfvénic or super-Alfvénic, but we must also examine transition cases. There is no reason to expect magnetic fields to have large-scale coherent structure in these cases, but in clouds undergoing strong gravitational collapse, as in our `MHD1200` simulation, which has a virial parameter of $\alpha_{\mathrm{vir}} = 0.56$, accretion flows onto the main filament result in a bimodal distribution of magnetic field orientation. Within the main filament, fields are aligned parallel to the long axis. Outside the main filament, magnetic fields show some alignment perpendicular to the main filament. The velocity field shows strong accretion flows radially toward the main filament.

   We compared the `MHD1200` and `MHD500` simulations at the same number of freefall times. The `MHD1200` showed a preference for parallel alignment of the magnetic field relative to the main trunk filament, with accretion flows radially onto the filament and along the filament axis towards the location of the star cluster. The `MHD500`, which had a higher average mass density, showed a much more chaotic magnetic field, but with a trend towards a more perpendicular alignment.

2. *Radiation feedback from massive star formation disrupts the structure of both filaments and magnetic fields.* We looked at the effect of star formation and stellar radiative feedback in the `MHD1200` simulation. Here we form a cluster of 7 massive stars, the most massive of which is about 16 $M_\odot$ and has a luminosity of almost 23,000 $L_\odot$. The other stars in the cluster have masses of about 3 $M_\odot$ or below. The massive star dominates the others and drives the formation of an HII region that appears as a blister on the side of the main trunk filament and expands outwards. This expanding bubble sweeps up a shell of gas and compresses the magnetic field. The magnetic field lines are seen to roughly trace the outline of the expanding shell. Within the bubble and in some parts outside the shell, the magnetic fields are chaotically orientated. Ultimately, the HII region destroys the main trunk filament, cutting off the accretion flow onto the massive star.

Additionally, we find that:

- *Highly bound clouds have a less random ordering of their magnetic fields than weakly bound clouds.* Our `MHD500` simulation was more sub-Alfvénic ($\mathcal{M}_A = 0.92$) than our `MHD1200` simulation ($\mathcal{M}_A = 0.99$), yet it had the more disordered magnetic field structure. We attribute this to the cloud being in virial balance ($\alpha_{\mathrm{vir}} = 0.95$) as opposed to the very bound case of $\alpha_{\mathrm{vir}} = 0.56$ for the `MHD1200` simulation. The kinetic energy of the cloud (including both thermal and non-thermal motions) was on par with both the magnetic field energy and the gravitational binding energy.

- *At small-scale sub-parsec length filaments, the relative magnetic field structure is very complex.* The filamentary and magnetic field structure are influenced by the supersonic, turbulent velocity field, and the globally rotating molecular cloud clump also drags magnetic field lines into the plane of rotation. Over the course of the simulation, and within much less than a freefall time, the distribution of magnetic field orientations spreads out from an initially uniform field aligned with the z-axis to a broad range of angular values.

  The `MHD500` simulation was more compact and had a higher average mass density. There did not appear a strong preference for aligning its filaments either parallel or perpendicular to the magnetic field as the simulation evolved. At late times and at lower density, some of the filaments did appear aligned perpenidcular to the magnetic field, although this was not a strong trend.

In this trans-Alfvénic regime, where magnetic energy balances turbulent kinetic energy, gravity's contribution to the energy budget is a determining factor in understanding how material is channeled onto filaments and the geometry of the magnetic field. We have studied an under-represented part of the parameter space and highlighted the importance of the virial parameter to be considered in tandem with the Alfvén Mach number. Filament-aligned flow helps feed star clusters forming in dense regions within massive filaments, and their radiative feedback, especially via photoionization, may set the lifetimes of molecular cloud clumps. Magnetic fields certainly act to channel diffuse gas onto the main filament trunk and must finally be overcome by gravity if filamentary flow onto a forming cluster is to occur.

Acknowledgments

We thank an anonymous referee for a very useful report that helped to improve our manuscript. We also thank Henrik Beuther, Jouni Kainulainen, Thomas Henning, and Ralf Klessen for stimulating discussions. We would also like to thank Thierry Sousbie for having shared a pre-release version of the DisPerSE code with us. M.K. acknowledges financial support from the Natural Sciences and Engineering Research Council (NSERC) of Canada. R.E.P. is supported by an NSERC Discovery Grant. R.E.P. also thanks the Institut für Theoretische Astrophysik and the Max Planck Institut für Astronomie at Heidelberg for support during his sabbatical leave during the final stages of this work. H.K. was supported by a Banting Fellowship during the early stages of this project. R.E.P. thanks the MPIA and the Institut für Theoretische Astrophysik (ITA) of the Zentrum für Astronomie Heidelberg for support of his sabbatical leave (2015/16) when this project was completed.

The flash code was in part developed by the DOE-supported Alliances Center for Astrophysical Thermonuclear Flashes (ASCI) at the University of Chicago. This work was made possible by the facilities of the Shared Hierarchical Academic Research Computing Network (SHARCNET: www.sharcnet.ca) and Compute/Calcul Canada.

Much of the analysis and data visualization was performed using the

`yt` toolkit[2] by Turk et al. [2011].

[2] http://yt-project.org

Chapter 5

Conclusion

Massive star formation is unlike low-mass star formation because of the importance of radiative feedback during their formation. In many other respects however, their formation has many similarities with the formation of low-mass stars including the importance of core collapse, disk formation, and the launch of powerful MHD jets and outflows in the very earliest stages of their formation. Understanding massive star formation has required diligent effort on the part of observers and theorists employing large surveys and high resolution observations as well as complex numerical simulations.

Early 3D simulations were stymied by the fact that ever more grid resolution was required to follow the dynamics of gravitational collapse to form stars. Even with adaptive grids, this resulted in simulations that could proceed no further than the formation of the first hydrostatic core, at which point the simulation timestep was so short, any further simulation was no longer practical.

The introduction of sink particles partially resolved this problem by drastically simplifying the computation of the evolution of sufficiently dense gas during the collapse process. Jeans-unstable regions could be represented by a particle that exchanged energy and momentum with the grid, and subgrid physics such as protostellar evolution could be modelled efficiently—research I was able to contribute to [Klassen et al., 2012b,a].

Radiation feedback has been implemented via flux-limited diffusion (FLD) approaches in various grid codes, including RAMSES [Commerçon et al., 2011b], CASTRO [Zhang et al., 2011], and PLUTO [Kolb et al., 2013]. This resulted in many simulations of clustered massive star formation that quantified their radiative heating and pressure, and sought quantify the impact that initial conditions had on star formation. These included magnetized and unmagnetized cases, and investigations into the impact of turbulence.

The next step was to improve upon the limitation of FLD approaches to radiative transfer. FLD methods generally lose accuracy in regions transitioning between optically thin and optically thick, especially if the medium is anisotropic or heterogeneous. FLD cannot handle shadows well, and underestimates the radiation pressure in radiatively-driven cavities such as massive stars are expected to produce.

To address these issue, hybrid approaches were considered that split the radiation field into direct and diffuse components, with different radiative transfer methods applied to each. The combination of raytracers and diffusion solvers addresses the above problems, combining the best aspects of each method, while still being an efficient way to solve the radiative transfer problem.

Increasingly high resolution simulations of individual protostellar cores have sought to understand how radiative feedback and magnetic fields act to launch jets, outflows, and drive HII regions and bubbles. The flashlight effect was identified as a mechanism for relieving radiative forces on the inner edges of accretion disks by allowing radiation to escape along polar channels. Simulations by Kuiper et al. [2010b,a, 2011a], introduced a more accurate treatment of the radiation field and showed that radiatively-driven bubbles were stable features of massive star formation and solidified the disk accretion mechanism as the only required means of assembling massive stars. Our own simulations built on this by demonstrating its validity in a 3D rather than axisymmetric geometry with moving sink particles and adaptive grids.

We produced the first ever implementation of such a hybrid radiative transfer scheme in an adaptive Cartesian grid code, which enables a wide range of interesting star formation problems for study. Our first major application of the technique was in the formation of massive stars from high-mass rotating cores, and, among other results summarized below, we showed how radiative feedback suppresses fragmentation and drives a stable outflow bubble, and how disk accretion is sufficient to form massive stars despite their high luminosities.

In the arena of molecular cloud clumps, we have contributed to the understanding of the role that magnetic fields play in filamentary structure [Kirk, Klassen, Pudritz, and Pillsworth, 2015], pioneered new techniques for the study of filamentary structure in 3D AMR simulations and studied the roles that turbulence and gravity play in influencing the magnetic field geometry.

5.1 Summary of results

We now summarize the key conclusions of each chapter of this thesis, highlighting the technical achievements and scientific impact of our results.

5.1.1 Chapter 2: A General Hybrid Radiation Transport Scheme for Star Formation on an Adaptive Grid

- We presented the first implementation of a hybrid radiative transfer scheme on an adaptive mesh with a Cartesian grid, opening up many important problems in star formation for study. Proper radiative transfer is crucial for calculating the correct gas temperature in simulations of molecular clouds. Heating from stars suppresses gas fragmentation and the formation of many low-mass stars. Calculating the correct gas temperature, therefore, has direct implications for the resulting stellar populations, accretion rates onto stars, and the stability of circumstellar disks.

- Our hybrid radiative transfer code also calculates the direct radiation pressure from stars. This is important in driving outflow bubbles (as we showed in Chapter 3) and is a major radiatve feedback mechanism. The radiation pressure from massive clusters plays a dominant role in disrupting and unbinding molecular clouds [Murray et al., 2010].

- In implementing this radiative transfer code in FLASH, we have enabled the study of protostellar disks, and clustered star formation in turbulent, magnetised, filamentary environments. Because FLASH has a modular code framework, our radiative transfer method sits well alongside other physics modules. In the coming months and years, we will add ionizing feedback and multifrequency radiative transfer, which will expand its capabilities even further.

5.1.2 Chapter 3: Simulating the Formation of Massive Protostars: I. Radiative Feedback and Accretion Disks

- We applied our hybrid radiative transfer code to the problem of massive protostellar cores. In three simulations, with initial masses of 30, 100, and 200 $M_\odot$, we formed in each only a single star, with final masses of 5.48, 28.84, and 43.65 $M_\odot$, respectively. The luminosities of the latter two were 30 and 100 times super-Eddington, respectively, driving massive radiative outflow bubbles and winds achieving speeds in excess of 50 km/s.

- The circumstellar disks accreted material from the surrounding envelope of gas. The cores began in rigid body rotation, but the rotation rates of the disks became Keplerian. These disks were observed to become Toomre unstable and formed large spiral arms, yet did not fragment into further stars. We used a Hill analysis to show that the spiral arms are still stable against fragmentation.

- At the onset of gravitational instability and the formation of spiral arms, the accretion rates onto the stars increased dramatically, as much as a factor of 2–10, with the most massive simulation seeing the greatest increase in accretion.

- The accretion disks do not fragment to form a binary or higher-order star system, at least during the course of our simulations. This despite being Toomre-unstable. A Hill analysis showed that the spiral arms were stable. When applying a combined Gammie [2001] and Toomre analysis, we found a disk region at $\sim$ 1200 AU distance from the main star predicted to be unstable, but it had not (as of yet) collapsed to form a star.

- Radiative pressure from the stars as they went super-Eddington drove radiative outflow bubbles, sometimes in successive shells. These did not show signs of radiative Rayleigh-Taylor instabilities, as other authors have observed in pure FLD simulations. Material was observed to flow along the outer shell wall of these bubbles and back onto the circumstellar disk, feeding them.
- Optically thick disks are responsible for the "flashlight effect", i.e. the channeling of radiative flux into the direction of the polar axis. This serves as a pressure release valve for radiation.
- Disk accretion alone is entirely sufficient to explain how massive stars continue to accrete material despite their great luminosities. At the time we terminated our simulations, accretion showed no signs of slowing down significantly and the stars could have gone on to accrete a large fraction of the total core mass.

5.1.3 Chapter 4: Filamentary Flow and Magnetic Geometry in Evolving Cluster-Forming Molecular Cloud Clumps

- We expanded our view to the cluster-forming environments of turbulent, magnetised, filamentary molecular cloud clumps and simulate the formation of a network of filaments in clouds with trans-Alfvénic turbulence, i.e. where the magnetic field energy is approximately balanced by the kinetic energy of the turbulence. The Alfvén Mach number, $\mathcal{M}_A$, characterizes this balance and most molecular clouds are observed to have $\mathcal{M}_A \sim 1$.

- We studied the relationship between the magnetic field geometry, filamentary structure, and accretion flows onto and along filaments. We find that boundedness of the molecular cloud, parameterized by the virial parameter $\alpha_{\rm vir}$, has a huge effect on the large-scale magnetic field geometry. Highly bound clouds show large gravitational infall in the form of accretion flows radially onto the primary filament, or "trunk", seen in our simulations. Magnetic fields are dragged along with the flow and this forms large-scale coherent magnetic field structure.

  In our simulation of a highly-bound massive molecular cloud clump ($\alpha_{\rm vir} = 0.56$), the magnetic fields are oriented parallel within the main filament, but mostly perpendicular to it outside of it. The velocity field shows strong flows radially towards the main filament. For the filaments mapped in 3D, magnetic fields tended to be oriented more parallel to filaments. This trend was erased by radiative feedback from a stellar cluster.

  In our simulation of a molecular cloud clump in virial balance ($\alpha_{\rm vir} = 0.95$), the velocity field was largely random. Large-scale gravitational infall was not visible. Within the main trunk filament, the magnetic field was still seen to align parallel to the long axis, but outside the main filament it appeared more chaotic. For the filaments mapped in 3D, magnetic fields tended to be oriented more perpendicular to filaments.

- Stars form inside the densest regions of the most massive filaments. Our more massive molecular cloud clump simulation included star formation and radiative feedback in the form of photoionisation. We observed the formation of a cluster of a 7 stars, one of which reaches about 16 $M_{\odot}$, an O star. Its luminosity is about 23,000 $L_{\odot}$. This massive star drives the formation of an HII region that eventually engulfs the entire cluster. It begins to disrupt and destroy the main trunk filament in which it formed. Inside the shell wall of the expanding HII region, we see the compression of magnetic field lines that appear to wrap the bubble. This feedback mechanism cuts off the star cluster from accreting new material and limits the masses of the stars in the cluster.

5.2 Outlook

Observations with ALMA are opening a new frontier in star formation research. The spatial resolution of this instrument at 350 microns is ~ 0.01 arcsec, or 50 AU at 5 kpc. This resolution allows for the mapping of molecular clouds in dust continuum to see where fragmentation is occuring. For the first time, astronomers are resolving the disks around massive protostars [Beltran and de Wit, 2015, Johnston et al., 2015] and measuring their kinematics. These papers are just starting to be published, confirming many of the things we simulated and described in this thesis, such as turbulent, filamentary molecular clumps as the sites of potentially high-mass cluster formation [Rathborne et al., 2015], filament fragmentation into cores [Sánchez-Monge et al., 2014, Beltrán et al., 2014], massive star formation mediated by Keplerian accretion disks [Beltrán et al., 2014]; and informing future work, such as the study of magnetised, turbulent, high-mass cores [Tan et al., 2013]. The Atacama Pathfinder Experiment (APEX) is a modified ALMA prototype antenna operating at submm wavelengths capable of polarimetry. Alves et al. [2014] were able to produce submm polarisation maps of a starless core using APEX. This type of polarimetry is still scarce, but we antipicate that future observations will allow for the study of magnetic field structure within star-forming cores. We also anticipate that ALMA observations will reveal isolated massive stars forming within high-mass dense cores.

The *Herschel Space Observatory* has been crucial for revealing at high resolution the filamentary structure of molecular clouds [André et al., 2010]and the properties of high-mass prestellar cores [Motte et al., 2010]. The next generation of infrared telescope will be the *James Webb Space Telescope* (JWST), scheduled for launch in 2018. Operating in the mid-infrared, it will be the successor to the *Hubble Space Telescope* and the *Spitzer Space Telescope* and have unprecedented, background-limited sensitivity. It will allow for the study of deeply embedded massive protostars and star-forming regions such as R136 in 30 Doradus or the Arches cluster.

From a numerical point of view, I expect we will see a wider deployment of hybrid radiative transfer codes like our own. It was recently implemented in the AZEuS code by Ramsey and Dullemond [2015]. There are also various natural extensions to this radiative transfer technique that will make the code more efficient. The current raytracer is limited by memory, since every processor must have access to a representation of the entire grid, not just the decomposed part of the domain. As a memory-saving technique, the raytracer was constructed such that rays are always traced from block corners instead of cell corners. Blocks in FLASH are typically 8x8x8 cells. This results in some loss of resolution in the true ray source position. Adaptive raytracers such as `FERVENT` [Baczynski et al., 2015], reduce the number of rays necessary to cover the domain by adaptively splitting rays as they traverse the grid. Coupled to a chemistry code for calculating the ionization fraction, `FERVENT` can be used to simulate feedback from HII regions—a highly important feedback mechanism, especially when studying star formation in the larger cluster environments, where HII regions can potentially unbind molecular clouds. `FERVENT` will be implemented as the new raytrace and ionization method in FLASH.

Another natural extension of current radiative transfer techniques is to add multifrequency capability. When using hybrid radiative transfer schemes such as ours, this is more relevant for the raytracer, since it carries the direct stellar radiation and has a high UV component. Grey atmosphere approaches underestimate the optical depth of UV radiation, while doing the opposite for IR radiation, which can penetrate much deeper into disks, but carries much less momentum. FLASH already has multigroup FLD, but we did not have time to explore its use in this thesis. Multifrequency raytracing should be a development goal for our research group, but not before the implementation of ionization feedback, which should be the easier problem to solve and more relevant for simulations of star cluster formation, building on [Howard et al., 2014].

After simulating the gravitational collapse of a rotating protostellar core with hybrid radiative feedback, as was done for this thesis, our forthcoming simulations will include turbulence, as protostellar cores are known to be turbulent [Caselli and Myers, 1995, McLaughlin and Pudritz, 1997, McKee and Tan, 2003]. The effect of the including turbulence as part of our simulation initial conditions might be to induce the already gravitationally unstable disk to fragment into one or two more protostars, resulting in a binary or low-order multiple star system. It will also be interesting to study the morphology of the radiatively-driven outflow bubble in a turbulent environment. Future simulations will also look at larger molecular cloud regions to study the effect of radiative feebdack simulated with our hybrid method.

Time also did not permit for the study of magnetized protostellar cores. How will magnetic fields affect the accretion history of the protostar? As the magnetic fields are wound up by rotation and a toroidal component developes during the disk formation stage, a magnetohydrodynamic jet forms. How will outflow bubbles driven by radiative pressure interact with the jet? An indication of the effects of turbulence and magnetic fields can be seen in the 100 $M_\odot$ collapse simulations of [Seifried et al., 2014], which did not include radiative feedback. Here the disk is built up by accretion from multiple filaments in a fairly disorganized magnetic geometry. Hydromagnetic outflows are launched which will precede the radiative bubbles. We anticipate that this will have important effects on the evolution of the radiative bubbles [Seifried et al., 2012b]. And of course, how will these results compare with the future ALMA observations of massive cores?

Taking a step back to consider the larger star forming environment, it will be interesting to see simulations of cluster formation within turbulent, filamentary environments. Will HII regions from evolving massive stars unbind molecular clouds? What are the consequences for estimates of molecular cloud lifetimes and star formation efficiency within molecular clouds? Will these simulations be able to inform galactic models of star formation feedback, which critically affect galactic evolution?

One smaller scales, the code development advanced in this thesis opens up important research possibilities within the study of disks and planet formation. The thermal and kinematic structure of simulated disks influence chemistry models and models of planet formation. FLASH admits the possibility of implementing chemistry codes for time-dependent chemical evolution within protostellar disks. Our code provides a detailed treatment of how disks are heated by their central protostars as the disk is assembled. This has important implications for suppressing gravitational instabilities that may lead to planet formation, at least in the inner parts of those disks [Rogers and Wadsley, 2012].

Massive star formation is at the nexus of much in astrophysics. There are still many open research questions. Simulations such as ours have opened up new avenues to explore and brought new problems within reach. New observations come at the heels of simulations and vice versa. Our understanding of star formation is better than ever, but with new facilities yielding up exciting results and other new facilities planned or proposed, there will undoubtedly be surprises.

Bibliography

A. Abergel, F. Boulanger, A. Mizuno, and Y. Fukui. Comparative analysis of the far-infrared and (13)CO (J = 0-1) emissions of the Taurus complex. *ApJL*, 423:L59–L62, March 1994. doi: 10.1086/187235.

O. Agertz, A. V. Kravtsov, S. N. Leitner, and N. Y. Gnedin. Toward a Complete Accounting of Energy and Momentum from Stellar Feedback in Galaxy Formation Simulations. *ApJ*, 770:25, June 2013. doi: 10.1088/0004-637X/770/1/25.

Y. Aikawa and E. Herbst. Molecular evolution in protoplanetary disks. Two-dimensional distributions and column densities of gaseous molecules. *A&A*, 351:233–246, Nov 1999.

M. L. Alme and J. R. Wilson. X-Ray Emission from a Neutron Star Accreting Material. *ApJ*, 186:1015–1026, Dec 1973. doi: 10.1086/152566.

A. S. Almgren, V. E. Beckner, J. B. Bell, M. S. Day, L. H. Howell, C. C. Joggerst, M. J. Lijewski, A. Nonaka, M. Singer, and M. Zingale. CASTRO: A New Compressible Astrophysical Solver. I. Hydrodynamics and Self-gravity. *ApJ*, 715:1221–1238, June 2010. doi: 10.1088/0004-637X/715/2/1221.

F. O. Alves, P. Frau, J. M. Girart, G. A. P. Franco, F. P. Santos, and H. Wiesemeyer. On the radiation driven alignment of dust grains: Detection of the polarization hole in a starless core. *A&A*, 569:L1, Sept 2014. doi: 10.1051/0004-6361/201424678.

J. Amanatides, A. Woo, et al. A fast voxel traversal algorithm for ray tracing. In *Proceedings of EUROGRAPHICS*, volume 87, pages 3–10, 1987.

P. André, A. Men'shchikov, S. Bontemps, V. Könyves, F. Motte, N. Schneider, P. Didelon, V. Minier, P. Saraceno, D. Ward-Thompson, J. di Francesco, G. White, S. Molinari, L. Testi, A. Abergel, M. Griffin, T. Henning, P. Royer,

B. Merín, R. Vavrek, M. Attard, D. Arzoumanian, C. D. Wilson, P. Ade, H. Aussel, J.-P. Baluteau, M. Benedettini, J.-P. Bernard, J. A. D. L. Blommaert, L. Cambrésy, P. Cox, A. di Giorgio, P. Hargrave, M. Hennemann, M. Huang, J. Kirk, O. Krause, R. Launhardt, S. Leeks, J. Le Pennec, J. Z. Li, P. G. Martin, A. Maury, G. Olofsson, A. Omont, N. Peretto, S. Pezzuto, T. Prusti, H. Roussel, D. Russeil, M. Sauvage, B. Sibthorpe, A. Sicilia-Aguilar, L. Spinoglio, C. Waelkens, A. Woodcraft, and A. Zavagno. From filamentary clouds to prestellar cores to the stellar IMF: Initial highlights from the Herschel Gould Belt Survey. *A&A*, 518:L102, July 2010. doi: 10.1051/0004-6361/201014666.

P. André, J. Di Francesco, D. Ward-Thompson, S.-I. Inutsuka, R. E. Pudritz, and J. E. Pineda. From Filamentary Networks to Dense Cores in Molecular Clouds: Toward a New Paradigm for Star Formation. *Protostars and Planets VI*, pages 27–51, 2014. doi: 10.2458/azu_uapress_9780816531240-ch002.

S. J. Arthur, W. J. Henney, G. Mellema, F. de Colle, and E. Vázquez-Semadeni. Radiation-magnetohydrodynamic simulations of H II regions and their associated PDRs in turbulent molecular clouds. *MNRAS*, 414: 1747–1768, June 2011. doi: 10.1111/j.1365-2966.2011.18507.x.

D. Arzoumanian, P. André, P. Didelon, V. Könyves, N. Schneider, A. Men'shchikov, T. Sousbie, A. Zavagno, S. Bontemps, J. di Francesco, M. Griffin, M. Hennemann, T. Hill, J. Kirk, P. Martin, V. Minier, S. Molinari, F. Motte, N. Peretto, S. Pezzuto, L. Spinoglio, D. Ward-Thompson, G. White, and C. D. Wilson. Characterizing interstellar filaments with Herschel in IC 5146. *A&A*, 529:L6+, May 2011. doi: 10.1051/0004-6361/201116596.

E. Audit and P. Hennebelle. Thermal condensation in a turbulent atomic hydrogen flow. *A&A*, 433:1–13, Apr 2005. doi: 10.1051/0004-6361:20041474.

C. Baczynski, S. C. O. Glover, and R. S. Klessen. Fervent: chemistry-coupled, ionizing and non-ionizing radiative feedback in hydrodynamical simulations. *MNRAS*, 454:380–411, Nov 2015. doi: 10.1093/mnras/stv1906.

J. Ballesteros-Paredes, R. S. Klessen, M.-M. Mac Low, and E. Vazquez-Semadeni. Molecular Cloud Turbulence and Star Formation. *Protostars and Planets V*, pages 63–80, 2007.

J. Bally, W. D. Lanber, A. A. Stark, and R. W. Wilson. Filamentary structure in the Orion molecular cloud. *ApJL*, 312:L45–L49, Jan 1987. doi: 10.1086/184817.

R. Banerjee and R. E. Pudritz. Outflows and Jets from Collapsing Magnetized Cloud Cores. *ApJ*, 641:949–960, Apr 2006. doi: 10.1086/500496.

R. Banerjee and R. E. Pudritz. Massive Star Formation via High Accretion Rates and Early Disk-driven Outflows. *ApJ*, 660:479–488, May 2007. doi: 10.1086/512010.

R. Banerjee, R. E. Pudritz, and L. Holmes. The formation and evolution of protostellar discs; three-dimensional adaptive mesh refinement hydrosimulations of collapsing, rotating Bonnor-Ebert spheres. *MNRAS*, 355:248–272, Nov 2004. doi: 10.1111/j.1365-2966.2004.08316.x.

R. Banerjee, R. E. Pudritz, and D. W. Anderson. Supersonic turbulence, filamentary accretion and the rapid assembly of massive stars and discs. *MNRAS*, 373:1091–1106, Dec 2006. doi: 10.1111/j.1365-2966.2006.11089.x.

R. Banerjee, E. Vázquez-Semadeni, P. Hennebelle, and R. S. Klessen. Clump morphology and evolution in MHD simulations of molecular cloud formation. *MNRAS*, 398:1082–1092, Sept 2009. doi: 10.1111/j.1365-2966.2009.15115.x.

M. R. Bate. The importance of radiative feedback for the stellar initial mass function. *MNRAS*, 392:1363–1380, Feb 2009. doi: 10.1111/j.1365-2966.2008.14165.x.

M. T. Beltran and W. J. de Wit. Accretion disks in luminous young stellar objects. *ArXiv e-prints*, Sept 2015.

M. T. Beltrán, J. Brand, R. Cesaroni, F. Fontani, S. Pezzuto, L. Testi, and S. Molinari. Search for massive protostar candidates in the southern hemisphere. II. Dust continuum emission. *A&A*, 447:221–233, Feb 2006. doi: 10.1051/0004-6361:20053999.

M. T. Beltrán, Á. Sánchez-Monge, R. Cesaroni, M. S. N. Kumar, D. Galli, C. M. Walmsley, S. Etoka, R. S. Furuya, L. Moscadelli, T. Stanke, F. F. S. van der Tak, S. Vig, K.-S. Wang, H. Zinnecker, D. Elia, and E. Schisano. Filamentary structure and Keplerian rotation in the high-mass star-forming region G35.03+0.35 imaged with ALMA. *A&A*, 571:A52, Nov 2014. doi: 10.1051/0004-6361/201424031.

M. J. Berger and P. Colella. Local adaptive mesh refinement for shock hydrodynamics. *Journal of Computational Physics*, 82:64–84, May 1989. doi: 10.1016/0021-9991(89)90035-1.

F. Bertoldi and C. F. McKee. Pressure-confined clumps in magnetized molecular clouds. *ApJ*, 395:140–157, Aug 1992. doi: 10.1086/171638.

H. Beuther, T. K. Sridharan, and M. Saito. Caught in the Act: The Onset of Massive Star Formation. *ApJL*, 634:L185–L188, Dec 2005. doi: 10.1086/498867.

H. Beuther, E. B. Churchwell, C. F. McKee, and J. C. Tan. The Formation of Massive Stars. *Protostars and Planets V*, pages 165–180, 2007.

H. Beuther, A. J. Walsh, and S. N. Longmore. Hot High-Mass Accretion Disk Candidates. *ApJS*, 184:366–386, Oct 2009. doi: 10.1088/0067-0049/184/2/366.

H. Beuther, T. Henning, H. Linz, O. Krause, M. Nielbock, and J. Steinacker. From high-mass starless cores to high-mass protostellar objects. *A&A*, 518: L78, July 2010a. doi: 10.1051/0004-6361/201014532.

H. Beuther, W. H. T. Vlemmings, R. Rao, and F. F. S. van der Tak. Magnetic Field Structure in a High-mass Outflow/Disk System. *ApJL*, 724:L113–L117, Nov 2010b. doi: 10.1088/2041-8205/724/1/L113.

H. Beuther, T. Henning, H. Linz, S. Feng, S. E. Ragan, R. J. Smith, S. Bihr, T. Sakai, and R. Kuiper. Hierarchical fragmentation and collapse signatures in a high-mass starless region. *A&A*, 581:A119, Sept 2015a. doi: 10.1051/0004-6361/201526759.

H. Beuther, S. E. Ragan, K. Johnston, T. Henning, A. Hacar, and J. T. Kainulainen. Filament fragmentation in high-mass star formation. *A&A*, 584:A67, Dec 2015b. doi: 10.1051/0004-6361/201527108.

R. D. Blandford and D. G. Payne. Hydromagnetic flows from accretion discs and the production of radio jets. *MNRAS*, 199:883–903, June 1982.

P. Bodenheimer, H. W. Yorke, M. Rozyczka, and J. E. Tohline. The formation phase of the solar nebula. *ApJ*, 355:651–660, June 1990. doi: 10.1086/168798.

S. Boldyrev. Kolmogorov-Burgers Model for Star-forming Turbulence. *ApJ*, 569:841–845, Apr 2002. doi: 10.1086/339403.

B. P. Bowler, W. H. Waller, S. T. Megeath, B. M. Patten, and M. Tamura. An Infrared Census of Star Formation in the Horsehead Nebula. *AJ*, 137: 3685–3699, March 2009. doi: 10.1088/0004-6256/137/3/3685.

L. Buntemeyer, R. Banerjee, T. Peters, M. Klassen, and R. E. Pudritz. Radiation Hydrodynamics using Characteristics on Adaptive Decomposed Domains for Massively Parallel Star Formation Simulations. *ArXiv e-prints*, Jan 2015.

J. R. Burke and D. J. Hollenbach. The gas-grain interaction in the interstellar medium - Thermal accommodation and trapping. *ApJ*, 265:223–234, Feb 1983. doi: 10.1086/160667.

M. J. Butler and J. C. Tan. Mid-infrared Extinction Mapping of Infrared Dark Clouds. II. The Structure of Massive Starless Cores and Clumps. *ApJ*, 754: 5, July 2012. doi: 10.1088/0004-637X/754/1/5.

S. J. Carey, P. A. Feldman, R. O. Redman, M. P. Egan, J. M. MacLeod, and S. D. Price. Submillimeter Observations of Midcourse Space Experiment Galactic Infrared-Dark Clouds. *ApJL*, 543:L157–L161, Nov 2000. doi: 10.1086/317270.

P. Caselli and P. C. Myers. The Line Width–Size Relation in Massive Cloud Cores. *ApJ*, 446:665, June 1995. doi: 10.1086/175825.

R. Cesaroni. High-mass star forming regions: An ALMA view. *Ap&SS*, 313: 23–28, Jan 2008. doi: 10.1007/s10509-007-9596-3.

N. L. Chapman, P. F. Goldsmith, J. L. Pineda, D. P. Clemens, D. Li, and M. Krčo. The Magnetic Field in Taurus Probed by Infrared Polarization. *ApJ*, 741:21, Nov 2011. doi: 10.1088/0004-637X/741/1/21.

E. I. Chiang and P. Goldreich. Spectral Energy Distributions of T Tauri Stars with Passive Circumstellar Disks. *ApJ*, 490:368–376, Nov 1997.

E. I. Chiang and P. Goldreich. Spectral Energy Distributions of Passive T Tauri Disks: Inclination. *ApJ*, 519:279–284, July 1999. doi: 10.1086/307351.

R. Chini, B. Reipurth, D. Ward-Thompson, J. Bally, L.-Å. Nyman, A. Sievers, and Y. Billawala. Dust Filaments and Star Formation in OMC-2 and OMC-3. *ApJL*, 474:L135–L138, Jan 1997. doi: 10.1086/310436.

R. Chini, V. H. Hoffmeister, A. Nasseri, O. Stahl, and H. Zinnecker. A spectroscopic survey on the multiplicity of high-mass stars. *MNRAS*, 424:1925–1929, Aug 2012. doi: 10.1111/j.1365-2966.2012.21317.x.

J. Cho and A. Lazarian. Compressible Sub-Alfvénic MHD Turbulence in Low- β Plasmas. *Physical Review Letters*, 88(24):245001, June 2002. doi: 10.1103/PhysRevLett.88.245001.

J. Cho and E. T. Vishniac. The Anisotropy of Magnetohydrodynamic Alfvénic Turbulence. *ApJ*, 539:273–282, Aug 2000. doi: 10.1086/309213.

E. Churchwell, C. M. Walmsley, and R. Cesaroni. A survey of ammonia and water vapor emission from ultracompact HII regions. *A&ASS*, 83:119–144, Apr 1990.

P. Colella and P. R. Woodward. The Piecewise Parabolic Method (PPM) for Gas-Dynamical Simulations. *Journal of Computational Physics*, 54:174–201, Sept 1984. doi: 10.1016/0021-9991(84)90143-8.

B. Commerçon, P. Hennebelle, E. Audit, G. Chabrier, and R. Teyssier. Protostellar collapse: radiative and magnetic feedbacks on small-scale fragmentation. *A&A*, 510:L3+, Feb 2010. doi: 10.1051/0004-6361/200913597.

B. Commerçon, P. Hennebelle, and T. Henning. Collapse of Massive Magnetized Dense Cores Using Radiation Magnetohydrodynamics: Early Fragmentation Inhibition. *ApJL*, 742:L9, Nov 2011a. doi: 10.1088/2041-8205/742/1/L9.

B. Commerçon, R. Teyssier, E. Audit, P. Hennebelle, and G. Chabrier. Radiation hydrodynamics with adaptive mesh refinement and application to prestellar core collapse. I. Methods. *A&A*, 529:A35, May 2011b. doi: 10.1051/0004-6361/201015880.

P. A. Crowther, O. Schnurr, R. Hirschi, N. Yusof, R. J. Parker, S. P. Goodwin, and H. A. Kassim. The R136 star cluster hosts several stars whose individual masses greatly exceed the accepted 150 $M_\odot$ stellar mass limit. *MNRAS*, 408: 731–751, Oct 2010. doi: 10.1111/j.1365-2966.2010.17167.x.

R. M. Crutcher. Magnetic Fields in Molecular Clouds: Observations Confront Theory. *ApJ*, 520:706–713, Aug 1999. doi: 10.1086/307483.

R. M. Crutcher. Magnetic Fields in Molecular Clouds. *ARA&A*, 50:29–63, Sept 2012. doi: 10.1146/annurev-astro-081811-125514.

R. M. Crutcher, B. Wandelt, C. Heiles, E. Falgarone, and T. H. Troland. Magnetic Fields in Interstellar Clouds from Zeeman Observations: Inference of Total Field Strengths by Bayesian Analysis. *ApJ*, 725:466–479, Dec 2010. doi: 10.1088/0004-637X/725/1/466.

T. Csengeri, J. S. Urquhart, F. Schuller, F. Motte, S. Bontemps, F. Wyrowski, K. M. Menten, L. Bronfman, H. Beuther, T. Henning, L. Testi, A. Zavagno, and M. Walmsley. The ATLASGAL survey: a catalog of dust condensations in the Galactic plane. *A&A*, 565:A75, May 2014. doi: 10.1051/0004-6361/201322434.

A. J. Cunningham, R. I. Klein, M. R. Krumholz, and C. F. McKee. Radiation-hydrodynamic Simulations of Massive Star Formation with Protostellar Outflows. *ApJ*, 740:107, Oct 2011. doi: 10.1088/0004-637X/740/2/107.

J. E. Dale, B. Ercolano, and I. A. Bonnell. Ionizing feedback from massive stars in massive clusters - II. Disruption of bound clusters by photoionization. *MNRAS*, 424:377–392, July 2012. doi: 10.1111/j.1365-2966.2012.21205.x.

J. E. Dale, J. Ngoumou, B. Ercolano, and I. A. Bonnell. Before the first supernova: combined effects of H II regions and winds on molecular clouds. *MNRAS*, 442:694–712, July 2014. doi: 10.1093/mnras/stu816.

G. D'Angelo and P. Bodenheimer. Three-dimensional Radiation-hydrodynamics Calculations of the Envelopes of Young Planets Embedded in Protoplanetary Disks. *ApJ*, 778:77, Nov 2013. doi: 10.1088/0004-637X/778/1/77.

L. Davis, Jr. and J. L. Greenstein. The Polarization of Starlight by Aligned Dust Grains. *ApJ*, 114:206, Sept 1951. doi: 10.1086/145464.

J. Diego Soler, P. Hennebelle, P. G. Martin, M.-A. Miville-Deschênes, C. Barth Netterfield, and L. M. Fissel. An Imprint of Molecular Cloud Magnetization in the Morphology of the Dust Polarized Emission. *ArXiv e-prints*, March 2013.

E. I. Doran, P. A. Crowther, A. de Koter, C. J. Evans, C. McEvoy, N. R. Walborn, N. Bastian, J. M. Bestenlehner, G. Gräfener, A. Herrero, K. Köhler, J. Maíz Apellániz, F. Najarro, J. Puls, H. Sana, F. R. N. Schneider, W. D. Taylor, J. T. van Loon, and J. S. Vink. The VLT-FLAMES Tarantula Survey. XI. A census of the hot luminous stars and their feedback in 30 Doradus. *A&A*, 558:A134, Oct 2013. doi: 10.1051/0004-6361/201321824.

B. T. Draine and H. M. Lee. Optical properties of interstellar graphite and silicate grains. *ApJ*, 285:89–108, Oct 1984. doi: 10.1086/162480.

A. Dubey, R. Fisher, C. Graziani, G. C. Jordan, IV, D. Q. Lamb, L. B. Reid, P. Rich, D. Sheeler, D. Townsley, and K. Weide. Challenges of Extreme Computing using the FLASH code. In N. V. Pogorelov, E. Audit, & G. P. Zank, editor, *Numerical Modeling of Space Plasma Flows*, volume 385 of *Astronomical Society of the Pacific Conference Series*, pages 145–+, Apr 2008.

A. Dubey, K. Antypas, M. K. Ganapathy, L. B. Reid, K. Riley, D. Sheeler, A. Siegel, and K. Weide. Extensible component-based architecture for flash, a massively parallel, multiphysics simulation code. *Parallel Computing*, 35(10–1):512–522, 2009. ISSN 0167-8191. doi: http://dx.doi.org/10.1016/j.parco.2009.08.001.

C. P. Dullemond. RADMC-3D: A multi-purpose radiative transfer tool, Feb 2012. Astrophysics Source Code Library.

C. P. Dullemond and C. Dominik. The effect of dust settling on the appearance of protoplanetary disks. *A&A*, 421:1075–1086, July 2004. doi: 10.1051/0004-6361:20040284.

C. P. Dullemond and R. Turolla. An efficient algorithm for two-dimensional radiative transfer in axisymmetric circumstellar envelopes and disks. *A&A*, 360:1187–1202, Aug 2000.

M. M. Dunham, H. G. Arce, D. Mardones, J.-E. Lee, B. C. Matthews, A. M. Stutz, and J. P. Williams. Molecular Outflows Driven by Low-mass Protostars. I. Correcting for Underestimates When Measuring Outflow Masses and Dynamical Properties. *ApJ*, 783:29, March 2014. doi: 10.1088/0004-637X/783/1/29.

L. J. Dursi and C. Pfrommer. Draping of Cluster Magnetic Fields over Bullets and Bubbles-Morphology and Dynamic Effects. *ApJ*, 677:993–1018, Apr 2008. doi: 10.1086/529371.

R. Edgar and C. Clarke. A new algorithm for radiative feedback and its application to the formation of massive stars. *MNRAS*, 338:962–972, Feb 2003. doi: 10.1046/j.1365-8711.2003.06139.x.

B. G. Elmegreen and J. Scalo. Interstellar Turbulence I: Observations and Processes. *ARA&A*, 42:211–273, Sept 2004. doi: 10.1146/annurev.astro.41.011802.094859.

L. Ensman. Test problems for radiation and radiation-hydrodynamics codes. *ApJ*, 424:275–291, March 1994. doi: 10.1086/173889.

N. J. Evans, II. Physical Conditions in Regions of Star Formation. *ARA&A*, 37:311–362, 1999. doi: 10.1146/annurev.astro.37.1.311.

N. J. Evans, II, M. M. Dunham, J. K. Jørgensen, M. L. Enoch, B. Merín, E. F. van Dishoeck, J. M. Alcalá, P. C. Myers, K. R. Stapelfeldt, T. L. Huard, L. E. Allen, P. M. Harvey, T. van Kempen, G. A. Blake, D. W. Koerner, L. G. Mundy, D. L. Padgett, and A. I. Sargent. The Spitzer c2d Legacy Results: Star-Formation Rates and Efficiencies; Evolution and Lifetimes. *ApJS*, 181:321, Apr 2009. doi: 10.1088/0067-0049/181/2/321.

D. Falceta-Gonçalves, A. Lazarian, and G. Kowal. Studies of Regular and Random Magnetic Fields in the ISM: Statistics of Polarization Vectors and the Chandrasekhar-Fermi Technique. *ApJ*, 679:537–551, May 2008. doi: 10.1086/587479.

E. Falgarone, T. H. Troland, R. M. Crutcher, and G. Paubert. CN Zeeman measurements in star formation regions. *A&A*, 487:247–252, Aug 2008. doi: 10.1051/0004-6361:200809577.

RobertD. Falgout and UlrikeMeier Yang. hypre: A library of high performance preconditioners. In PeterM.A. Sloot, AlfonsG. Hoekstra, C.J.Kenneth Tan, and JackJ. Dongarra, editors, *Computational Science – ICCS 2002*, volume 2331 of *Lecture Notes in Computer Science*, pages 632–641. Springer Berlin Heidelberg, 2002. ISBN 978-3-540-43594-5. doi: 10.1007/3-540-47789-6_66. URL http://dx.doi.org/10.1007/3-540-47789-6_66.

S. M. Fall, M. R. Krumholz, and C. D. Matzner. Stellar Feedback in Molecular Clouds and its Influence on the Mass Function of Young Star Clusters. *ApJL*, 710:L142–L146, Feb 2010. doi: 10.1088/2041-8205/710/2/L142.

M. Fatenejad, J. Bachan, S. Couch, C. Daley, A. Dubey, N. Flocke, C. Graziani, D. Lamb, D. Lee, A. Scopatz, P. Tzeferacos, and K. Weide. Improvements to the FLASH code for Simulating HEDP Experiments. In *APS Meeting Abstracts*, page 8081P, Oct 2012.

C. Federrath. On the universality of interstellar filaments: theory meets simulations and observations. *MNRAS*, 457:375–388, March 2016. doi: 10.1093/mnras/stv2880.

C. Federrath and R. S. Klessen. The Star Formation Rate of Turbulent Magnetized Clouds: Comparing Theory, Simulations, and Observations. *ApJ*, 761:156, Dec 2012. doi: 10.1088/0004-637X/761/2/156.

C. Federrath, R. S. Klessen, and W. Schmidt. The Density Probability Distribution in Compressible Isothermal Turbulence: Solenoidal versus Compressive Forcing. *ApJL*, 688:L79–L82, Dec 2008. doi: 10.1086/595280.

C. Federrath, R. Banerjee, P. C. Clark, and R. S. Klessen. Modeling Collapse and Accretion in Turbulent Gas Clouds: Implementation and Comparison of Sink Particles in AMR and SPH. *ApJ*, 713:269–290, Apr 2010a. doi: 10.1088/0004-637X/713/1/269.

C. Federrath, R. Banerjee, P. C. Clark, and R. S. Klessen. Modeling Collapse and Accretion in Turbulent Gas Clouds: Implementation and Comparison of Sink Particles in AMR and SPH. *ApJ*, 713:269–290, Apr 2010b. doi: 10.1088/0004-637X/713/1/269.

C. Federrath, R. Banerjee, D. Seifried, P. C. Clark, and R. S. Klessen. Implementing and comparing sink particles in AMR and SPH. In J. Alves,

B. G. Elmegreen, J. M. Girart, & V. Trimble, editor, *IAU Symposium*, volume 270 of *IAU Symposium*, pages 425–428, Apr 2011. doi: 10.1017/S1743921311000755.

C. Federrath, M. Schrön, R. Banerjee, and R. S. Klessen. Modeling Jet and Outflow Feedback during Star Cluster Formation. *ApJ*, 790:128, Aug 2014. doi: 10.1088/0004-637X/790/2/128.

M. Fernández-López, H. G. Arce, L. Looney, L. G. Mundy, S. Storm, P. J. Teuben, K. Lee, D. Segura-Cox, A. Isella, J. J. Tobin, E. Rosolowsky, A. Plunkett, W. Kwon, J. Kauffmann, E. Ostriker, K. Tassis, Y. L. Shirley, and M. Pound. CARMA Large Area Star Formation Survey: Observational Analysis of Filaments in the Serpens South Molecular Cloud. *ApJL*, 790: L19, Aug 2014. doi: 10.1088/2041-8205/790/2/L19.

J. D. Fiege and R. E. Pudritz. Helical fields and filamentary molecular clouds - I. *MNRAS*, 311:85–104, Jan 2000. doi: 10.1046/j.1365-8711.2000.03066.x.

D. F. Figer. An upper limit to the masses of stars. *Nature*, 434:192–194, March 2005. doi: 10.1038/nature03293.

J. Fischera and P. G. Martin. Physical properties of interstellar filaments. *A&A*, 542:A77, June 2012. doi: 10.1051/0004-6361/201218961.

M. Flock, S. Fromang, M. González, and B. Commerçon. Radiation magnetohydrodynamics in global simulations of protoplanetary discs. *A&A*, 560: A43, Dec 2013. doi: 10.1051/0004-6361/201322451.

J. K. J. Fogel, T. J. Bethell, E. A. Bergin, N. Calvet, and D. Semenov. Chemistry of a Protoplanetary Disk with Grain Settling and Lyα Radiation. *ApJ*, 726:29, Jan 2011. doi: 10.1088/0004-637X/726/1/29.

A. Frank and G. Mellema. A radiation-gasdynamical method for numerical simulations of ionized nebulae: Radiation-gasdynamics of PNe I. *A&A*, 289: 937–945, Sept 1994.

B. Fryxell, K. Olson, P. Ricker, F. X. Timmes, M. Zingale, D. Q. Lamb, P. MacNeice, R. Rosner, J. W. Truran, and H. Tufo. FLASH: An Adaptive Mesh Hydrodynamics Code for Modeling Astrophysical Thermonuclear Flashes. *ApJS*, 131:273–334, Nov 2000a. doi: 10.1086/317361.

B. Fryxell, K. Olson, P. Ricker, F. X. Timmes, M. Zingale, D. Q. Lamb, P. MacNeice, R. Rosner, J. W. Truran, and H. Tufo. FLASH: An Adaptive Mesh Hydrodynamics Code for Modeling Astrophysical Thermonuclear Flashes. *ApJS*, 131:273–334, Nov 2000b. doi: 10.1086/317361.

G. Fuller, N. Peretto, A. Traficante, A. Avison, J. Pineda, S. Molinari, and M. Lackington. Filaments and Massive Clumps: Probing The Initial Conditions for Massive Star Formation. *IAU General Assembly*, 22:57928, Aug 2015.

C. F. Gammie. Nonlinear Outcome of Gravitational Instability in Cooling, Gaseous Disks. *ApJ*, 553:174–183, May 2001. doi: 10.1086/320631.

J. M. Girart, M. T. Beltrán, Q. Zhang, R. Rao, and R. Estalella. Magnetic Fields in the Formation of Massive Stars. *Science*, 324:1408–, June 2009. doi: 10.1126/science.1171807.

P. Girichidis, C. Federrath, R. Banerjee, and R. S. Klessen. Importance of the initial conditions for star formation - I. Cloud evolution and morphology. *MNRAS*, 413:2741–2759, June 2011a. doi: 10.1111/j.1365-2966.2011.18348.x.

P. Girichidis, C. Federrath, R. Banerjee, and R. S. Klessen. Importance of the initial conditions for star formation - I. Cloud evolution and morphology. *MNRAS*, 413:2741–2759, June 2011b. doi: 10.1111/j.1365-2966.2011.18348.x.

S. C. O. Glover and P. C. Clark. Is molecular gas necessary for star formation? *MNRAS*, 421:9–19, March 2012. doi: 10.1111/j.1365-2966.2011.19648.x.

P. F. Goldsmith. Molecular Depletion and Thermal Balance in Dark Cloud Cores. *ApJ*, 557:736–746, Aug 2001. doi: 10.1086/322255.

P. F. Goldsmith, M. Heyer, G. Narayanan, R. Snell, D. Li, and C. Brunt. Large-Scale Structure of the Molecular Gas in Taurus Revealed by High Linear Dynamic Range Spectral Line Mapping. *ApJ*, 680:428–445, June 2008. doi: 10.1086/587166.

A. Gomez de Castro and R. E. Pudritz. Global aspects of dynamics and star formation in Taurus. *ApJ*, 395:501–515, Aug 1992. doi: 10.1086/171671.

M. González, E. Audit, and P. Huynh. HERACLES: a three-dimensional radiation hydrodynamics code. *A&A*, 464:429–435, March 2007. doi: 10.1051/0004-6361:20065486.

A. A. Goodman, P. J. Benson, G. A. Fuller, and P. C. Myers. Dense cores in dark clouds. VIII - Velocity gradients. *ApJ*, 406:528–547, Apr 1993. doi: 10.1086/172465.

S. P. Goodwin and P. Kroupa. Limits on the primordial stellar multiplicity. *A&A*, 439:565–569, Aug 2005. doi: 10.1051/0004-6361:20052654.

S. P. Goodwin, A. P. Whitworth, and D. Ward-Thompson. Simulating star formation in molecular cloud cores. I. The influence of low levels of turbulence on fragmentation and multiplicity. *A&A*, 414:633–650, Feb 2004. doi: 10.1051/0004-6361:20031594.

M. Habibi, A. Stolte, W. Brandner, B. Hußmann, and K. Motohara. The Arches cluster out to its tidal radius: dynamical mass segregation and the effect of the extinction law on the stellar mass function. *A&A*, 556:A26, Aug 2013. doi: 10.1051/0004-6361/201220556.

A. Hacar and M. Tafalla. Dense core formation by fragmentation of velocity-coherent filaments in L1517. *A&A*, 533:A34, Sept 2011. doi: 10.1051/0004-6361/201117039.

A. Hacar, M. Tafalla, J. Kauffmann, and A. Kovács. Cores, filaments, and bundles: hierarchical core formation in the L1495/B213 Taurus region. *A&A*, 554:A55, June 2013. doi: 10.1051/0004-6361/201220090.

L. Haemmerlé and T. Peters. Impact of initial models and variable accretion rates on the pre-main-sequence evolution of massive and intermediate-mass stars and the early evolution of H II regions. *MNRAS*, March 2016. doi: 10.1093/mnras/stw517.

T. J. Harries. An algorithm for Monte Carlo time-dependent radiation transfer. *MNRAS*, 416:1500–1508, Sept 2011. doi: 10.1111/j.1365-2966.2011.19147.x.

T. J. Harries. Radiation-hydrodynamical simulations of massive star formation using Monte Carlo radiative transfer - I. Algorithms and numerical methods. *MNRAS*, 448:3156–3166, Apr 2015. doi: 10.1093/mnras/stv158.

T. J. Harries, T. J. Haworth, and D. M. Acreman. Radiation Hydrodynamics Simulations of Massive Star Formation Using Monte Carlo Radiation Transfer. *Astrophysics and Space Science Proceedings*, 36:395, 2014. doi: 10.1007/978-3-319-03041-8_77.

L. Hartmann. Flows, Fragmentation, and Star Formation. I. Low-Mass Stars in Taurus. *ApJ*, 578:914–924, Oct 2002. doi: 10.1086/342657.

L. Hartmann, J. Ballesteros-Paredes, and E. A. Bergin. Rapid Formation of Molecular Clouds and Stars in the Solar Neighborhood. *ApJ*, 562:852–868, Dec 2001. doi: 10.1086/323863.

J. F. Hawley. Non-linear evolution of a non-axisymmetric disc instability. *MNRAS*, 225:677–694, Apr 1987.

J. C. Hayes and M. L. Norman. Beyond Flux-limited Diffusion: Parallel Algorithms for Multidimensional Radiation Hydrodynamics. *ApJS*, 147:197–220, July 2003. doi: 10.1086/374658.

C. Heiles and M. Haverkorn. Magnetic Fields in the Multiphase Interstellar Medium. *Space Sci. Rev.*, 166:293–305, May 2012. doi: 10.1007/s11214-012-9866-4.

C. Heiles, A. A. Goodman, C. F. McKee, and E. G. Zweibel. Magnetic fields in star-forming regions - Observations. In E. H. Levy & J. I. Lunine, editor, *Protostars and Planets III*, pages 279–326, 1993.

F. Heitsch, J. M. Stone, and L. W. Hartmann. Effects of Magnetic Field Strength and Orientation on Molecular Cloud Formation. *ApJ*, 695:248–258, Apr 2009. doi: 10.1088/0004-637X/695/1/248.

P. Hennebelle. On the origin of non-self-gravitating filaments in the ISM. *A&A*, 556:A153, Aug 2013. doi: 10.1051/0004-6361/201321292.

M. Hennemann, F. Motte, N. Schneider, P. Didelon, T. Hill, D. Arzoumanian, S. Bontemps, T. Csengeri, P. André, V. Konyves, F. Louvet, A. Marston, A. Men'shchikov, V. Minier, Q. Nguyen Luong, P. Palmeirim, N. Peretto, M. Sauvage, A. Zavagno, L. D. Anderson, J.-P. Bernard, J. Di Francesco, D. Elia, J. Z. Li, P. G. Martin, S. Molinari, S. Pezzuto, D. Russeil, K. L. J. Rygl, E. Schisano, L. Spinoglio, T. Sousbie, D. Ward-Thompson, and G. J. White. The spine of the swan: a Herschel study of the DR21 ridge and filaments in Cygnus X. *A&A*, 543:L3, July 2012. doi: 10.1051/0004-6361/201219429.

T. Henning, H. Linz, O. Krause, S. Ragan, H. Beuther, R. Launhardt, M. Nielbock, and T. Vasyunina. The seeds of star formation in the filamentary infrared-dark cloud G011.11-0.12. *A&A*, 518:L95, July 2010. doi: 10.1051/0004-6361/201014635.

M. Heyer, H. Gong, E. Ostriker, and C. Brunt. Magnetically Aligned Velocity Anisotropy in the Taurus Molecular Cloud. *ApJ*, 680:420–427, June 2008. doi: 10.1086/587510.

M. H. Heyer and C. M. Brunt. The Universality of Turbulence in Galactic Molecular Clouds. *ApJL*, 615:L45–L48, Nov 2004. doi: 10.1086/425978.

R. H. Hildebrand. Magnetic alignment of grains. *Astrophysical Letters and Communications*, 26:263–275, 1988.

R. H. Hildebrand, M. Dragovan, and G. Novak. Detection of submillimeter polarization in the Orion nebula. *ApJL*, 284:L51–L54, Sept 1984. doi: 10.1086/184351.

T. Hill, M. G. Burton, V. Minier, M. A. Thompson, A. J. Walsh, M. Hunt-Cunningham, and G. Garay. Millimetre continuum observations of southern massive star formation regions - I. SIMBA observations of cold cores. *MNRAS*, 363:405–451, Oct 2005. doi: 10.1111/j.1365-2966.2005.09347.x.

T. Hill, F. Motte, P. Didelon, S. Bontemps, V. Minier, M. Hennemann, N. Schneider, P. André, A. Men'shchikov, L. D. Anderson, D. Arzoumanian, J.-P. Bernard, J. di Francesco, D. Elia, T. Giannini, M. J. Griffin, V. Könyves, J. Kirk, A. P. Marston, P. G. Martin, S. Molinari, Q. Nguyen Luong, N. Peretto, S. Pezzuto, H. Roussel, M. Sauvage, T. Sousbie, L. Testi, D. Ward-Thompson, G. J. White, C. D. Wilson, and A. Zavagno. Filaments and ridges in Vela C revealed by Herschel: from low-mass to high-mass star-forming sites. *A&A*, 533:A94, Sept 2011. doi: 10.1051/0004-6361/201117315.

T. Hoang and A. Lazarian. Radiative torque alignment: essential physical processes. *MNRAS*, 388:117–143, July 2008. doi: 10.1111/j.1365-2966.2008.13249.x.

T. Hosokawa and K. Omukai. Evolution of Massive Protostars with High Accretion Rates. *ApJ*, 691:823–846, Jan 2009. doi: 10.1088/0004-637X/691/1/823.

C. S. Howard, R. E. Pudritz, and W. E. Harris. Cluster formation in molecular clouds - I. Stellar populations, star formation rates and ionizing radiation. *MNRAS*, 438:1305–1317, Feb 2014. doi: 10.1093/mnras/stt2275.

T. Inoue and Y. Fukui. Formation of Massive Molecular Cloud Cores by Cloud-Cloud Collision. *ApJL*, 774:L31, Sept 2013. doi: 10.1088/2041-8205/774/2/L31.

T. Inoue and S.-i. Inutsuka. Two-Fluid Magnetohydrodynamics Simulations of Converging H I Flows in the Interstellar Medium. II. Are Molecular Clouds Generated Directly from a Warm Neutral Medium? *ApJ*, 704:161–169, Oct 2009. doi: 10.1088/0004-637X/704/1/161.

S.-i. Inutsuka and S. M. Miyama. A Production Mechanism for Clusters of Dense Cores. *ApJ*, 480:681–693, May 1997.

A. Isella and A. Natta. The shape of the inner rim in proto-planetary disks. *A&A*, 438:899–907, Aug 2005. doi: 10.1051/0004-6361:20052773.

E. Jacquet and M. R. Krumholz. Radiative Rayleigh-Taylor Instabilities. *ApJ*, 730:116, Apr 2011. doi: 10.1088/0004-637X/730/2/116.

J. H. Jeans. The Stability of a Spherical Nebula. *Philosophical Transactions of the Royal Society of London Series A*, 199:1–53, 1902. doi: 10.1098/rsta.1902.0012.

J. Jijina and F. C. Adams. Infall Collapse Solutions in the Inner Limit: Radiation Pressure and Its Effects on Star Formation. *ApJ*, 462:874, May 1996. doi: 10.1086/177201.

I. Jiménez-Serra, P. Caselli, F. Fontani, J. C. Tan, J. D. Henshaw, J. Kainulainen, and A. K. Hernandez. Gas kinematics and excitation in the filamentary IRDC G035.39-00.33. *MNRAS*, 439:1996–2013, Apr 2014. doi: 10.1093/mnras/stu078.

B. M. Johnson and C. F. Gammie. Nonlinear Outcome of Gravitational Instability in Disks with Realistic Cooling. *ApJ*, 597:131–141, Nov 2003. doi: 10.1086/378392.

K. G. Johnston, T. P. Robitaille, H. Beuther, H. Linz, P. Boley, R. Kuiper, E. Keto, M. G. Hoare, and R. van Boekel. A Keplerian-like disk around the forming O-type star AFGL 4176. *ArXiv e-prints*, Sept 2015.

D. Johnstone and J. Bally. JCMT/SCUBA Submillimeter Wavelength Imaging of the Integral-shaped Filament in Orion. *ApJL*, 510:L49–L53, Jan 1999. doi: 10.1086/311792.

F. D. Kahn. Cocoons around early-type stars. *A&A*, 37:149–162, Dec 1974.

J. Kainulainen and J. C. Tan. High-dynamic-range extinction mapping of infrared dark clouds. Dependence of density variance with sonic Mach number in molecular clouds. *A&A*, 549:A53, Jan 2013. doi: 10.1051/0004-6361/201219526.

E. Keto. The Formation of Massive Stars: Accretion, Disks, and the Development of Hypercompact H II Regions. *ApJ*, 666:976–981, Sept 2007. doi: 10.1086/520320.

H. Kirk, P. C. Myers, T. L. Bourke, R. A. Gutermuth, A. Hedden, and G. W. Wilson. Filamentary Accretion Flows in the Embedded Serpens South Protocluster. *ApJ*, 766:115, Apr 2013. doi: 10.1088/0004-637X/766/2/115.

H. Kirk, M. Klassen, R. Pudritz, and S. Pillsworth. The Role of Turbulence and Magnetic Fields in Simulated Filamentary Structure. *ApJ*, 802:75, Apr 2015. doi: 10.1088/0004-637X/802/2/75.

M. Klassen, T. Peters, and R. E. Pudritz. H II Region Variability and Pre-main-sequence Evolution. *ApJ*, 758:137, Oct 2012a. doi: 10.1088/0004-637X/758/2/137.

M. Klassen, R. E. Pudritz, and T. Peters. Simulating protostellar evolution and radiative feedback in the cluster environment. *MNRAS*, 421:2861–2871, Apr 2012b. doi: 10.1111/j.1365-2966.2012.20523.x.

M. Klassen, R. Kuiper, R. E. Pudritz, T. Peters, R. Banerjee, and L. Buntemeyer. A General Hybrid Radiation Transport Scheme for Star Formation Simulations on an Adaptive Grid. *ApJ*, 797:4, Dec 2014. doi: 10.1088/0004-637X/797/1/4.

M. Klassen, R. E. Pudritz, and H. Kirk. Filamentary flow and magnetic geometry in evolving cluster-forming molecular cloud clumps. *ArXiv e-prints*, May 2016a.

M. Klassen, R. E. Pudritz, R. Kuiper, T. Peters, and R. Banerjee. Simulating the Formation of Massive Protostars. I. Radiative Feedback and Accretion Disks. *ApJ*, 823:28, May 2016b. doi: 10.3847/0004-637X/823/1/28.

R. Klein, B. Posselt, K. Schreyer, J. Forbrich, and T. Henning. A Millimeter Continuum Survey for Massive Protoclusters in the Outer Galaxy. *ApJS*, 161:361–393, Dec 2005. doi: 10.1086/496962.

R. S. Klessen, M. R. Krumholz, and F. Heitsch. Numerical Star-Formation Studies - A Status Report. *Advanced Science Letters*, 4:258–285, Feb 2011. doi: 10.1166/asl.2011.1207.

S. M. Kolb, M. Stute, W. Kley, and A. Mignone. Radiation hydrodynamics integrated in the PLUTO code. *A&A*, 559:A80, Nov 2013. doi: 10.1051/0004-6361/201321499.

V. Könyves, P. André, A. Men'shchikov, N. Schneider, D. Arzoumanian, S. Bontemps, M. Attard, F. Motte, P. Didelon, A. Maury, A. Abergel, B. Ali, J.-P. Baluteau, J.-P. Bernard, L. Cambrésy, P. Cox, J. di Francesco, A. M. di Giorgio, M. J. Griffin, P. Hargrave, M. Huang, J. Kirk, J. Z. Li, P. Martin, V. Minier, S. Molinari, G. Olofsson, S. Pezzuto, D. Russeil, H. Roussel, P. Saraceno, M. Sauvage, B. Sibthorpe, L. Spinoglio, L. Testi, D. Ward-Thompson, G. White, C. D. Wilson, A. Woodcraft, and A. Zavagno. The Aquila prestellar core population revealed by Herschel. *A&A*, 518:L106, July 2010. doi: 10.1051/0004-6361/201014689.

K. M. Kratter and C. D. Matzner. Fragmentation of massive protostellar discs. *MNRAS*, 373:1563–1576, Dec 2006. doi: 10.1111/j.1365-2966.2006.11103.x.

K. M. Kratter, C. D. Matzner, and M. R. Krumholz. Global Models for the Evolution of Embedded, Accreting Protostellar Disks. *ApJ*, 681:375–390, July 2008. doi: 10.1086/587543.

M. R. Krumholz and J. C. Tan. Slow Star Formation in Dense Gas: Evidence and Implications. *ApJ*, 654:304–315, Jan 2007. doi: 10.1086/509101.

M. R. Krumholz, C. F. McKee, and R. I. Klein. Embedding Lagrangian Sink Particles in Eulerian Grids. *ApJ*, 611:399–412, Aug 2004. doi: 10.1086/421935.

M. R. Krumholz, R. I. Klein, and C. F. McKee. Radiation Pressure in Massive Star Formation. In *Protostars and Planets V Posters*, page 8271, 2005a.

M. R. Krumholz, C. F. McKee, and R. I. Klein. How Protostellar Outflows Help Massive Stars Form. *ApJL*, 618:L33–L36, Jan 2005b. doi: 10.1086/427555.

M. R. Krumholz, C. D. Matzner, and C. F. McKee. The Global Evolution of Giant Molecular Clouds. I. Model Formulation and Quasi-Equilibrium Behavior. *ApJ*, 653:361–382, Dec 2006. doi: 10.1086/508679.

M. R. Krumholz, R. I. Klein, and C. F. McKee. Radiation-Hydrodynamic Simulations of Collapse and Fragmentation in Massive Protostellar Cores. *ApJ*, 656:959–979, Feb 2007a. doi: 10.1086/510664.

M. R. Krumholz, R. I. Klein, C. F. McKee, and J. Bolstad. Equations and Algorithms for Mixed-frame Flux-limited Diffusion Radiation Hydrodynamics. *ApJ*, 667:626–643, Sept 2007b. doi: 10.1086/520791.

M. R. Krumholz, R. I. Klein, C. F. McKee, S. S. R. Offner, and A. J. Cunningham. The Formation of Massive Star Systems by Accretion. *Science*, 323:754–, Feb 2009. doi: 10.1126/science.1165857.

R. Kuiper and R. S. Klessen. The reliability of approximate radiation transport methods for irradiated disk studies. *A&A*, 555:A7, July 2013. doi: 10.1051/0004-6361/201321404.

R. Kuiper and H. W. Yorke. On the Effects of Optically Thick Gas (Disks) around Massive Stars. *ApJ*, 763:104, Feb 2013a. doi: 10.1088/0004-637X/763/2/104.

R. Kuiper and H. W. Yorke. On the Simultaneous Evolution of Massive Protostars and Their Host Cores. *ApJ*, 772:61, July 2013b. doi: 10.1088/0004-637X/772/1/61.

R. Kuiper, H. Klahr, H. Beuther, and T. Henning. Circumventing the Radiation Pressure Barrier in the Formation of Massive Stars via Disk Accretion. *ApJ*, 722:1556–1576, Oct 2010a. doi: 10.1088/0004-637X/722/2/1556.

R. Kuiper, H. Klahr, C. Dullemond, W. Kley, and T. Henning. Fast and accurate frequency-dependent radiation transport for hydrodynamics simulations in massive star formation. *A&A*, 511:A81, Feb 2010b. doi: 10.1051/0004-6361/200912355.

R. Kuiper, H. Klahr, H. Beuther, and T. Henning. Three-dimensional Simulation of Massive Star Formation in the Disk Accretion Scenario. *ApJ*, 732: 20, May 2011a. doi: 10.1088/0004-637X/732/1/20.

R. Kuiper, H. Klahr, H. Beuther, and T. Henning. Radiation pressure feedback in the formation of massive stars. *Bulletin de la Societe Royale des Sciences de Liege*, 80:211–216, Jan 2011b.

R. Kuiper, H. Klahr, H. Beuther, and T. Henning. On the stability of radiation-pressure-dominated cavities. *A&A*, 537:A122, Jan 2012. doi: 10.1051/0004-6361/201117808.

R. Kuiper, H. Yorke, and N. J. Turner. Protostellar outflows and radiative feedback from massive stars. *submitted to ApJ*, 2014.

R. Kuiper, H. W. Yorke, and N. J. Turner. Protostellar Outflows and Radiative Feedback from Massive Stars. *ApJ*, 800:86, Feb 2015. doi: 10.1088/0004-637X/800/2/86.

S. Kumar, J. Bachan, S. Couch, C. Daley, A. Dubey, M. Fatenejad, N. Flocke, C. Graziani, D. Q. Lamb, D. Lee, and K. Weide. Improvements to the High Energy Density Physics Capabilities in FLASH. In *APS Meeting Abstracts*, page 9131P, Nov 2011.

C. J. Lada and E. A. Lada. Embedded Clusters in Molecular Clouds. *ARA&A*, 41:57–115, 2003. doi: 10.1146/annurev.astro.41.011802.094844.

D. Q. Lamb, S. M. Couch, A. Dubey, S. Gopal, C. Graziani, D. Lee, K. Weide, and G. Xia. Making FLASH an Open Code for the Academic High-Energy Density Physics Community. In *APS Meeting Abstracts*, page 8010, Nov 2010.

A. Laor and B. T. Draine. Spectroscopic constraints on the properties of dust in active galactic nuclei. *ApJ*, 402:441–468, Jan 1993. doi: 10.1086/172149.

R. B. Larson. Turbulence and star formation in molecular clouds. *MNRAS*, 194:809–826, March 1981.

R. B. Larson. The physics of star formation. *Reports on Progress in Physics*, 66:1651–1697, Oct 2003. doi: 10.1088/0034-4885/66/10/R03.

R. B. Larson and S. Starrfield. On the formation of massive stars and the upper limit of stellar masses. *A&A*, 13:190–197, July 1971a.

R. B. Larson and S. Starrfield. On the formation of massive stars and the upper limit of stellar masses. *A&A*, 13:190–197, July 1971b.

A. Lazarian. Tracing magnetic fields with aligned grains. *J. Quant. Spec. Radiat. Transf.*, 106:225–256, July 2007. doi: 10.1016/j.jqsrt.2007.01.038.

A. Leonardis, H. Bischof, and A. Pinz. *Computer Vision - ECCV 2006: 9th European Conference on Computer Vision, Graz, Austria, May 7-13, 2006 : Proceedings*. Computer Vision– ECCV 2006: 9th European Conference on Computer Vision, Graz, Austria, May 7-13, 2006 : Proceedings. Springer, 2006. ISBN 9783540338321.

C. D. Levermore. Relating Eddington factors to flux limiters. *J. Quant. Spec. Radiat. Transf.*, 31:149–160, Feb 1984. doi: 10.1016/0022-4073(84)90112-2.

C. D. Levermore and G. C. Pomraning. A flux-limited diffusion theory. *ApJ*, 248:321–334, Aug 1981. doi: 10.1086/159157.

H.-b. Li, M. Fang, T. Henning, and J. Kainulainen. The link between magnetic fields and filamentary clouds: bimodal cloud orientations in the Gould Belt. *MNRAS*, 436:3707–3719, Dec 2013. doi: 10.1093/mnras/stt1849.

H.-B. Li, A. Goodman, T. K. Sridharan, M. Houde, Z.-Y. Li, G. Novak, and K. S. Tang. The Link Between Magnetic Fields and Cloud/Star Formation. *Protostars and Planets VI*, pages 101–123, 2014. doi: 10.2458/azu_uapress_9780816531240-ch005.

P. S. Li, C. F. McKee, R. I. Klein, and R. T. Fisher. Sub-Alfvénic Non-ideal MHD Turbulence Simulations with Ambipolar Diffusion. I. Turbulence Statistics. *ApJ*, 684:380–394, Sept 2008. doi: 10.1086/589874.

R. Löhner. An adaptive finite element scheme for transient problems in CFD. *Computer Methods in Applied Mechanics and Engineering*, 61:323–338, Apr 1987. doi: 10.1016/0045-7825(87)90098-3.

D. Lynden-Bell. On why discs generate magnetic towers and collimate jets. *MNRAS*, 341:1360–1372, June 2003. doi: 10.1046/j.1365-8711.2003.06506.x.

M. Lyutikov. Magnetic draping of merging cores and radio bubbles in clusters of galaxies. *MNRAS*, 373:73–78, Nov 2006. doi: 10.1111/j.1365-2966.2006.10835.x.

M.-M. Mac Low and R. S. Klessen. Control of star formation by supersonic turbulence. *Reviews of Modern Physics*, 76:125–194, Jan 2004. doi: 10.1103/RevModPhys.76.125.

P. MacNeice, K. M. Olson, C. Mobarry, R. de Fainchtein, and C. Packer. PARAMESH: A parallel adaptive mesh refinement community toolkit. *Computer Physics Communications*, 126:330–354, Apr 2000. doi: 10.1016/S0010-4655(99)00501-9.

B. C. Matthews, J. D. Fiege, and G. Moriarty-Schieven. Magnetic Fields in Star-forming Molecular Clouds. III. Submillimeter Polarimetry of Intermediate-Mass Cores and Filaments in Orion B. *ApJ*, 569:304–321, Apr 2002. doi: 10.1086/339318.

T. G. Matthews, P. A. R. Ade, F. E. Angilè, S. J. Benton, E. L. Chapin, N. L. Chapman, M. J. Devlin, L. M. Fissel, Y. Fukui, N. N. Gandilo, J. O. Gundersen, P. C. Hargrave, J. Klein, A. L. Korotkov, L. Moncelsi, T. K. Mroczkowski, C. B. Netterfield, G. Novak, D. Nutter, L. Olmi, E. Pascale, F. Poidevin, G. Savini, D. Scott, J. A. Shariff, J. D. Soler, K. Tachihara, N. E. Thomas, M. D. P. Truch, C. E. Tucker, G. S. Tucker, and D. Ward-Thompson. Lupus I Observations from the 2010 Flight of the Balloon-borne Large Aperture Submillimeter Telescope for Polarimetry. *ApJ*, 784:116, Apr 2014. doi: 10.1088/0004-637X/784/2/116.

C. D. Matzner. On the Role of Massive Stars in the Support and Destruction of Giant Molecular Clouds. *ApJ*, 566:302–314, Feb 2002. doi: 10.1086/338030.

C. D. Matzner and R. Krasnopolsky. Radiative bubbles blown by slow stellar winds. *MNRAS*, 386:903–908, May 2008. doi: 10.1111/j.1365-2966.2008.13056.x.

C. D. Matzner and C. F. McKee. Bipolar Molecular Outflows Driven by Hydromagnetic Protostellar Winds. *ApJL*, 526:L109–L112, Dec 1999. doi: 10.1086/312376.

C. F. McKee and E. C. Ostriker. Theory of Star Formation. *ARA&A*, 45: 565–687, Sept 2007a. doi: 10.1146/annurev.astro.45.051806.110602.

C. F. McKee and E. C. Ostriker. Theory of Star Formation. *ARA&A*, 45: 565–687, Sept 2007b. doi: 10.1146/annurev.astro.45.051806.110602.

C. F. McKee and J. C. Tan. The Formation of Massive Stars from Turbulent Cores. *ApJ*, 585:850–871, March 2003. doi: 10.1086/346149.

C. F. McKee and E. G. Zweibel. On the virial theorem for turbulent molecular clouds. *ApJ*, 399:551–562, Nov 1992. doi: 10.1086/171946.

C. F. McKee, E. G. Zweibel, A. A. Goodman, and C. Heiles. Magnetic Fields in Star-Forming Regions - Theory. In E. H. Levy & J. I. Lunine, editor, *Protostars and Planets III*, pages 327–+, 1993.

D. E. McLaughlin and R. E. Pudritz. Gravitational Collapse and Star Formation in Logotropic and Nonisothermal Spheres. *ApJ*, 476:750–765, Feb 1997.

S. T. Megeath, R. Gutermuth, J. Muzerolle, E. Kryukova, K. Flaherty, J. L. Hora, L. E. Allen, L. Hartmann, P. C. Myers, J. L. Pipher, J. Stauffer, E. T. Young, and G. G. Fazio. The Spitzer Space Telescope Survey of the Orion A and B Molecular Clouds. I. A Census of Dusty Young Stellar Objects and a Study of Their Mid-infrared Variability. *AJ*, 144:192, Dec 2012. doi: 10.1088/0004-6256/144/6/192.

G. Mellema and P. Lundqvist. Stellar wind bubbles around WR and [WR] stars. *A&A*, 394:901–909, Nov 2002. doi: 10.1051/0004-6361:20021164.

A. Men'shchikov. A multi-scale filament extraction method: getfilaments. *A&A*, 560:A63, Dec 2013. doi: 10.1051/0004-6361/201321885.

A. Men'shchikov, P. André, P. Didelon, V. Könyves, N. Schneider, F. Motte, S. Bontemps, D. Arzoumanian, M. Attard, A. Abergel, J.-P. Baluteau, J.-P. Bernard, L. Cambrésy, P. Cox, J. di Francesco, A. M. di Giorgio, M. Griffin, P. Hargrave, M. Huang, J. Kirk, J. Z. Li, P. Martin, V. Minier, M.-A. Miville-Deschênes, S. Molinari, G. Olofsson, S. Pezzuto, H. Roussel, D. Russeil, P. Saraceno, M. Sauvage, B. Sibthorpe, L. Spinoglio, L. Testi, D. Ward-Thompson, G. White, C. D. Wilson, A. Woodcraft, and A. Zavagno. Filamentary structures and compact objects in the Aquila and Polaris clouds observed by Herschel. *A&A*, 518:L103, July 2010. doi: 10.1051/0004-6361/201014668.

A. Mignone, G. Bodo, S. Massaglia, T. Matsakos, O. Tesileanu, C. Zanni, and A. Ferrari. PLUTO: A Numerical Code for Computational Astrophysics. *ApJS*, 170:228–242, May 2007a. doi: 10.1086/513316.

A. Mignone, G. Bodo, S. Massaglia, T. Matsakos, O. Tesileanu, C. Zanni, and A. Ferrari. PLUTO: A Numerical Code for Computational Astrophysics. *ApJS*, 170:228–242, May 2007b. doi: 10.1086/513316.

D. Mihalas and B. W. Mihalas. *Foundations of radiation hydrodynamics*. Oxford University Press, 1984.

G. N. Minerbo. Maximum entropy Eddington factors. *J. Quant. Spec. Radiat. Transf.*, 20:541–545, 1978. doi: 10.1016/0022-4073(78)90024-9.

M.-A. Miville-Deschênes, P. G. Martin, A. Abergel, J.-P. Bernard, F. Boulanger, G. Lagache, L. D. Anderson, P. André, H. Arab, J.-P. Baluteau, K. Blagrave, S. Bontemps, M. Cohen, M. Compiegne, P. Cox, E. Dartois, G. Davis, R. Emery, T. Fulton, C. Gry, E. Habart, M. Huang, C. Joblin, S. C. Jones, J. Kirk, T. Lim, S. Madden, G. Makiwa, A. Menshchikov, S. Molinari, H. Moseley, F. Motte, D. A. Naylor, K. Okumura, D. Pinheiro Gonçalves, E. Polehampton, J. A. Rodón, D. Russeil, P. Saraceno, N. Schneider, S. Sidher, L. Spencer, B. Swinyard, D. Ward-Thompson, G. J. White, and A. Zavagno. Herschel-SPIRE observations of the Polaris flare: Structure of the diffuse interstellar medium at the sub-parsec scale. *A&A*, 518: L104, July 2010. doi: 10.1051/0004-6361/201014678.

A. Mizuno, T. Onishi, Y. Yonekura, T. Nagahama, H. Ogawa, and Y. Fukui. Overall distribution of dense molecular gas and star formation in the the Taurus cloud complex. *ApJL*, 445:L161–L165, June 1995. doi: 10.1086/187914.

N. Moeckel and A. Burkert. The Formation of Filamentary Bundles in Turbulent Molecular Clouds. *ApJ*, 807:67, July 2015. doi: 10.1088/0004-637X/807/1/67.

S. Molinari, B. Swinyard, J. Bally, M. Barlow, J.-P. Bernard, P. Martin, T. Moore, A. Noriega-Crespo, R. Plume, L. Testi, A. Zavagno, A. Abergel, B. Ali, L. Anderson, P. André, J.-P. Baluteau, C. Battersby, M. T. Beltrán, M. Benedettini, N. Billot, J. Blommaert, S. Bontemps, F. Boulanger, J. Brand, C. Brunt, M. Burton, L. Calzoletti, S. Carey, P. Caselli, R. Cesaroni, J. Cernicharo, S. Chakrabarti, A. Chrysostomou, M. Cohen, M. Compiegne, P. de Bernardis, G. de Gasperis, A. M. di Giorgio, D. Elia, F. Faustini, N. Flagey, Y. Fukui, G. A. Fuller, K. Ganga, P. Garcia-Lario, J. Glenn, P. F. Goldsmith, M. Griffin, M. Hoare, M. Huang, D. Ikhenaode, C. Joblin, G. Joncas, M. Juvela, J. M. Kirk, G. Lagache, J. Z. Li, T. L. Lim, S. D. Lord, M. Marengo, D. J. Marshall, S. Masi, F. Massi, M. Matsuura, V. Minier, M.-A. Miville-Deschênes, L. A. Montier, L. Morgan, F. Motte, J. C. Mottram, T. G. Müller, P. Natoli, J. Neves, L. Olmi, R. Paladini, D. Paradis, H. Parsons, N. Peretto, M. Pestalozzi, S. Pezzuto, F. Piacentini, L. Piazzo, D. Polychroni, M. Pomarès, C. C. Popescu, W. T. Reach, I. Ristorcelli, J.-F. Robitaille, T. Robitaille, J. A. Rodón, A. Roy, P. Royer, D. Russeil, P. Saraceno, M. Sauvage, P. Schilke, E. Schisano, N. Schneider,

F. Schuller, B. Schulz, B. Sibthorpe, H. A. Smith, M. D. Smith, L. Spinoglio, D. Stamatellos, F. Strafella, G. S. Stringfellow, E. Sturm, R. Taylor, M. A. Thompson, A. Traficante, R. J. Tuffs, G. Umana, L. Valenziano, R. Vavrek, M. Veneziani, S. Viti, C. Waelkens, D. Ward-Thompson, G. White, L. A. Wilcock, F. Wyrowski, H. W. Yorke, and Q. Zhang. Clouds, filaments, and protostars: The Herschel Hi-GAL Milky Way. *A&A*, 518:L100, July 2010. doi: 10.1051/0004-6361/201014659.

F. Motte, S. Bontemps, P. Schilke, N. Schneider, K. M. Menten, and D. Broguière. The earliest phases of high-mass star formation: a 3 square degree millimeter continuum mapping of Cygnus X. *A&A*, 476:1243–1260, Dec 2007. doi: 10.1051/0004-6361:20077843.

F. Motte, A. Zavagno, S. Bontemps, N. Schneider, M. Hennemann, J. di Francesco, P. André, P. Saraceno, M. Griffin, A. Marston, D. Ward-Thompson, G. White, V. Minier, A. Men'shchikov, T. Hill, A. Abergel, L. D. Anderson, H. Aussel, Z. Balog, J.-P. Baluteau, J.-P. Bernard, P. Cox, T. Csengeri, L. Deharveng, P. Didelon, A.-M. di Giorgio, P. Hargrave, M. Huang, J. Kirk, S. Leeks, J. Z. Li, P. Martin, S. Molinari, Q. Nguyen-Luong, G. Olofsson, P. Persi, N. Peretto, S. Pezzuto, H. Roussel, D. Russeil, S. Sadavoy, M. Sauvage, B. Sibthorpe, L. Spinoglio, L. Testi, D. Teyssier, R. Vavrek, C. D. Wilson, and A. Woodcraft. Initial highlights of the HOBYS key program, the Herschel imaging survey of OB young stellar objects. *A&A*, 518:L77, July 2010. doi: 10.1051/0004-6361/201014690.

T. C. Mouschovias and L. Spitzer, Jr. Note on the collapse of magnetic interstellar clouds. *ApJ*, 210:326, Dec 1976. doi: 10.1086/154835.

N. Murray, E. Quataert, and T. A. Thompson. The Disruption of Giant Molecular Clouds by Radiation Pressure & the Efficiency of Star Formation in Galaxies. *ApJ*, 709:191–209, Jan 2010. doi: 10.1088/0004-637X/709/1/191.

N. Murray, B. Ménard, and T. A. Thompson. Radiation Pressure from Massive Star Clusters as a Launching Mechanism for Super-galactic Winds. *ApJ*, 735:66, July 2011. doi: 10.1088/0004-637X/735/1/66.

S. D. Murray, J. I. Castor, R. I. Klein, and C. F. McKee. Accretion disk coronae in high-luminosity systems. *ApJ*, 435:631–646, Nov 1994. doi: 10.1086/174842.

P. C. Myers. Filamentary Structure of Star-forming Complexes. *ApJ*, 700: 1609–1625, Aug 2009. doi: 10.1088/0004-637X/700/2/1609.

P. C. Myers and G. A. Fuller. Density structure and star formation in dense cores with thermal and nonthermal motions. *ApJ*, 396:631–642, Sept 1992. doi: 10.1086/171744.

P. C. Myers and A. A. Goodman. Evidence for magnetic and virial equilibrium in molecular clouds. *ApJL*, 326:L27–L30, March 1988. doi: 10.1086/185116.

Z. Nagy, T. Megeath, W. J. Fischer, J. Tobin, A. M. Stutz, B. Ali, T. Wilson, C. Poteet, T. Stanke, J. Di Francesco, and J. Booker. Measuring rotation in protostellar envelopes: ALMA Observations of Edge-On Orion Protostars. *IAU General Assembly*, 22:54106, Aug 2015.

F. Nakamura and Z.-Y. Li. Magnetically Regulated Star Formation in Three Dimensions: The Case of the Taurus Molecular Cloud Complex. *ApJ*, 687: 354–375, Nov 2008. doi: 10.1086/591641.

T. Nakano. Conditions for the formation of massive stars through nonspherical accretion. *ApJ*, 345:464–471, Oct 1989. doi: 10.1086/167919.

T. Nakano, T. Hasegawa, and C. Norman. The Mass of a Star Formed in a Cloud Core: Theory and Its Application to the Orion A Cloud. *ApJ*, 450: 183, Sept 1995. doi: 10.1086/176130.

Q. Nguyen Luong, F. Motte, M. Hennemann, T. Hill, K. L. J. Rygl, N. Schneider, S. Bontemps, A. Men'shchikov, P. André, N. Peretto, L. D. Anderson, D. Arzoumanian, L. Deharveng, P. Didelon, J. di Francesco, M. J. Griffin, J. M. Kirk, V. Könyves, P. G. Martin, A. Maury, V. Minier, S. Molinari, M. Pestalozzi, S. Pezzuto, M. Reid, H. Roussel, M. Sauvage, F. Schuller, L. Testi, D. Ward-Thompson, G. J. White, and A. Zavagno. The Herschel view of massive star formation in G035.39-00.33: dense and cold filament of W48 undergoing a mini-starburst. *A&A*, 535:A76, Nov 2011. doi: 10.1051/0004-6361/201117831.

M. Nielbock, R. Launhardt, J. Steinacker, A. M. Stutz, Z. Balog, H. Beuther, J. Bouwman, T. Henning, P. Hily-Blant, J. Kainulainen, O. Krause, H. Linz, N. Lippok, S. Ragan, C. Risacher, and A. Schmiedeke. The Earliest Phases of Star formation (EPoS) observed with Herschel: the dust temperature and density distributions of B68. *A&A*, 547:A11, Nov 2012. doi: 10.1051/0004-6361/201219139.

M. L. Norman, D. R. Reynolds, G. C. So, R. P. Harkness, and J. H. Wise. Fully Coupled Simulation of Cosmic Reionization. I. Numerical Methods and Tests. *ApJS*, 216:16, Jan 2015. doi: 10.1088/0067-0049/216/1/16.

G. Novak, J. L. Dotson, C. D. Dowell, P. F. Goldsmith, R. H. Hildebrand, S. R. Platt, and D. A. Schleuning. Polarized Far-Infrared Emission from the Core and Envelope of the Sagittarius B2 Molecular Cloud. *ApJ*, 487: 320–327, Sept 1997.

D. Nutter, J. M. Kirk, D. Stamatellos, and D. Ward-Thompson. SCUBA and Spitzer observations of the Taurus molecular cloud - pulling the bull's tail. *MNRAS*, 384:755–763, Feb 2008. doi: 10.1111/j.1365-2966.2007.12750.x.

B. B. Ochsendorf, S. Verdolini, N. L. J. Cox, O. Berné, L. Kaper, and A. G. G. M. Tielens. Radiation-pressure-driven dust waves inside bursting interstellar bubbles. *A&A*, 566:A75, June 2014. doi: 10.1051/0004-6361/201423545.

S. S. R. Offner, R. I. Klein, C. F. McKee, and M. R. Krumholz. The Effects of Radiative Transfer on Low-Mass Star Formation. *ApJ*, 703:131–149, Sept 2009. doi: 10.1088/0004-637X/703/1/131.

L. Olmi, E. D. Araya, E. L. Chapin, A. Gibb, P. Hofner, P. G. Martin, and C. M. Poventud. High Angular Resolution Observations of Four Candidate BLAST High-mass Starless Cores. *ApJ*, 715:1132–1142, June 2010. doi: 10.1088/0004-637X/715/2/1132.

K. M. Olson, P. MacNeice, B. Fryxell, P. Ricker, F. X. Timmes, and M. Zingale. PARAMESH: A Parallel, Adaptive Mesh Refinement Toolkit and Performance Oof the ASCI/FLASH code. In *American Astronomical Society Meeting Abstracts*, volume 31 of *Bulletin of the American Astronomical Society*, pages 1430–+, Dec 1999.

E. C. Ostriker, J. M. Stone, and C. F. Gammie. Density, Velocity, and Magnetic Field Structure in Turbulent Molecular Cloud Models. *ApJ*, 546:980–1005, Jan 2001. doi: 10.1086/318290.

J. Ostriker. The Equilibrium of Polytropic and Isothermal Cylinders. *ApJ*, 140:1056, Oct 1964. doi: 10.1086/148005.

P. Padoan. Supersonic turbulent flows and the fragmentation of a cold medium. *MNRAS*, 277:377–388, Nov 1995.

P. Padoan and Å. Nordlund. The Stellar Initial Mass Function from Turbulent Fragmentation. *ApJ*, 576:870–879, Sept 2002. doi: 10.1086/341790.

P. Padoan, M. Juvela, A. A. Goodman, and Å. Nordlund. The Turbulent Shock Origin of Proto-Stellar Cores. *ApJ*, 553:227–234, May 2001. doi: 10.1086/320636.

F. Palla and S. W. Stahler. The Pre-Main-Sequence Evolution of Intermediate-Mass Stars. *ApJ*, 418:414, Nov 1993. doi: 10.1086/173402.

P. Palmeirim, P. André, J. Kirk, D. Ward-Thompson, D. Arzoumanian, V. Könyves, P. Didelon, N. Schneider, M. Benedettini, S. Bontemps, J. Di Francesco, D. Elia, M. Griffin, M. Hennemann, T. Hill, P. G. Martin, A. Men'shchikov, S. Molinari, F. Motte, Q. Nguyen Luong, D. Nutter, N. Peretto, S. Pezzuto, A. Roy, K. L. J. Rygl, L. Spinoglio, and G. L. White. Herschel view of the Taurus B211/3 filament and striations: evidence of filamentary growth? *A&A*, 550:A38, Feb 2013. doi: 10.1051/0004-6361/201220500.

J. C. B. Papaloizou and J. E. Pringle. The dynamical stability of differentially rotating discs with constant specific angular momentum. *MNRAS*, 208: 721–750, June 1984.

I. Pascucci, S. Wolf, J. Steinacker, C. P. Dullemond, T. Henning, G. Niccolini, P. Woitke, and B. Lopez. The 2D continuum radiative transfer problem. Benchmark results for disk configurations. *A&A*, 417:793–805, Apr 2004. doi: 10.1051/0004-6361:20040017.

B. Paxton. EZ to Evolve ZAMS Stars: A Program Derived from Eggleton's Stellar Evolution Code. *PASP*, 116:699–701, July 2004. doi: 10.1086/422345.

N. Peretto, P. André, V. Könyves, N. Schneider, D. Arzoumanian, P. Palmeirim, P. Didelon, M. Attard, J. P. Bernard, J. Di Francesco, D. Elia, M. Hennemann, T. Hill, J. Kirk, A. Men'shchikov, F. Motte, Q. Nguyen Luong, H. Roussel, T. Sousbie, L. Testi, D. Ward-Thompson, G. J. White, and A. Zavagno. The Pipe Nebula as seen with Herschel: formation of filamentary structures by large-scale compression? *A&A*, 541:A63, May 2012. doi: 10.1051/0004-6361/201118663.

N. Peretto, G. A. Fuller, A. Duarte-Cabral, A. Avison, P. Hennebelle, J. E. Pineda, P. André, S. Bontemps, F. Motte, N. Schneider, and S. Molinari. Global collapse of molecular clouds as a formation mechanism for the most massive stars. *A&A*, 555:A112, July 2013. doi: 10.1051/0004-6361/201321318.

T. Peters, R. Banerjee, R. S. Klessen, M.-M. Mac Low, R. Galván-Madrid, and E. R. Keto. H II Regions: Witnesses to Massive Star Formation. *ApJ*, 711:1017–1028, March 2010a. doi: 10.1088/0004-637X/711/2/1017.

T. Peters, R. Banerjee, R. S. Klessen, M.-M. Mac Low, R. Galván-Madrid, and E. R. Keto. H II Regions: Witnesses to Massive Star Formation. *ApJ*, 711:1017–1028, March 2010b. doi: 10.1088/0004-637X/711/2/1017.

T. Peters, R. S. Klessen, M.-M. Mac Low, and R. Banerjee. Limiting Accretion onto Massive Stars by Fragmentation-induced Starvation. *ApJ*, 725:134–145, Dec 2010c. doi: 10.1088/0004-637X/725/1/134.

T. Peters, M.-M. Mac Low, R. Banerjee, R. S. Klessen, and C. P. Dullemond. Understanding Spatial and Spectral Morphologies of Ultracompact H II Regions. *ApJ*, 719:831–843, Aug 2010d. doi: 10.1088/0004-637X/719/1/831.

T. Peters, R. Banerjee, R. S. Klessen, and M.-M. Mac Low. The Interplay of Magnetic Fields, Fragmentation, and Ionization Feedback in High-mass Star Formation. *ApJ*, 729:72, March 2011. doi: 10.1088/0004-637X/729/1/72.

T. Peters, P. D. Klaassen, M.-M. Mac Low, R. S. Klessen, and R. Banerjee. Are Molecular Outflows around High-mass Stars Driven by Ionization Feedback? *ApJ*, 760:91, Nov 2012. doi: 10.1088/0004-637X/760/1/91.

T. Peters, P. D. Klaassen, M.-M. Mac Low, M. Schrön, C. Federrath, M. D. Smith, and R. S. Klessen. Collective Outflow from a Small Multiple Stellar System. *ApJ*, 788:14, June 2014. doi: 10.1088/0004-637X/788/1/14.

J. P. Phillips. Rotation in molecular clouds. *A&ASS*, 134:241–254, Jan 1999. doi: 10.1051/aas:1999137.

G. L. Pilbratt, J. R. Riedinger, T. Passvogel, G. Crone, D. Doyle, U. Gageur, A. M. Heras, C. Jewell, L. Metcalfe, S. Ott, and M. Schmidt. Herschel Space Observatory. An ESA facility for far-infrared and submillimetre astronomy. *A&A*, 518:L1, July 2010. doi: 10.1051/0004-6361/201014759.

T. Pillai, F. Wyrowski, S. J. Carey, and K. M. Menten. Ammonia in infrared dark clouds. *A&A*, 450:569–583, May 2006. doi: 10.1051/0004-6361:20054128.

J. E. Pineda, A. A. Goodman, H. G. Arce, P. Caselli, J. B. Foster, P. C. Myers, and E. W. Rosolowsky. Direct Observation of a Sharp Transition to Coherence in Dense Cores. *ApJL*, 712:L116–L121, March 2010. doi: 10.1088/2041-8205/712/1/L116.

L. Pirogov, I. Zinchenko, P. Caselli, L. E. B. Johansson, and P. C. Myers. N_2H^+(1-0) survey of massive molecular cloud cores. *A&A*, 405:639–654, July 2003. doi: 10.1051/0004-6361:20030659.

L. E. Pirogov. Density profiles in molecular cloud cores associated with high-mass star-forming regions. *Astronomy Reports*, 53:1127–1135, Dec 2009. doi: 10.1134/S1063772909120051.

Planck Collaboration XIX. Planck intermediate results. XIX. An overview of the polarized thermal emission from Galactic dust. *A&A*, 576:A104, Apr 2015. doi: 10.1051/0004-6361/201424082.

Planck Collaboration XXXII. Planck intermediate results. XXXII. The relative orientation between the magnetic field and structures traced by interstellar dust. *A&A*, 586:A135, Feb 2016. doi: 10.1051/0004-6361/201425044.

Planck Collaboration XXXIII. Planck intermediate results. XXXIII. Signature of the magnetic field geometry of interstellar filaments in dust polarization maps. *A&A*, 586:A136, Feb 2016. doi: 10.1051/0004-6361/201425305.

Planck Collaboration XXXIV. Planck intermediate results. XXXIV. The magnetic field structure in the Rosette Nebula. *A&A*, 586:A137, Feb 2016. doi: 10.1051/0004-6361/201525616.

Planck Collaboration XXXV. Planck intermediate results. XXXV. Probing the role of the magnetic field in the formation of structure in molecular clouds. *A&A*, 586:A138, Feb 2016. doi: 10.1051/0004-6361/201525896.

J. B. Pollack, D. Hollenbach, S. Beckwith, D. P. Simonelli, T. Roush, and W. Fong. Composition and radiative properties of grains in molecular clouds and accretion disks. *ApJ*, 421:615–639, Feb 1994. doi: 10.1086/173677.

D. Polychroni, E. Schisano, D. Elia, A. Roy, S. Molinari, P. Martin, P. André, D. Turrini, K. L. J. Rygl, J. Di Francesco, M. Benedettini, G. Busquet, A. M. di Giorgio, M. Pestalozzi, S. Pezzuto, D. Arzoumanian, S. Bontemps, M. Hennemann, T. Hill, V. Könyves, A. Men'shchikov, F. Motte, Q. Nguyen-Luong, N. Peretto, N. Schneider, and G. White. Two Mass Distributions in the L 1641 Molecular Clouds: The Herschel Connection of Dense Cores and Filaments in Orion A. *ApJL*, 777:L33, Nov 2013. doi: 10.1088/2041-8205/777/2/L33.

D. J. Price and M. R. Bate. Inefficient star formation: the combined effects of magnetic fields and radiative feedback. *MNRAS*, 398:33–46, Sept 2009. doi: 10.1111/j.1365-2966.2009.14969.x.

J. E. Pringle. Self-induced warping of accretion discs. *MNRAS*, 281:357–361, July 1996. doi: 10.1093/mnras/281.1.357.

R. Pudritz. The formation of star clusters - 3D simulations of hydrodynamic turbulence in self-gravitating gas. In *CfA Colloquium Lecture Series Talk*, March 2004.

R. E. Pudritz and N. K.-R. Kevlahan. Shock interactions, turbulence and the origin of the stellar mass spectrum. *Philosophical Transactions of the Royal Society of London Series A*, 371:20248, Oct 2013. doi: 10.1098/rsta.2012.0248.

R. E. Pudritz and C. A. Norman. Centrifugally driven winds from contracting molecular disks. *ApJ*, 274:677–697, Nov 1983. doi: 10.1086/161481.

R. E. Pudritz, R. Ouyed, C. Fendt, and A. Brandenburg. Disk Winds, Jets, and Outflows: Theoretical and Computational Foundations. *Protostars and Planets V*, pages 277–294, 2007a.

R. E. Pudritz, R. Ouyed, C. Fendt, and A. Brandenburg. Disk Winds, Jets, and Outflows: Theoretical and Computational Foundations. *Protostars and Planets V*, pages 277–294, 2007b.

R. R. Rafikov. The local axisymmetric instability criterion in a thin, rotating, multicomponent disc. *MNRAS*, 323:445–452, May 2001. doi: 10.1046/j.1365-8711.2001.04201.x.

J. P. Ramsey and C. P. Dullemond. Radiation hydrodynamics including irradiation and adaptive mesh refinement with AZEuS. I. Methods. *A&A*, 574: A81, Feb 2015. doi: 10.1051/0004-6361/201424954.

J. M. Rathborne, J. M. Jackson, and R. Simon. Infrared Dark Clouds: Precursors to Star Clusters. *ApJ*, 641:389–405, Apr 2006. doi: 10.1086/500423.

J. M. Rathborne, S. N. Longmore, J. M. Jackson, J. F. Alves, J. Bally, N. Bastian, Y. Contreras, J. B. Foster, G. Garay, J. M. D. Kruijssen, L. Testi, and A. J. Walsh. A Cluster in the Making: ALMA Reveals the Initial Conditions for High-mass Cluster Formation. *ApJ*, 802:125, Apr 2015. doi: 10.1088/0004-637X/802/2/125.

S. Redfield and J. L. Linsky. The Structure of the Local Interstellar Medium. IV. Dynamics, Morphology, Physical Properties, and Implications of Cloud-Cloud Interactions. *ApJ*, 673:283–314, Jan 2008. doi: 10.1086/524002.

M. A. Reid and C. D. Wilson. High-Mass Star Formation. I. The Mass Distribution of Submillimeter Clumps in NGC 7538. *ApJ*, 625:891–905, June 2005. doi: 10.1086/429790.

E.-J. Rijkhorst, T. Plewa, A. Dubey, and G. Mellema. Hybrid characteristics: 3D radiative transfer for parallel adaptive mesh refinement hydrodynamics. *A&A*, 452:907–920, June 2006a. doi: 10.1051/0004-6361:20053401.

E.-J. Rijkhorst, T. Plewa, A. Dubey, and G. Mellema. Hybrid characteristics: 3D radiative transfer for parallel adaptive mesh refinement hydrodynamics. *A&A*, 452:907–920, June 2006b. doi: 10.1051/0004-6361:20053401.

T. P. Robitaille. HYPERION: an open-source parallelized three-dimensional dust continuum radiative transfer code. *A&A*, 536:A79, Dec 2011. doi: 10.1051/0004-6361/201117150.

P. D. Rogers and J. Wadsley. The importance of photosphere cooling in simulations of gravitational instability in the inner regions of protostellar discs. *MNRAS*, 414:913–929, June 2011. doi: 10.1111/j.1365-2966.2011.18523.x.

P. D. Rogers and J. Wadsley. The fragmentation of protostellar discs: the Hill criterion for spiral arms. *MNRAS*, 423:1896–1908, June 2012. doi: 10.1111/j.1365-2966.2012.21014.x.

J. Rosdahl, J. Blaizot, D. Aubert, T. Stranex, and R. Teyssier. RAMSES-RT: radiation hydrodynamics in the cosmological context. *MNRAS*, 436: 2188–2231, Dec 2013. doi: 10.1093/mnras/stt1722.

E. Rosolowsky. Giant Molecular Clouds in M31. I. Molecular Cloud Properties. *ApJ*, 654:240–251, Jan 2007. doi: 10.1086/509249.

D. Russeil, N. Schneider, L. D. Anderson, A. Zavagno, S. Molinari, P. Persi, S. Bontemps, F. Motte, V. Ossenkopf, P. André, D. Arzoumanian, J.-P. Bernard, L. Deharveng, P. Didelon, J. Di Francesco, D. Elia, M. Hennemann, T. Hill, V. Könyves, J. Z. Li, P. G. Martin, Q. Nguyen Luong, N. Peretto, S. Pezzuto, D. Polychroni, H. Roussel, K. L. J. Rygl, L. Spinoglio, L. Testi, J. Tigé, R. Vavrek, D. Ward-Thompson, and G. White. The Herschel view of the massive star-forming region NGC 6334. *A&A*, 554:A42, June 2013. doi: 10.1051/0004-6361/201219971.

Youcef Saad and Martin H Schultz. Gmres: A generalized minimal residual algorithm for solving nonsymmetric linear systems. *SIAM J. Sci. Stat. Comput.*, 7(3):856–869, July 1986. ISSN 0196-5204. doi: 10.1137/0907058.

C. Safranek-Shrader, M. Agarwal, C. Federrath, A. Dubey, M. Milosavljević, and V. Bromm. Star formation in the first galaxies - I. Collapse delayed by Lyman-Werner radiation. *MNRAS*, 426:1159–1177, Oct 2012. doi: 10.1111/j.1365-2966.2012.21852.x.

V. S. Safronov. On the gravitational instability in flattened systems with axial symmetry and non-uniform rotation. *Annales d'Astrophysique*, 23:979, Feb 1960.

Á. Sánchez-Monge, M. T. Beltrán, R. Cesaroni, S. Etoka, D. Galli, M. S. N. Kumar, L. Moscadelli, T. Stanke, F. F. S. van der Tak, S. Vig, C. M. Walmsley, K.-S. Wang, H. Zinnecker, D. Elia, S. Molinari, and E. Schisano. A necklace of dense cores in the high-mass star forming region G35.20-0.74 N: ALMA observations. *A&A*, 569:A11, Sept 2014. doi: 10.1051/0004-6361/201424032.

D. B. Sanders, N. Z. Scoville, R. P. J. Tilanus, Z. Wang, and S. Zhou. A multi-transition CO and 13CO survey of the Galactic Plane. In S. S. Holt and F. Verter, editors, *Back to the Galaxy*, volume 278 of *American Institute of Physics Conference Series*, pages 311–314, 1993. doi: 10.1063/1.43993.

E. Saury, M.-A. Miville-Deschênes, P. Hennebelle, E. Audit, and W. Schmidt. The structure of the thermally bistable and turbulent atomic gas in the local interstellar medium. *A&A*, 567:A16, July 2014. doi: 10.1051/0004-6361/201321113.

J. Scalo and B. G. Elmegreen. Interstellar Turbulence II: Implications and Effects. *ARA&A*, 42:275–316, Sept 2004. doi: 10.1146/annurev.astro.42.120403.143327.

N. Schneider, T. Csengeri, S. Bontemps, F. Motte, R. Simon, P. Hennebelle, C. Federrath, and R. Klessen. Dynamic star formation in the massive DR21 filament. *A&A*, 520:A49, Sept 2010. doi: 10.1051/0004-6361/201014481.

N. Schneider, S. Bontemps, R. Simon, V. Ossenkopf, C. Federrath, R. S. Klessen, F. Motte, P. André, J. Stutzki, and C. Brunt. The link between molecular cloud structure and turbulence. *A&A*, 529:A1+, May 2011. doi: 10.1051/0004-6361/200913884.

N. Schneider, T. Csengeri, M. Hennemann, F. Motte, P. Didelon, C. Federrath, S. Bontemps, J. Di Francesco, D. Arzoumanian, V. Minier, P. André, T. Hill, A. Zavagno, Q. Nguyen-Luong, M. Attard, J.-P. Bernard, D. Elia, C. Fallscheer, M. Griffin, J. Kirk, R. Klessen, V. Könyves, P. Martin, A. Men'shchikov, P. Palmeirim, N. Peretto, M. Pestalozzi, D. Russeil, S. Sadavoy, T. Sousbie, L. Testi, P. Tremblin, D. Ward-Thompson, and G. White. Cluster-formation in the Rosette molecular cloud at the junctions of filaments. *A&A*, 540:L11, Apr 2012. doi: 10.1051/0004-6361/201118566.

D. Seifried and S. Walch. The impact of turbulence and magnetic field orientation on star-forming filaments. *MNRAS*, 452:2410–2422, Sept 2015. doi: 10.1093/mnras/stv1458.

D. Seifried, R. Banerjee, R. S. Klessen, D. Duffin, and R. E. Pudritz. Magnetic fields during the early stages of massive star formation - I. Accretion and disc evolution. *MNRAS*, 417:1054–1073, Oct 2011a. doi: 10.1111/j.1365-2966.2011.19320.x.

D. Seifried, R. Banerjee, R. S. Klessen, D. Duffin, and R. E. Pudritz. Magnetic fields during the early stages of massive star formation - I. Accretion and disc evolution. *MNRAS*, 417:1054–1073, Oct 2011b. doi: 10.1111/j.1365-2966.2011.19320.x.

D. Seifried, R. Banerjee, R. E. Pudritz, and R. S. Klessen. Disc formation in turbulent massive cores: circumventing the magnetic braking catastrophe. *MNRAS*, 423:L40–L44, June 2012a. doi: 10.1111/j.1745-3933.2012.01253.x.

D. Seifried, R. E. Pudritz, R. Banerjee, D. Duffin, and R. S. Klessen. Magnetic fields during the early stages of massive star formation - II. A generalized outflow criterion. *MNRAS*, 422:347–366, May 2012b. doi: 10.1111/j.1365-2966.2012.20610.x.

D. Seifried, R. Banerjee, R. E. Pudritz, and R. S. Klessen. Disc Formation in Turbulent Cloud Cores: Circumventing the Magnetic Braking Catastrophe. *Astrophysics and Space Science Proceedings*, 36:75, 2014. doi: 10.1007/978-3-319-03041-8_13.

D. Seifried, R. Banerjee, R. E. Pudritz, and R. S. Klessen. Accretion and magnetic field morphology around Class 0 stage protostellar discs. *MNRAS*, 446:2776–2788, Jan 2015. doi: 10.1093/mnras/stu2282.

F. H. Shu. Self-similar collapse of isothermal spheres and star formation. *ApJ*, 214:488–497, June 1977. doi: 10.1086/155274.

F. H. Shu, S. Lizano, and F. C. Adams. Star formation in molecular cloud cores. In M. Peimbert and J. Jugaku, editors, *Star Forming Regions*, volume 115 of *IAU Symposium*, pages 417–433, 1987.

M. A. Skinner and E. C. Ostriker. A Two-moment Radiation Hydrodynamics Module in Athena Using a Time-explicit Godunov Method. *ApJS*, 206:21, June 2013. doi: 10.1088/0067-0049/206/2/21.

R. J. Smith, S. C. O. Glover, and R. S. Klessen. On the nature of star-forming filaments - I. Filament morphologies. *MNRAS*, 445:2900–2917, Dec 2014. doi: 10.1093/mnras/stu1915.

T. Sousbie. The persistent cosmic web and its filamentary structure - I. Theory and implementation. *MNRAS*, 414:350–383, June 2011. doi: 10.1111/j.1365-2966.2011.18394.x.

T. Sousbie, C. Pichon, and H. Kawahara. The persistent cosmic web and its filamentary structure - II. Illustrations. *MNRAS*, 414:384–403, June 2011. doi: 10.1111/j.1365-2966.2011.18395.x.

L. Spitzer. *Physical processes in the interstellar medium*. Wiley, 1978. ISBN 9780471293354.

T. K. Sridharan, H. Beuther, P. Schilke, K. M. Menten, and F. Wyrowski. High-Mass Protostellar Candidates. I. The Sample and Initial Results. *ApJ*, 566:931–944, Feb 2002. doi: 10.1086/338332.

T. K. Sridharan, H. Beuther, M. Saito, F. Wyrowski, and P. Schilke. High-Mass Starless Cores. *ApJL*, 634:L57–L60, Nov 2005. doi: 10.1086/498644.

S. W. Stahler. The birthline for low-mass stars. *ApJ*, 274:822–829, Nov 1983. doi: 10.1086/161495.

S. W. Stahler, F. Palla, and P. T. P. Ho. The Formation of Massive Stars. *Protostars and Planets IV*, pages 327–352, May 2000.

J. L. Starck, D. L. Donoho, and E. J. Candès. Astronomical image representation by the curvelet transform. *A&A*, 398:785–800, Feb 2003a. doi: 10.1051/0004-6361:20021571.

J.-L. Starck, F. Murtagh, E. J. Candes, and D. L. Donoho. Gray and color image contrast enhancement by the curvelet transform. *IEEE Transactions on Image Processing*, 12:706–717, June 2003b. doi: 10.1109/TIP.2003.813140.

J. Stil, N. Wityk, R. Ouyed, and A. R. Taylor. Three-dimensional Simulations of Magnetized Superbubbles: New Insights into the Importance of MHD Effects on Observed Quantities. *ApJ*, 701:330–347, Aug 2009. doi: 10.1088/0004-637X/701/1/330.

S. Storm, L. G. Mundy, M. Fernández-López, K. I. Lee, L. W. Looney, P. Teuben, E. Rosolowsky, H. G. Arce, E. C. Ostriker, D. M. Segura-Cox, M. W. Pound, D. M. Salter, N. H. Volgenau, Y. L. Shirley, C.-Y. Chen, H. Gong, A. L. Plunkett, J. J. Tobin, W. Kwon, A. Isella, J. Kauffmann, K. Tassis, R. M. Crutcher, C. F. Gammie, and L. Testi. CARMA Large Area Star Formation Survey: Project Overview with Analysis of Dense Gas Structure and Kinematics in Barnard 1. *ApJ*, 794:165, Oct 2014. doi: 10.1088/0004-637X/794/2/165.

K. Sugitani, F. Nakamura, M. Watanabe, M. Tamura, S. Nishiyama, T. Nagayama, R. Kandori, T. Nagata, S. Sato, R. A. Gutermuth, G. W. Wilson, and R. Kawabe. Near-infrared-imaging Polarimetry Toward Serpens South:

Revealing the Importance of the Magnetic Field. *ApJ*, 734:63, June 2011. doi: 10.1088/0004-637X/734/1/63.

S. Z. Takahashi, Y. Tsukamoto, and S.-i. Inutsuka. A revised condition for self-gravitational fragmentation of protoplanetary disks. *ArXiv e-prints*, March 2016.

J. C. Tan and C. F. McKee. Outflow-Confined HII Regions and the Formation of Massive Stars by Accretion. *ArXiv Astrophysics e-prints*, Sept 2003.

J. C. Tan, S. Kong, M. J. Butler, P. Caselli, and F. Fontani. The Dynamics of Massive Starless Cores with ALMA. *ApJ*, 779:96, Dec 2013. doi: 10.1088/0004-637X/779/2/96.

G. Tenorio-Tagle. The gas dynamics of H II regions. I - The champagne model. *A&A*, 71:59–65, Jan 1979.

A. G. G. M. Tielens. *The Physics and Chemistry of the Interstellar Medium*. Aug 2005.

D. A. Tilley and R. E. Pudritz. The formation of star clusters - II. 3D simulations of magnetohydrodynamic turbulence in molecular clouds. *MNRAS*, 382:73–94, Nov 2007. doi: 10.1111/j.1365-2966.2007.12371.x.

K. Tomisaka. Collapse-Driven Outflow in Star-Forming Molecular Cores. *ApJL*, 502:L163–L167, Aug 1998. doi: 10.1086/311504.

A. Toomre. On the gravitational stability of a disk of stars. *ApJ*, 139:1217–1238, May 1964. doi: 10.1086/147861.

C. A. Tout, O. R. Pols, P. P. Eggleton, and Z. Han. Zero-age main-seqence radii and luminosities as analytic functions of mass and metallicity. *MNRAS*, 281:257–262, July 1996.

J. K. Truelove, R. I. Klein, C. F. McKee, J. H. Holliman, II, L. H. Howell, and J. A. Greenough. The Jeans Condition: A New Constraint on Spatial Resolution in Simulations of Isothermal Self-gravitational Hydrodynamics. *ApJL*, 489:L179–L183, Nov 1997. doi: 10.1086/310975.

J. K. Truelove, R. I. Klein, C. F. McKee, J. H. Holliman, II, L. H. Howell, J. A. Greenough, and D. T. Woods. Self-gravitational Hydrodynamics with Three-dimensional Adaptive Mesh Refinement: Methodology and Applications to Molecular Cloud Collapse and Fragmentation. *ApJ*, 495:821–852, March 1998. doi: 10.1086/305329.

J. Trujillo Bueno and P. Fabiani Bendicho. A Novel Iterative Scheme for the Very Fast and Accurate Solution of Non-LTE Radiative Transfer Problems. *ApJ*, 455:646, Dec 1995. doi: 10.1086/176612.

M. J. Turk, B. D. Smith, J. S. Oishi, S. Skory, S. W. Skillman, T. Abel, and M. L. Norman. yt: A Multi-code Analysis Toolkit for Astrophysical Simulation Data. *ApJS*, 192:9, Jan 2011. doi: 10.1088/0067-0049/192/1/9.

N. J. Turner and J. M. Stone. A Module for Radiation Hydrodynamic Calculations with ZEUS-2D Using Flux-limited Diffusion. *ApJS*, 135:95–107, July 2001. doi: 10.1086/321779.

J. E. Vaillancourt. Polarized Emission from Interstellar Dust. In M.-A. Miville-Deschênes and F. Boulanger, editors, *EAS Publications Series*, volume 23 of *EAS Publications Series*, pages 147–164, 2007. doi: 10.1051/eas:2007010.

A. J. van Marle, Z. Meliani, and A. Marcowith. Shape and evolution of wind-blown bubbles of massive stars: on the effect of the interstellar magnetic field. *ArXiv e-prints*, Sept 2015.

N. Vaytet, E. Audit, and B. Dubroca. A Numerical Model for Multigroup Radiation Hydrodynamics. In N. V. Pogorelov, E. Audit, and G. P. Zank, editors, *Numerical Modeling of Space Plasma Flows, Astronum-2009*, volume 429 of *Astronomical Society of the Pacific Conference Series*, page 160, Sept 2010.

E. Vazquez-Semadeni, E. C. Ostriker, T. Passot, C. F. Gammie, and J. M. Stone. Compressible MHD Turbulence: Implications for Molecular Cloud and Star Formation. *Protostars and Planets IV*, page 3, May 2000.

E. Vázquez-Semadeni, J. Ballesteros-Paredes, and R. S. Klessen. A Holistic Scenario of Turbulent Molecular Cloud Evolution and Control of the Star Formation Efficiency: First Tests. *ApJL*, 585:L131–L134, March 2003. doi: 10.1086/374325.

J. G. Vestuto, E. C. Ostriker, and J. M. Stone. Spectral Properties of Compressible Magnetohydrodynamic Turbulence from Numerical Simulations. *ApJ*, 590:858–873, June 2003. doi: 10.1086/375021.

S. Walch, A. P. Whitworth, T. G. Bisbas, D. A. Hubber, and R. Wünsch. Comparing simulations of ionization triggered star formation and observations in RCW 120. *MNRAS*, 452:2794–2803, Sept 2015. doi: 10.1093/mnras/stv1427.

S. K. Walch, A. P. Whitworth, T. Bisbas, R. Wünsch, and D. Hubber. Dispersal of molecular clouds by ionizing radiation. *MNRAS*, 427:625–636, Nov 2012. doi: 10.1111/j.1365-2966.2012.21767.x.

R. L. Ward, J. Wadsley, A. Sills, and N. Petitclerc. Connecting the Dots: Analyzing Synthetic Observations of Star-forming Clumps in Molecular Clouds. *ApJ*, 756:119, Sept 2012. doi: 10.1088/0004-637X/756/2/119.

D. Ward-Thompson, J. M. Kirk, P. André, P. Saraceno, P. Didelon, V. Könyves, N. Schneider, A. Abergel, J.-P. Baluteau, J.-P. Bernard, S. Bontemps, L. Cambrésy, P. Cox, J. di Francesco, A. M. di Giorgio, M. Griffin, P. Hargrave, M. Huang, J. Z. Li, P. Martin, A. Men'shchikov, V. Minier, S. Molinari, F. Motte, G. Olofsson, S. Pezzuto, D. Russeil, M. Sauvage, B. Sibthorpe, L. Spinoglio, L. Testi, G. White, C. Wilson, A. Woodcraft, and A. Zavagno. A Herschel study of the properties of starless cores in the Polaris Flare dark cloud region using PACS and SPIRE. *A&A*, 518:L92, July 2010. doi: 10.1051/0004-6361/201014618.

C. Weidner and P. Kroupa. Evidence for a fundamental stellar upper mass limit from clustered star formation. *MNRAS*, 348:187–191, Feb 2004. doi: 10.1111/j.1365-2966.2004.07340.x.

C. Weidner, P. Kroupa, and I. A. D. Bonnell. The relation between the most-massive star and its parental star cluster mass. *MNRAS*, 401:275–293, Jan 2010. doi: 10.1111/j.1365-2966.2009.15633.x.

S. C. Whitehouse and M. R. Bate. The thermodynamics of collapsing molecular cloud cores using smoothed particle hydrodynamics with radiative transfer. *MNRAS*, 367:32–38, March 2006. doi: 10.1111/j.1365-2966.2005.09950.x.

J. P. Williams, L. Blitz, and C. F. McKee. The Structure and Evolution of Molecular Clouds: from Clumps to Cores to the IMF. *Protostars and Planets IV*, page 97, May 2000.

M. G. Wolfire and J. P. Cassinelli. The temperature structure in accretion flows onto massive protostars. *ApJ*, 310:207–221, Nov 1986. doi: 10.1086/164676.

M. G. Wolfire and J. P. Cassinelli. Conditions for the formation of massive stars. *ApJ*, 319:850–867, Aug 1987. doi: 10.1086/165503.

H. W. Yorke and P. Bodenheimer. The Formation of Protostellar Disks. III. The Influence of Gravitationally Induced Angular Momentum Transport on Disk Structure and Appearance. *ApJ*, 525:330–342, Nov 1999. doi: 10.1086/307867.

H. W. Yorke and E. Krügel. The dynamical evolution of massive protostellar clouds. *A&A*, 54:183–194, Jan 1977.

H. W. Yorke and C. Sonnhalter. On the Formation of Massive Stars. *ApJ*, 569:846–862, Apr 2002. doi: 10.1086/339264.

W. Zhang, L. Howell, A. Almgren, A. Burrows, and J. Bell. CASTRO: A New Compressible Astrophysical Solver. II. Gray Radiation Hydrodynamics. *ApJS*, 196:20, Oct 2011. doi: 10.1088/0067-0049/196/2/20.

W. Zhang, L. Howell, A. Almgren, A. Burrows, J. Dolence, and J. Bell. CASTRO: A New Compressible Astrophysical Solver. III. Multigroup Radiation Hydrodynamics. *ApJS*, 204:7, Jan 2013. doi: 10.1088/0067-0049/204/1/7.

H. Zinnecker and H. W. Yorke. Toward Understanding Massive Star Formation. *ARA&A*, 45:481–563, Sept 2007. doi: 10.1146/annurev.astro.44.051905.092549.

B. Zuckerman and N. J. Evans, II. Models of massive molecular clouds. *ApJL*, 192:L149–L152, Sept 1974. doi: 10.1086/181613.